Synthese, Charakterisierung und Anwendung von Membranen auf Basis von Metall-Organischen Gerüstverbindungen

Inauguraldissertation

zur

Erlangung des Doktorgrades *Dr. rer. nat.*

der Mathematisch-Naturwissenschaftlichen Fakultät

der Heinrich-Heine-Universität Düsseldorf

vorgelegt von

Janina Dechnik

aus Düsseldorf

Düsseldorf, Juni 2017

aus dem Institut für Anorganische und Strukturchemie I
der Heinrich-Heine Universität Düsseldorf

Gedruckt mit der Genehmigung der
Mathematisch-Naturwissenschaftlichen Fakultät der
Heinrich-Heine-Universität Düsseldorf

Referent:	Prof. Dr. C. Janiak
Korreferent:	Prof. Dr. C. Ganter

Tag der mündlichen Prüfung: 20.07.2017

Die vorliegende Arbeit wurde in der Zeit von September 2012 bis Juni 2017 an der Heinrich-Heine-Universität Düsseldorf im Institut für Anorganische Chemie und Strukturchemie I im Arbeitskreis von Prof. Dr. Christoph Janiak angefertigt.

- Im Februar 2014 wurde ein Teil der Arbeiten an der University of Zaragoza (Spanien), in der Arbeitsgruppe von Prof. Dr. Coronas im Rahmen eines Workshops durchgeführt.
- Im April 2014 wurde ein Teil der Arbeiten am Institute of Technology Kharagpur (Indien), in der Arbeitsgruppe von Prof. Dr. De im Rahmen eines Workshops durchgeführt.
- Im Februar 2015 wurde ein Teil der Arbeiten an der Faculty of Science der Suez University (Ägypten), in der Arbeitsgruppe von Prof. Dr. El-Shaarawy im Rahmen eines Austauschprogramms durchgeführt.
- Im März 2015 wurde ein Teil der Arbeiten an der Wuhan University of Technology (China), in der Arbeitsgruppe von Prof. Dr. Xiao-Yu Yang im Rahmen eines Austauschprogramms durchgeführt.
- Im September 2015 wurde ein Teil der Arbeiten am Institute of Chemistry of the Academy of Sciences of Moldova (Moldawien), in der Arbeitsgruppe von Prof. Dr. Lozan im Rahmen eines Workshops durchgeführt.

Publikationen

Sankha Karmakar, **Janina Dechnik**, Christoph Janiak and Sirshendu De
Aluminium fumarate metal-organic framework: A super adsorbent for fluoride from water
J. Hazard. Mater., **2016**, 303, 10-20.

Janina Dechnik, Friedrich Mühlbach, Dennis Dietrich, Tobias Wehner, Marcus Gutmann, Tessa Lühmann, Lorenz Meinel, Christoph Janiak and Klaus Müller-Buschbaum
Luminescent Metal–Organic Framework Mixed-Matrix Membranes from Lanthanide Metal–Organic Frameworks in Polysulfone and Matrimid
Eur. J. Inorg. Chem., **2016**, 27, 4408-4415.

Gamall Makhloufi, Biju Francis, **Janina Dechnik**, Alexander Strzelczyk and Christoph Janiak
Hydrophilic microporous lanthanide-organic frameworks based on 4,4′-biphenyldiacetate: Synthesis, crystal structures and sorption properties
Polyhedron, **2017**, 127, 59-67.

Adelaida Perea-Cachero, **Janina Dechnik**, Ruth Lahoz, Christoph Janiak, Carlos Téllez and Joaquin Coronas
HKUST-1 coatings on laser-microperforated brass supports for water adsorption
CrystEngComm, **2017**, 19, 1470-1478.

Janina Dechnik, Jorge Gascon, Christian Doonan, Christoph Janiak and Christopher James Sumby,
Mixed-Matrix Membranes
Angew. Chem., Int. Ed., **2017**, in press, DOI: 10.1002/anie.201701109.

Janina Dechnik, Alexander Nuhnen, Christoph Janiak
Mixed-Matrix Membranes of the air-stable MOF-5 analog $[Co_4(\mu_4\text{-}O)(Me_2pzba)_3]$ with mixed-functional pyrazolate-carboxylate linker for CO_2/CH_4 separation
Cryst. Growth Des., **2017**, in press, DOI: 10.1021/acs.cgd.7b0020

Janina Dechnik, Christopher James Sumby, Christoph Janiak
Enhancing Mixed-Matrix Membrane Performance with Metal-Organic Framework Additives
Cryst. Growth Des., **2017,** in press, DOI: 10.1021/acs.cgd.7b00595.

Für meine Familie

Danksagung

Im Folgenden möchte ich mich bei all denjenigen bedanken, die zum Gelingen dieser Arbeit beigetragen haben. Mein besonderer Dank gilt meinem Doktorvater Prof. Dr. Christoph Janiak, für die Möglichkeit diese Dissertation in seinem Arbeitskreis anfertigen zu können. Weiterhin bedanke ich mich für die konstruktiven Diskussionen, die Korrektur von Manuskripten, die mir gewährten fachlichen Freiräume und das in mich gesetzte Vertrauen in meiner Zeit an seinem Lehrstuhl sowie die Ermöglichung des internationalen wissenschaftlichen Austauschs.

Herrn Prof. Dr. Christian Ganter danke ich für die freundliche Übernahme des Co-Referates dieser Arbeit und für die interessanten wissenschaftlichen Anregungen im gemeinsamen Seminar.

Herzlich danke ich allen Mitarbeitern der beiden Arbeitsgruppen des Instituts für Anorganische Chemie I für die fortwährende Unterstützung, gute Zusammenarbeit und freundliche Atmosphäre. Für die organisatorische und geduldige Hilfe in vielen Fragen des Institutsalltags danke ich Claudia Schäfer, Birgit Tommes, Annette Ricken, Marcell Demandt, Dietmar Frunzke und Axel Mundt. In ganz besonderen Maße möchte ich folgenden Personen für ihren großen Beitrag zur entspannten und produktiven Arbeitsatmosphäre Danken: Gamall Makhloufi, Jana Reineke, Anna Goldman, Simon Millan, Kai Schütte, Sebastian Appel und Kai Ries. Danke für die tolle Stimmung und das schöne Zusammensein in jeder Phase dieser Arbeit sowohl fachlich als auch privat, die Motivation zum richtigen Zeitpunkt und die Herausforderungen. Für die freundlichen Ratschläge zu Messungen und anderen Aufbauten danke ich Dennis Dietrich und Annika Herbst für die REM Messungen und den immerwährenden sehr interessierten fachlichen Austausch. In gleicher Weise gilt mein Dank Sebastian Glomb, Niels Tannert und Emrah Hastürk für die Unterstützung bei Sorptionsmessungen, Carsten Schlüsener und Ülkü Kökçam-Demir zur Röntgenpulverdiffraktometrie sowie Christian Heering bei Fragen zur Synthese. Ich danke den B.Sc. Absolventen für ihre engagierte Zusammenarbeit, besonders Alexander Nuhnen für seine Unterstützung im Labor, für das über die Abschlussarbeit hinausgehende Interesse an dem Forschungsgebiet und die tolle Arbeitsatmosphäre. Meinen ehemaligen Bürokollegen Martin Wickenheisser, Sebastian Glomb, Dennis Dietrich, Subarna Dey, Anna Kautz, Dr. Reda Elshaarawy und Susann Wegner Danke ich für die guten Gespräche und nette Büroatmosphäre.

Mein ganz besonderer Dank gilt meiner Familie und vor allem meinen Eltern für das Vertrauen, die liebevolle Unterstützung, das Verständnis und die Geduld während meiner gesamten Ausbildung. Ohne diese Grundlage wäre diese Arbeit nicht möglich gewesen.

Düsseldorf, im Juni 2017

Zusammenfassung

Metall-organische Gerüstverbindungen (MOFs), haben aufgrund ihrer strukturellen Vielfalt, Flexibilität und Anpassbarkeit, sowie einer hohen potentiellen Porosität ein enormes Forschungsinteresse sowohl in der akademischen Welt als auch in der Industrie erregt, da sie durch ihre Eigenschaften als poröses Material für ein breites Spektrum von Anwendungen wie z.B. Gasspeicherung und -trennung, Sorption von Wasser oder anderen Lösemitteln, gastabhängige Lumineszenz und selektive heterogene Katalyse in Frage kommen. Die Verwendung von MOFs für membranbasierte Gastrennung oder -speicherung ist der Schwerpunkt dieser Arbeit und beschäftigt sich mit der Herstellung, Charakterisierung und dem Anwendungspotential dieser Materialien. Die Resultate der in der Fachliteratur dargestellten Entwicklung der neuesten Methoden zum Aufbau von MOF-Mixed-Matrix-Membranen (MMMs) und die Auswirkung der Herstellung und Modifikationsmethoden von MOFs auf Permeabilität und Selektivität wenn diese als Füllstoffe in Polymere eingebettet werden, beziehen sich vorwiegend auf optimale Füllstoffbeladung und Membranintegrität bei hohen Füllstoffbeladungen oder verbesserter Füllstoffleistung zur Steigerung der Trennleistungen von MMMs. Deutlich wird, dass Strategien wie die Modulation der MOF-Synthese und die Kontrolle der Partikelgröße entscheidend sind, um Additive für leistungsstarke MMMs zu entwerfen. Die Verwendung chemischer Modifikationen können ebenfalls genutzt werden, um nicht nur die Leistung für eine spezifische Anwendung zu erhöhen, sondern auch die Stabilität dieser Füllstoffe. In der vorliegenden Arbeit wurde das zu MOF-5 analoge $[Co_4(\mu_4\text{-}O)(Me_2pzba)_3]$ für die Herstellung von MMMs auf Matrimid-Basis verwendet und die Feuchtigkeitsstabilität im Vergleich zum prototypischen MOF-5 ausgiebig untersucht, mit dem Ergebnis, dass eine moderat verbesserte Stabilität durch die Einführung des bifunktionellen Liganden in das Netzwerk bewirkt wird. Eine Optimierung der Synthese konnte durch eine Synthese in der Mikrowelle erreicht werden, so dass das Material hinsichtlich Ausbeute, Reaktionszeit, BET-Oberfläche, Partikelgrößenverteilung und Aggregation für die Einbettung in MMMs besser geeignet war, als das konventionell hergestellte Produkt. Die MMMs zeigten in der CO_2/CH_4-Selektivität für 24 Gew.-% Füllstoffbeladung eine Erhöhung von mehr als 46 % im Vergleich zur reinen Matrimid-Membran. Zusätzlich verbesserte sich die Permeabilität für CO_2 um 49 %. Im Vergleich zu anderen Matrimid-basierten MMMs mit MOF-5 oder anderen prototypischen MOFs und Derivaten zeigen die hier hergestellten Materialien eine deutliche Verbesserung der Selektivität.

Die Herstellung von reinen MOF-Schichten auf porösen Trägermaterialien für Trenn- oder Sorptionsprozesse bietet häufig die Herausforderung, dass die Stabilität der hergestellten reinen MOF-Filme durch schlechte Anbindung an das Trägermaterial nicht gewährleistet

werden kann. Durch die Verwendung von lasermikroperforierten Messingträgern in Kombination mit einem Temperaturgradienten-Verfahren konnten gleichmäßige HKUST-1 Schichten mit guter Kristallinität und hoher Gasaufnahme sowie guter Anbindung an das Trägermaterial hergestellt werden. Stickstoff- und Wassersorptionsmessungen zeigen, dass die Porosität auch nach der Trägerung erhalten bleibt und so ein vollständiger Adsorbatzugang zu den Poren für mögliche Anwendung in sorptionsbasierten Prozessen gewährleistet ist.

Die Herstellung von MMMs bringt im Verbund der Materialien auch den Vorteil mit sich, dass stark hydrolyse- oder oxidationsempfindliche Füllstoffe im Polymerfilm gegenüber Umgebungseinflüsse wie Luftsauerstoff oder Feuchtigkeit stabilisiert werden können. MMMs aus 3D-$[Sr_{0.9}Eu_{0.1}Im_2]$ und 2D-$[Tb_2Cl_6(bipy)_3]\cdot 2bipy$ wurden zur besseren Verarbeitbarkeit der Bulk-MOFs mit dem Polysulfon Ultrason S und mit Polyimid Matrimid als Matrix hergestellt. Für die MMMs aus $[Sr_{0.9}Eu_{0.1}Im_2]$ mit PSF, $[Sr_{0.9}Eu_{0.1}Im_2]$ mit Matrimid und $[Tb_2Cl_6(bipy)_3]\cdot 2bipy$ mit PSF, blieb die Lumineszenz des MOF auch nach der Filmherstellung erhalten und ist besonders stark für die MMMs aus $[Sr_{0.9}Eu_{0.1}Im_2]$ mit PSF. Die Membranpolymere beeinflussen die Lumineszenzintensität: In den Polysulfonmembranen zeigen beide MOFs eine höhere Emissionsintensität bei niedrigen MOF-Anteilen, während Matrimid als Matrix das entgegengesetzte Verhalten zeigt.

Short Summary

Due to their structural diversity, flexibility and adaptability as well as their high porosity, metal-organic frameworks (MOFs) have attracted tremendous interest both in academic and in industry as a class of porous materials. They show high potential for a wide range of applications such as gas storage and separation, sorption of water or other solvents, guest dependent luminescence and heterogeneous catalysis. The use of MOFs for membrane-based separation or storage is the main focus of this work and deals with the fabrication, characterization and application potential of these materials. The results of the development of the latest methods for the synthesis of MOF mixed-matrix membranes (MMMs) as well as the effect of the preparation and modification methods of MOFs on permeability and selectivity when embedded as fillers in polymers are mainly based on optimal filler loading and membrane integrity at higher loading levels or improved filler capacity for increasing the separation performance of MMMs. It becomes apparent that strategies such as modulation of MOF synthesis and particle size control are substantial in designing additives for high-performance MMMs and that the use of chemical modifications can also be used to increase not only the performance for a specific application, but also the stability of the fillers. The MOF-5-analog $[Co_4(\mu_4\text{-}O)(Me_2pzba)_3]$ was used for the preparation of MOF-MMMs with Matrimid and was extensively tested concerning moisture stability compared to the prototypic MOF-5 which showed moderately improved stability by introducing the bifunctional ligand into the network. Optimization of the synthesis was achieved by means of a microwave-assisted synthesis route, so that the material was better suited than the solvothermal product for the embedment in MMMs in terms of yield, reaction time, BET surface area, particle size distribution and aggregation. The MMMs show an increase of more than 46% in the CO_2/CH_4 selectivity for 24 wt% filler loading in relation to the pure Matrimid membrane together with an improved permeability of 49 % for CO_2. Compared to other Matrimid-based MMMs with MOF-5 or other prototypic MOFs and derivatives, the materials produced show a high increase in selectivity.

The fabrication of pure MOF layers on porous support materials for separation or sorption processes often brings the problem that the stability of the pure MOF films is not ensured due to poor attachment to the supports. The use of laser-micro-perforated brass supports in combination with a thermal gradient synthesis enabled the formation of uniform HKUST-1 layers with good crystallinity and high gas adsorption capacities as well as good bonding to the support material. Nitrogen and water sorption experiments show that the porosity is retained and thus a complete adsorbent access to the pores is ensured for possible application in sorption-based processes.

The preparation of MMMs also have the advantage, while combining the two materials, that strongly hydrolysis- or oxidation-sensitive fillers can be stabilized against ambient influences such as oxygen or moisture in the polymer film. MMMs were prepared from 3D-[$Sr_{0.9}Eu_{0.1}Im_2$] and 2D-[$Tb_2Cl_6(bipy)_3$]·2bipy with the polysulfone Ultrason S and with the polyimide Matrimid as a matrix to improve the processability of bulk MOFs. For the MMMs from [$Sr_{0.9}Eu_{0.1}Im_2$] with PSF, [$Sr_{0.9}Eu_{0.1}Im_2$] with Matrimid and [$Tb_2Cl_6(bipy)_3$]·2bipy with PSF, the luminescence of the MOF also remained after film formation and is particularly strong for the MMMs from [$Sr_{0.9}Eu_{0.1}Im_2$] with PSF. The membrane polymers influence the luminescence intensity. In the polysulfone membranes, both MOFs show higher emission intensity at low MOF loading ratios, whereas Matrimid as a matrix shows the opposite behavior.

Inhaltsverzeichnis

1. Enhancing Mixed-Matrix Membrane Performance with Metal−Organic Framework Additives[i]

1.1 Introduction

Artificial membranes are frequently used in chemical industrial processes. Membranes are thin layers which provide a resistance to the passage of different substances. Theoretically they can be used in any process for the separation of substances. Gas purification, the production of drinking water from seawater (water desalination), the purification of sewage or the recovery of fuel vapors are some of the most important examples of membrane applications.[3]

Membrane Separation Processes are very versatile and are specified by their application demand, i.e. in industrial processes, or in the production of purified substances. The specification of which kind of membrane material or process is applied depends on the given separation problem and the conditions like feed composition, compression of feed streams, or contamination by substances which influence the separation process. The process or membrane material that is to be chosen for a specific separation problem is mainly determined by the size of the components of the mixture. Research into the development of new membrane materials mostly focuses on the development of dense polymer membranes where the effect of modifications is also studied compared to the pure or unmodified polymer material. Such membranes are characterized for gas separations because of the very similar size of the substances and the demand for industrial application. Industrial separation processes are commonly carried out with conventional methods, such as, distillation, crystallization or absorption. The use of membrane separation processes often proves to be more advantageous than these methods for many applications. Particularly the lower costs, the lower energy consumption and simpler process condition make membrane separation processes the preferred technology for the purification of mixtures.[4] Membrane separation processes can give energy savings of up to 50% of the production cost over other separation technologies.[5-6] Membrane processes, which are already in place in industry, include the removal of CO_2 from natural gas (before the natural gas can be passed to the pipeline), the isolation and recovery of hydrogen (for example in cracking processes), and oxygen/nitrogen separation from air (for enriched oxygen in

[i] This Section reviews the recent reported significant strategies for metal-organic framework inclusion in mixed-matrix membranes and fundamentals of gas separation processes are introduced. The work was published, in this form, as a review article in Crystal Growth & Design 2017 ref[1]. With a different focus (i.e. in the context of new materials choices compared to new MMM fillers like porous organic frameworks and porous molecular additives like porous metalorganic Polyhedra (POMs) and porous organic Cages (POCs)) a similar and shorter version was published as part of a review article in Angewandte Chemie in 2017 ref.[2] (cf. chapter 3.1.).

medical devices and enriched nitrogen used for oxygen sensitive materials).[4,7] Membrane processes for vapor[8] or monomer recovery, e.g. ethylene/N_2 or propylene/N_2 separation,[9-10] or for the removal of water or larger molecules from organic solvents[11] are increasingly applied. Organic polymers are typically used for commercial membranes as they are inexpensive and easy to manufacture.

1.1.1 Membrane performance characteristics for gas separation

Permeability and selectivity (*permselectivity*) are basic characteristics for membrane materials and the industrial feasibility of membrane processes.[12] Permeability or the permeability coefficient P_i is defined as the Flux of the gas *i* through the membrane, normalized by the difference of the partial pressure (Δp) of this gas on both sites of the membrane per unit layer thickness (*d*) of the membrane. (Eq. 1). The *Flux* of the gas *i* corresponds to the flow rate (*Q*) per unit of the membrane area (*A*) (Eq. 2). The permeability is given in the unit *Barrer* [1 Barrer = 1×10^{-10} cm^3 (STP) cm/(cm^2 s cmHg) or 7.5005×10^{-18} m^2 s^{-1} Pa^{-1} in SI units] or *gas permeation unit (GPU)* if the thickness of the separating layer is not well known [1 GPU = 10^{-6} cm^3(STP) cm^{-2} $cmHg^{-1}$ = 0.344×10^{-10} mol m^{-2} s^{-1} Pa^{-1}].[13]

$$P_i = \frac{Flux_i \cdot d}{\Delta p_i} \qquad (1)$$

$$Flux_i = \frac{Q_i}{A} \qquad (2)$$

Through Fick's first law, Eq. (1) can be rearranged so that permeability is expressed as a product of the diffusivity, D_i, and solubility, S_i, of penetrant *i* (Eq. (3)).[14]

$$P_i = D_i \cdot S_i \qquad (3)$$

Selectivity is the separation factor for a component from the mixture: For mixtures of gases *i* and *j* the selectivity *a* is calculated by Eq. (4),

$$\alpha_{i,j} = \frac{Y_i / Y_j}{X_i / X_j} \qquad (4)$$

where Y_i and Y_j are the mole fractions of the components produced in the permeate, while X_i and X_j are their corresponding mole fractions in the feed. Mole fractions for the feed side appear to be difficult to determine on a lab scale and often the feed fraction *X* is taken as (1 –*Y*).[15] Alternatively, the separation factor $S_{i,j} = P_i/P_j$ is calculated as the ratio of the permeability *P* of the more permeable compound (*i*) to the permeability of the less permeable compound (*j*), for single-gas ($S_{i,j,ideal}$) and mixed-gas measurements ($S_{i,j,real}$).[16] In the case where the gases do not interact strongly with each other or with the membrane

material, the ideal and real selectivity are the same and are also equal to the separation factor a_{ij} (Eq. (4))

The permeability P_i from the 'constant volume – variable pressure' method is calculated by Eq. (5) where V_d is the downstream collection volume [cm^3], d is the thickness of the membrane, p_2 is the absolute pressure of the feed gas, A is the area of the membrane available for permeation [cm^2], R is the universal gas constant, T [K] is the experimental temperature, as well as $(dp_1 / dt)_{ss}$ and $(dp_1 / dt)_{leak}$ for the equilibrium rates of pressure rise caused by permeation of the gas and leak rate of the permeate volume of the plant in [mbar/min].[15-16]

$$P_i = \frac{V_d * d}{p_2 * A * R * T} * \left[\left(\frac{dp_1}{dt}\right)_{ss} - \left(\frac{dp_1}{dt}\right)_{leak}\right] \qquad (5)$$

For measurement approaches with continuous flow or 'constant-pressure and variable-volume', direct measurement of the steady-state gas flow rate (Q) on the permeate side of a membrane is achieved using a flow meter.

In mixed-gas measurements with the 'sweep gas' method, the concentration of the permeate components in the sweep gas stream and the sweep gas flow rate Q_{sweep} is measured. The permeability P_i of gas i can be calculated according to Eq. (6) where $x_{1,i}$ is the molar fraction of gas i in the permeate, $x_{2,i}$ is the molar fraction of gas i in the feed and $x_{1,\,sweep}$ is the molar fraction of helium in the permeate.

$$P_i = \frac{x_{1,i} * Q_{sweep} * d}{x_{1,sweep} * A * (p_2 * x_{2,i} - p_1 * x_{1,i})} \qquad (6)$$

The gas flow through the membrane is usually measured at 'constant pressure and variable volume' or with 'variable pressure and constant volume'. For mixed gas additionally a special sensor is used to determine the mole fractions of the components in gas streams. In the method to measure gas permeation with constant volume and variable pressure, the permeate flow is determined by detecting the pressure increase by a pressure transducer in a constant-volume cell in which permeate flows through the membrane.[16] For measurement approaches with 'continuous flow' or 'constant-pressure and variable-volume', direct measurement of the steady-state gas flow rate on the permeate side of a membrane is achieved using a flow meter. Commonly electronic flow meters or capillary soap-bubble flow meters are used for this purpose. Both methods can be used to directly measure the single gas permeability when pure gases are used as feed. If a gas mixture is applied as the feed gas, either the collected gas volume at steady state or a sample of the continuous flowing gas stream is directed to, for example, a gas chromatograph to determine the permeate composition. Alternatively the permeating gas is directed from the membrane to the sensor system using a sweep gas stream at atmospheric pressure.

All abovementioned methods are commonly used in studies on membrane gas separation performance (cf. Table 1) but in order to evaluate the practical separation performance of membranes, mixed-gas permeation tests should be performed. The mixed-gas permeability of membranes can be reduced, compared to their corresponding single gas permeabilities, due to the effect of permeate competition from the competitive sorption and diffusion of both gases.[17] Ideally a membrane should have both a high permeability and a high selectivity. The lower the permeability the larger the membrane area needed or the number of membrane modules for the given gas volume and time factor. Lower selectivity requires more steps in the separation with more complex operations, typically leading to higher costs. Large volume separations, such as O_2/N_2 for oxy-combustion or CO_2/CH_4 for natural gas treatments require highly permeable membranes. In some cases ultrahigh membrane selectivity is not necessarily desirable for large-scale gas separations, as for example, CO_2 separation from natural gas. This is because the permeate concentration of the more permeable gas reaches a plateau even as the selectivity continues to increase. Thus, a membrane with very high permeability and good selectivity may be more industrially attractive for large-scale applications.[18] In many industrial gas separations, process economics also limit the pressure ratio (feed pressure/permeate pressure) that can be used. As a consequence, the optimum membrane may not be the one with the highest selectivity, and membranes with different selectivities may be preferred in different portions of separation plants.[19] The factors which influence the process economics and thereby determine the properties of the optimum membrane are illustrated in Figure 1.

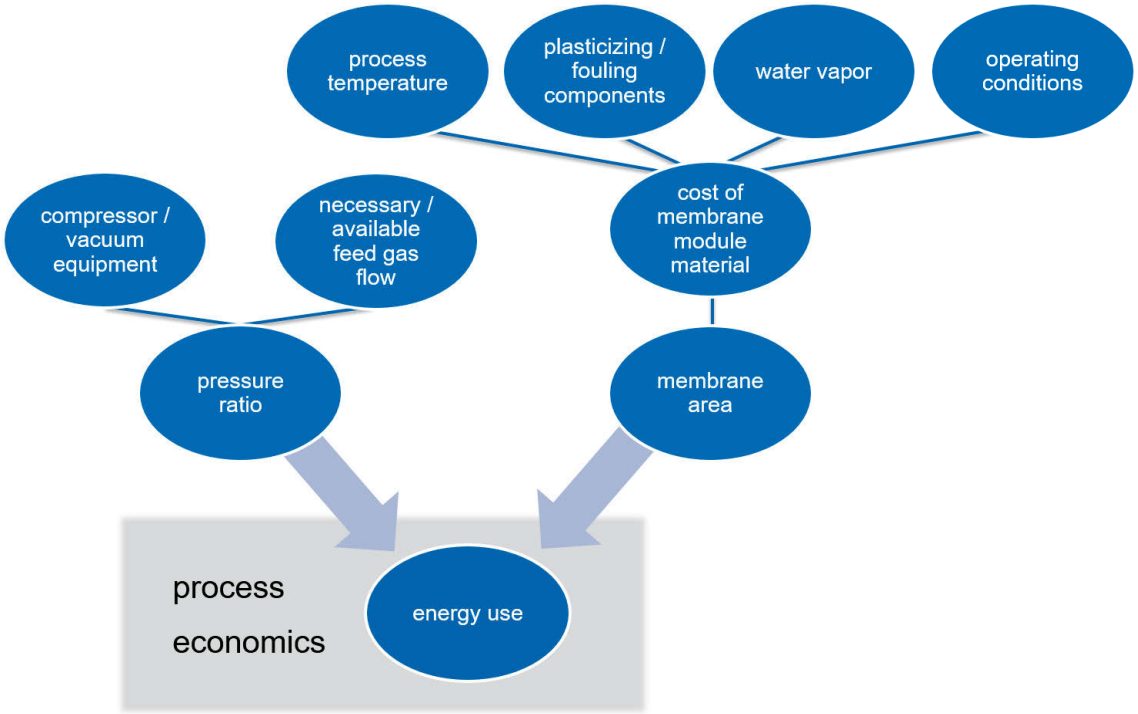

Figure 1. Factors which influence the process economics of a membrane gas separation process, in particular energy use, and thereby determine the properties of the optimum membrane.

Highly permeable membranes are always the aim in the development of new materials, but the optimum membrane selectivity depends on the process and the operating conditions, especially the pressure ratio. The cost of the compressor package may be much more than the cost of the membrane unit, and the cost of electricity used to power the compressor is usually the largest operating expense. For these reasons, pressure ratios used in industrial processes are normally below 20, and are typically in the range of 5–15. The compressor/vacuum energy use is directly related to the membrane pressure ratio (Figure 1). A competitive process requires an affordably low pressure ratio, and this determines the preferred membrane selectivity.[19] Calculations of Merkel et al.[18] on the design for a post-combustion CO_2 capture process with membranes shows that at a given pressure ratio a trade-off exists between membrane area and permeate CO_2 concentration, which results in a narrow range of optimum selectivity for this separation. Even for a more selective membrane the process would still require a larger membrane area to improve the purity of CO_2 in the permeate gas stream.

1.1.2 Membrane material and shape

In commercial biogas purification, feed streams typically contain a high fraction of CO_2 and impurities like H_2S and H_2O. Conventional biogas purification is achieved through CO_2 and H_2S gas absorption in suitable solvents but absorption processes are highly energy-intensive and not well-suited for large-scale applications due to the large size and weight of the process equipment. Membranes used for industrial biogas purification are made from cellulose acetate and separate small polar molecules such as CO_2, moisture and the remaining hydrogen sulfide.[20] Currently, the benefits of CO_2 removal by membrane plants, including low capital cost, high energy efficiency and high product recovery, are restricted by challenges such as membrane plasticization, low contaminant resistance, lower product purity than solvent absorption.[21] Plasticization is the phenomenon that the permeability of both components increases and the selectivity decreases. This is caused by an increase in the segmental motion of polymer chains at high feed pressures due to the presence of one or more sorbates.[22]

Another important constraint in the development of membrane applications is the inverse correlation between permeability and selectivity. Organic polymer membranes are particular susceptible to this gas permeability and selectivity relationship, such that membranes with high permeability have a low selectivity and vice versa. The well-known Robeson plots[23-24] for gas pairs, or related plots for pervaporation from Lue and Peng et al.,[25] summarize the permeability and selectivity of known dense membranes and thereby illustrate that as permeability increases the selectivity of the membrane decreases, giving an upper bound of membrane performance (Figure 2). These upper bounds of performance

for organic polymer membranes increase gradually with further development but these do not approach the performances observed by other materials, for example inorganic membranes. Efforts are being undertaken to pass this 'Robeson upper bound' by the development of new polymeric materials,[26] pure inorganic membranes like zeolites (crystalline, porous aluminosilicates),[27-28] metal-organic frameworks (MOFs),[29] carbon molecular sieves (CMS),[30-31] carbon nanotubes (CNTs),[32] and graphene[33] or by combining different materials in so-called mixed-matrix membranes (MMMs) (see below).

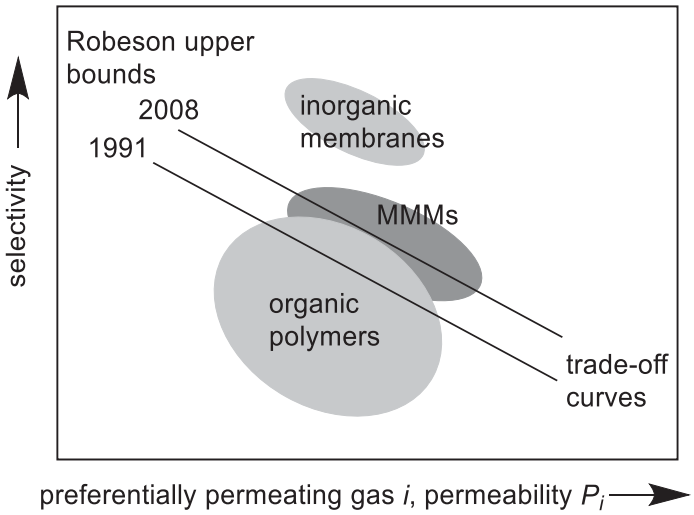

Figure 2 Schematic presentation of the inverse correlation (trade-off) between permeability and selectivity of dense membranes in gas separation with the 1991 and 2008 Robeson upper bounds.[23-24] Technologically interesting and better performing membranes lie around or above the Robeson upper bound. Figure reproduced from ref.[34] with permission, copyright Royal Society of Chemistry, 2012.

Pure (also called *continuous*) inorganic zeolite or hybrid MOF membranes combine very good selectivity with high permeability.[35-38] The problems with fabricating such continuous membranes from individual microcrystals is the defect-free preparation and mechanical stability of the membrane during operation. The occurrence of cracks or holes will result in a loss of selectivity. There are numerous studies on sophisticated and specialized engineering techniques to produce supported MOF[39-40] and zeolite[37,41-42] thin films as a selective layer. Fabrication of a mechanically strong and stable, well-intergrown defect-free pure MOF membrane is still challenging and difficult to scale up for industrial application.[37-38,43-44]

Mixed-matrix membranes (MMMs) consist of a micro- or nano-sized additive or filler component which is dispersed in the continuous organic polymer phase (Figure 3).[12,34,41,45-60] MMMs target the combination of the good flexibility and processability of polymers and the very high gas separation performance of porous inorganic materials to thereby surpass the Robeson upper bound.[24] The addition of fillers to polymer materials can also meet the challenges of commercially used polymer materials, like membrane plasticization, low contaminant resistance, low product purity and provide high performance gas separation MMMs, on the condition that defects at the filler–polymer interphase can be avoided. Various porous or non-porous inorganic additives have been tested as filler materials.[12,24,34,41,47-62]

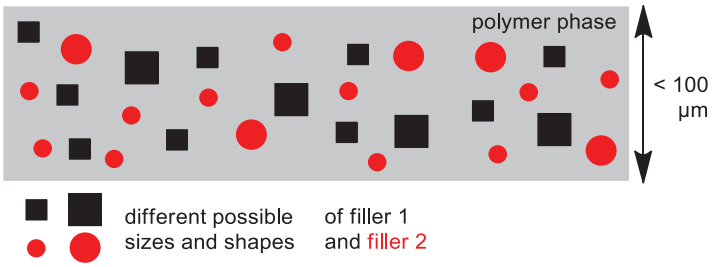

Figure 3 Schematic representation of a mixed-matrix membrane with two different additives (fillers), thereby also indicating different possible sizes, shapes and components for the inorganic filler materials. Figure taken from ref.[34] with permission, copyright Royal Society of Chemistry, 2012.

Improvements in membrane separation performance are expected for nanostructured porous additives such as zeolites or MOFs with size-selective adsorption and separation properties.[12,49] Concerning the filler, its chemical properties, functional groups on the surface, the distribution of particle sizes and its shape are other important variables.

Gas separation MMMs are produced in different shapes. On the one hand symmetrical MMMs, in which the filler particles should be uniformly embedded in the polymer matrix, and on the other hand asymmetric MMMs which consist of a thin polymer layer with filler and a thicker, porous carrier layer. Membranes used in industrial applications are usually integrated as asymmetric membranes which can be produced as flat sheets or as hollow fibers.[63]

Flat asymmetric MMMs can be prepared by the phase inversion method. The polymer and filler dispersion is poured onto a flat surface and solidifies after solvent exchange. During solidification, defects can occur within the membrane or on the surface. To minimize the defects on the surface an additional layer of polymer can be applied by spin coating.[15] The additional polymer layer can also be chemically crosslinked to the membrane layers which can increase the thermal and chemical stability as well as the selectivity usually with reduction in permeability.[64-65]

Asymmetric hollow fiber membranes are a focus when there is the problem of low gas flow through the membrane. Because of the high membrane area per module volume, the high packing density and the high gas flow through the hollow fiber, this membrane shape is optimal for industrial applications, as seen from an engineering and process economics point of view. In the preparation of MMM hollow fibers either a layer of the polymer-filler dispersion is applied onto the already prefabricated hollow fiber substrate, or the hollow fiber is directly fabricated from the target material.[66-67]

In the development of novel polymer and filler materials and the investigation of effects of polymer and filler interaction, a symmetrical MMM is often chosen because the comparability of the production methods is better and effects on separations can be discussed more easily from a chemical point of view. The step towards module design and optimization of the

membrane area / module volume is done in the engineering process. Such membrane shape and engineering aspects are significant for the industrial future of new membrane materials, including MMMs but go beyond the scope of this section.

1.1.3 Zeolites and MOF additives – background and opportunities for MOFs

MOFs have been investigated as inorganic-organic hybrid additives for MMMs[13,68-72] as they are highly porous and should be able to interact better than purely inorganic zeolites with the surrounding polymer. MOFs have adaptable chemical properties and porosities through the metal-linker combination.[73] The interaction of the organic ligands of the MOF with the polymer, which can be enhanced with functional groups for specific supramolecular or even covalent bonding, should prevent interfacial micro-gaps, which lead to loss in selectivity.[34,41,47-49] In order to obtain materials with optimized separation properties, a perfect interaction between the two components is highly important for the preparation of MMMs.

Gas separation is the most studied field with MOF-MMMs which is due to the very similar size of the substances in gas mixtures and microporous fillers with designable pore characteristics. The types of gas separations investigated with MOF-MMMs include CO_2/CH_4 separations for natural gas sweetening and biogas purification, CO_2/N_2 for the purification of flue gas streams, precombustion H_2/CO_2 capture and air separation (O_2/N_2).[13] Lab-scale adsorptive gas separation and purification processes have already shown the high potential of MOFs as a porous material compared to other adsorbers.[29,74] It has been reported that Mg and Fe-MOF-74, packed in a column, exhibit enhanced CO_2 separation from methane and C_1 to C_3 hydrocarbons.[75-76] Another example, where the overall capacity of the MOF material outperformed commercially available activated carbon materials as adsorbents, namely Norit (type RB4) and CarboTech (type C38/4), is the removal of tetrahydrothiophene (THT) from natural gas in a fixed bed reactor.[77] The outstanding molecular size cutoff properties and high selectivity of MOFs would be maximally utilized in a neat supported layer prepared from intergrown MOF-crystals. However, when MOFs are used as a filler in MMMs it is still possible to access their separation properties with high filler loading, but there will always be a compromise with the separation properties of the polymer-matrix, which is in most cases less efficient than the pure MOF material.

Zeolites possess a sharp molecular “cut-off” when used as fillers or neat, supported membranes, due to their fixed pore size and have been one of the most common inorganic materials used for the preparation of MMMs.[37] [50] Because of their molecular sieving properties, they have been an extensively studied class of materials for membrane fabrication in multiple membrane forms and shapes (hollow fiber, supported molecular sieve membrane) with focus on industrial separation.[78,79,41,80] Zeolite membranes can exhibit

remarkable separation properties, when they are fabricated as composite membranes which consist of a zeolite top layer on a mesoporous ceramic or metal support.[36] The company NGK INSULATORS, LTD has developed and produced a pure, supported MFI (ZS*M*-5, *fi*ve)-type zeolite gas separation membrane by forming a film on a porous ceramic substrate, which extracts *para*-xylene from xylene isomers produced in the petroleum refinery process. For the refinement of biogas generated from raw garbage by fermentation, a deca-dodecasil 3R (DDR)-type zeolite membrane was developed by the same company. This is also supported on a porous ceramic substrate and could isolate CO_2 from a mixture of methane and CO_2.[81] For neat, supported MOF-membranes, phenomena like “gate opening” and “breathing” make it hard to obtain the theoretical selectivities (cut off because of pore size) when MOFs are processed as a thin-film membrane.[37] Despite this, MOF/polymer MMMs usually show improved fluxes compared to pure polymer membranes and zeolite-based MMMs. Additionally, water is known to inhibit the CO_2 adsorption capacity of zeolites due to CO_2 and water competition for the sorbent sites.[82] These effects are also known for MOFs, but in certain instances, such as the case of hydrated MIL-101, terminal water molecules can act as additional binding sites for CO_2 adsorption, promoting CO_2/CH_4 separation at low pressures.[83] These reasons make MOFs a preferred material, when processed as fillers in polymer/MOF MMMs while zeolites are superior, when processed as supported thin-film membranes.[37]

Besides gas separation, industrially interesting separation technologies include liquid filtration like nanofiltration and pervaporation. The field of MOF-MMMs has also expanded to these applications and has been the subject of recent reviews.[84-85] For example, in organic solvent nanofiltration from styrene oligomers, the addition of MIL-101(Cr) to a polyamide matrix showed a remarkably increased flux while preserving rejection.[86] Further, the combination of MIL-101(Cr) and ZIF-11 in a polyamide (PA) thin film nanocomposite membrane resulted in an enhanced and versatile membrane for organic solvent nanofiltration from organic dyes combining the high porosity of MIL-101(Cr) and the hydrophobicity of the ZIF-11.[87] In pervaporation the separation of water from ethanol was carried out with a HKUST-1/Matrimid MMM, at 40 wt% the addition of HKUST-1 to the MMM led to an increased flux of 0.43 $kg/m^2\ h^1$ (compared to 0.24 $kg/m^2\ h^1$ for pure Matrimid) without decreasing selectivity due to the hydrophilicity of HKUST-1.[88]

1.1.4 Challenges with MOF additives

The hydrothermal stability of the MMM, including the filler material, is a crucial issue. It is not economically possible to fully dry industrial gases before separation to prevent membrane degradation. On the contrary, the membrane and its components must be stable towards moisture. Unfortunately MOFs, which are metal-ligand coordination compounds, are

inherently unstable towards reaction with water and linker displacement by aqua ligands.[89-90] Zinc-carboxylate MOFs, such as MOF-5 and the IRMOF-series have a low moisture stability, HKUST-1 ($Cu_3(BTC)_2$) is intermediate but eventually decomposes.[89,91-93] MIL-type compounds, including MIL-101(Cr),[94-96] NH_2-MIL-53(Al), Al-fumarate,[92,97] CAU-10-H[98] and ZIF-8 exhibit higher water stability.[89,91-93,99-100] Therefore, hydrolytically stable MOF materials must be employed as additives for MMMs to have a realistic chance for further technical development. Concerning other contaminants in biogas purification, and in pre- and post-combustion CO_2 separation, gases such as H_2S, SO_x, NO_x, CO, NH_3 are known as membrane poisons, effecting the separation process by plasticization and aging effects or degradation of the material. Testing MOFs for not only water stability, but also pH dependent stability, shows that the chemical stability towards acids and bases is overall disappointing, but again MIL-101(Cr), MIL-53(Al) and UiO-66(Zr) gave the best results concerning pH stability.[90] MOFs are studied for the adsorptive removal of hazardous compounds from gas streams and air and their adsorptive capacities have shown excellent potential. However, there is a lack of studies which discuss their regenerability, i.e. stability.[101] Many of pristine MOFs are often not suitable for the sorptive treatment of the reactive and corrosive gases such as H_2S and SO_2. To overcome this limitation structural functionalization of MOFs can be utilized.[102]

1.2 Significant developments of MOF inclusion in MMMs

MOFs are widely studied as fillers in mixed matrix membranes and compared for their impact on the separation performance of pure polymer materials.[13,34,37,44] Most reported studies on the preparation and characterization of MOF-based MMMs are often fundamental but in the following sections an analysis of these results is presented to develop an understanding of the separation mechanisms, the role of the MOFs and the effect of the polymer/MOF particle interface. This knowledge is needed to develop MOF-MMMs which are suitable for industrial applications. MOF-MMMs have been the subject of recent reviews.[13,34,38,43,49] Here, the current trends of MMM fabrication will be examined with a focus on recent significant developments in the MMM field concerning MOF and polymer compositions and newer aspects, such as the role of particle size and shape control in MOF-MMM fabrication. This will demonstrate how developments in membrane separation performance can be advanced through the incorporation of designed MOF additives. With MOF-MMM works expanding to higher complexity and more material combinations the new synthetic approaches for MOF additives needed updating in a comparative manner to point out the successful strategies which could lead to the fabrication of high performing MMMs. The impact of these additives on the separation performance is analyzed by the comparison of the permeability and selectivity data of the highlighted MMMs and corresponding polymer membranes. The

numerical values are summarized in Table 1. To provide guidance on the shape and structural dimension of pore sizes and secondary building units of the frameworks, images and structure descriptions of the MOF-fillers are given in chapter 8.1 The membrane polymers, which are noted in the following sections, are depicted in Figure 4 with their repeat unit.

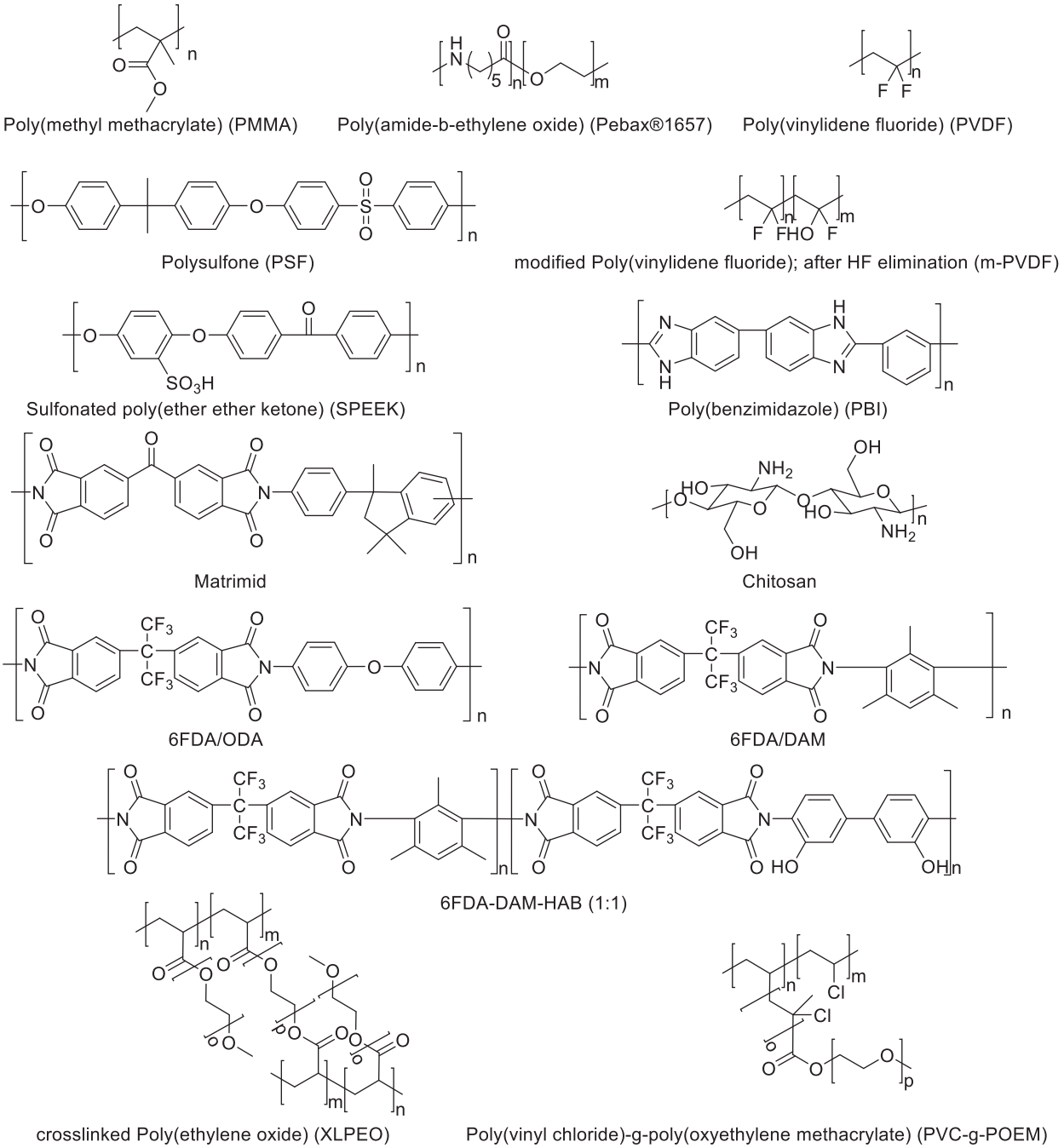

Figure 4 Repeat units of commercial polymers which are frequently used in polymer/MOF MMMs.

1.2.1 Linkers with functional groups

MOFs with polar functional groups on their linkers can give a better selectivity for one of the gases in a mixture.[103] Polar functional groups such as amine, -NH_2, hydroxo, -OH, nitro, -NO_2 and sulfonic acid -SO_3H on the linkers in MOFs like NH_2-MIL-125(Ti)[104-105] or HSO_3-MIL-101(Cr)[106] improve interactions with CO_2 due to their polarizability and/or hydrogen bonding interactions with the CO_2 molecule.[107] Further, the suitable selection of a corresponding polymer can enhance the polymer/MOF-particle interface interaction. Especially in polyimides, interactions such as hydrogen bonding between the polymer backbone and the surface-functional groups of the MOF filler particle led to increased compatibility. The improved gas separation properties of MMMs based on amine-containing MOFs, including NH_2-UiO-66(Zr) and NH_2-MOF-199 (MOF-199 is also known as Cu-BTC or HKUST-1)[46], NH_2-MIL-53(Al)[45,60,108-109] and NH_2-MIL-101(Al),[108-109] were explained accordingly.

A good comparison is provided by a polysulfone (PSF)/NH_2-MIL-125(Ti)[104-105] MMM where the selectivity for CO_2:CH_4 separation dropped at high filler loadings (30 wt%) because of voids from poor polymer-filler adhesion.[110] On the other hand, a Matrimid/NH_2-MIL-125(Ti) MMM at 30 wt% loading showed a 550% increase in CO_2:CH_4 selectivity together with 35% higher CO_2 permeability than the PSF MMM (Figure 5).[111] However, no spectroscopic proof was given for the anticipated hydrogen or even covalent bonding between the polyimide and NH_2-groups on the MOF-surface.[112]

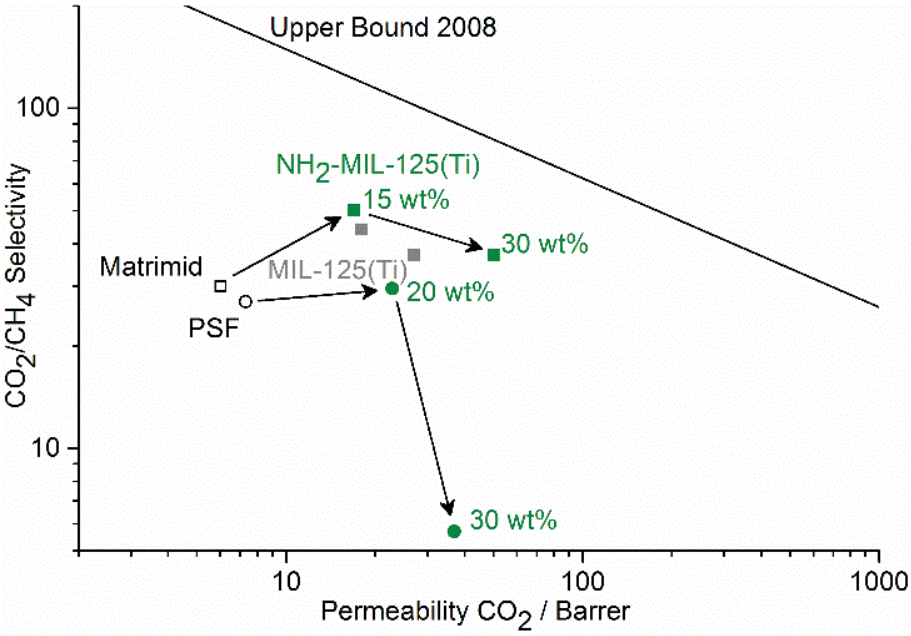

Figure 5 Comparative CO_2/CH_4 permselectivity and upper bound plot for Matrimid/MIL-125(Ti) MMMs (squares) with unmodified MIL-125(Ti) (grey) and NH_2- MIL-125(Ti) (green) for different MOF/MMM mass fractions[111] and PSF-based MMMs (circles) with NH_2- MIL-125(Ti) with a strong drop in selectivity at higher filler loading.[110] See chapter 8.1.5 for a graphic and structure description of MIL-125.[104]

HSO_3-MIL-101(Cr)[106] MMMs[113] exhibited a better CO_2/CH_4 gas selectivity (50 at a CO_2 permeability of 2064 Barrer) compared with the MMM from unmodified MIL-101(Cr) (31 at a CO_2 permeability of 1600 Barrer). In both of these MMMs humidification or bound water led to increased CO_2 permeability and improved selectivity (Figure 6). Hydrated sulfonic acid groups will improve hydrophilic CO_2 solubility in the MMM and thereby lead to increased permeability and selectivity over hydrophobic CH_4.[114] The sulfonic acid groups from both the polymer matrix, which was a sulfonated poly(ether ether ketone) (SPEEK), and the sulfonated MOF may construct facilitated transport pathways for CO_2 and, thereby, improve CO_2 solubility and selectivity (cf. Figure 13). We note that the SPEEK polymer itself, with sulfonic acid as hydrophilic groups, can adsorb up to 11 wt% water with a sulfonation degree of 67%.[115-116] As a hydrogel with $-SO_3H$ groups, humidified SPEEK already has a relatively high CO_2 selective solubility which is beneficial for CO_2 transport based on the solution-diffusion mechanism.[116]

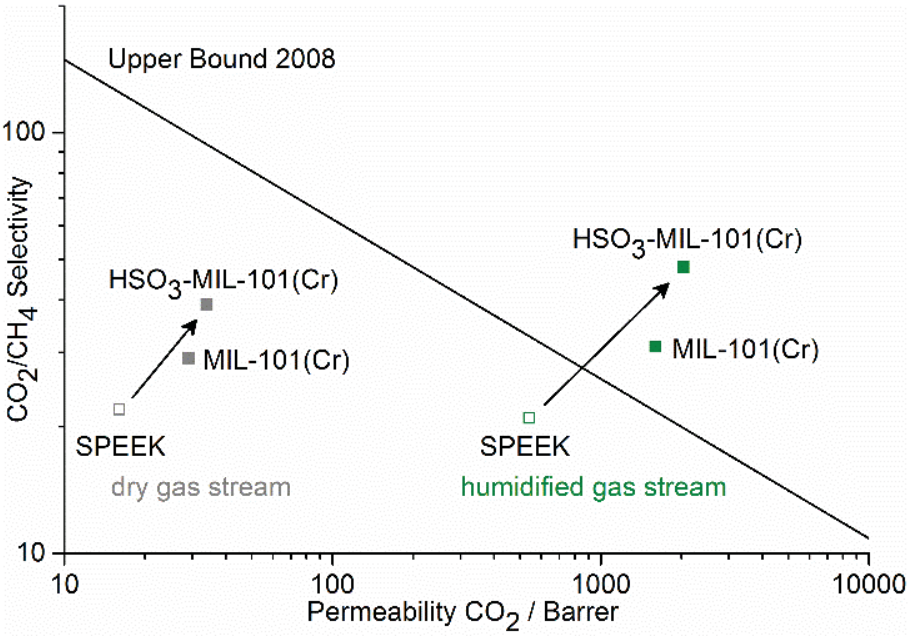

Figure 6 Comparative CO_2/CH_4 permselectivity and upper bound plot for sulfonated poly(ether ether ketone) (SPEEK)/MIL-101(Cr) MMMs with 40 wt% non-functionalized or sulfonated MIL-101(Cr). Permeability and selectivity show a strong increase, when a humidified gas stream (green) is used, compared to dry gas streams (grey).[114] See chapter 8.1.4 for a graphic and structure description of MIL-101.[94]

1.2.2 Modulated MOF-Synthesis

Linker or node modification of known MOFs can be used to improve the MOF-polymer interaction and thereby the separation performance of the MOF-MMM (see above).[44,50] Such linker modification can be carried out by replacing the linker in the initial MOF-synthesis, or by so-called post-synthetic linker modification (PSM)[117-120] and solvent-assisted linker exchange (SALE).[121-122] Post-synthetic modification (PSM) of MOFs refers to the alteration of

a MOF framework after its synthesis, for example, through chemical reaction of the linker (covalent PSM), solvent ligand replacement on the metal (grafting, dative PSM) or post-synthetic deprotection of a functional group on the linker (PSD) (Figure 7).[119,123-125] The technique permits functionalization of the MOF crystallites while retaining the overall framework structure and porosity.[126]

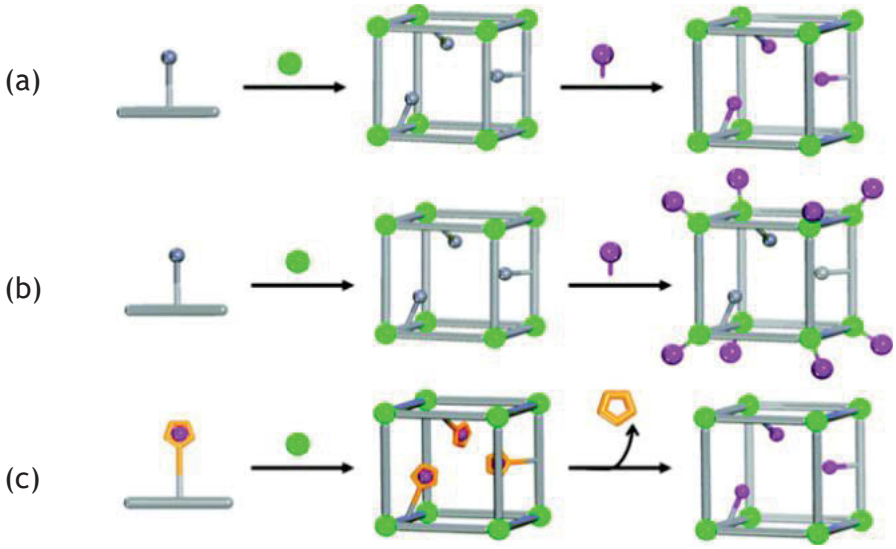

Figure 7 Schematic depiction of synthetic approaches to modify a MOF after synthesis. The different routes are specified after the type of chemical bond that is formed or broken during the post-synthetic approach for (a) chemical reaction on the linker (covalent PSM), (b) ligand replacement on the metal (dative PSM), and (c) post-synthetic functional group deprotection (PSD). Figure reproduced with permission of the American Chemical Society. Reprinted with permission from ref.[125]. Copyright 2012 American Chemical Society.

Besides the MOF linker and node, also the MOF crystal size, particle morphology, and outer surface ligands can be adjusted. This is, for example, done by using monodentate carboxylate ligands, monoatomic anions or surfactants as so-called 'modulators' during the synthesis of the MOF. The modulators compete with the actual linkers for coordination to the metal sites. Modulators may lead to particles of similar and desired size, as well as particles possessing a specific surface chemistry due to capping with modulator molecules.[127-129]

Benzoic acid (BA) and 4-aminobenzoic acid (ABA) were added as modulators in the synthesis of UiO-66(Zr)[130-131] and NH_2-UiO-66(Zr)[127] in a 50:1 molar ratio relative to the linker. Reaction of the amine groups on the MOF surface was seen by the appearance of amide signals in the IR spectra of Matrimid MMMs with high amino-MOF filler loading. The membrane of Matrimid/NH_2-UiO-66(Zr)-ABA gave the best performance in CO_2/CH_4 mixed-gas separations being over 50% more selective and 540% more permeable than the continuous Matrimid membrane and 30% and 140% more selective and permeable than the Matrimid/UiO-66(Zr) MMM (Figure 8).[132]

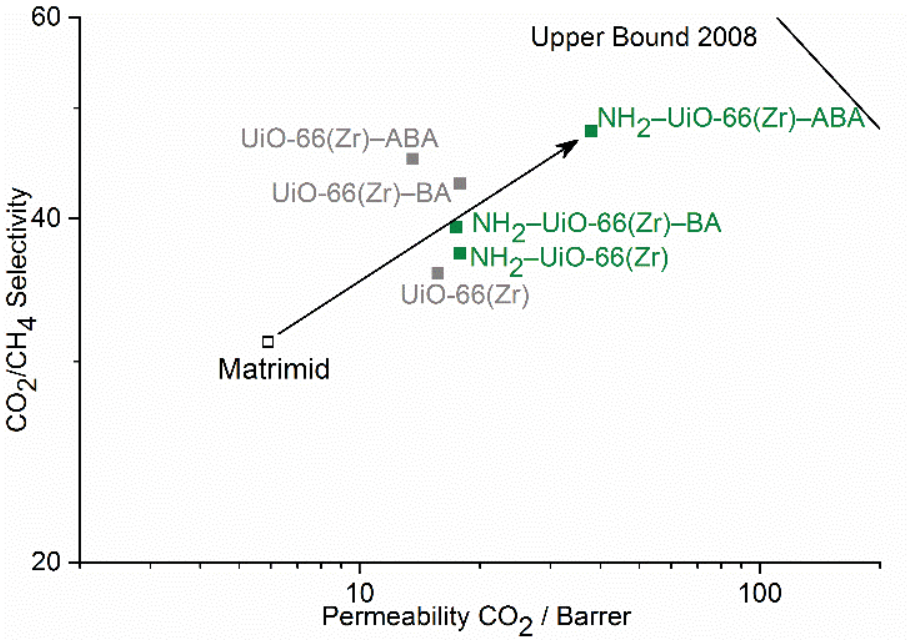

Figure 8 Comparative CO_2/CH_4 permselectivity and upper bound plot for Matrimid/UiO-66(Zr) MMMs with 30 wt% standard UiO-66(Zr) (grey) and amino-functionalized NH_2-UiO-66(Zr) (green) in addition with benzoic acid (BA) or aminobenzoic acid (ABA) used as modulator during the UiO-66(Zr) synthesis.[132] See chapter 8.1.7 for a graphic and structure description of UiO-66.[130,133]

Another aspect with high impact on the separation properties of the MMM material, besides the abovementioned chemical functionality of the linker, is the pore size and shape of the MOF-filler. The pore aperture (pore window diameter) in ZIF-8[134-135] is about 3.4 Å, so it could be assumed that a ZIF-8 membrane should be able to separate CO_2 with a kinetic diameter of 3.3 Å from larger gas molecules such as CH_4 with a kinetic diameter of 3.8 Å. However, this cut-off size cannot be observed in gas permeation measurements. Neat ZIF-8[135] membranes exhibit only moderate CO_2 selectivities and CH_4 can slowly pass through the ZIF-8 pore network, resulting in no sharp cutoff at 3.4 Å.[136-137] This is rationalized to be due to the flexibility of the ZIF-8 network.[138] A reduction of the cut-off size of ZIF-8 for CO_2 separation was achieved by incorporating room-temperature ionic liquids (RTILs) into the ZIF-8 cavities through an ionothermal synthesis of ZIF-8 in the RTIL butyl-methyl imidazolium bis(trifluoromethyl-sulfonyl) imide, [bmim][Tf_2N], which also shows good affinity to CO_2. The pore size distribution calculated from N_2 adsorption measurements indicated that the effective cage size of ZIF-8 was remarkably reduced after incorporation of the IL.[139] For a 6 wt% PSF/IL@ZIF-8 MMM the selectivities of CO_2/N_2, and CO_2/CH_4 were remarkably improved from 29 to 115 and from 19 to 34 at only slightly reduced CO_2 permeability compared to MMMs with unmodified ZIF-8 (Figure 9). The affinity of the IL for CO_2 dissolution[140] may have helped in the increase in selectivity.

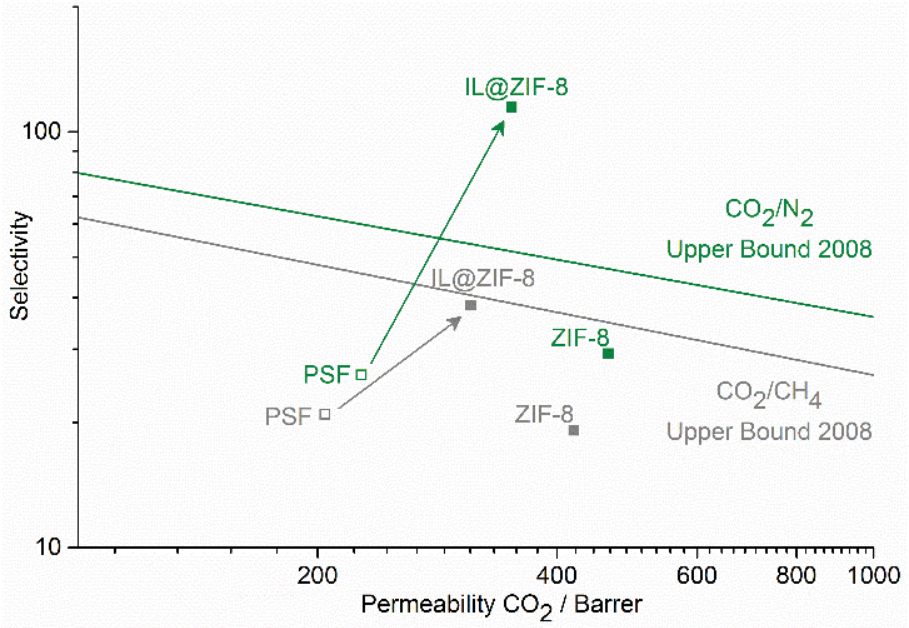

Figure 9 Permeability and selectivity of PSF/IL@ZIF-8 MMMs compared to ZIF-8 MMMs and the pure polysulfone (PSF) membrane. CO_2/CH_4 (grey) CO_2/N_2 (green) permselectivity; the mixed gas permeabilities were measured at 30 °C and 6 bar pressure difference. Membranes were prepared by dip coating of the polymer or polymer/MOF-mixture on an asymmetric gamma aluminum disc. This preparation method results in significantly higher permeation rates than for neat self-supported polymer films.[139] See chapter 8.1.8.1 for a graphic and structure description of ZIF-8.[134-135]

A thin polydopamine (PDA) coating (from polymerization of dopamine hydrochloride) was applied on the particles of the MOF NH_2-CAU-1[141] as a solubilizer for the poly(methyl methacrylate) (PMMA) matrix.[142] The PMMA/NH_2-CAU-1@PDA MMM showed a high O_2 and low CO_2 permeability with increased ideal O_2/CO_2 and O_2/N_2 selectivity over an MMM formed with non-coated NH_2-CAU-1 (Figure 10).[142] Pure PMMA films were not fabricated or characterized in this work, which is often necessary to prove the accuracy of the characterization methods. Thereby the permselectivities of the MMMs are multiple orders of magnitude higher than the rare values found in the literature for pure PMMA.[143-144]

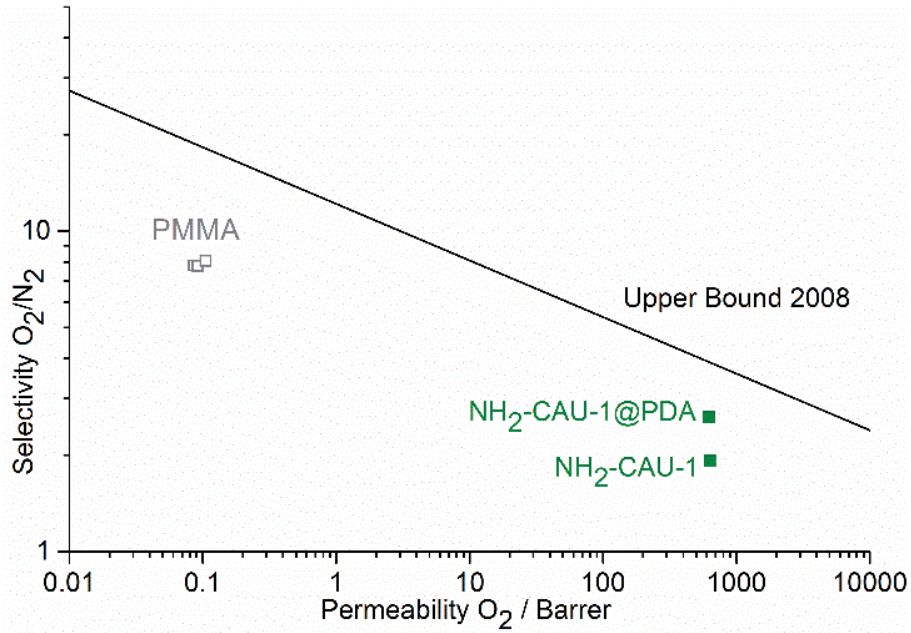

Figure 10 O_2/N_2 permselectivity and upper bound plot for PMMA/NH_2-CAU-1 MMMs (green) with and without polydopamine (PDA) coating.[142] The very rare literature values for pure PMMA membranes[143-144] (grey) were added for comparison to the permselectivity of the MMMs and are not necessarily correlated with the reported MMM values. See chapter 8.1.6 for a graphic and structure description of CAU-1.[141]

NH_2-UiO-66(Zr) was post-synthetically modified with polar succinic acid (HO_2C-$(CHOH)_2$-CO_2H), non-polar decanoyl chloride (n-$C_9H_{17}COCl$) or aromatic phenyl acetyl chloride (PhCOCl) (covalent PSM with amide bond formation) and combined with Matrimid to give MMMs for CO_2/N_2 single gas permeation measurements.[126] Larger PhCOCl and n-$C_9H_{17}COCl$ molecules cannot diffuse into the MOF pores and react only with the amine groups on the MOF particle surface. The smaller succinic acid reacted also with the internal amino groups. The imide groups in the Matrimid polymer can interact with the MOF-NH_2 groups or PSM-amide linkages through hydrogen bonding (Figure 11). Aromatic rings from PhCO- can further interact through π–π stacking. While no spectroscopic evidence for such polymer-MOF interaction was provided, Matrimid and PSM-NH_2-UiO-66(Zr) showed good film formation and no cavity formation around the particles was seen by scanning electron microscopy (SEM). MMMs with the aromatic PhCOCl-functionalized NH_2-UiO-66(Zr) showed an increase in CO_2/N_2 selectivity and CO_2 permeability over unmodified NH_2-UiO-66(Zr) while the polar and non-polar modification gave a decrease in selectivity (Figure 12).

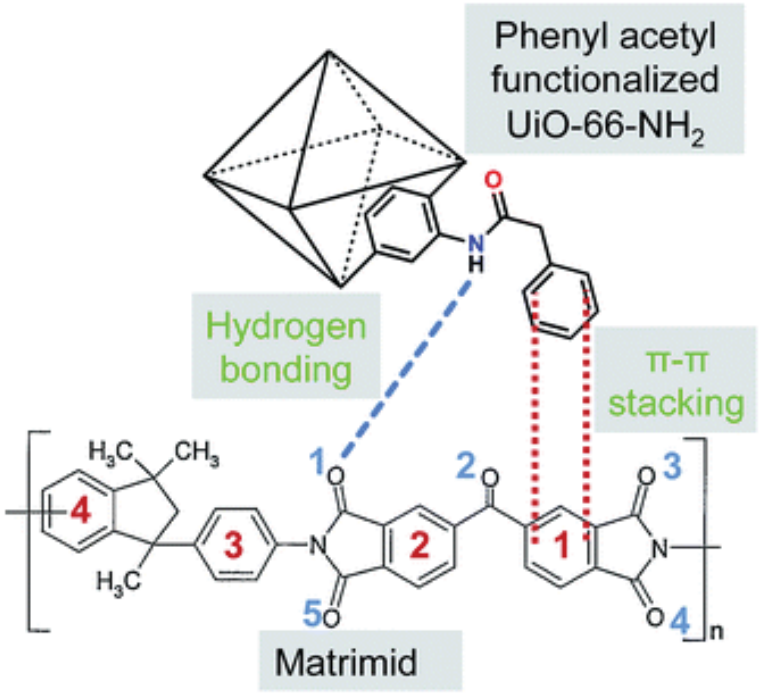

Figure 11 Possible interactions between the Matrimid polymer and phenyl acetyl functionalized NH_2- UiO-66(Zr). Figure reproduced from ref.[126] with permission, copyright Royal Society of Chemistry, 2015.

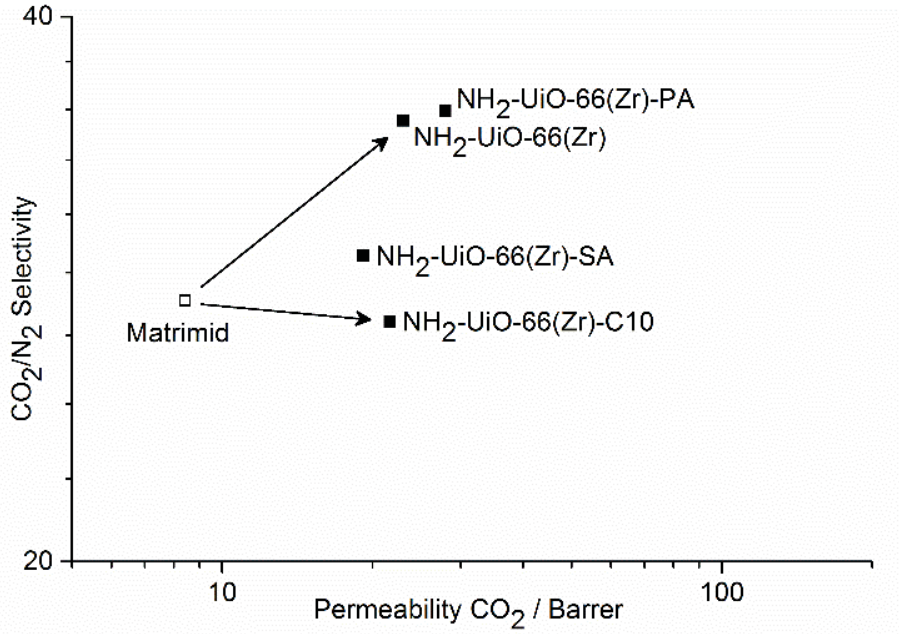

Figure 12 Comparative CO_2/N_2 permselectivity for Matrimid MMMs with NH_2- UiO-66(Zr) post-synthetically functionalized with succinic acid (SA, HO_2C-$(CHOH)_2$-CO_2H), decanoyl chloride (C10, n-$C_9H_{17}COCl$) or phenyl acetyl chloride (PA, PhCOCl).[126] See supporting information for a graphic and structure description of UiO-66.[130,133]

Employing dative PSM, polyethylenimine (PEI) of low molecular weight (300 Da) was immobilized on and in MIL-101(Cr)[94,145] possibly by grafting to the metal sites (dative PSM, cf. Figure 7b), although spectroscopic proof for the coordination of the amine group onto the metal sites in MIL-101(Cr) was lacking.[146-149] IR spectroscopy on the MMM formed from

SPEEK/PEI@MIL-101(Cr) indicated hydrogen bonding between SPEEK sulfonic acid groups and PEI amine groups presumably at the polymer-MOF interface. SPEEK itself is known to change its perm-selectivity when water is absorbed because of the hydrophilic sulfonic acid groups leading to formation of a hydrogel. This is connected to high CO_2 selective absorption which is in turn beneficial for CO_2 transport based on the solution-diffusion mechanism.[115-116] CO_2 can react with the abundant PEI amine groups in the humidified SPEEK/PEI@MIL-101(Cr) membrane producing, via the carbamate, alkyl ammonium groups and HCO_3^- (Scheme 1) which could then facilitate CO_2 transport by "HCO_3^- ion hopping" from one ammonium site to another (Figure 13).[116]

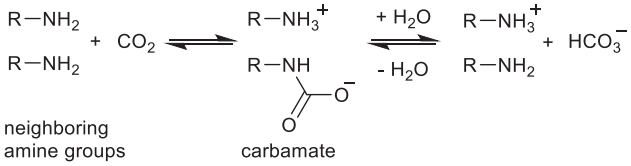

Scheme 1 Reaction scheme for the reversible chemical absorption of CO_2 by primary amines to carbamate and in the presence of water to hydrogen carbonate products.

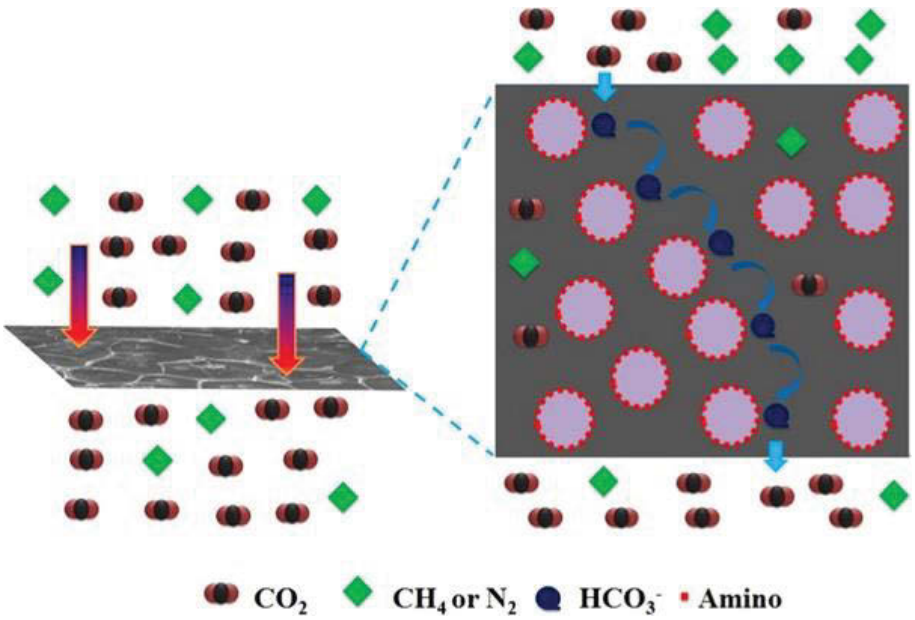

Figure 13 Facilitated transport pathway of CO_2 in amino-containing MMMs where the reversible reaction between facilitated transport carriers and CO_2 molecules enhances the CO_2 separation performance. Figure reproduced from ref.[116] with permission, copyright Elsevier 2014.

Gas permeation experiments showed that the PEI@MIL-101(Cr) filled MMMs outperformed those prepared from unmodified MIL-101(Cr) and pure SPEEK. The CO_2 permeability, CO_2/CH_4 selectivity, and CO_2/N_2 selectivity all increased with the PEI@MIL-101(Cr) filler content. The membrane loaded with 40 wt% PEI@MIL-101(Cr) exhibited the highest selectivity of 72 and 80 for CO_2/CH_4 and CO_2/N_2 mixtures, respectively, with a CO_2 permeability of 2490 Barrer at 1.0 bar and 25 °C (Figure 14). Further, there was a strong correlation between total water

content and the selectivity for CO_2/CH_4 and CO_2/N_2 gas selectivity. For water and CO_2 loaded membranes a sharp IR band at 2346 cm^{-1} was attributed to carbamate formation $RHNCOO^-$ and bands at 839 and 963 cm^{-1} were assigned to the subsequently formed HCO_3^- (Scheme 1) which could permeate through the MMM with lower energy barrier by the hopping mechanism (cf. Figure 13 above).[146]

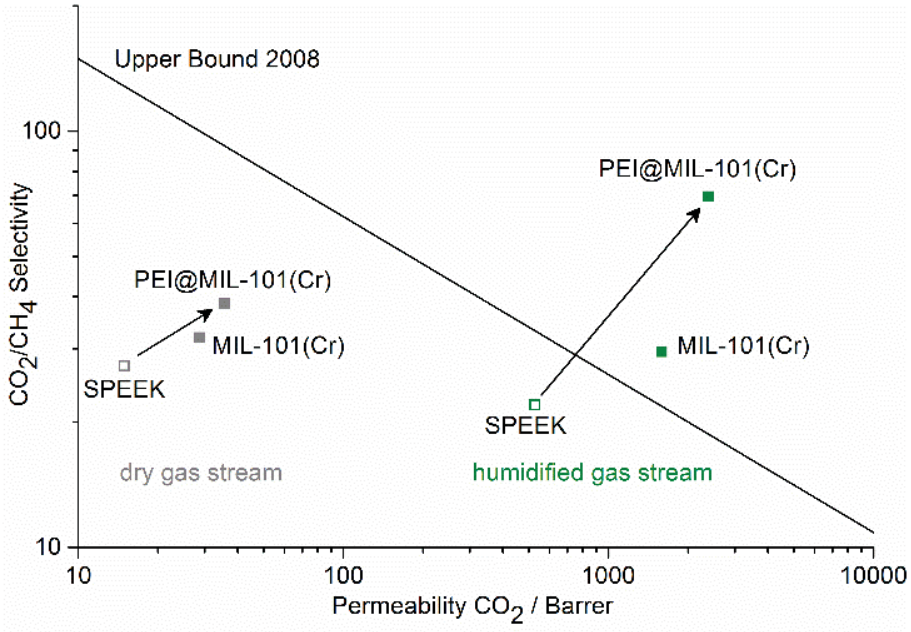

Figure 14 Comparative CO_2/CH_4 permselectivity and upper bound plot for sulfonated poly(ether ether ketone) (SPEEK)/MIL-101(Cr) MMMs with 40 wt% non-functionalized MIL-101 or functionalized PEI@MIL-101. Permeability and selectivity show a strong increase, when a humidified gas stream (green) is used, compared to dry gas streams (grey).[146] Compare also to the case depicted in Fig. 6 above. See chapter 8.1.4 for a graphic and structure description of MIL-101.[94]

The postsynthetic modification of MOFs requires the accessibility of the pores, otherwise reactants cannot diffuse into the channels and only react on the surface of the particles or at the pore openings. In many studies of MMMs the accessibility of the filler MOF pores are not the focus; typically the mechanical and morphological properties of the membranes and properties related to a specific separation are examined. Also the MOF loading is often relatively low (up to 30 wt%). For the specific characterization and understanding of a processable mixed-MMM material, the properties of the MOFs as an important component in separation processes should not be overlooked. Properties like pore shape, pore size, surface area and chemical accessibility have an important influence on the transport mechanisms inside a MMM material and should be closely studied in relation to the transport phenomena. Cohen et al. have developed a technique to fabricate MMMs with very high MOF loading such that the properties of the composite material are not dominated by the polymer.[117] In these examples the loading is high enough (50 to 67 wt%) such that the composite material can no longer be viewed as a MOF filler in a polymer matrix but as MOF particles connected by a polymeric binder. This allows the MOF particles to dominate the properties of the membrane

material, giving behavior approaching that of a pure MOF film but with better mechanical characteristics. Due to the limited particle and pore accessibility of MOF fillers in MMMs, the PSM of the fillers is usually carried out before incorporation into the polymer matrix.[44,50] Here, in this case, PSM was possible in the membrane material, demonstrating that the MOF filler was functionally accessible. For this purpose, a UiO-66 MMM was immersed in a solution of NH_2-bdc for 24 h at 55 °C which resulted in a postsynthetic exchange (PSE) reaction to give UiO-66-NH_2 MMMs, with approximately 33 % of the bdc ligands exchanged for NH_2-bdc. The technique can be used for inclusion of a diverse range of MOFs into the polymer poly(vinylidene fluoride) (PVDF). The MOFs used in Cohen's studies were of UiO-66[133], HKUST-1[150], MIL-101[94,151], MIL-53[152-153] and ZIF-8[135]. Conventional membrane preparation methods are carried out by solution casting (casting of a polymer solution with dispersed MOF particles) or by using a priming protocol (priming is a technique where the MOF particle suspension is combined stepwise with part of the polymer solution, and sonicated to form a suspension, which avoids potential agglomeration of the filler material and reduces the stress at the particle-polymer interface). In contrast to this, for the preparation of MOF/PVDF MMMs, a mixture of solvents was used to prepare the polymer/MOF casting suspension. The MOF was first dispersed in acetone, a solvent with low viscosity and low boiling point, i.e. the dispersion of the particles is easy to achieve and the solvent can be removed before casting. Then the polymer solution (7.5 wt% of PVDF in DMF or NMP) was added, followed by sonication again (to ensure the homogeneity of the mixed solvent system) and removal of acetone, to leave the dispersed particles in the viscous polymer solution.[117] The advantages of casting a viscous polymer solution with homogeneously dispersed fillers is that the film can be casted mechanically (with a blade) on a support and the particles are restricted in their movement during film formation, avoiding agglomeration, phase separation or sedimentation. DMF or NMP can be removed at elevated temperature, resulting in flexible, mechanically stable membranes with the highest filler loading achieved for applicable MOF-MMMs.[13,68-72]

To test the applicability of these PVDF based MMMs, the PVDF/UiO-66 membranes were used for liquid filtration of coomassie blue from an aqueous solution of methyl orange.[117] The HKUST-1 membranes were investigated for the selective uptake of ammonia from air. For the separation of ammonia from air, the water stability of HKUST-1 was tested under realistic conditions, including the presence of humidity in the gas mixtures.[154] HKUST-1 powder is not stable when exposed to water as confirmed by PXRD measurements, FTIR spectra and nitrogen adsorption (exposed to several different temperatures and relative humidity levels (% RH)). The most aggressive aging condition was 40 °C and 90% RH where the change of the HKUST-1 structure starts after 7 days and changes in the IR spectra occur with the gradual appearance of bands at 1708 and 1243 cm^{-1} corresponding to the C=O and

C–OH bands of a carboxylic acid. Also a decrease in the intensity of bands at 1650 and the 1422 cm^{-1} indicate the transformation of the HKUST-1 carboxylate nodes to their protonated acid analogs.[155] The PVDF/HKUST-1 MMMs were aged under the same conditions and PXRD patterns remained unchanged over 28 days. Furthermore, FTIR spectra did not reveal the formation of the carboxylic acid bands. The bulk powder of HKUST-1 loses 90% of its capacity for ammonia uptake after 7 days aging whereas for the MMMs only a change below 20% was observed. The MOF performance characteristics were retained in the MMMs utilizing PVDF as a binder but the stability of the MOF material was increased significantly.

1.2.3 Polymer-MOF-hybrids (polyMOFs)

Polymer-MOF hybrids (polyMOFs) have organic polymers built into MOFs or are MOFs constructed from organic polymer linkers. In one material these combine the advantages of flexible and easy to process polymer materials with the porosity of MOFs.[156-157] Consequently, the polymer-MOF hybrid materials are intended as neat membrane materials.
Structures of polyMOFs with the same topology (isoreticular) as MOF-5[158-159] and the IRMOF-*n* series,[160] as well as high porosity, can be synthesized from 2,5-substituted derivatives of H_2bdc or 2,2'-linked di-H_2bdc ligands[147,148] or 2,5-connected poly-H_2bdc ligands[156,161-162] (Figure 15). See supporting information for a graphic and structure description of MOF-5.[158]
A systematic investigation of the synthesis conditions of Zn-based poly MOFs with different spacer length showed, that depending on the temperature and spacer length of the 2,5-connected poly-H_2bdc, the resulting material morphologies ranged from spherical superstructures to crystalline films.[156]

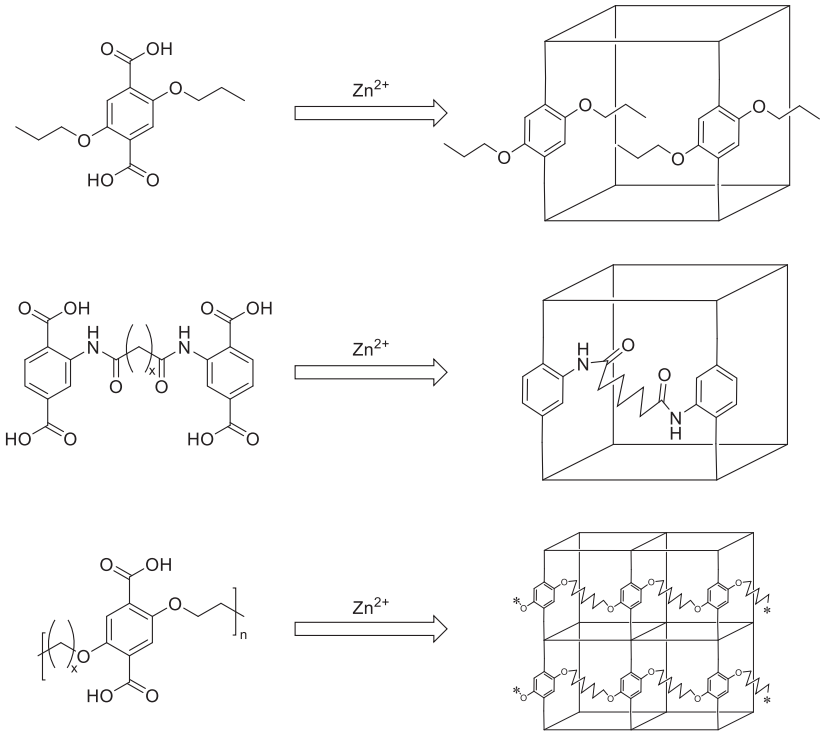

Figure 15 IRMOF derivatives constructed from (top to bottom): a H_2bdc ligand derivative, a 2,2'-linked di-H_2bdc ligand, and a polymeric H_2bdc polymer ligand with variable spacer length (*x*).

Very high surface areas (S_{Lang} = 4000 m^2/g)[158-159] and selective adsorption of CO_2 over CH_4[163] make MOF-5 and other IRMOFs interesting as fillers in MMMs for gas separation.[164] However, Zn-carboxylate MOFs have the problem of rapid Zn-carboxylate hydrolysis when exposed to air humidity.[89-90] Contact angle measurements for the polyMOFs showed increased hydrophobicity of the material with a better stability against air/humidity, which should make separation tests as membranes more realistic. The polyMOFs have much smaller BET surface areas than MOF-5 because of the incorporation of polymer chains in the framework but adsorb more CO_2 due to stronger interactions in smaller pores.[165]

A polyMOF could also be formed from Zn^{2+}, 4,4'-bipyridine (bpy) and a 2,5-connected poly-H_2bdc ligand, akin to the known mixed-ligand MOF $[Zn_2(bme\text{-}bdc)_2(bpy)]_n$ (bme-bdc = 2,5-bis(2-methoxyethoxy)-1,4-benzenedicarboxylate) (Figure 16).[166-168] The polyMOF formed particles which pack into uniform dense and defect-free films without any extra binder or polymer. These films exhibited relatively high CO_2 sorption but very low N_2 sorption, making them promising materials for CO_2/N_2 separation. The mixed-ligand polyMOFs also demonstrated good water or water vapor stability in contrast to the parent material $[Zn_2(bme\text{-}bdc)_2(bpy)]_n$.[157]

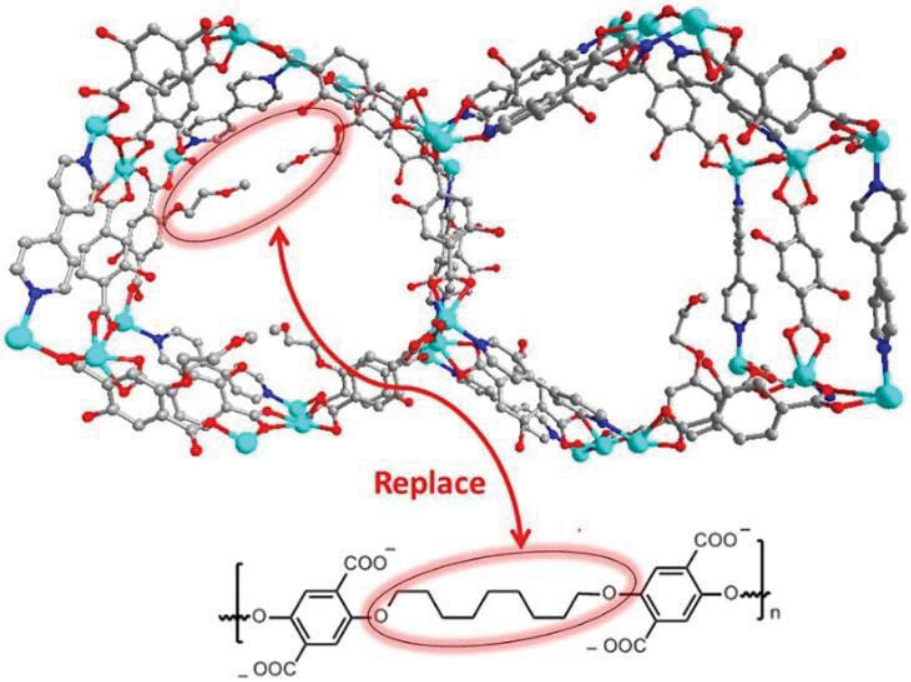

Figure 16 Structural representation of $[Zn_2(bme\text{-}bdc)_2(bpy)]]_n$ and design concept for polyMOF $[Zn_2(2,5\text{-}poly\text{-}bdc)_2(bpy)]_n$ by formal replacement of bme-bdc (2,5-bis(2-methoxyethoxy)-1,4-benzenedicarboxylate) with the 2,5-poly-bdc ligand (bottom). This is an unofficial adaptation from ref.[157] that appeared in an ACS publication. ACS has not endorsed the content of this adaptation or the context of its use.

1.2.4 Functionalized polymers for MMMs

In the previous sections modifications of the MOF-fillers were presented without attention to changes in the polymers for the MMMs. As noted above however, interesting behavior of MIL-53[152,169-170] composites with different polyimides has been observed when the structure of the polymer is altered by substitution of the diamine monomer to enhance the flexibility of the polymer chain.[108] MIL-53(Al)[58,60,171] and NH_2-MIL-53(Al)[45,57,108-109,172] are two intensively examined fillers in MOF-based MMMs because they show good adhesion with different polymers and often act as a model system for the influence of the NH_2-group on the polymer filler interaction. Here the interaction of different polymers with (NH_2-)MIL-53(Al) is examined with a focus on polymer functionalization.

Basic polymer structures can be modified by covalent attachment of groups onto the polymer chain (grafting)[173] or by substitution of monomer units to introduce other functionalities. The influence of different diamine monomers in 6-FDA-based polyimides was investigated by studying the morphology and separation performance of NH_2-MIL-53 MMMs.[174] With 6FDA–ODA (6FDA = 4,4′-hexafluoroisopropylidene diphthalic anhydride, ODA = 4,4′-oxidianiline, cf. Figure 4), the MMMs showed a very low CO_2 permeability of less than 15 Barrer (Figure 17), together with MOF particle agglomeration and weak polymer–MOF adhesion.[58] Also in the 6FDA–DAM/NH_2-MIL-53 membrane (DAM = 2,4-diaminomesitylene) the MOF particles agglomerated into clusters separated from the polymer.[174] In contrast to these 6FDA–ODA

and 6FDA-DAM based MMMs, membranes prepared from the copolyimide 6FDA-DAM-HAB (1 : 1) (HAB = 3,3′-dihydroxy-4,4′-diamino-biphenyl) and 10 wt% NH_2-MIL-53 approached the permeability/selectivity of the 2008 Robeson's upper bound (Figure 17). The hydroxyl groups in the HAB moiety were seen as the cause of a better interaction between the NH_2-MOF particles and the polymer matrix, giving an improved particle dispersion with no interfacial voids.[174]

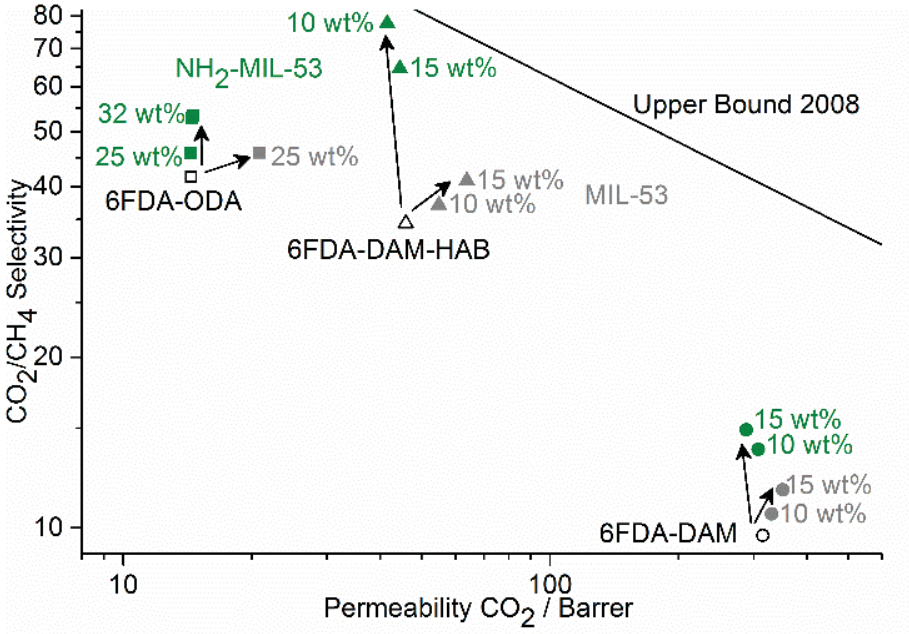

Figure 17 CO_2/CH_4 permselectivity and upper bound plot for 6-FDA based polyimides with different diamine monomers (ODA, DAM and HAB) and their (NH_2-)MIL-53 MMMs with standard (grey) and NH_2-MIL-53 (green) for different MOF/MMM mass fractions. The influence of the fillers on permeability and selectivity are compared for 6FDA-ODA[58] (squares), 6FDA-DAM-HAB (triangles) and 6FDA-DAM[174] (circles). See chapter 8.1.3 for a graphic and structure description of MIL-53.[152,169-170]

These copolyimides, which have intrinsic permeabilities of 40-60 Barrer, display relatively low permeabilities and high separation factors compared to other polyimides. The polymer poly(vinylidene fluoride) (PVDF), which acts more like a gas barrier with a CO_2 permeability of below 1 Barrer, was also studied. With a permeability this low, and a CO_2/CH_4 separation factor of 20 the influences of the filler on the separation process can be examined much more closely because the difference in flux and selectivity between polymer and filler is higher compared to most other studies. Thus PVDF was studied as a model polymer even though it has no potential to reach the requirements for industrial application as a dense polymer film.[175] Additionally, a method to post-synthetically modify PVDF by a mixture of KOH and $KMnO_4$ in order to effect HF elimination was chosen. During this reaction carbonyl and hydroxyl groups were created in the PVDF structure which are expected to interact with the amine groups of the NH_2-MIL-53 filler to enhance particle-polymer adhesion and have a positive effect on the separation performance of the MMMs because nonselective voids at the interface are likely to be avoided.[176] The performance of the mixed matrix membranes

based on modified PVDF (m-PVDF) MMMs was significantly improved compared with that of unmodified PVDF (Figure 18). The interaction between the modified polymer and the MIL-53 MOFs was studied by tensile tests, IR and DSC measurements and confirmed the formation of hydrogen bonds between the NH_2-groups and carbonyl groups in the material resulted in stronger adhesion with the amine-functionalized filler.

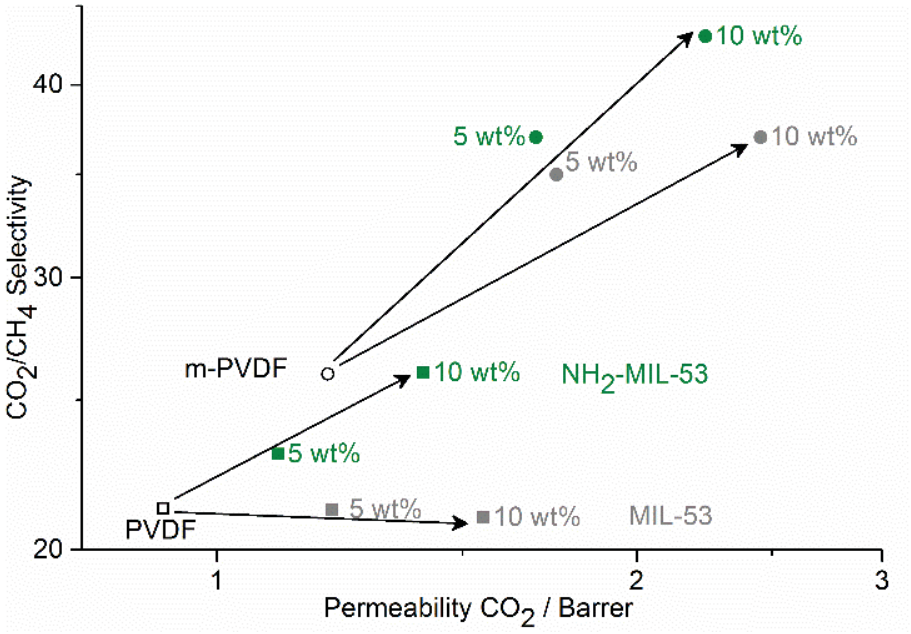

Figure 18 CO_2/CH_4 permselectivity plot for PVDF/MIL-53 MMMs[175] (squares) with standard (grey) and NH_2-MIL-53 (green) for different MOF/MMM mass fractions. With introduction of carbonyl and hydroxyl groups to PVDF the selectivity and permeability of the m-PVDF MMMs[176] (circles) increased due to stronger polymer-filler interaction. See chapter 8.1.3 for a graphic and structure description of MIL-53.[152,169-170]

Poly(amide-b-ethylene oxide) (Pebax®1657, Arkema) is a commercially available PEO/PA copolymer. It is a rubbery copolymer that contains poly(ethylene oxide), PEO segments as the permeable phase and a polyamide (PA) crystalline phase that gives mechanical strength to the membrane. With its high chain mobility and functional groups it is expected to have a good interaction with most fillers. Additionally it is easier to prepare defect-free MMMs using low glass transition temperature polymers and rubbery polymers. Using this polymer, thin layers (less than 1 mm) mixed with ZIF-7[177] nanoparticles could be fabricated on a porous poly(acrylonitrile) (PAN) support and these displayed high efficiency in CO_2/CH_4 and CO_2/N_2 separations. An intermediate gutter layer of polytrimethylsilylpropyne (PTMSP) was applied to serve as a flat and smooth surface for coating to avoid polymer penetration into the porous support (it has a very high permeability and does not contribute to the membranes selectivity, because its relative resistance is negligible). Pebax®1657 features relatively high CO_2 permeability and a moderate selectivity over N_2 and CH_4. As a MMM with ZIF-7, permeability (up to 145 Barrer for CO_2) and gas selectivity (CO_2/N_2 up to 97 and CO_2/CH_4 up to 30) were increased (Figure 18). The enhanced performance is due to the combination of a molecular sieving effect by the ZIF-7 filler and the high solubility of CO_2 in the polymer.[178]

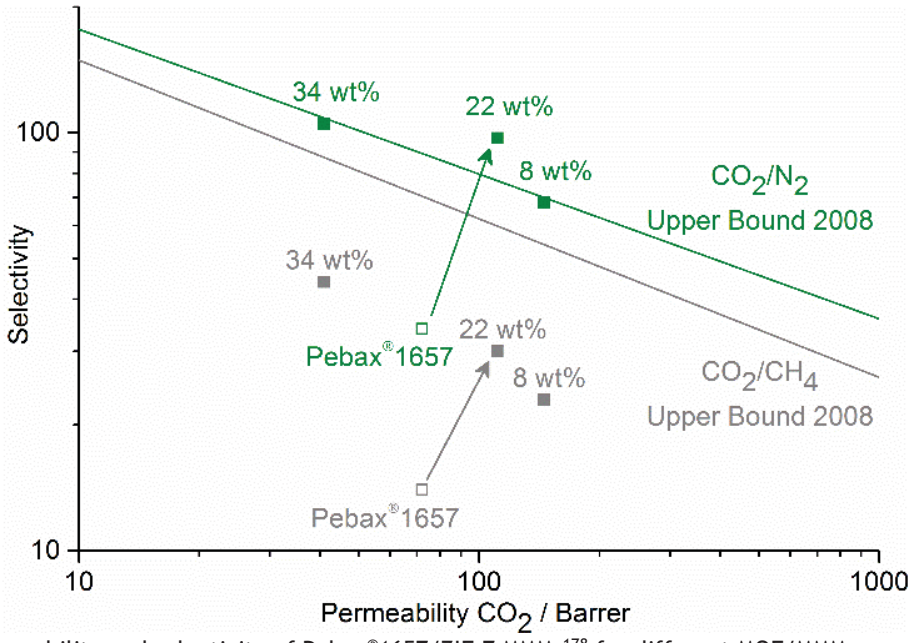

Figure 19 Permeability and selectivity of Pebax®1657/ZIF-7 MMMs[178] for different MOF/MMM mass fractions with CO_2/CH_4 (grey) CO_2/N_2 (green) permselectivity. The selective Pebax®1657/ZIF-7 layer was deposited on a porous polyacrylonitrile support with a PTMSP gutter layer, with 22 wt% ZIF-7 content in Pebax®1657 as the best performing MMMs for both gas pairs. See chapter 8.1.8.2 for a graphic and structure description of ZIF-7.[177]

Further to the introduction of functional groups by chemical modification of the polymer backbone, the possibilities to modify the properties of the polymer matrix are extendable to all areas of polymer chemistry, material science and plastic processing. One of these techniques is the fabrication of hybrid polymer matrices by mixing a second component into the polymer to gradually influence properties like the thermal stability and flexibility. Additionally, this second component can be incorporated into the space between the filler/polymer phases to interact with both phases. These ternary MMMs can be fabricated as solid/solid-MMMs by using a polymer blend as the matrix or liquid/solid-MMM by mixing with room temperature ionic liquids (RTILs) or low molecular weight polyetyleneglycol (PEG).[179] Ionic liquids were already discussed above as an additive to enhance the CO_2 uptake of the fillers or to tune the pore size of the fillers for controlled sieving effects. ILs can also be blended with polymers as polymeric ionic liquids (PILs). Ionic liquids such as [emim][Ac] are considered good solvents for polysaccharides like chitosan (CS), a biodegradable, biocompatible, non-toxic and hydrophilic membrane polymer which is a linear polysaccharide obtained by deacetylation of chitin. Excellent solvation of CS is achieved because of strong H-bonds between the acetate anion and the OH groups in the polysaccharide chain.[180] Hybrid solid IL–CS membranes can be prepared by introducing a small amount of [emim][Ac] IL into the CS polymer film.[181] This gave a binary material displaying good adhesion between the components, improved flexibility, as well as a decrease in the influence of temperature on CO_2/N_2 separation. This hybrid matrix was then

used to fabricate ternary MMMs with ZIF-8 or HKUST-1 nanoparticles as a porous filler to improve the selectivity of the IL–CS hybrid continuous polymer matrix.[182] The highest CO_2 permeability and CO_2/N_2 ideal selectivity were obtained for 10 wt% ZIF-8 and 5 wt% HKUST-1/IL–CS membranes (5413 Barrer and 11.5, and 4754 Barrer and 19.3, respectively, at 50 °C and 2 bar (Figure 20). The increase in permselectivity was attributed to the good adhesion and compatibility between the IL, the MOFs and the polymer matrix. For both MOFs, higher or lower loadings gave poorer results. The higher filler loading in the highest performing IL-CS/ZIF-8 MMMs versus IL-CS/HKUST is because of better compatibility between ZIF-8 and the IL.

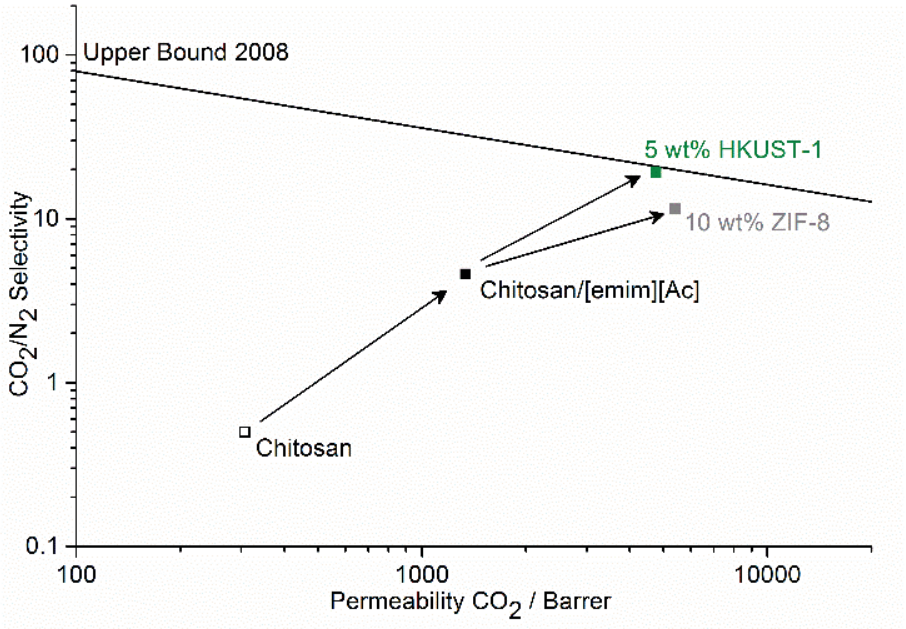

Figure 20 Increase of permeability and selectivity of chitosan-based membranes when [emim][Ac] and MOF fillers are incorporated. The open symbol corresponds to the pure chitosan membrane[181], closed symbols to the hybrid solid IL–CS membranes[182] with (green) 5 wt% HKUST-1 and (grey) 10 wt% ZIF-8 as the optimum loadings and best performing MMMs with MOF-fillers. For a graphic and structure description of ZIF-8[134-135] see chapter 8.1.8.1 and for HKUST-1[150] see chapter 8.1.1.

Polymer properties like plasticization, mechanical stability and permselectivity can be changed by thermal annealing of the membranes. The polyimide Matrimid, can be crosslinked at high temperatures by annealing. If enough mobility can be obtained through heat treatment, the aromatic imide and phenylene groups in adjacent polymer chains will approach each other closely enough to allow for π-electron interaction, which leads to the formation of charge-transfer complexes. This behavior increases the packing density of the polymer chains and decreases the free volume leading to increased size selectivity in gas separation.[183-184] The influence of the filler in MOF-based MMMs on the annealing of Matrimid was studied by Mahdi et al.[185] evaluating the structure-mechanical property correlations from nanocomposites to a prototypical MOF-polymer MMM composed of Matrimid and ZIF-8 nanoparticles. It was confirmed that the addition of ZIF-8 nanoparticles and annealing are

both beneficial for gas selectivity. The combination of mechanical characterization and gas separation showed that annealed 10 wt% ZIF-8/Matrimid MMMs would be ideal for practical separation applications because they retained a sizable level of damage tolerance and mechanical robustness, without compromising their toughness relative to annealed neat Matrimid (Figure 21). For the fracture energy and strengths there is an inverse relation with nanoparticle wt% loading.

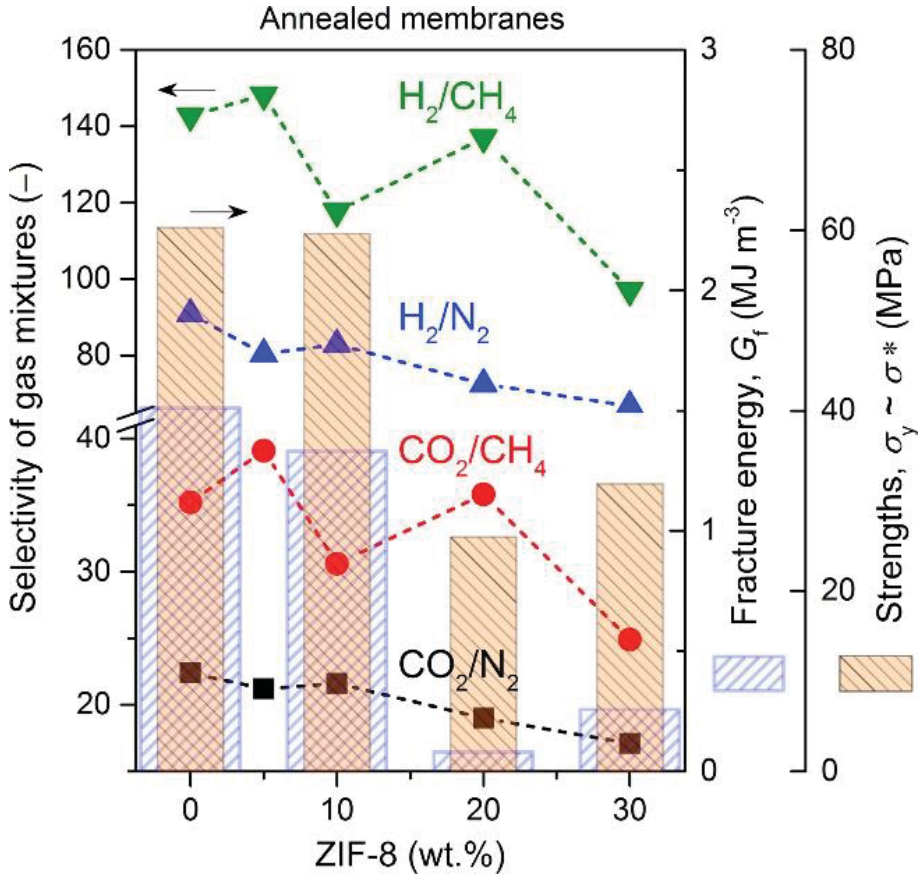

Figure 21 Comparison of the gas selectivity data of annealed Matrimid/ZIF-8 nanocomposite MMMs.[186] versus single gas permeation properties of pure annealed membranes, and the mechanical properties of annealed membranes (fracture energy and strengths). Figure taken from ref.[185] with permission, copyright Elsevier 2016.

1.2.5 Morphology, assembly and size of filler particles

The morphology and size of the filler particles are important properties for the preparation of MOF-MMMs. Predominantly these properties influence the distribution of the filler particles within the polymer matrix and the interactions between filler and matrix. Low degrees of aggregation and smaller particle size are important characteristics of MOF additives for mixed-matrix membranes in order to achieve a uniform distribution of the MOF particles without sedimentation.[50] High filler loadings are desirable to maximize the positive effect of the filler on the polymer matrix. However, there is an optimum loading where a good dispersion of the filler and excellent interfacial contact with the polymer chains results

in an optimum MMM performance. At higher loadings often a loss in selectivity is a result of formation of undesirable channels between the particles which aggregate because polymer chains are not able to completely surround and thereby separate the particles anymore.[49] At this optimum loading the permselectivity should be increased with smaller particles because less polymer material is needed to isolate a single particle. Additionally smaller particles are also helpful and essential in the formation of thinner MMMs which have higher permeation rates.[12] Particles in the sub-micron range have a much better chance of being accommodated inside a thin polymer film or layer, whereby bigger particles risk the formation of pinholes and polymer phase defects.[187] Additionally, with control of the size of MOF particles also the properties and applications are affected.[188] For gas adsorption with MOF nanocrystals not only are the adsorption kinetics improved compared to the bulk material,[189] but also there are cases where the total gas uptake is increased with decreasing particle size.[190-191] This emphasizes the positive effects of using nanosized MOF crystals as filler in MMMs.

Besides other synthesis conditions like pH, solvent and use of modulators, the heating method in MOF preparation has been extensively shown to be crucial for the resulting morphology and especially for the particle size.[192] For example the synthesis by microwave (MW) heating has been reported as an effective method to prepare small and uniformly sized MOF particles as suitable fillers for MMMs.[45] The benefit of rapid heating during a microwave-assisted synthesis is that it decreases the particle size of a MOF material in comparison with conventional heating and commonly a narrower size distribution can be achieved.[193-194] Another example is the sonochemical synthesis of submicron $Zn(pyrz)_2(SiF_6)$[195-196] (also known as SIFSIX-3-Zn[197]) for the preparation of MMMs for CO_2/CH_4 separation.[198] $Zn(pyrz)_2(SiF_6)$ is composed of square grids of Zn and pyrazine pillared by hexafluorosilicate (SiF_6^{2-}) anions, which form one-dimensional channels having a 3.8 Å diagonal dimension.[165] Thus the material exhibits excellent adsorptive size selectivity of CO_2 over N_2 and CH_4. The bulk material, synthesized by a RT mixing route, with an average particle size of 6 µm, and the submicron sonochemically synthesized $Zn(pyrz)_2(SiF_6)$ particles (average particle size: 860 nm) were comparatively studied as fillers in MMMs with crosslinked poly(ethylene oxide) (XLPEO) as a polymer matrix. The film formation was achieved by radical polymerization of the macro-monomers poly(ethylene glycol) diacrylate and poly(ethylene glycol) methyl ether acrylate using the initiator azobisisobutylonitrile between two glass plates with spacers to get films with well-defined thickness. Gas permeation experiments with CO_2/CH_4 (50/50) binary mixtures as feed gas and incorporation of 10 wt% $Zn(pyrz)_2(SiF_6)$ micrometer (average particle size of 5.7 µm) crystals into the membrane showed an improved separation performance, with CO_2 permeability and CO_2/CH_4 selectivity increased to 540 Barrer and 23, respectively. When 10 wt% $Zn(pyrz)_2(SiF_6)$ submicron crystals were used instead of the larger

material, the CO_2 permeability and CO_2/CH_4 selectivity were further enhanced to 620 Barrer and 27, respectively (Figure 22). For CO_2/N_2 (20/80) mixtures the same performance trend was observed for the comparison between micrometer and submicron particles as filler material.[198]

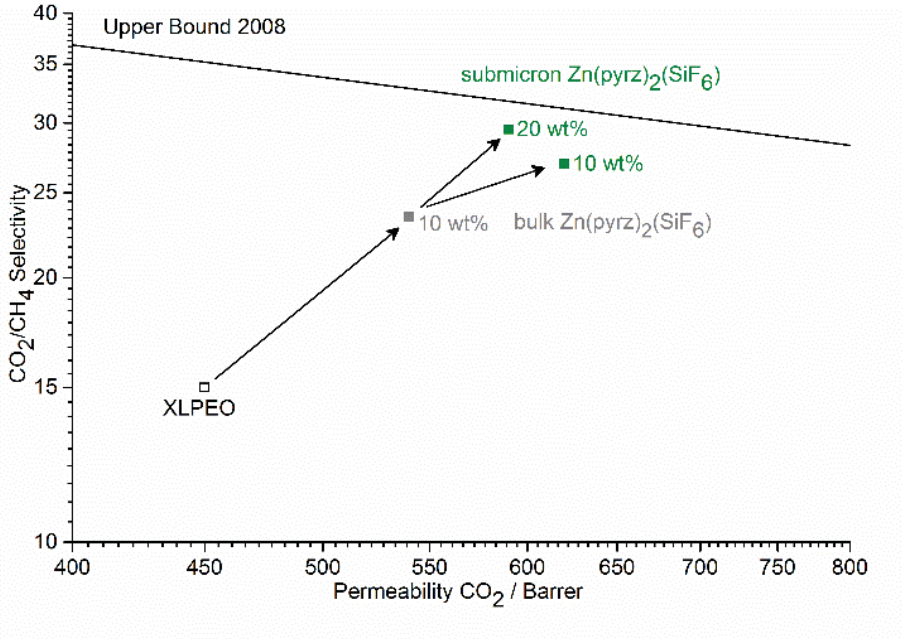

Figure 22 Stepwise increase of permeability and selectivity of crosslinked poly(ethylene oxide) (XLPEO) membranes when $Zn(pyrz)_2(SiF_6)$ fillers are incorporated.[198] The open symbol corresponds to the pure polymer membrane, closed symbols to the MMMs with (grey) 10 wt% micrometer $Zn(pyrz)_2(SiF_6)$ and (green) 10 and 20 wt% submicron $Zn(pyrz)_2(SiF_6)$ as the optimum loadings and best performing MMMs. See chapter 8.1.9 for a graphic and structure description of $Zn(pyrz)_2(SiF_6)$.[195-196]

Besides variation of the heating method, the use of modulators during the conventional solvothermal synthesis can also facilitate the formation of nanoparticles, suited as a filler for MMMs. $(OH)_2$-UiO-66(Hf) exhibits excellent H_2/CO_2 adsorptive separation performance and can be obtained with nanoparticle morphology when synthesized with acetic acid as a modulator.[199] MMMs containing $(OH)_2$-UiO-66(Hf) nanoparticles dispersed in poly(benzimidazole) (PBI) exhibited excellent H_2/CO_2 separation performance with the potential application in precombustion CO_2 capture.[200] Due to the strong CO_2 adsorption sites and extra free volume contributed by $(OH)_2$-UiO-66(Hf), the MMMs exhibited increased H_2 permeability and H_2/CO_2 selectivity compared to pure PBI membranes. 10 wt% $(OH)_2$-UiO-66(Hf) was found to be the optimum loading with a H_2 permeability of 8 Barrer and H_2/CO_2 selectivity of 19 at 5 bar, which puts it above the 2008 Robeson upper bound (Figure 23).

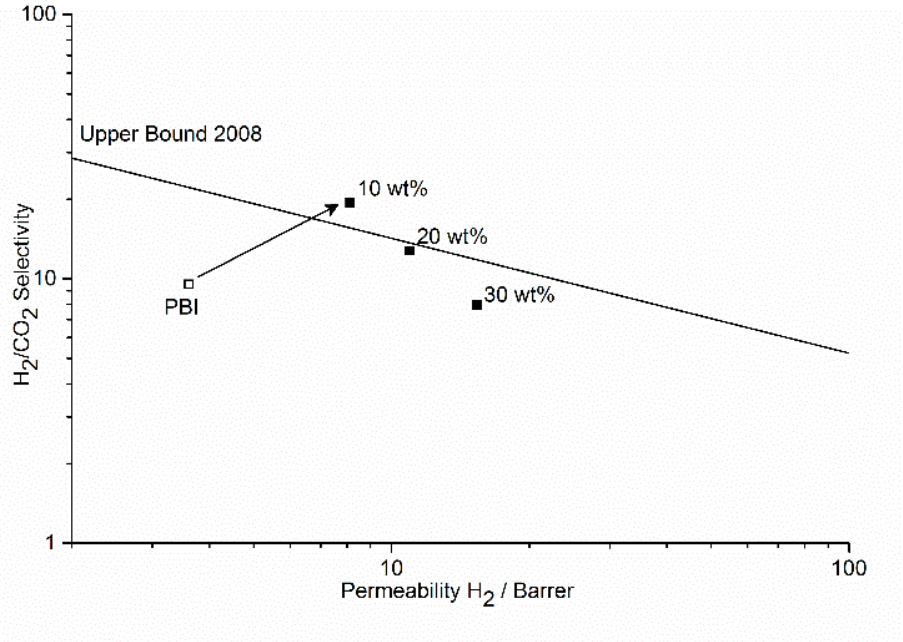

Figure 23 Comparative plot of permeability and selectivity of PBI-based MMMs with different amounts of $(OH)_2$-UiO-66(Hf).[200] The open symbol corresponds to the pure polymer membrane, closed symbols to the MMMs with the arrow indicating the optimum loading at 10 wt% $(OH)_2$-UiO-66(Hf), exceeding the 2008 Robeson upper bound. See chapter 8.1.7 for a graphic and structure description of UiO-66.[130,133]

Another interesting morphological effect (besides the particle size of the filler material) is the form of the MOF particles and has been the subject of recent reviews.[201-202] In case of the crystal form, crystal morphologies ranging from nanosheets, nanoparticles, nanorods were comparatively studied. The morphology of MOFs as nanosheets is clearly the optimal particle shape, compared to other non-sheet morphologies.[203-205] Other than the influence of the filler shape on the separation properties of MMMs, the use of hierarchical structured MOF assemblies composed of organized MOF-particles in terms of structure and function also show some interesting recent results on the permeation of MMMs.[206]

MMMs from Matrimid and ZIF-8 were fabricated by a novel approach by using the self-assembly of MOF and polymer particles followed by their controlled fusion to form membranes by DMF vapor annealing. This approach was studied to compare if the separation performance for CO_2/CH_4 gas mixtures of the material can be enhanced when the morphology of the membrane material is optimized and to achieve higher filler loadings.[207] The particle fusion approach can be divided into several steps. First, Matrimid polymer particles were prepared whose surface was then modified by the introduction of imidazole groups through grafting of 1-(3-aminopropyl)-imidazole onto the polymer backbone (Figure 24) to enhance the growth of ZIF-8 nanoparticles as a shell with good attachment to these linker groups anchored to the polymer particles. Then dense MMMs were formed in a DMF-vapor environment to induce particle fusion.

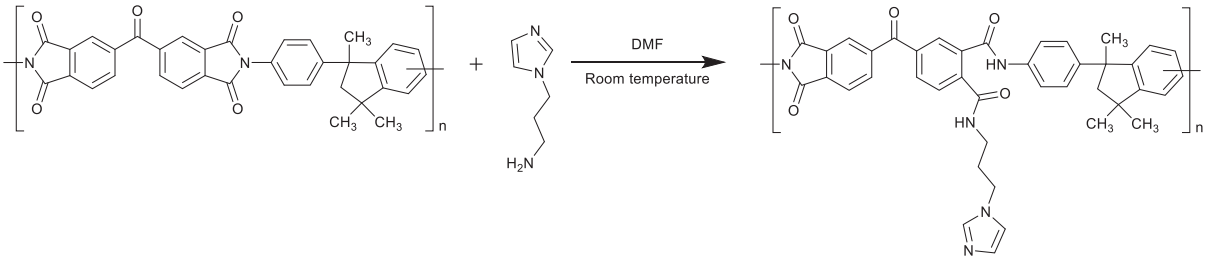

Figure 24 Grafting of 1-(3-aminopropyl)-imidazole on Matrimid.

Grafted Matrimid MMMs with ZIF-8 loadings up to 30 wt% could be achieved without any loss in selectivity. In the separation of CO_2/CH_4 mixtures the CO_2 permeability increased up to 200% combined with a 65% increase in CO_2/CH_4 selectivity, compared to the native Matrimid. The material also outperforms membranes with the same ZIF-8 loading, prepared without the particle fusion approach, but with an already optimized prime protocol including dispersion and slow evaporation of the solvent (Figure 25).[208] This clearly shows the potential to achieve high performing MMMs with highly compatible, well dispersed and high filler loading when the membrane fabrication technique is optimized in terms of avoiding morphological defects.

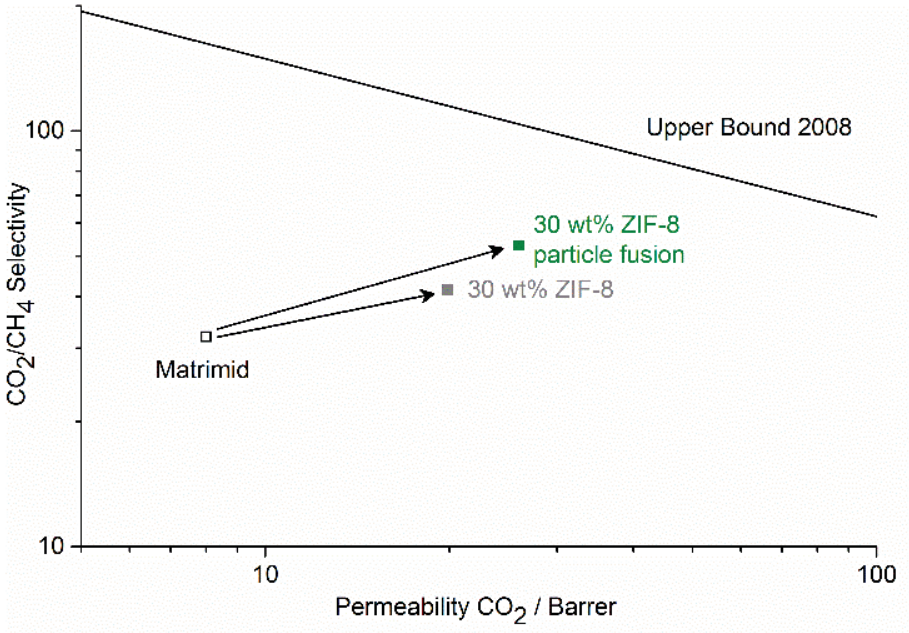

Figure 25 Permeability and selectivity of a 30 wt% Matrimid/ZIF-8 MMM[208] (grey) and increased permselectivity for a Matrimid/ZIF-8 MMM prepared by particle fusion and the same amount of ZIF-8[207] (green). See chapter 8.1.8.1 for a graphic and structure description of ZIF-8.[134-135]

Hierarchical structures can also be used to achieve increased permeability when spherical, hollow fillers are incorporated to form extra voids inside of the membrane, and where the sieve particles build a selective shell.[209] With the aim of improving filler-polymer contact, dispersion and gas permeability, hollow ZIF-8 spheres were used as the filler to prepare MMMs containing with the copolymer poly(vinyl chloride)-g-poly(oxyethylene methacrylate) (PVC-g-POEM) as the polymer matrix. The hollow MOF-spheres were prepared by

solvothermal coating of polystyrene (PS) nanoparticles with ZIF-8, followed by the removal of PS by immersion in DMF. Free standing, defect free MMMs were prepared via a solution casting method with filler loadings up to 30 wt%. SEM-images of the MMMs cross-sections show that the hollow MOF-spheres were homogeneously mixed with the PVC-*g*-POEM polymer matrix without any apparent interfacial voids or particle aggregation. (Figure 26)

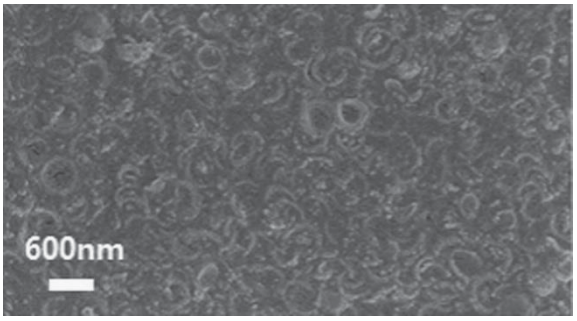

Figure 26 SEM image of the cross section of a 30 wt% PVC-g-POEM/hollow ZIF-8 sphere MMM. Figure adapted from ref.[209] with permission, copyright Elsevier 2015.

The CO_2/CH_4 gas separation performance of the MMMs was evaluated by pure gas permeation measurements at 35 °C. For MMMs with 30 wt% ZIF-8 the CO_2 permeability increased from 70 Barrer for neat PVC-*g*-POEM membranes to 623 Barrer with a slight loss in selectivity from 14 to 11 (Figure 27).

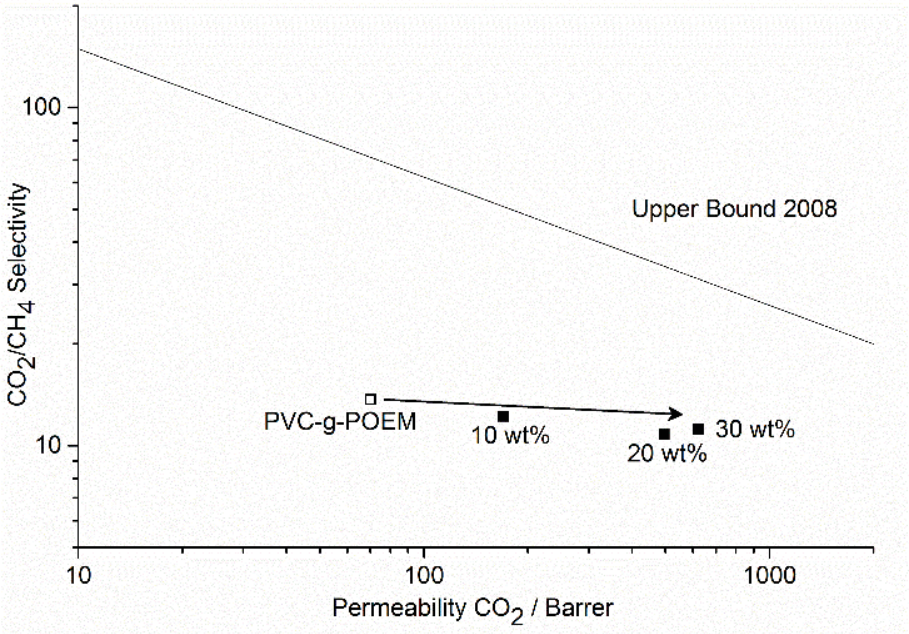

Figure 27 Effect of increased permeability on PVC-g-POEM/ZIF-8 MMMs[209] with increasing filler loading when ZIF-8 is fabricated as a hollow sphere before incorporation into the MMM in order to create extra voids with higher permeation compared to the dense material. See chapter 8.1.8.1 for a graphic and structure description of ZIF-8.[134-135]

ZIF-8 has the potential to have a molecular sieving effect as a filler in MMMs. The loss in selectivity for PVC-g-POEM/ZIF-8 MMMs may be due to the effect that the walls of the hollow spheres do not consist of completely intergrown ZIF-8 particles. In this case, cracks or holes

between the crystals show no resistance to the passage of both gases creating nonselective areas inside the spheres and thereby decreasing the selectivity of the MMM.

1.3 Conclusions and perspective

The combination of MOFs and polymers to fabricate MMMs is a promising strategy to avoid the trade-off between permeability and selectivity for organic polymers and to realize materials with separation properties exceeding the Robeson upper bound, reaching the potential for industrial application. Most work focuses on the separation of CO_2/CH_4 for natural gas sweetening or CO_2/N_2 separation for the purification of flue gases (cf. Table 1). In summary, all described MMMs exhibited enhanced separation performance depending on optimal filler loading and membrane integrity at high filler loadings or enhanced filler performance.

Permeation data for the MMMs presented in this section is collated in Table 1. This data was collected from studies which use a variety of characterization methods for gas separation and variable, but similar measurement conditions, at temperatures ranging from 25-50 °C and transmembrane pressures between 1 and 10 bar. As a consequence, this overview adds to the systematic comparison of the pure polymer material and the effect of the presented MOF fillers on permeability and selectivity presented throughout the review. For better comparison “round robin” tests under very similar conditions, including three different labs, have been already reported by Sanchez-Lainez et al. for ZIF-8 MMMs.[210]. The “round robin” study showed exemplary reproducibility of the membrane permeation analysis methodology by tests involving different European universities (UNIZAR from Zaragoza, Spain, LUH from Hannover, Germany and TUDelft from Delft, The Netherlands).

It should be emphasized that more studies like this which employ identical conditions for testing gas permeation under industrially relevant conditions should be developed. Particularly, mixed gas permeation and the influence of contaminants on the separation performance should be quantified. This is illustrated for the case of SPEEK in the combination of sulfonated MIL-101(Cr)[114] or with functionalized PEI@MIL-101[146] as a filler. The presence of water as a contaminant in the gas stream enabled and reinforced facilitated transport for CO_2 through the MMM material, thereby drastically enhancing the selectivity and permeability at 40 wt% loading in the separation of a CO_2/CH_4 gas mixture beyond the upper bound.

The discussed methods to tailor the MMM properties especially showed great effects in the case, where a combination of a filler with designed pore size by IL incorporation ([bmim][Tf_2N]@ZIF-8) and a asymmetric MMM with a very thin selective PSF/MOF layer was utilized for the separation of a CO_2/N_2 gas mixture.[139] Both the excellent size selective pores

of the modified filler, which resulted in enhanced selectivity, and the increased permeation rate of the thin MMM, resulted in a gas separation performance surpassing the Robeson upper bound. In a similar way a high separation performance of a CO_2/N_2 gas mixture was achieved for Pebax®1657 MMMs with ZIF-7 nanoparticles as a filler. At 22 wt % loading the thin selective MMM layer, supported by a porous poly(acrylonitrile) support with a PTMSP gutter layer, was still intact due to the homogeneous dispersion of the ZIF-7 nanoparticles in the MMM (Figure 28).[178]

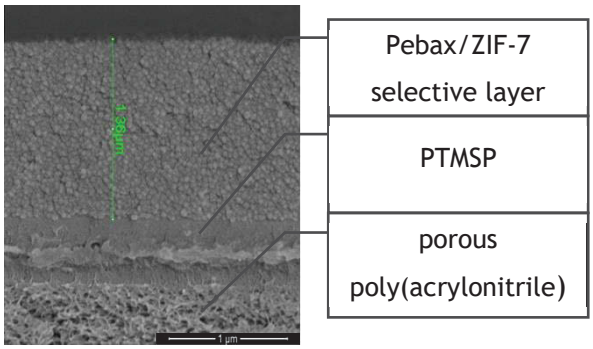

Figure 28 SEM cross-section of a composite membrane with (from top to bottom) selective MMM layer of Pebax®1657 with 34 wt% ZIF-7, PTMSP gutter layer and porous poly(acrylonitrile) support as representation of an asymmetric membrane. The scale bar is 1 µm. Figure adapted from ref.[178] with permission, copyright Elsevier 2013.

In a similar manner recent research on hollow fiber MOF mixed-matrix membranes have shown interesting results pointing the way to the industrial future of MOF based membranes and providing the possibility for MOF membranes to be industrially viable products for separations.[67] Koros et al. have incorporated ZIF-8 into an Ultem matrix and produced dual layer asymmetric hollow fiber membranes. The fibers showed increased permselectivity enhancements as high as 20% over the pure polymer.[52] Another approach is the coating of asymmetric hollow fiber membranes from PSF with a PDMS solution containing suspended HKUST-1 by a dip-coating technique.[66] *Continuous*, that is, pure MOF membranes inside polymer hollow fibers could be synthesized by a microfluidic approach. Nair et al. have fabricated continuous molecular sieving ZIF-8 membranes in poly(amide-imide) hollow fibers, with H_2/C_3H_8 and C_3H_6/C_3H_8 separation factors as high as 370 and 12.[211] The key challenge in the synthesis of continuous MOF-membranes is the control over the crystal growth position on the fiber and could be managed by a room temperature interfacial method for growing MOFs (ZIF-8 and HKUST-1) on either the outer or inner side of a polybenzimidazole-based hollow fiber (PBI-BuI-HF) membrane surface.[212] Coronas et al. have successfully expanded the microfluidic approach to a variety of continuous MOF-membranes. Microfluidics provides a constant reactant concentration along the membrane for growing homogeneous, continuous and thin MOF layers. ZIF-93 continuous membranes were synthesized on the inner side of P84 co-polyimide hollow fiber supports, and high

selectivities in the separation of H_2/CH_4 (59.7) and CO_2/CH_4 (16.9) mixtures were obtained.[213] ZIF-7 and ZIF-8 membranes were synthesized on the inner surface of a polysulfone hollow fiber.[214] The separation performance of ZIF-8 and ZIF-93 membranes can be further enhanced when grown inside of a co-polyimide P84 hollow fiber together with in situ thermal annealing. Gas separation selectivity increased without any significant reduction in the gas permeance, and H_2/CH_4 and CO_2/CH_4 selectivities of 103 and 18 (ZIF-8) and 101 and 20 (ZIF-93) were obtained.[215]

These results demonstrate the importance of membrane fabrication in respect to module geometries suited for industrial large scale separation processes, where the productivity of a membrane is increased by the usage of asymmetric membranes. With selective layers, lower than 1 µm, the performance of low flux polymers like PSF can be enhanced to move the separation properties to a commercially interesting area, as mentioned above. Thereby strategies like modulation of the MOF-synthesis and control of the particle size are powerful tools to design additives for high performing MMMs. The fine tuning of the MMM properties by utilization of the chemical functionality of the MOF linker,[111] or by introduction of functional groups by post synthetic modification,[126,132] and also the design of new polyMOFs[156,161-162] which, while creating a new subclass of MOF-materials with a great potential for being high performing membranes for gas separation, confirms that the high expectations of MOFs as multifunctional organic-inorganic hybrid materials are being successfully fulfilled. The high versatility of MOF chemistry enables the research community to target interesting effects, like the usage of the chemical modifications to not only increase the performance for a specific application, but also to increase the stability, which is an important step in making industrial applications possible.[216]

Table 1. Permeability and Selectivity Data of the Highlighted MMMs and Corresponding Polymer Membranes.[a]

filler (specification)	polymer	filler-ldg. [wt%]	P^b [Barrer]	*selectivity*		Measurement conditions[d]			ref.
			CO_2	CO_2/CH_4	CO_2/N_2[c]	T [°C]	Δp [bar]	method	
	PSF	0	7	27		30	10	mixed sweep	110
NH_2-MIL-125(Ti)		10	15	29					
		20	23	30					
		30	37	6					
	Matrimid 9725	0	6	30		35	9	mixed const vol.	111
MIL-125(Ti)		15	18	44					
		30	27	37					
NH_2-MIL-125(Ti)		15	17	50					
		30	50	37					
MIL-101(Cr)	SPEEK	0	16	23	34	30	1.5	single sweep, dry	114
		40	31	31	37				
HSO_3-MIL-101(Cr)		40	35	40	41				
MIL-101(Cr)	SPEEK	0	543*	23*	34*	30	1.5	single sweep, humid	
		40	1623	33	40				
HSO_3-MIL-101(Cr)		40	2064	50	53				
MIL-101(Cr)	SPEEK	0	16*	22*	33*	30	1.5	mixed sweep, dry, CO_2/CH_4 (30/70) CO_2/N_2 (20/80)	
		40	29	29	36				
HSO_3-MIL-101(Cr)		40	34	39	40				
	SPEEK	0	540*	21*	32*	30	1.5	mixed sweep, humid CO_2/CH_4 (30/70), CO_2/N_2 (20/80)	
MIL-101(Cr)		40	1600*	31*					
		40	1609*		39*				
HSO_3-MIL-101(Cr)		40	2029*	48*					
		40	2013*		51*				
	Matrimid 9725	0	6	31		35	9	mixed const. vol.	132
UiO-66(Zr)		30	16	36					
UiO-66(Zr)-BA		30	18	43					
UiO-66(Zr)-ABA		30	14	45					
NH_2-UiO(Zr)-66		30	18	37					
NH_2-UiO-66(Zr)-BA		30	17	39					
NH_2-UiO-66(Zr)-ABA		30	38	48					
	PSF asymm.	0	204	21		30	6	mixed sweep	139
ZIF-8		6	420	19					
IL@ZIF-8		6	312	34					
		0	227		26				
ZIF-8		6	464		29				
IL@ZIF-8		6	351		115				
	PMMA	0	(O_2) 0,09		(O_2/N_2) 8	35	2	single const. vol.	143
	PMMA	0	(O_2) 0.09		(O_2/N_2) 8	35	2	single const. vol.	144
			(O_2) 0.11		(O_2/N_2) 8				
NH_2-CAU-1	PMMA	15	(O_2) 633		(O_2/N_2) 2	25	1	single const. vol.	142
NH_2-CAU-1@PDA		15	(O_2) 627		(O_2/N_2) 3				
	Matrimid 5218	0	8		29	25	n.s.	single const. vol.	126
NH_2-UiO-66		23	23*		35*				
NH_2-UiO-66-PA		23	28*		36*				
NH_2-UiO-66-C10		23	22*		27*				
NH_2-UiO-66-SA		23	19*		30*				
	SPEEK	0	15*	27*	37*	30	1.5	single sweep, dry	146
MIL-101(Cr)		40	29	32	39				
PEI@MIL-101(Cr)		40	36	40	48				
	SPEEK	0	545	25	36	30	1.5	single sweep, humid	
MIL-101(Cr)		40	1623	32	40				
PEI@MIL-101(Cr)		40	2490	72	80				
MIL-101(Cr)	SPEEK	40	29	32	38	30	1	mixed sweep, dry CO_2/CH_4 (30/70), CO_2/N_2 (10/90)	
PEI@MIL-101(Cr)		40	36	39	47				
	SPEEK	0	529*	22*	33*	30	1	mixed sweep, humid CO_2/CH_4 (30/70), CO_2/N_2 (10/90)	146
MIL-101(Cr)		40	1586	30					
		40	1548		38				
PEI@MIL-101(Cr)		40	2384	70					
		40	2437		78				

filler (specification)	polymer	filler-ldg. [wt%]	P^b [Barrer]	selectivity		Measurement conditions[d]			ref.
			CO_2	CO_2/CH_4	CO_2/N_2[c]	T [°C]	Δp [bar]	method	
	6FDA-ODA	0	14*	50*		35	10	mixed const. vol.	58
MIL-53(Al)		25	21*	44*					
NH_2-MIL(Al)-53		10	14*	49*					
		15	14*	50*					
		20	14*	53*					
		25	14*	65*					
		30	15*	71*					
		32	15*	78*					
	6FDA-DAM	0	315	10		35	10	mixed const. vol.	174
MIL-53(Al)		10	330*	11*					
		15	351*	12*					
NH_2-MIL(Al)-53		10	307*	14*					
		15	288*	15*					
		20	298*	9*					
	6FDA-DAM-HAB	0	46*	34		35	10	mixed const. vol.	174
MIL-53(Al)		10	55*	37*					
		15	64*	41*					
NH_2-MIL(Al)-53		10	42*	78*					
		15	44*	65*					
		20	54*	35*					
	6FDA-DAM-HAB	0	54	18		35	10	single const. vol.	174
MIL-53(Al)		10	61	16					
		15	71	15					
NH_2-MIL(Al)-53		10	47	79					
		15	47	58					
		20	44	28					
	PVDF	0	0,9	21		25	6	mixed const. vol.	176
	m-PVDF	0	1,2	26					
MIL-53(Al)		5	1,8	35					
		10	2,5	37					
NH_2-MIL(Al)-53		5	1,7	37					
		10	2,2	43					
MIL-53(Al)-53	PVDF	5	1.2	21		25	6	mixed const. vol.	175
		10	1.6	21					
NH_2-MIL(Al)-53		5	1.1	23					
		10	1.4	26					
	Pebax® 1657[e]	0	72	14	34	20	3.75	single const. press.	178
ZIF-7		8	145	23	68				
ZIF-7		22	111	30	97				
ZIF-7		34	41	44	105				
	Chitosan	0	307		0,5	50	2	single const. vol.	182
	Chitosan/ [emim][Ac]	0	1338		5				
ZIF-8		10	5413		12				
HKUST-1		5	4754		19				
	XLPEO	0	450	15		25	1	mixed sweep	198
bulk $Zn(pyrz)_2(SiF_6)$		10	540	23					
submicron $Zn(pyrz)_2(SiF_6)$		10	620	27					
		20	590	30					
	XLPEO	0	470		19	25	1	mixed sweep CO_2/N_2 (20/80)	198
bulk $Zn(pyrz)_2(SiF_6)$		10	540		25				
submicron $Zn(pyrz)_2(SiF_6)$		10	670		29				
		20	630		29				
	PBI	0	(H_2) 4		(H_2/CO_2) 10	35	5	single const. vol.	200
$(OH)_2$-UiO-66(Hf)		10	(H_2) 8		(H_2/CO_2) 19				
		20	(H_2) 11		(H_2/CO_2) 13				
		30	(H_2) 15		(H_2/CO_2) 8				
	Matrimid	0	8*	32*		35	5	mixed const. vol.	207
ZIF-8 (particle fusion)		30	26*	53*					
ZIF-8		30	20*	41*					
	PVC-g-POEM	0	70	14		35	1	single const. vol.	209
ZIF-8		10	170	12					
		20	495	11					
		30	623	11					

[a] The data was used to plot the comparative permselectivity graphs to visualize the impact of the different strategies to modify MMM materials for separation; [b]Permeability of preferentially permeating gas. If another gas other than CO_2 is the preferentially permeating gas, it is specified in brackets next to the value; [c]if another gas other than CO_2 is the preferentially permeating gas the gas pair is specified in parentheses next to the value; [d]if not specified, in mixed gas experiments the feed gas composition is 50/50 vol%; [e] composite membrane [*]Data obtained and calculated from figures

Abbreviations: single const. vol. = single gas, constant volume method; single const. pres. = single gas, constant pressure method; mixed const. vol. = mixed gas, constant volume method; mixed const. pres. = mixed gas, constant pressure method; mixed sweep = sweep gas method

2. Zielsetzung und Motivation

Aufgrund des hohen Potentials von MOFs, als poröse Materialien durch Wirt-Gast Wechselwirkungen in Separations-, Sensorik- und Gaseinlagerungsprozessesen effektiv und zukunftsnah einen entscheidenden Anteil zur Steigerung der Leistungsfähigkeit von bereits existenten Materialien in industriellen Anwendungen beizutragen, haben sich drei Forschungsschwerpunkte ergeben, die den Rahmen dieser Arbeit definieren. MOF-Membranen können entweder als reine kristalline Materialien als Schicht auf Trägermaterialien hergestellt werden, um die Stabilität der häufig sehr brüchigen Filme zu gewährleisten oder die MOFs werden für eine einfachere Verarbeitbarkeit und Stabilität in Polymeren eingebettet.

In der Entwicklung von Membranen zur Gastrennung sind besonders die Mixed-Matrix Membranen eine Materialklasse mit hohem Anwendungspotential. In der Fachliteratur sind aufgrund der Vielfalt der Forschungsschwerpunkte (Prozessentwicklung, materialwissenschaftliche Studien, Eigenschaften von Kompositmaterialien, Membranformen, ingenieurswissenschaftliche Schwerpunkte) ein breites Spektrum an Füllstoffen und Matrixmaterialien zu finden welche zur Einordnung und Konkurrenzfähigkeit neu entwickelter Mixed-Matrix-Membranen beitragen. Daher wird die Entwicklung der neuesten Methoden zum Aufbau von MMMs basierend auf MOFs und die entscheidenden Aspekte zur Beeinflussung von Trennleistung und Stabilität der für die langfristig als Ziel definierte industrielle Anwendung dieser Materialien anhand der aktuellen Literatur dargestellt und die Wirkung der Herstellung und Modifikationsmethoden auf Permeabilität und Selektivität diskutiert (Kapitel 1 und Kapitel 3.1).

Aufbauend darauf ergibt sich der Fokus, dass Wasserstabilität, CO_2-Selektivität und Porosität der Füllstoffe entscheidende Aspekte des Anwendungspotentials von MOF-MMMs sind und häufig leider auch die begrenzenden Faktoren in der Erreichbarkeit der theoretischen Trennkapazität der hergestellten Membranmaterialien sind. Die Einführung von Linkern mit Donorgruppen mit stärkerer Basizität wie Imidazolate oder Pyrazolate kann zu einer höheren Kovalenz der Metall-Ligand-Bindungen führen und damit zu einer deutlich erhöhten Wasserstabilität beitragen. Membranen werden in ihrer Leistungsfähigkeit durch ihre Permeabilität und Selektivität beschrieben. Reine Polymermembranen besitzen eine Kompromissbeziehung zwischen diesen beiden Größen. Wenn MOFs für die Herstellung von MMMs in der Gastrennung verwendet werden, dann können durch das Einbringen der Partikel in Polymerfilme die positiven Eigenschaften (Porosität, selektive Gasaufnahme) auf das resultierende Material übertragen werden. Ein prototypisches MOF, welches aufgrund seiner hohen Porosität, BET-Oberfläche und CO_2-Affinität ein guter Füllstoff für MMMs in der

CO_2/CH_4 Trennung wäre, ist MOF-5. Dieses ist jedoch aufgrund seiner schlechten Hydrolysestabilität nicht für die industrielle Anwendung geeignet. Im Gegensatz zu MOF-5 zersetzt sich das isostrukturelle MOF $[Co_4(\mu_4\text{-}O)(Me_2pzba)_3]$ nicht an feuchter Luft. $[Co_4(\mu_4\text{-}O)(Me_2pzba)_3]$ soll durch eine verbesserte Syntheseroute in größeren Mengen und geringerer Partikelgröße hergestellt werden, um die MOF-Mikrokristalle in MMMs mit dem handelsüblichen Polymer Matrimid für die Abtrennung von Kohlendioxid aus Erdgas oder Biogas zu verwenden (Kapitel 3.2).

Die Herstellung von reinen MOF-Schichten für Trenn- oder Sorptionsprozesse bietet häufig die Herausforderung, dass die Stabilität der hergestellten reinen MOF-Filme durch schlechte Anhaftung an das Trägermaterial nicht gewährleistet ist und dass während der Belastung durch Sorptionsstress oder mechanische Belastung durch Druckunterschiede in Trennprozessen Defekte entstehen. Durch die Laserperforierung von Metallträgern wird ein Trägermaterial hergestellt, welches gasdurchlässig ist und mit selektiven Trennschichten belegt werden kann. Zusätzlich wird die Metalloberfläche während der Perforierung angeraut, was dem Kristallwachstum auf der Oberfläche förderlich ist. Die bevorzugte Abscheidung von MOFs auf dem Trägermaterial kann durch Verwendung eines thermischen Gradienten (selektives Heizen auf der Oberfläche des Metallträgers) erfolgen. Als MOF-Metallverbundwerkstoff wurde hier Messing mit HKUST-1 eingesetzt, da sich HKUST-1 gut als Prototyp für Sorptionsanwendungen eignet. Das Netzwerk besteht aus Cu^{2+} Paddle-Wheel Clustern, welche durch 1,3,5-Benzoltricarboxylat (BTC) verbrückt werden. Jedes Cu^{2+}-Ion wird durch 4 BTC-Sauerstoffatome und einem Sauerstoff Atom in axialer Position eines aqua Liganden koordiniert. Durch einen Aktivierungsschritt kann das Wasser Molekül von der HKUST-1 Struktur entfernt werden, wodurch koordinativ ungesättigte Metallzentren (CUS) erzeugt werden können. An diese koordinativen Leerstellen können dann bevorzugt Gastmoleküle, wie z.B. wiederum Wassermoleküle oder andere polar Adsorbentien koordinieren. Das Beschichten von Metallträgern mit MOFs hat für Sorptionsanwendungen den Vorteil, dass Adsorptionswärme besser abgeführt werden kann und so Wärme und Massentransfer verbessert werden (Kapitel 3.3).

Ein anderer Vorteil der Einbettung von stark hydrolyse- oder oxidationsempfindlichen Füllstoffen in Polymerfilme ist die Stabilisierung dieser gegen Umgebungseinflüsse wie Luftsauerstoff oder Feuchtigkeit. Wenn dadurch der Erhalt der Eigenschaften des Materials gewährleistet werden kann, wird so erst das Anwendungspotential des Materials erreicht. Lanthanoid-MOFs sind als potentielle Sensormaterialien von speziellem Interesse, da diese durch ihre Elektronenstruktur und durch passende Metall-Ligand Kombinationen oder Dotierungseffekte nützliche photophysikalische Eigenschaften besitzen können und ihre Emissionseigenschaften häufig Gastmolekülabhängig sind. Die beiden Ln-MOFs

3D-$[Sr_{0.9}Eu_{0.1}Im_2]$ und 2D-$[Tb_2Cl_6(bipy)_3]\cdot 2bipy$ sind empfindlich gegenüber Hydrolyse und Oxidation, was zu einem Verlust der Lumineszenz führt und so zur Detektion von Feuchtigkeit oder Luftsauerstoff verwendet werden kann. Um ihre Verarbeitbarkeit für praktische Anwendungen zu erweitern, sollen die beiden Verbindungen durch Einbettung oder Beschichtung mit einem geeigneten Polymer stabilisiert werden und die Lumineszenz und Stabilität der Polymer MOF Komposite unter dem Gesichtspunkt des Erhalts der Lumineszenzeigenschaften für potentielle Anwendung in der Sensorik untersucht werden (Kapitel 3.4).

3. Kumulativer Teil

Die Abschnitte 3.1 bis 3.4 beinhalten die Ergebnisse dieser Dissertation, die in Form von Veröffentlichungen in internationalen Journalen publiziert oder eingereicht wurden und werden in kumulativer Form dargestellt. Jede der folgenden Publikationen steht für sich und enthält ein separates Quellenverzeichnis. Vor jedem Abschnitt dieses kumulativen Teils wird ein kurzer Überblick über die Publikation gegeben sowie der Anteil der Arbeit des Autors an der Veröffentlichung beschrieben. Einzelheiten zu den Methoden und dem Messprinzip von Gemischtgas-Permeationsexperimenten finden sich in Abschnitt 4.

3.1 Mixed-Matrix Membranes

Janina Dechnik, Jorge Gascon, Christian J. Doonan, Christoph Janiak and Christopher J. Sumby

Angew. Chem. Int. Ed. **2017**, *56*, in press.
DOI: 10.1002/anie.201701109, Quelle[2]

Die Forschung zu ausgedehnten porösen Materialien wie Metall-organischen Gerüstverbindungen (MOFs) und porösen organischen Gerüstverbindungen (POFs) sowie deren molekularen Analoga, Metall-organischen Polyedern (MOPs) und porösen organischen Käfigen (POCs) hat sich im letzten Jahrzehnt stark entwickelt. Mit ihrer chemischen und strukturellen Variabilität und bemerkenswerten Porositäten wurden MOFs als neue Adsorbentien für industrielle Gastrennungen diskutiert. In diesem Zusammenhang zeigte sich auch ihr Potential als vielversprechende Füllstoffkomponenten für leistungsstarke Mixed-Matrix-Membranen (MMMs). Die Forschung in diesem Bereich konzentrierte sich auf die Verbesserung der chemischen Kompatibilität der MOFs und der Polymerphase durch sinnvolle Funktionalisierung der organischen Linker des MOFs und der Modifizierung der MOF-Oberflächenchemie. In jüngster Zeit wurden Untersuchungen zum Einfluss von Partikelgröße, -morphologie und –verteilung auf die (Erhöhung der) Trennleistung unternommen. Andere Füllstoffmaterialien, wie POFs, MOPs und POCs, werden ebenfalls als Additive für MMMs untersucht und zeigten unerwartet bemerkenswertes Verhalten gegen Polymeralterung und ausgezeichnete chemische Kompatibilität gegenüber handelsüblichen Polymeren. Dieses Review gibt einen Überblick zum Stand der Technik im MOF-MMM-Aufbau und über neuere Anwendungen von porösen organischen Gerüsten und porösen molekularen Additiven für MMMs.

Anteil an der Veröffentlichung:

- Schreiben der MOF-bezogenen Kapitel und Einleitung, Literaturrecherche und Konzeptentwicklung der MOF-Füllstoff basierenden Abschnitte und Bearbeitung des Manuskripts nach Revision. Korrekturen wurden durch Christoph Janiak vorgenommen.
- Das Kapitel zur MOF-Morphologie wurde von Jorge Gascon geschrieben
- Der Abschnitt zu porösen organischen Netzwerk-Additiven wurde von Christian Doonan beabeitet.
- Christopher J. Sumby schrieb die Abschnitte zu porösen molekularen Additiven und koordinierte die Arbeit zwischen den Coautoren.

Mixed-Matrix Membranes

International Edition: DOI: 10.1002/anie.201701109
German Edition: DOI: 10.1002/ange.201701109

Mixed-Matrix Membranes

Janina Dechnik, Jorge Gascon, Christian J. Doonan, Christoph Janiak, and Christopher J. Sumby**

Keywords:
gas separation · metal-organic frameworks · mixed-matrix membranes · porous materials

Research into extended porous materials such as metal-organic frameworks (MOFs) and porous organic frameworks (POFs), as well as the analogous metal-organic polyhedra (MOPs) and porous organic cages (POCs), has blossomed over the last decade. Given their chemical and structural variability and notable porosity, MOFs have been proposed as adsorbents for industrial gas separations and also as promising filler components for high-performance mixed-matrix membranes (MMMs). Research in this area has focused on enhancing the chemical compatibility of the MOF and polymer phases by judiciously functionalizing the organic linkers of the MOF, modifying the MOF surface chemistry, and, more recently, exploring how particle size, morphology, and distribution enhance separation performance. Other filler materials, including POFs, MOPs, and POCs, are also being explored as additives for MMMs and have shown, unexpectedly, remarkable anti-aging performance and excellent chemical compatibility with commercially available polymers. This Review briefly outlines the state-of-the-art in MOF-MMM fabrication, and the more recent use of POFs and molecular additives.

From the Contents

1. Introduction

Membrane processes are highly advantageous for the chemical industry by allowing energy to be saved during the separation of mixtures commonly encountered during production.[1] Energy savings of up to 50% of the production costs can be achieved by applying membrane technology.[1a,b] The membrane processes used in industry include natural gas sweetening (CO_2 removal), hydrogen isolation and recovery (i.e. in cracking processes), and oxygen (medical devices) and nitrogen enrichment from air (as a protecting atmosphere for oxygen-sensitive compounds).[2] Membrane processes such as vapor recovery systems,[3] monomer recovery units (e.g. ethylene/N_2 or propylene/N_2 separation),[4] the dehydration of organic solvents, and the removal of larger molecules from organic solvents[5] have a fast-growing market potential. At present, organic polymers are mostly used in the preparation of commercially applied membranes, as they are cheap to produce and easy to process compared with inorganic materials.

Although polymeric membranes have been used in industry for gas separation since the 1980s, they face challenges because of their compromise between gas permeability and selectivity. The well-known Robeson plot (log permeability versus log selectivity), states that as permeability increases, the selectivity of the membranes decreases—the so-called upper bound of membrane performance (Figure 1).[6] Enormous, ongoing efforts are being undertaken to meet this challenge through the development of new polymeric materials[7] and membranes of materials such as zeolites,[8] metal-organic frameworks (MOFs),[9] carbon molecular sieves,[10] carbon nanotubes,[11] and graphenes.[12]

Permeability and selectivity ("permselectivity") are the most important membrane parameters that determine the economics of separation processes.[13] Lower selectivity necessitates more complex, higher cost operations because of multistep processing, while the permeability correlates with the productivity of the membrane and, therefore, determines the area or the number of membrane modules required. Both factors affect the capital expenditure of the process. For example, precombustion separation of H_2/CO_2,

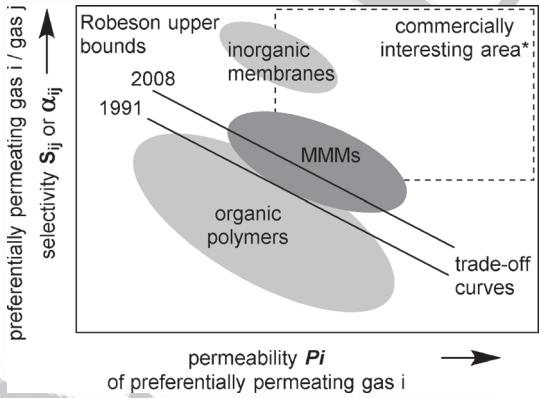

Figure 1. Schematic representation of the relationship between permeability and selectivity, with the 1991 and 2008 Robeson upper bounds shown. The distance or position relative to the upper bound can vary depending on the separation problem.

[*] J. Dechnik, Prof. Dr. C. Janiak
Institut für Anorganische Chemie und Strukturchemie
Universität Düsseldorf
Düsseldorf (Germany)
E-mail: janiak@uni-duesseldorf.de
Prof. Dr. J. Gascon
Department of Chemical Engineering
Technical University Delft, Delft (The Netherlands)
Prof. C. J. Doonan, Prof. C. J. Sumby
Department of Chemistry and the Centre for Advanced Nanomaterials, University of Adelaide
Adelaide (Australia)
E-mail: christopher.sumby@adelaide.edu.au

Supporting information and the ORCID identification number(s) for the author(s) of this article can be found under https://doi.org/10.1002/anie.201701109.

oxy-combustion O_2/N_2 separation, and natural gas treatments require highly permeable membranes for large-volume gas-feed streams. Pure MOF membranes, such as inorganic zeolite membranes, have very good permselectivity characteristics.[6,14] The challenges are, however, to develop manufacturing methods that would eventually allow for the reliable preparation of membranes (especially in the case of zeolites and other molecular sieves) and to maintain the integrity of such membranes (avoid cracks or pinholes) which result in the loss of separation performance.[15]

1.1. Mixed-Matrix Membranes

Mixed-matrix membranes (MMMs) are composite membranes made by combining an inorganic or inorganic-organic hybrid material in the form of micro- or nanoparticles (the discrete or dispersed phase; additive or filler) and a polymer matrix (the continuous phase; Scheme 1).[16] By using two materials with different transport properties, such membranes have the potential to combine synergistically the easy processability of polymers and the superior gas-separation performance of porous filler materials. MMMs may provide separation properties which can be above the Robeson upper bound[6] by overcoming the trade-off between the selectivity and permeability that is typical for pure polymer membranes.

Different types of inorganic additives—impermeable and permeable ones—have been used as filler materials.[16f,i–r,17] In particular, improvements in gas-permeation performance would be expected if nanostructured, highly porous additives such as zeolites or MOFs were used. Since a MMM is the dispersion of filler particles in a polymeric matrix, the properties of both the polymer and filler affect the separation performance.[16f,j–r] The chemical structure, surface chemistry, particle size distribution, and aspect ratio are other important factors of a filler material.

1.2. Zeolites and MOF Additives—Advantages and Challenges

MOFs offer various advantages over zeolites and are, therefore, promising additives for MMMs.[18] MOFs are chemically mutable, highly porous materials prepared from the combination of metal ions or metal-oxo clusters and organic ligands. In comparison with purely inorganic zeolites, the chemical diversity of MOF structures can be used to facilitate strong interactions with the polymer bulk material. This is achieved through judicious choice of ligands with appropriate chemical functionalities (Scheme 1a), which allows the formation of microgaps between the inorganic and organic phases, which cause loss of selectivity, to be reduced.[16i–r] Furthermore, the chemical mutability of the MOF scaffold can be utilized to provide enhanced adsorption of a particular chemical species and to facilitate improved separation performance. The limited chemical complexity of zeolites does not provide the level of tunability displayed by

Janina Dechnik (1986) graduated from Heinrich-Heine University with a Master in Chemistry in 2013. She is currently a PhD student at the Institute of Bioinorganic Chemistry in Düsseldorf. Her research focuses on the development of MOF devices as well as the application and characterization of new MOF-based materials for gas separation and adsorption.

Jorge Gascon (1977) is "Anthonie van Leeuwenhoek Professor" of Catalysis Engineering at TUDelft. His research interests include fundamental aspects and applications of nanostructured materials and composites. He has co-authored over 170 publications and several patents. He has been the recipient of several fellowships and awards, including VENI (2010), VIDI (2013), and ERC Starting (2013) grants and the 2013 ExxonMobil Chemical European Science and Engineering Award.

Christian Doonan is Director for the Centre for Advanced Nanomaterials and Professor of Chemistry at the University of Adelaide. His research interests encompass extended and molecular porous materials.

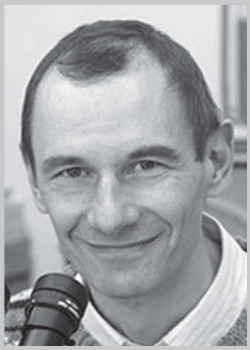

Christoph Janiak is full professor for Bioinorganic Chemistry and catalysis at the University of Düsseldorf, with research interests in the synthesis and properties of metal and porous organic frameworks (MOFs, COFs), metal nanoparticles, ionic liquids and catalysis. Until 2018 he is a visiting professor at Wuhan University of Technology in China.

Christopher Sumby is Deputy Dean for Research and Professor of Chemistry at the University of Adelaide, where he undertakes research into the synthesis and properties of nanomaterials for energy and environmental challenges. He has co-authored over 90 publications and been awarded various fellowships and awards, including an ARC Future Fellowship (2009) and a JSPS International Invitational Fellowship (2014).

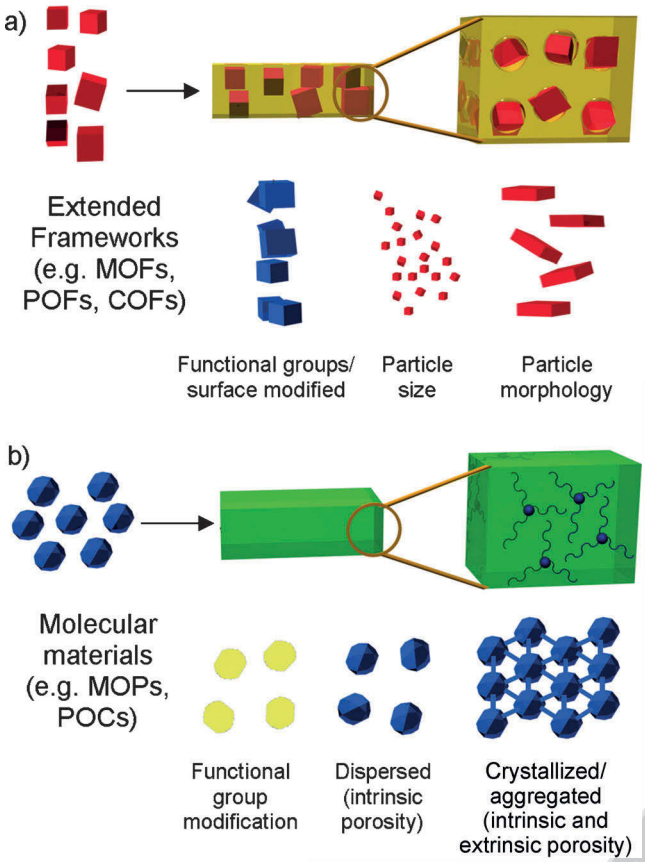

Scheme 1. Schematic representations of the structure of mixed-matrix membranes containing a) an extended framework or b) molecular additives (fillers). A selection of parameters is shown for the extended frameworks with different possible components for the filler materials, particle sizes, and shapes. For molecular materials, the intimate blending of the continuous and filler phase is indicated by a change in the membrane color and a lack of apparent particles. Similarly, some of the possible permutations for molecular fillers are shown: external functional groups and full dispersion or the possibility of crystallites forming in the polymer phase.

MOFs. In addition to the incorporation of chemical functionality through judicious choice of starting material, MOFs can also be modified post-synthesis (post-synthetic modification, as discussed later) to enhance the separation performance or facilitate stronger polymer–additive interactions. MOFs are not only tunable in terms of their chemical groups, but also their pore volumes, pore shapes, and surface areas, thus enabling them to contribute to either the permeability or selectivity of the MMM.[19] Many MOFs display considerably higher surface areas and larger pore volumes than zeolites, and can often display performance characteristics commensurate with the polymer matrix.

Despite these significant advantages, the hydrothermal stability of MOFs is a key, but often overlooked, factor for their potential applications in separation. Moisture is a major concern in industrial gas separations, and it is not economically feasible to use completely dry feed-gas streams. Although in some cases synergy between the two MMM components results in an improved stability of the MOF and polymer,[20] hydrolytically stable MOF materials are preferred as additives for the preparation of MMMs where a realistic technical application is envisioned.[21,22] Another challenge includes the scale-up of commercially useful MOF additives to facilitate the formation of the desired membrane modules; this has recently been a research focus.[23] Zeolites, in comparison, are commercially available materials with a long history of use in industry as a result of their ready availability as well as hydrothermal and chemical stability.

1.3. Alternative Additives

Although MOF fillers have attracted considerable attention, alternative crystalline and noncrystalline organic porous materials, such as covalent organic frameworks (COFs),[24] and a broad range of porous organic polymers[25] have also been also been explored very recently. In contrast to MOFs, these additives, which can be broadly referred to as porous organic frameworks (POFs), have entirely organic extended frameworks with either crystalline (e.g. COFs)[26] or amorphous structures (e.g. porous aromatic frameworks, PAFs).[27] The distinct advantages of POFs are their organic structures, which display excellent chemical compatibility with the organic polymer phase, and the chemical stability conferred by irreversible covalent bonding, particularly for materials such as PAFs and PIMs. Selected COFs also have chemically robust structures as a consequence of chemical modifications post-synthesis.[28]

The majority of the MMM additives examined are extended solids which possess strong directional bonding and open architectures with interconnected pores. However, the use of molecular porous additives such as shape-persistent porous organic cage molecules (POCs)[29] and metal-organic polyhedra (MOPs)[30] have recently garnered attention (Scheme 1b).[31] POCs are discrete organic molecules, often formed by a dynamic chemistry approach, that possess a defined cagelike structure that envelops an intrinsic void volume, whereas MOPs are metal-organic variants. Organic cages and MOPs with a range of cage geometries can be procured through judicious control of the molecular precursors. Their highly convergent bonding provides excellent stability and a recent advance of POC chemistry has included all-C–C-bonded variants.[32] These materials afford ultrahigh porosities common to extended solids, but retain their molecular identity. This allows them to be readily solubilized and in turn to be processed into composite materials.[24,25] Chemical compatibility between the filler and polymer can facilitate homogeneous dispersion of the MOP or POC within the continuous phase of a MMM. This can be exploited, as many POC and MOP series can be prepared with an identical cage topology but diverse exterior functionality. Similar to their extended porous analogues such as MOFs and COFs, discrete porous materials can also be carefully tuned to achieve exceptional performance in gas separations.

1.4. Overview and Scope

This Review outlines the state-of-the-art in the fabrication of MOF-MMMs, examining how the chemical functionality of

Dateiname: A701109e
Pfad: I:/daten/verlage/vch/ach/hefte/pool/
Status Neusatz
Datum: 24 KW., 6. Juni 2017 (Dienstag)
Pagina: 5
Seite: 4 te von 21
Umfang (Seiten): 21
Zeit: 15:42:07 Uhr

both the porous filler additive and organic chemical matrix combine to produce high-performance MMMs. Newer aspects of MOF-MMMs, particularly the role of MOF particle size, distribution, and importantly morphology will also be examined, as will the role of the MOF surface and post-synthetic modification. New composites with higher filler compositions or greater integration (e.g. so-called polyMOFs) between a crystalline MOF and the organic polymer component will also be discussed.

Additional sections of the Review will assess the use of porous organic frameworks and molecular additives. Materials such as COFs, POCs, and MOPs provide potentially greater chemical compatibility with the organic polymer support of a MMM than do MOF fillers. Finally, future challenges in the field will be considered, with a view to developing applications for these bespoke composites. To assist the reader, some general considerations of membrane performance and a glossary of polymer and selected filler structures are given in the Supporting Information.

2. Emerging Directions

2.1. MOF Inclusion—Significant Strategies

The identification of MOFs as excellent fillers with great potential because of their high porosity, tunable pore networks, and chemical variability of their structures[33c] has led to MOF-MMMs being intensively investigated.[16c,18a,33] These properties provide■ok?■ opportunities to enhance the performance or avoid defects at the polymer/particle interface, which result in loss of separation performance. Although most current studies of MOF-based MMMs are fundamental in nature, directed toward understanding the interactions and processes which occur at the phase interface, they will ultimately assist the development of materials for industrial application. Emerging aspects of MMM fabrication will be examined in the following sections, with a focus on recent, significant developments concerning MOFs (linker functionalization, surface modification, and post-synthetically modified MOFs, polyMOFs) as well as the choice of the polymer continuous phase. An overview of newer aspects of particle size and shape control in the fabrication of MOF-MMMs is also provided. Overall, these examples will demonstrate how separation performance can be advanced through the incorporation of compositionally and morphologically designed MOF additives.

2.1.1. Organic Linkers with Functional Groups

Depending on the type of gas separation, MOFs which have polar functional groups on their linkers can give rise to several different improvements in the performance of the MOF-MMM.[34] The interactions of the quadrupolar gas CO_2 with the linkers in MOFs can be enhanced by introducing NH_2 and SO_3H groups in chemically stable MOFs such as MIL-125(Ti)-NH_2[35] and MIL-101(Cr)-SO_3H.[36] Amine-functionalized linkers are a common focus because of their preferential adsorption of the weakly acidic CO_2. DFT also predicts that polar functional groups such as OH, NO_2, and NH_2 would be advantageous for the separation of polar gases.[37] A second way in which the functionality of the organic linker can be utilized is to achieve better compatibility with the polymer matrix and to enhance the morphology of the polymer/particle interface. Potential hydrogen bonding in MMMs between the polymer backbone and functional groups on the surface of the MOF filler particle can lead to increased compatibility and improvements, as seen in the gas separation properties of MMMs based on the amine-containing MOFs UiO-66-NH_2, MOF-199-NH_2,[16b] MIL-53(Al)-NH_2,[16a,r,36] and MIL-101(Al)-NH_2.[38]

Detrimental performance can also be encountered when a titanium-based and amine-functionalized MIL-125(Ti)-NH_2 ($Ti_8O_8(OH)_4(NH_2\text{-bdc})_6$) ($NH_2$-bdc = 2-amino-1,4-benzenedicarboxylate)[35] was investigated as a filler in MMMs for the separation of CO_2/CH_4 gas mixtures. With polysulfone (PSF) as the polymer matrix, the selectivity dropped from 27 for neat PSF membranes to 6 at high filler loadings (30 wt%), together with enhanced permeability from 7 to 37 Barrer as a result of nonselective voids arising from poor polymer-filler adhesion.[39] However, MIL-125-NH_2 MMMs with Matrimid (30 wt% loading) gave significantly improved separation results, leading to a 550% increase in selectivity combined with 35% higher CO_2 permeability compared to the PSF-based MMMs previously reported. Compared to pure Matrimid films (CO_2 permeability: 6 Barrer, CO_2/CH_4 selectivity: 30), the separation properties were enhanced for the MMMs with 30 wt% loading (CO_2 permeability: 50 Barrer, CO_2/CH_4 selectivity: 37).[40] Covalent bonding between the polyimide and the filler as a result of the linker amine group was postulated, although not demonstrated, as the main reason for the better performance of the membrane.[41]

The presence of sulfonic acid groups in the polymer or MOF filler materials can also be effective for increasing the separation performance of the membrane.[38a,42] The combination of a sulfonated derivative of MIL-101(Cr)[36] and sulfonated poly(ether ether ketone) (SPEEK) in a MMM was originally used as a proton-exchange membrane with improved proton conductivity for fuel cells.[43] These films also showed significant gain in CO_2/CH_4 gas selectivity compared with those loaded with unmodified MIL-101(Cr) fillers. The highest ideal selectivity for CO_2/CH_4 was 50 (at a CO_2 permeability of 2064 Barrer) with a 40 wt% MIL101-(Cr)-SO_3H loading in a humidified environment; in comparison, the pure SPEEK membrane had an ideal selectivity of 30 (at a CO_2 permeability of 540 Barrer; Figure 2). The sulfonic acid groups from both the polymer matrix and sulfonated MOF may construct facilitated transport pathways for CO_2 and, thereby, improve CO_2 solubility and hence■ok?■ selectivity.[44]

2.1.2. Pre- and Post-Synthetic MOF Modifications

There are many strategies to overcome defective membrane morphology or to influence the selectivity and permeability of particular MOF fillers in MMMs.[16h,33a] For the modification of a MOF synthesis, a distinction is drawn between in situ modulation during formation of the MOF

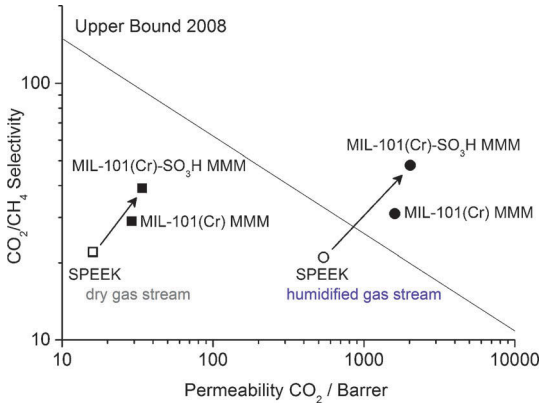

Figure 2. Example of a high-performing MMM from MIL101(Cr)-SO_3H/SPEEK with a 40 wt% filler loading that exceeds the Robeson upper bound for CO_2/CH_4 separations compared to the pure polymer SPEEK and nonfunctionalized MIL-101(Cr) MMM. Permselectivity data obtained from Ref. [44] (Data measured and calculated from figures).

crystallites and post-synthetic modification (PSM, see below). Modulation of the MOFs is a technique through which the internal MOF structure, as well as the crystal size, particle morphology, and outer-surface functionalities, can be controlled by using, for example, monodentate ligands during the synthesis of the material.[45] The modulators compete with conventional multidentate ligands for coordination to the metal cations, thereby allowing the surface of the particles to be better tuned for a desired application.[46]

Anjum et al. used the modulation approach during the synthesis of UiO-66 $[Zr_6O_4(OH)_4(bdc)_6]$[47] ■Anjum not in Ref 47, please check■ (bdc = 1,4-benzenedicarboxylate) and UiO-66-NH_2 $[Zr_6O_4(OH)_4(NH_2\text{-}bdc)_6]$[46a] to increase the affinity of the fillers for the Matrimid matrix and reduce leaks along the crystal-membrane interface. Benzoic acid (BA) or 4-aminobenzoic acid (ABA) was added to the MOF synthesis as a modulator in a 50:1 molar ratio relative to the linker to study the impact of amine groups in the modulator. The amine groups on the outer surface of the MOF can interact with the imide groups of polyimides, as confirmed by ATR-FTIR spectroscopic analysis of MMMs with high loadings of amino-MOF fillers. The membranes were tested for their performance in the separation of CO_2/CH_4 mixes. The results showed that the combination of the amine-functionalized modulator and linker in UiO-66-NH_2-ABA gave the best performance among the MMMs with different filler/modulator combinations. The MMMs with 30 wt% filler loading (CO_2 permeability: 38 Barrer, CO_2/CH_4 selectivity: 48) were over 50% more selective and 540% more permeable than the reference Matrimid membrane (CO_2 permeability: 6 Barrer, CO_2/CH_4 selectivity: 31) as well as 30% and 140% more selective and permeable, respectively, than MMMs based on the reference UiO-66 (CO_2 permeability: 16 Barrer, CO_2/CH_4 selectivity: 36).[48]

Neat ZIF-8[49] membranes exhibit only moderate CO_2/CH_4 selectivities (kinetic diameter of CO_2 3.3 Å; CH_4 3.8 Å), much less than anticipated based on the pore aperture (ca. 3.4 Å).[14b,50] Thus, an in situ ionothermal synthesis method was used to incorporate a room-temperature ionic liquid (RTIL), for example, butylmethylimidazolium bis(trifluoromethylsulfonyl)imide [bmim][Tf_2N], into the nanocages of ZIF-8. RTILs are ideal cavity occupants because of their negligible vapor pressure, high thermal stability, and good affinity to CO_2.[51] The sorption of N_2 and CH_4 by IL@ZIF-8 was notably decreased as a result of the reduced pore volume. In contrast, the uptake of CO_2 was enhanced (especially in the low relative pressure region), which can be attributed to the good solubility of CO_2 in [bmim][Tf_2N]. Gas permeability measurements on an IL@ZIF-8 MMM made with PSF showed that the selectivities of CO_2/N_2 and CO_2/CH_4 were remarkably improved from 29 to 115 and from 19 to 34 compared to MMMs incorporating unmodified ZIF-8.[52] Advantageously, MMMs prepared with the IL-incorporated filler showed excellent stability against plasticization at evaluated pressure.

Post-synthetic modification (PSM) of MOFs is a widely investigated method to influence the stability, properties, and chemical environment within the material.[53] PSM can also be used to control the properties and interaction of the fillers in MMMs. PSM of MOFs can be divided into several methodological categories; for details, readers are directed to reviews on the subject.[53a] PSM in the context of MMMs allows the introduction of chemical moieties that interact well with the polymer matrix onto the surface of the MOF particles. The technique can also permit surface functionalization of MOF crystallites, while not altering the internal MOF structure.

Thin polymer coatings can be added to MOF particles by controlled polymerization of a suspension of the particles. Cao et al.[54] coated a layer of polydopamine (PDA) on CAU-1-NH_2[55] by using pH-dependent polymerization through the addition of dopamine hydrochloride to the dispersed particles. The coated particles showed enhanced interfacial properties when embedded into polymethylmethacrylate (PMMA) because of the adhesive PDA layer between the CAU-1-NH_2 particles and the polymer matrix. These films were characterized as oxygen-permeable layers for the air electrode of Li-air batteries working under real ambient atmosphere conditions. The films enhanced the stability of the Li-air cell by repelling CO_2 and moisture in the air. Gas permeability measurements indicate that the MMMs exhibit a high O_2 permeability (627 Barrer) and low CO_2 permeability (114 Barrer). Additionally, the ideal O_2/N_2 selectivity of 3 for the MMM with PDA-coated MOF was higher than that (selectivity: 2) without the coating, which facilitated O_2 enrichment from air.[54]

PSM UiO-66-NH_2 has been studied as a filler, with the aim of improving the mechanical and gas separation properties of MMMs.[56] Three different functionalities—polar (acidic), nonpolar (C10), or aromatic—were introduced systematically into UiO-66-NH_2 and the PSM derivatives were characterized as fillers in MMMs with Matrimid. Analysis revealed that the two larger reactants, phenylacetyl chloride and decanoyl chloride, do not diffuse inside the network and only react with the amine groups on the crystallite surface of the MOF. In contrast, succinic acid is smaller and could react with the internal amino groups. The morphology of all the MMMs from Matrimid with the various UiO-66-NH_2-modified fillers showed good film formation as

Dateiname: A701109e
Pfad: l:/daten/verlage/vch/ach/hefte/pool/
Status Neusatz
Datum: 24 KW., 6. Juni 2017 (Dienstag)

Pagina: 7
Seite: 6 te von 21
Umfang (Seiten): 21
Zeit: 15:42:09 Uhr

well as strong interaction between the polymer and the particles (scanning electron microscopy (SEM) images showed no observable cavity formation around the particles and no sieve-in cage morphology). The influence of the different functionalities on the membrane morphology was shown with CO_2/N_2 single gas permeation measurements. An increased selectivity and permeability confirmed a defect-free interface in the case of MMMs possessing 23 wt% filler. MMMs with the phenylacetyl-functionalized UiO-66-NH_2 showed the strongest increase (CO_2 permeability: 28 Barrer, CO_2/N_2 selectivity: 36), followed by the unmodified UiO-66-NH_2 (CO_2 permeability: 23 Barrer, CO_2/N_2 selectivity: 35), decanoyl-functionalized (CO_2 permeability: 22 Barrer, CO_2/N_2 selectivity: 27), and the succinic acid functionalized UiO-66-NH_2 (CO_2 permeability: 19 Barrer, CO_2/N_2 selectivity: 30). The favored interaction of MOF particles with NH_2 and phenylacetyl functionalities was explained by the presence of aromatic and imide groups in the polymer (Figure 3).

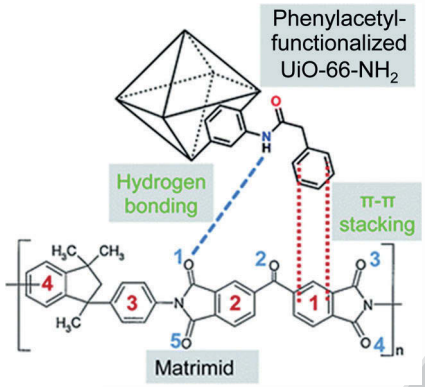

Figure 3. Scheme demonstrating the favorable interactions between the Matrimid polymer and phenylacetyl-functionalized UiO-66-NH_2 based on surface functionality. Figure adapted from Ref. [56] with permission. Copyright Royal Society of Chemistry, 2015.

2.1.3. *Polymer-MOF Hybrids (polyMOFs)*

A new subclass of porous materials, so-called polymer-MOF hybrids (polyMOFs),[57] use organic polymers as an inherent component of the MOF structure. These harness not only the advantages of polymers, such as the facile fabrication of films, good processability, and chemical stability, but also the best traits of MOFs, including crystallinity, well-determined structures, and permanent porosity. Polymer-MOF hybrid materials can be understood in the context of the broader metallopolymer field, in which metal centers are linked to classic polymeric structures.[58] These newly developed polymer-MOF hybrid materials could be used as neat membrane materials if their prototypical MOF structures possess high selectivity and porosity, and at the same time have the capability to form films with high mechanical stability similar to polymeric materials. This would obviate the challenges of traditional pure MOF membranes, but also allow the generally, high selectivity of the MOF material to be used without dilution in a polymer matrix.

There are several routes for the fabrication of polymer-MOF hybrid materials. PSM approaches to form polymer monoliths (MOF-to-polymer conversion) have been followed and resulted in the transformation of cubic MOF crystals into polymer gels by inner cross-linking of the organic linkers in the void space of the MOFs.[59] For example, an azide-tagged MOF was prepared from a functionalized ligand and subjected to reaction with a tetraacetylene cross-linker to obtain a cross-linked MOF (CLM). In another post-synthetic approach, a Cu-based MOF with bifunctional linkers (2,5-divinylterephthalate) that could participate in radical polymerization was synthesized.[60] The radical polymerization of isolated parallel chains and their cross-linking was performed by reaction with styrene or methyl methacrylate inside the pores of the MOF (host-guest cross-polymerization). Once the polymerization was completed, a cross-linked polymer could be obtained easily by selective dissolution of the MOF matrix.[60] However, these strategies for polymerization within the pores of MOFs have not yet enabled the preparation of thin films for separation applications or allowed the resulting polyMOFs to obtain the separation potential of their prototypical MOFs.

Stemming from an interest in the interface between MOFs and polymer materials, Zhang et al.[57] have developed a strategy to transform 1D, nonporous, amorphous polymers into three-dimensional, highly porous, crystalline MOFs. This synthetic approach can be seen as a presynthetic modification of MOFs, since the ligands are polymerized before synthesis of the MOF (Figure 4). IRMOF-1 (MOF-5) possesses a very

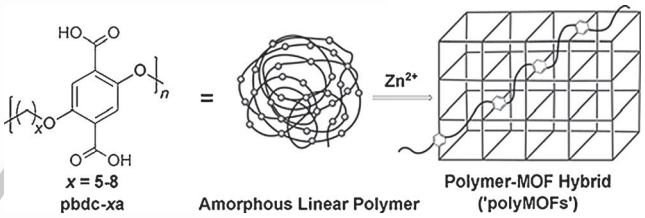

Figure 4. The synthesis of a polyMOF, isoreticular with MOF-5, from 2,5-connected bdc polymeric ligands with different lengths (x) of methylene spacers. Figure reproduced from Ref. [57a] with permission. Copyright John Wiley and Sons, 2015.

high surface area ($S_{BET} \approx 3000\ m^2\ g^{-1}$)[61] and selectively adsorbs CO_2 over CH_4.[62] These characteristics make it interesting as a filler in MMMs for gas separation,[63] but with the problem that it is labile in humid conditions. To overcome this, new polymer-MOF hybrid materials were synthesized from 2,2′-cross-linked bdc ligands[64] and 2,5-connected bdc polymeric ligands (pbdc).[57a] Depending on the length of the methylene spacers in the polymer backbone, networks with IRMOF structures could be obtained. The morphology of the polyMOFs obtained at low synthesis temperatures (80 °C) was also studied and revealed that morphologies ranging from spherical superstructures to crystalline films are obtained. The film morphology for two Zn-based polyMOFs was revealed to be an intergrown network of crystallites around 20 μm thick. Such films may

be useful for small-molecule and gas separations, but have not been characterized for this application.

The potential for the industrial application of the polyMOFs derived from IRMOF-1 was also examined. Contact angle measurements showed increased hydrophobicity of the IRMOF-1 polyMOFs and better stability against exposure to air/humidity. Whereas MOF-5 loses crystallinity and gas adsorption properties, the Zn-based carboxylate polyMOFs remained stable. This enhanced stability can be rationalized by the increased hydrophobicity limiting egress, such that water vapor cannot enter the MOF and hydrolyze the Zn-carboxylate bond. These results offer the tantalizing prospect of examining realistic technical application conditions whereby a humidified gas stream is used to test the separation performance of membranes. The polyMOFs derived from IRMOF-1 exhibit much smaller BET surface areas than IRMOF-1, but were found to take up more CO_2 because of the incorporation of polymer chains in the framework.[65]

Other MOF prototypes can also be used for the synthesis of polyMOFs, including the UiO-66 topology.[57b] Mixed-ligand MOF systems with bdc and ligands such as bpy = 4,4′-bipyridine and bpe = 1,2-bis(4-pyridyl)ethane are well-investigated.[66] These MOF topologies were used as a design template to synthesize new polyMOFs from a polyether dicarboxylate ligand in combination with N-donor coligands. Again, the polyMOFs were found to form particles that were packed into uniform films. Experiments to determine the polymer to metal stoichiometry indicated that the polyMOFs may contain structural defects such that not all the bdc units from the polymer ligands are coordinated to the secondary bonding units (SBUs). This also includes the possibility that polymer ligands extend outside the crystal domain and serve as a binder on the surface of the MOF particles. The polyMOF hybrids exhibit relatively high CO_2 sorption but very low N_2 sorption, thus making them promising materials for CO_2/N_2 separation. In addition, the mixed-ligand polyMOFs also demonstrate good stability to water or water vapor compared to the parent materials.[57b]

2.1.4. Functionalized Polymers

The application of polymers grafted with functional groups as a continuous phase combined with suitable MOFs as the dispersed phase for MMMs is also expected to enhance the polymer-MOF interaction. Furthermore, the distribution of MOF particles could be improved and the intrinsic permeability of the polymer tuned. Grafting is a method wherein groups are covalently bonded (modified) onto the polymer chain.[67] Combining MIL-53(Al)-NH_2 with 6FDA-ODA (6FDA = 4,4′-hexafluoroisopropylidene diphthalic anhydride, ODA = 4,4′-oxidianiline), a nonfunctional polyimide with very low gas permeation (CO_2 permeability: 14 Barrer, CO_2/CH_4 selectivity: 50), results in a MMM providing less than 15 Barrer for CO_2 permeability but an enhanced selectivity of 78, a noticeable particle agglomeration, and a weak polymer-MOF adhesion. The performance suggested that the MOF particles were agglomerating to form clusters rather than being dispersed homogeneously in the bulk polymer.[16p] To confirm this behavior, a MIL-53(Al)-NH_2/6FDA-DAM (DAM = diaminomesitylene) membrane was prepared, in which the MOF-NH_2 particles also agglomerated into clusters with diameters of about 500 nm and their bare surface could be observed easily.[68] In contrast to these 6FDA-ODA and 6FDA-DAM based MMMs, membranes prepared from 6FDA-DAM-HAB (1:1, where HAB = 3,3′-dihydroxy-4,4′-diaminobiphenyl) copolyimide (CO_2 permeability: 46 Barrer, CO_2/CH_4 selectivity: 34) and 10 wt% MIL-53(Al)-NH_2 showed a permeability/selectivity behavior approaching the 2008 Robeson upper bound (CO_2 permeability: 42 Barrer, CO_2/CH_4 selectivity: 78). Furthermore, the OH groups on the polymer appeared to play a critical role in improving the interaction between the MOF-NH_2 particles and the polymer matrix, thereby enhancing the particle dispersion as well as effectively eliminating interfacial voids.[68]

2.1.5. Controlling MOF Particle Size and Morphology

In addition to changing the chemical properties of either the filler or the polymer, another powerful approach towards enhanced membrane performance consists of changing the morphological properties of the filler. It is indeed easy to envisage that issues such as particle aggregation, dispersion of the filler in the continuous polymer matrix, orientation of the porosity of the filler with respect to the membrane, and filler utilization in general will be greatly affected by the particle morphology and distribution. Such multiscale crystal engineering of MOFs has achieved significant recent attention and has been the subject of reviews.[69,70]

Although still scarce, a few examples highlighting the importance of filler particle size and morphology have been published. Submicrometer ZIF-90 particles (0.81 ± 0.05 μm) in the polyimide 6FDA-DAM (15 wt%) gave a CO_2 permeability of 720 Barrer with a CO_2/CH_4 selectivity of 37 (mixed gas, 1:1 CO_2/CH_4 mixture). The small size was deemed crucial for the permeability, as ZIF-90 with 2.0 ± 0.6 μm sized particles in 6FDA-DAM (15 wt%) yielded a permeability of 590 Barrer with a selectivity of 34 (for a 1 μm MMM, the permeance was 720 and 590 GPU, respectively).[71] To provide some context, these values can be compared to a CO_2 permeance of 100 GPU and selectivity of 15 for commercial CO_2/CH_4 membranes.[71] Membranes with very high permeability and good selectivity, as encountered for these ZIF-90/6FDA-DAM MMMs, may be industrially attractive.[72]

In a similar manner, ZIF-7 nanoparticles with sizes of around 30–35 nm were incorporated as a suspension into commercially available poly(amide-*b*-ethylene oxide) (Pebax 1657) formed on a porous polyacrylonitrile (PAN) support with a PTMSP gutter layer (CO_2/CH_4 selectivity: 14, CO_2/N_2 selectivity: 34).[73] The SEM data showed ideal blending between the two phases and no apparent voids or clusters. The separation performance of the composite membranes was investigated by single gas permeation experiments and analyzed for CO_2/N_2 and CO_2/CH_4 mixtures. Both the permeability (up to 145 Barrer from 72 Barrer) and gas selectivity (CO_2/N_2 up to 97 and CO_2/CH_4 up to 30) are increased at a low ZIF loading into Pebax 1657.

The first real consideration of particle morphology was reported by Rodenas et al.[20a] These researchers identified that the ideal morphology of a MOF nanofiller would be a nanosheet form. As previously discussed by Konduri and Nair[74] as well as Tsaptsis[75] and co-workers, the use of 2D materials in MMMs offers several advantages, such as an almost full utilization of the filler and a better matching with the polymer matrix. Based upon this hypothesis, Cu(bdc) MOF lamellae (CuBDC) of micrometer lateral dimensions and nanometer thickness were prepared. These nanosheets were readily dispersed within a polyimide (PI) matrix at different filler loadings (2–12 wt%) by a solution processing method to give cast membranes with a thickness of 30–50 μm. The composites showed outstanding CO_2 separation performance from CO_2/CH_4 gas mixtures, with the separation selectivity for 8 wt% nanosheet-CuBDC@PI being 30–80% higher than for the pure polymeric membrane and 75–800% higher than for the bulk-CuBDC@PI counterpart. Notably, the intrinsic sorption properties of bulk-type and nanosheet CuBDC precursors are similar and, thus, the difference in crystal morphology accounts for the difference in performance. Tomographic focused ion beam SEM provided evidence for better occupation of the membrane cross-section by the MOF nanosheets compared with isotropic crystals, and explains the improved separation efficiency (Figure 5). By

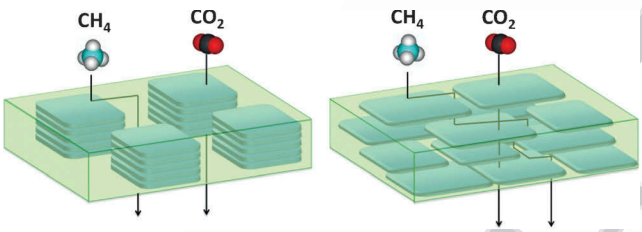

Figure 5. Representations of composite membranes containing bulk-type (left) and nanosheet (right) CuBDC MOF embedded in polyimide. The morphology and dispersion of the nanosheet form in the MMM enhances the separation performance.

using the same approach, Zhao and co-workers[76] developed a method for the preparation of $[Cu_2(ndc)_2(dabco)]_n$ in the morphologies of nanocubes and nanosheets, and observed an improved performance of the nanosheet-based MMMs with polybenzimidazole (PBI) and 20 wt% loading, with the overall H_2/CO_2 separation performance (H_2 permeability: 6 Barrer, H_2/CO_2 selectivity: 27) exceeding the 2008 polymer upper bound.

A systematic investigation of particle morphology was recently reported[77] in which MMMs composed of MIL-53(Al)-NH_2 in three different morphologies— nanoparticles, nanorods, and microneedles—and Matrimid or 6FDA-DAM, at loadings between 5 and 20 wt%, were prepared. Matrimid membranes were tested for CO_2/CH_4 (1:1) separations at 3 bar and 298 K for 8 wt% MOF loading, where it was observed that the incorporation of MIL-53(Al)-NH_2 nanoparticles gave the largest improvement in performance compared to nanorods and microneedles. It was also noted that the best performing morphology of nanofiller (particles) gave a more pronounced improvement in performance when incorporated into a highly permeable matrix (6FDA-DAM). The best performing membranes have a permeability of 660 Barrer, with a CO_2/CH_4 separation factor of 28, thus placing them close to the 2008 Robeson upper bound. Overall, these results demonstrate that tuning particle morphology is a very powerful approach to tune MMM performance.

2.2. Porous Organic Frameworks as Additives

The term porous organic framework (POF) includes a number of porous solids based only on organic constituents.[78] POFs possess high surface areas, tunable pore sizes, and adjustable scaffolds. When the organic constituents are aromatic, the term porous aromatic framework (PAF) is adopted.[27] In this section, the fabrication of MMMs from POFs, which has only recently been explored, will be outlined. These organic additives can be broadly categorized as having either crystalline (e.g. COFs) or amorphous (e.g. POPs) structures. PAFs, one of the classes of porous polymers, are 3D extended materials constructed by linking tetrahedral building units together through irreversible C–C coupling reactions.[27] PAFs can exhibit unusually high porosity and narrow pore-size distributions for amorphous solids and, by virtue of their covalent backbone, are chemically robust. MMMs composed of PAFs and poly(1-trimethylsilyl-1-propyne) (PTMSP) were first explored by Lau et al.[25a] PTMSP is a super-glassy polymer with excellent potential for gas separations, however, its practical use is limited by rapid aging, which leads to a significant decrease in its free volume (the CO_2 permeability of PTMSP decreases from 29796 Barrer to 8045 Barrer over one year). An unforeseen benefit of adding PAF particles to PTMSP was that physical aging was dramatically halted in the host polymer. Indeed, the CO_2 permeability decreased by only approximately 7% after 240 days, nearly sixfold less than pure PTMSP membranes. Solid-state NMR experiments indicate that the pore network of the PAF incorporates the pendant methyl groups of the PTMSP polymer and, as a result, "freezes" the polymer backbone in place (Figure 6). An important observation is that this mechanism is not general for nanoporous additives (such as MOFs), as the chemical compatibility of the additive and polymer appear to be essential. To this end, PAFs also modify the aging properties of PIMs (polymers of intrinsic microporosity),[79] another class of glassy polymer that show promising separation properties. In this case, the PAFs give rise to selective aging in the MMM, where the H_2/N_2 selectivity increases approximately threefold after 400 days of aging. A feature of PAFs is that their pores can be routinely functionalized to tune adsorbent/adsorbate interactions. This chemistry was exploited by Lau et al., who showed that MMMs composed of PTMSP and a series of functionalized PAFs (-NH_2, -SO_3H, C_{60}, and Li_6C_{60}) showed a significant enhancement in permeability for industrially relevant gases (CH_4, CO_2, H_2, and N_2) compared to neat PAF MMMs.[80] The best performing composite was found to be PTMSP/PAF-Li_6C_{60}, which showed both outstanding gas permeability and anti-aging properties. For example, PTMSP/PAF-Li_6C_{60} mem-

Dateiname: A701109e
Pfad: l:/daten/verlage/vch/ach/hefte/pool/
Status Neusatz
Datum: 24 KW., 6. Juni 2017 (Dienstag)
Pagina: 10
Seite: 9te von 21
Umfang (Seiten): 21
Zeit: 15:42:11 Uhr

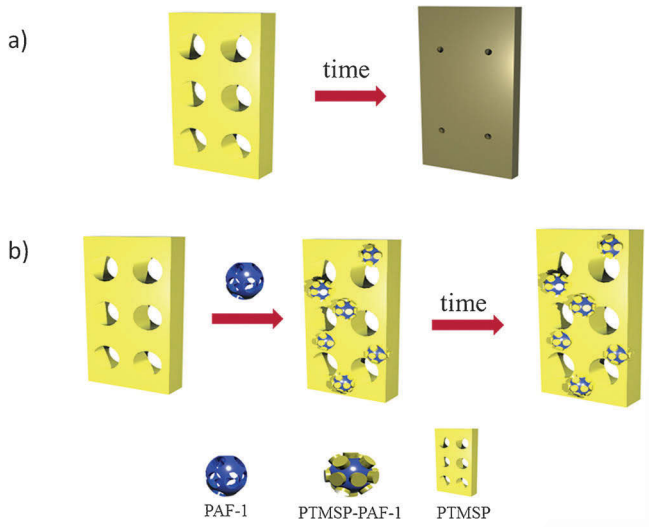

Figure 6. a) The pronounced physical aging that occurs in pure PTMSP membranes. b) Anchoring the PTMSP side chains to the PAF network to halt aging.

branes showed an 85% increase in CO_2 permeability compared to their PTMSP/PAF counterparts.

Based on the excellent anti-aging properties of PAFs, hyper-cross-linked polymers (HCPs) were also explored as MMM additives.[81] A clear advantage that this class of materials offer is their facile synthesis relative to PAFs.[82] To this end the aromatic-rich HCP α,α′-dichloro-*p*-xylene (*p*-DCX) was added to the glassy polymer PTMSP and the performance characteristics of the material examined. Indeed, *p*-DCX was found to be a more effective additive for decreasing physical aging than PAF materials, especially with respect to CO_2 permeability. For example, the CO_2 permeability of PTMSP/*p*-DCX MMMs reduced by only 2% after 60 days of aging, while a 40% reduction in N_2 permeability was observed for the as-cast membrane. It is noteworthy that such relative aging gives rise to outstanding CO_2/N_2 selectivity. NMR studies inferred that the fundamental anti-aging mechanisms of the HCP additives were similar to PAFs, namely that interactions between the *p*-DCX and the trimethylsilyl groups of PTMSP "froze" the main chains of the bulk polymer. HCPs (polystyrene) have also shown positive anti-aging effects when used as additives in PIM-based membranes.[25b] Again, analogous aging experiments indicate that the loss of permeability of N_2 is more rapid than that of CO_2 over time, thus leading to an enhanced CO_2/N_2 selectivity from 7 to 12.

COFs are a class of extended porous materials that are defined by their crystalline structures.[26] Given their high porosity, organic composition, and wide range of pore sizes it is surprising that their application as porous MMM additives has not been more widely explored. Only a few studies of 2D COFs as additives to polymer matrices have been reported, this may be in part due to challenging synthetic procedures and, for some COFs, limited stability under humid conditions. Recently, water-stable, exfoliated imine-based COFs were added to poly(ether imide) or polybenzimidazole (PBI) to yield MMMs.[24a] The as-synthesized COFs were exfoliated by sonication, thereby giving rise to sheets down to monolayer thickness with high aspect ratios. MMMs with up to 30% COF filler were cast and, according to microscopy studies, the membranes were defect-free. This was attributed to good compatibility between the COF and the polymer matrix. In general, the COF additives lead to increased gas permeability and in some cases improvement in gas selectivity. A clear increase in the H_2/CO_2 selectivity from 9 up to 31 upon 20 wt% COF loading (surpassing the 2008 Robeson upper bound) was observed.

Similar, robust COFs (TPa-1 and TPBD)[28] have been employed to synthesize MMMs with PBI.[24b] In this case, membranes composed of up to 50% COF could be cast before defects in the material were observed, once again indicating the excellent chemical compatibility of COFs and polymer hosts. These high COF loadings showed significant increases (almost sevenfold) in gas permeability for H_2, N_2, CH_4, and CO_2 compared to PBI. Furthermore, as may be expected, the gas permeability increased as the pore size of the COF increased. MMMs comprised of azine-linked COFs and the commercial polymer Matrimid have also been fabricated.[24c] Once again, the addition of the COF material leads to a notable increase in gas permeability (130% for CO_2 in the case of the 16 wt% loaded polymer) and, compared to the neat polymer, an increase in selectivity for CO_2/CH_4 from approximately 19 to 27.

2.3. Porous Molecular Compounds as Additives

The recent use of porous molecular compounds[29,30] rather than extended porous materials as additives is outlined in this section, firstly summarizing the role of MOPs as fillers before discussing applications of the purely organic equivalents (POCs). In contrast to extended framework additives, here the porous molecular additive may be fully dispersed within the membrane support or be present as a suspension of crystallites (Scheme 1b).[31c] Thus, the potential porosity of the molecular additive may be intrinsic (utilizing only the shape-persistent cavity of the species), extrinsic (relying on the voids formed from crystalline or frustrated amorphous packing of the cage units), or a combination.[29c]

2.3.1. Metal-Organic Polyhedra as Additives

The alkyl chain decorated MOP-18 ($[Cu_{24}(ddbdc)_{24}(S)_{24}]$, where ddbdc = 5-dodecyloxy-1,3-benzenedicarboxylate) was first reported as a component of MMMs only relatively recently.[31a] Inspired by the work of Kim and co-workers, who used it as a membrane channel builder for cation transport,[83] the authors sought to prepare MMMs by dispersing MOP-18 in Matrimid. MOP-18 is exohedrally decorated with alkyl chain substituents in the 5-position of the ligand, which enhances its solubility in organic solvents. The formation of homogeneous, phase-integrated MMMs with loadings as high as 80 wt% was shown by SEM data. Furthermore, there was no evidence of polymer rigidification at the MOP-18/polymer interface that characterizes MMMs prepared from extended framework materials,[16] with up to 44 wt% MOP-18/Matri-

mid MMMs retaining flexibility and low loadings (16 wt%) of MOP-18 increasing the strength of the composite. This was presumably due to the strong affinity of the polymer chains for the alkyl chains of MOP-18. The MOP-18/Matrimid composites became more permeable as the temperature was increased to 70 °C and CO_2 plasticization was minimized. Permeability and solubility data showed that the pore, core, and alkyl chains of embedded MOP-18 introduced new sorption sites that significantly affected the gas transport properties of the membranes.

A similar approach was implemented by Ma et al.,[84] who incorporated a soluble anionic MOP, Na_6H_{18}-[Cu_{24}(5-SO_3-1,3-BDC)$_{24}$(S)$_{24}$]·xS (where S = methanol/*N*,*N*′-dimethylacetamide), as a filler in polysulfone (PSF). The design strategy was to use the aromatic rings of both the MOP additive and PSF to enhance the chemical compatibility as well as the sulfonate groups to augment CO_2 binding and deliver effective separation of CO_2/CH_4 mixtures. Similar strategies have been employed for MOF additives (see Section 2.1.1). Solution casting gave a MMM with homogeneous dispersion of the MOP cages which retained their chemical connectivity. Analysis of the separation performance for 8, 12, and 18 wt% MOP loadings revealed that the permeabilities of CO_2 and CH_4 both increased with an increase in MOP loading, with permeabilities up to 113% and 76% higher, respectively, than those in the pure PSF membrane. Moreover, the separation factor for CO_2 in the mixture also showed significant improvement compared to a pure PSF membrane (from 28 up to 45, a 60% increase). Although the higher permeability can be largely ascribed to new diffusion pathways, the improved separation factor was attributed to the polar -SO_3Na groups, which interact more strongly with quadrupolar CO_2. These observations were supported by corresponding data for a OH-functionalized MOP, which showed an increase in permeability but not selectivity with MOP loading.

Thus, MOPs can be incorporated into MMMs without phase segregation, and such materials, with the right composition, can deliver superior separation performance compared to a neat polymer membrane. With this in mind, Kitchin et al.[31b] set about carefully controlling the interplay between components in a MMM at the molecular level to achieve control over the process of physical aging.[85] The authors utilized PTMSP, which is highly prone to physical aging, and a series of soluble MOPs with various external chain lengths and polarities, namely a nonpolar tertiary butyl (^{t}Bu-MOP), polar diethylene glycol (DEG MOP), polar triethylene glycol (TEG MOP), and nonpolar dodecane (MOP-18), to prepare MOP-MMMs. All the composites revealed homogeneous dispersion and intimate mixing between the polymer and the porous additive of the MOP additive at the loadings reported. It was observed that although all the MOP-PTMSP combinations had slightly lower initial CO_2 permeability, the MOP additives with shorter chains (i.e. ^{t}Bu-MOP, DEG-MOP) had a reduced loss of permeability over a one year aging cycle (Figure 7): the 20% loaded ^{t}Bu-MOP-MMM only lost 20% of its CO_2 permeability compared with the 73% loss exhibited by the pure PTMSP membrane. As a predictive tool, the anti-aging performance was found to correlate with the viscosity of the casting solutions as well as the level of interaction between the polymer chains and the MOP additive.

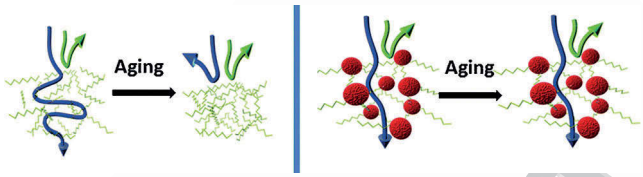

Figure 7. Schematic representation showing the postulated role that MOPs have in preventing aging and enhancing selectivity over time. Figure adapted from Ref. [31b] with permission. Copyright Royal Society of Chemistry, 2015.

Although not the focus of this Review, MOP additives have been utilized to enhance the performance of pervaporation membranes for hydrocarbon separations. In one case, the reticular chemistry possible for MOPs was utilized to prepare a series of isostructural MOPs with different external functional groups. These were combined with a polymer to fabricate functionalized MOPs/hyperbranched polymer hybrid membranes,[86] whereby the selectivity was found to be governed primarily by the polarity of the MOP functional groups. In a similar manner, hybrid membranes of the ^{t}Bu-MOP and hyperbranched polymer Boltorn W3000 were fabricated on a ceramic hollow tube by a simple immerse-coating method.[87] These modules demonstrated excellent pervaporation separation performance for aromatic-aliphatic hydrocarbon mixtures.

2.3.2. *Porous Organic Cages*

Whereas MOPs have been of significant interest as a class of porous solids for some time, POCs have more recently attracted significant attention.[29] These chemically stable, readily soluble, and solely organic additives should intimately mix with the polymer matrix, potentially ameliorating the gas transport issues that can befall other systems. Similar to MOPs, POCs also afford extremely high porosities but still retain their molecular identity, and can be readily processed into composite materials.[29c] In addition to the close chemical complementarity of POCs to the polymer matrix, control over the interior and exterior chemical functionality as well as the intrinsic porosity of POCs is easily accomplished. Indeed, Song et al. demonstrated that it was possible to solution-process POCs into continuous and defect-free microporous thin films without the need for a supporting polymer.[88] Although much remains to be explored in the field of POCs, their potential application as additives for MMMs are summarized in this section. There has, however, been previous interest in bowl-shaped and toroidal host molecules, such as calixarenes[89] and cyclodextrins,[90] which are also briefly discussed.

Studies on cyclodextrin fillers as components of pervaporation membranes have been reported.[91] Jiang et al.[90a] also investigated these Matrimid/β-cyclodextrin nanocomposite membranes for O_2/N_2 separation and found changes in permeability and selectivity that were dependent on the loading. Along these lines, Chapala et al.[90b] systematically studied the effect of incorporating α-, β-, and γ-cyclodextrins

with Me or Me_3Si substituents into a poly(3-trimethylsilyltricyclononene-7) (PTCNSi1) matrix. Under these conditions, they observed that bulky Me_3Si groups led to minor reductions in the permeability coefficients for He and H_2, while a marked decrease was found for other gases. Methyl-substituted cyclodextrins led to reductions in permeability for all the studied gases, although this effect was more significant for larger gas molecules. Thus, a MMM comprised of Me-substituted α-cyclodextrin resulted in an increase in selectivity for H_2/N_2 from 5.2 for the pure polymer to 9.1. An earlier study on substituted calixarenes by the same authors[89b] showed these additives could also be blended with PTCNSi1. The advantage of such additives was that the nature of the substituents on both the upper and lower rims of the calixarenes could be used to modify the gas permeability and selectivity of the resulting membranes. The composites generally showed decreased permeability and increased selectivity towards different gas pairs compared with pure membranes; for example, a calixarene substituted on the upper rim with ethyl groups and the lower rim with ^{t}Bu groups showed a 104% increase in H_2/N_2 selectivity (to 11.4) but a near halving of permeability.

Bushell et al. reported the first synthesis of a POC composite membrane,[31c] whereby the cage molecules were induced to crystallize within the membrane matrix. Starting from a solution of PIM-1 and POC, a dispersed but phase-separated composite was generated by in situ crystallization (Figure 8). The cage utilized was an imine POC formed from 1,3,5-triformylbenzene and (*R*,*R*)-1,2-diaminocyclohexane (CC3). The study showed that the incorporation of POCs significantly enhances the permeability, whereas nonporous cage molecules (in this case generated by chemical reduction of the imine POC CC3) have the opposite effect; in the former case permeability increases with increasing weight percent of the porous cage, while in the latter permeability decreases as the concentration of the nonporous reduced cage increases. The effect of using preformed nanocrystals (PIM-1/nanocage) was also investigated. The authors concluded that the nanocage membranes extend the upper bound of performance for various relevant gas pairs, while the in situ crystallized systems provide better resistance towards physical ageing.

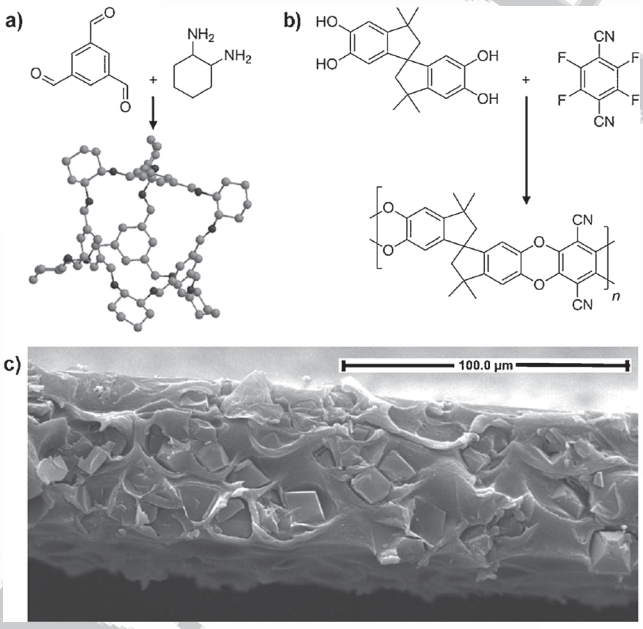

Figure 8. The syntheses of a) imine cage CC3, b) PIM-1, and c) a membrane produce by the in situ crystallization approach of Bushell et al.[31c] Figure taken from Ref. [31c] with permission. Copyright John Wiley and Sons, 2013.

In a computational study, Evans et al. assessed how POCs act as soluble additives that could ameliorate nonselective gas transport pathways in MMMs.[92] Five POCs were investigated, comprising three different families of materials, including the tetrahedral imine cages (CC1, CC2, CC3) reported by Cooper and co-workers,[93] an adamantoid cage from the group of Mastalerz,[94] and the elongated, all-carbon-bonded, triangular dipyramidal cage.[32a] The PIM-1/cage MMM composites were generated in silico and benchmarked against experimental data reported by Bushell et al.[31c] The power of this approach was to allow analysis of numerous polymer/POC compositions, thereby generating the permeabilities and selectivities for 40% volume compositions of MMMs comprised of POCs and the polymer hosts Matrimid, Ultem, PIM-1, and PIM-7. This revealed that larger cage structures in the MMMs significantly improves the permeability for H_2/N_2 and H_2/CO_2 separations and is concomitant with a minor increase in the selectivity for H_2.

Mao and Zhang[31d] investigated MMM composites incorporating the waterwheel-shaped POC Noria. Noria was first synthesized[95] from resorcinol and pentanedial and shown to be porous by Atwood and co-workers.[96] The hydroxy groups render Noria soluble in polar solvents and allow its physical properties to be tailored by PSM. MMMs were prepared by incorporating Noria as well as its derivatives Noria-Boc and Noria-CO^{t}Bu as the fillers in the polyimide 6FDA-DAM. The substituted derivatives achieved better integration, giving a homogeneous dispersion of the nanoaggregates and close interfacial mixing of the phases, particularly in the cases where hydrophobic substituents were used. The separation performance of the resulting composites was strongly related to the chemical structures of the additives. Noria/6FDA-DAM composites gave a minor improvement in CO_2/CH_4 selectivity (15% increase) concomitant with a 53% decrease in permeability for CH_4. In contrast, the introduction of Noria-CO^{t}Bu tends to increase the free volume and gas permeability of the MMMs (e.g. methane permeability increases by nearly 40%).

Cooper and co-workers have also recently utilized their tetrahedral imine cages to render materials porous by solution co-processing.[97] Scrambled POC cage mixtures were prepared by a co-reaction approach that yields an amorphous material with a porosity almost twice that of the corresponding phase-pure POCs. A combinatorial approach was then used to explore the effect of doping with a series of nonporous polymers, including polyethyleneimine (PEI), polyvinylpyrrolidone (PVP), poly(methyl methacrylate) (PMMA), and polystyrene (PS). A notable observation was that the cage-polymer composites maintained their porosity to N_2 up to 40 wt% polymer loading, which confirms the

ability to convert nonporous commodity polymers into porous composites simply by combination with POCs. Desirable CO_2 uptake was achieved for a PEI/POC composite (17 wt% PEI), with the material delivering a higher CO_2 uptake than either of the two isolated organic components as well as an ideal CO_2/N_2 gas selectivity of 8 (295 K, 1 bar).

3. Scope and Outlook

The increased permselectivities obtained for many MOF-MMMs show that the choice of the MOF filler/material combination, especially with certain MOF functional groups positioned on the linker or as a coating, can lead to better polymer-filler interactions and improved performance. Similarly, modified polymers displaying chemically complementary groups can achieve a comparable outcome. To understand this more fully, the polymer-filler interface can be modeled with integrated density-function theory calculations and force-field-based molecular dynamic simulations. This method has already been used successfully for MMMs from PIM-1 and ZIF-8, and has shown, for example, that the structure of the membrane at the polymer-filler interface is the result of chemical affinity between PIM-1 and ZIF-8, with a preferred interaction between the CN groups of PIM-1 and the terminal NH functionality of the organic linker on the ZIF-8 surface.[98] Nonetheless, in general, these interactions are often not fully understood and clear spectroscopic evidence or the use of other appropriate characterization techniques is often lacking as a supplement to the theory. Thus, the development and utilization of advanced surface and material characterization techniques along with computational methods to simulate filler particle surfaces and their interactions with polymer chains will be needed. This knowledge will engender the design of better filler-polymer interfaces that should result in great improvements in separation performance.

Many of the reported studies on MOF-MMMs simply combine individual MOFs, which possess potentially desirable attributes, with commercially available polymers. These few studies do not readily facilitate the development of structure–performance relationships because of differences in the samples or experimental design. The growing number of filler material classes and examples makes it imperative to develop accurate testing and characterization protocols that are able to attribute specific properties associated with the fillers to the separation performance of the material. An example of this is a comparative study of gas separation using MMMs containing a variety of different nanoparticles.[99] In this case, the gas permeation properties of a series of MMMs of Matrimid (fillers = Cu-BTC, ZIF-8, Carbon C, Carbon B, Carbon A, and POP-2) were measured to determine the dominant particle properties and explain the permeation by using a simple model based on the free volume. The gas permeabilities of all the MMMs were shown to increase as the filler loading increased without any reduction in the gas selectivity, with the enhancement for the MOF-MMMs at high volume fractions being significantly larger than for carbon-MMMs. Analysis of the permeability data showed that, of all the particle properties, the particle surface area provided the strongest correlation to the permeability enhancement. The permeability of all the gas species was shown to be strongly correlated with the fractional free volume (FFV) of the MMM.

The MOF-related studies presented have also shown that the modification of the surface chemistry and texture, particle size and morphology, as well as dispersion of the filler particles have a significant influence on the separation properties of the MMMs. Thus, particles should be < 50 nm in size[73] and their nature, shape, and orientation in the membrane should be known to be able to assign the separation properties. Techniques to probe these aspects are known, for example, Raman spectroscopy can be used to determine the homogeneity of the filler distribution in a MMM.[100] By using this approach, the filler dispersion in the polymer can be determined at different locations of a sample. Additional advanced characterization techniques such as tomographic SEM/TEM, when used as quantification tools, can give great insight into the presence of large structural defects and particle orientation.[20a,38b,101] In addition to these powerful visualization techniques, more care should be paid when studying the effect of filler addition on the intrinsic properties of the final composites. Changes in polymer rigidity or free volume can be responsible for changes in permeability, and these should be properly quantified.[99,102]

The field of POF-based MMMs is in its infancy and further studies are required to assess the potential of these materials as additives in polymeric membranes. Nonetheless, the studies have shown that porous organic additives can afford remarkable, selective, anti-aging properties for glassy polymers. Further aging studies are essential to discover new combinations that provide enhanced effects and ultimately information about the long-term viability of these MMMs. However, from the available data, it appears that 3D amorphous materials offer greater enhancement in terms of anti-aging and selective transport than the 2D, crystalline COF materials that have been examined. Accordingly, it would be of interest to also examine 3D COFs as additives. Furthermore, further studies aimed at uncovering why amorphous POP materials show such drastic enhancements in the performance characteristics of polymer membranes are essential. Given the chemical mutability of PAFs and HCPs it is anticipated that a vast library of novel MMMs with commercially interesting properties will be developed in the near future. The use of fully organic additives opens new challenges in the characterization of these composites, ruling out classical visualization techniques such as SEM or TEM and making the interpretation of other classical analyses such as thermogravimetry harder. Demonstrating the integrity of amorphous fillers upon inclusion in MMMs will not be trivial.

To date, all the MOPs used for the fabrication of MMMs are based on the archetypal $Cu_{24}L_{24}$ MOP-1 core developed by Yaghi and co-workers[103] which is formed from a Cu^{II} paddlewheel unit and 1,3-benzene dicarboxylate linkers. Further opportunities lie in being able to tune the chemistry of the MOP exterior surface to match or complement that of the pure polymer membrane.[104] An additional opportunity to

vary the MOP chemistry without changes to the cage topology also arises from studies on MOPs with alternative metals at the paddlewheel node,[105] and also recent studies whereby MOPs were constructed from heterometallic Pd^{II}-M^{II} (M = Cu, Ni, Zn) paddlewheel nodes.[106] MOPs with various topologies can also be prepared with different internal and external reactivities, internal void volumes, and pore windows.[30,107] Along similar lines to the concept of a polyMOF, Hosono, Kitagawa et al.[108] recently reported a strategy to utilize MOPs as building blocks for the formation of star-shaped polymers. Two strategies were elaborated: a divergent route relying on the synthesis of MOPs exohedrally decorated with dithiobenzoate or trithioester chain-transfer groups primed for polymerization, and a convergent route using polymer macroligands. Although the gas adsorption or separation potential of such materials has not been explored, the synthetic approaches elaborated will be useful for developing highly integrated MOP filler-polymer composite membranes.

The field of POCs is still in its infancy and exciting breakthroughs continue to emerge, including new cage types with increasingly porous structures. Thus, there are opportunities for the investigation of further POC/polymer compositions. In the field of MOP-MMMs, the external chemical functionality on the MOP cage has been instrumental in developing tight filler-polymer interfaces; similar variation is possible with several cage types, as exemplified by the imine-POCs with copper, where many exterior functional groups can be tolerated. As such, the chemical compatibility between the filler and continuous phase can be further tuned. An important breakthrough for potential industrial applications of POC-MMMs is the development of chemically robust cages, for example, all-carbon-bonded cages.[29,32] As noted, hydrolytically stable fillers are preferred for the preparation of MMMs where a realistic technical application is targeted. Soluble, chemically robust additives also offer the possibility of chemical cross-linking of the polymer matrix or being chemically grafted onto a polymer chain.

Structural flexibility is widely known for MOF materials,[109] and the weak packing that governs the solid-state arrangements of molecular porous structures also engenders flexibility.[29] Thus, it is important to consider the flexibility of all filler additives, as weak packing forces define the pore structures in MOPs and POCs as well as the framework flexibility. For example, ZIF-8 and ZIF-90/Matrimid membranes show H_2/CH_4 selectivities that are significantly higher than predicted and the selectivity increase can be linked to hindered distortion of the imidazolate linkers in the ZIF frameworks.[110]

The application of MMMs to industrial gas separations necessitates the production of the membrane modules on a commercial scale. Recent studies regarding the scale-up of MOF[23] and POC[32b] syntheses provides optimism that these promising additives can be delivered at scales necessary for commercial use. It should also be stressed at this point that most studies on MOF-MMMs to date are based on flat, self-supported membranes and that very little work has been done on the upscaling of such membranes to configurations appropriate for industrial application,[1c] which also necessitates the availability of the additives on larger scales. The target for maximizing membrane productivity is the production of selective layers with thicknesses less than a micrometer. This is usually achieved in asymmetric configurations through the formation of a selective layer supported on a nonselective porous support that provides the necessary strength. Methods to manufacture asymmetric membranes are available, including phase separation, interfacial polymerization, solution-coating, and plasma polymerization.[111] In particular, module geometries, such as spiral wound flat sheets, supported composites and hollow fiber (HFb) membrane modules are preferred for thin separating layers,[112] with the HFb architecture providing high densities and supporting transmembrane pressure differences of up to 70 bar. Given that there has been greater progress in the area of MOF-MMMs, it is not surprising that a number of reports already exist on MOF-based asymmetric MMMs. Notably, similar separation performance as that of self-supported membranes has been demonstrated.[13,73,113] The field is advancing at a slower pace for the HFb configuration.[111,112b,c,114] Nonetheless, impressive results on MOF-based HBf-MMMs have been published. For example, Dai et al. prepared dual-layer MOF-MMM-HFbs by using Ultem 100 and 200 nm ZIF-8 particles for CO_2/N_2 separation.[16j] Gas permeation measurements demonstrated permeance and permselectivity higher than that of the polymer-only HFb membranes. The same group also reported the successful preparation of highly loaded ZIF-8 (up to 30 % wt) MMM HFbs for the separation of different hydrocarbons with outstanding results.[115] Given these observations, more attention should be devoted in the near future to the preparation of MMMs bearing desirable module configurations and to examine module fabrication with a broader range of polymer/additive combinations. Given that a focus is the preparation of even thinner separation layers able to achieve higher fluxes, the use of filler particles with very high aspect ratios will be instrumental.

Although many of the polymer continuous phases (e.g. polyimides, PSF) have excellent intrinsic mechanical stabilities that make them ideal for applications, the additive materials (MOFs, COF etc) typically display much poorer mechanical properties.[15] In terms of MMMs, the introduction of an additive can often reduce the mechanical stability of the polymer support (dependent on the stability of the native polymer). Some reports provide data on mechanical stability as the filler composition is tuned, but a number of contributions lack these data. For MMMs formed from Matrimid and post-synthetically modified UiO-66-NH_2, however, the mechanical strength was reported to be better than that of the pure polymer and also to be tuned by the functional group grafted onto the MOF (which directly affects the MOF-polymer interface).[56] The mechanical stability has also been reported for MOF-MMMs comprised of very high filler loadings.[116] In this case, a unique approach to casting the MMMs was employed to form stable membranes with a polyvinylidene fluoride (PVDF) polymer. An "ink" was produced from MOF and PVDF in nonviscous solvents before casting and complete solvent removal. Mechanical stability was demonstrated by measuring the ultimate tensile strength

(UTS) for UiO-66-PVDF composites with 10–67 wt% loading. The UTS decreased in line with the MOF loading, but the elastic modulus actually increased at low loadings.[116a] Even better results were achieved with MMMs based on styrene/butadiene copolymers and high MOF loadings.[116b] As an interesting aside, alternative approaches to MOF-MMM fabrication should be more widely explored to improve the mechanical strength (and other properties). For example, Sabic Global Technologies B.V. reported MMMs obtained by in situ cross-linking of short oligomers in the presence of the MOF filler.[117] One of the drivers for the development of PolyMOFs[57] was to achieve improved mechanical stability for MOFs, although no quantitative mechanical data were presented. The mechanical properties with molecular porous additives have in some cases been reported. Noria-MMM composites maintained their tensile strength on addition of the filler but become more brittle at higher loadings (a reduction in the elongation at break measurements).[31d] MOP-18/Matrimid MMMs show similar behavior to MOF additives: the Young's modulus was shown to increase as the loading increased up to a 16 wt% MOP-18 before a gradual decrease, consistent with aggregation of the filler and weakening of the MOP-polymer interface.[31a] A common challenge for self-supporting membranes is that the thickness of the MMM required for mechanical stability creates resistance for gas molecules and lower permeability. Importantly, the asymmetric configurations discussed above can obviate this challenge and allow the development of usable membrane modules.

The types of gas separations already examined need to be considered for a focus on potential applications (Tables SI1 and 2 in the Supporting Information summarize these data). CO_2/CH_4 separations (natural gas sweetening, biogas purification) have been a common focus because of the combined filler and polymer performance and operating conditions being ideally suited to this separation.[20a,24c,31d,44,48,52,71,73,77,84] Additionally, pure polymer membranes have found application in this area, supplanting aqueous amine-based adsorbents and thereby easing the path for improved membrane technology. Activity in the patent literature points to a growing industrial interest in MOF- and MOP-based MMMs for natural gas sweetening.[118,119] CO_2/N_2 separations are commonly examined due to a ready availability of the data for this gas pair, but challenges such as the relatively low concentration of the target gas in flue streams, low pressure feed, and the large volumes needing to be processed, mean this still represents a major challenge to the field. A comprehensive review on CO_2-capturing MMMs has been published.[18a] Precombustion capture of H_2/CO_2 also features commonly in the separations studied, and many MOF and COF additives have shown marked increases in separation performance.[24a,76,92] A challenge here will be to balance the favorable separation characteristics that have been achieved with the likely engineering requirements (i.e. hydrogen may need to be preferentially retained in the gas feed rather than being allowed to permeate). This has been considered more generally for hydrogen recovery membranes, where nonporous additives can enhance the performance of so-called "reverse-selective" membranes.[120] Air separation (O_2/N_2) has also been examined,[54,90a] as MOF and related filler MMMs offer a potential way to overcome the small difference in the kinetic diameter of O_2 and N_2 (3.46 and 3.64 Å respectively) because of the potential tunability of the additive structure.

It is apparent that various performance enhancements and desirable membrane characteristics can be imparted by judicious choice of the additive and matrix. The research highlighted in this Review further suggests that novel filler materials may advance the field of MMMs and overcome long-standing challenges, such as polymer aging. Although many of the initial reports are promising, much work remains to be done before rational design principles can be established for any of the filler materials. In particular, systematic studies that employ identical conditions for testing gas permeation under industrially relevant conditions are required for a library of known polymers. Importantly, mixed-gas studies and investigations into the role contaminants play in separation performance need to be quantified. The mechanical properties of the resulting composites need to be routinely assessed and steps to perfect the fabrication of operating membrane modules with these bespoke fillers should be examined. Accordingly, this emerging field will provide chemists, materials scientists, and chemical engineers with many challenges over the coming years. Given that there is such a broad selection of filler materials, many with excellent separation performances themselves, facile processing, and excellent compatibility with the continuous phase, MMMs formed from these additives have exciting potential for clean energy applications and energy-efficient separations.

Acknowledgements

C.J.D. and C.J.S. acknowledge the Australian Research Council and the University of Adelaide, the latter for funding the visit of C.J. C.J.S. and C.J.D. thank Dr. Matthew Hill for the provision of images used in the manuscript. J.G. gratefully acknowledges funding from the European Union Seventh Framework Programme (FP7/2007–2013) under grant agreement no. 608490, project M^4CO_2 and (FP/2007–2013) ERC Stg, Grant Agreement no. 335746, CrystEng-MOF-MMM. C.J. thanks the DFG for support through grant Ja466/29-1 and the Anton-Betz foundation.

Conflict of interest

The authors declare no conflict of interest.

[1] a) J. C. Davis, R. J. Valus, R. Eshragi, A. E. Velikoff, *Sep. Sci. Technol.* **1993**, *28*, 463–476; b) M. G. Buonomenna, *RSC Adv.* **2013**, *3*, 5694–5740; c) W. J. Koros, C. Zhang, *Nat. Mater.* **2017**, DOI: https://doi.org/10.1038/nmat4805. ■■ Can you update? ■■

[2] a) X. He, M.-J. Hägg, *Membranes* **2012**, *2*, 706–726; b) W. J. Koros, R. Mahajan, *J. Membr. Sci.* **2000**, *175*, 181–196.

[3] K. Ohlrogge, K. Stürken, *Membrane technology in the chemical industry* (Eds.: S. P. Nunez, K.-V. Peinemann), Wiley-VCH, Weinheim, **2001**; pp. 69 – 94.

[4] a) R. W. Baker, *Ind. Eng. Chem. Res.* **2002**, *41*, 1393 – 1411; b) BORSIG Membrane Technology GmbH, http://www.borsig-china.com/#productrecovery.

[5] Sulzer Chemtech AG, http://www.sulzer.com/en/Products-and-Services/Separation-Technology/Membrane-Technology/Organic-Solvent-Nanofiltration-OSN.

[6] L. M. Robeson, *J. Membr. Sci.* **2008**, *320*, 390 – 400.

[7] S. Qiu, T. Ben, *Porous Polymers*: *Design*, *Synthesis and Applications*, RSC, Cambridge, **2015**.

[8] a) M. E. Davis, *Ind. Eng. Chem. Res.* **1991**, *30*, 1675 – 1683; b) J. Liu, J. Yu, *Toward Greener and Designed Synthesis of Zeolite Materials* (Eds.: B. Sels, L. Kustov), Elsevier, Amsterdam, **2016**, pp. 1 – 32; c) N. Kosinova, J. Gascon, F. Kapteijn, E. J. M. Hensen, *J. Membr. Sci.* **2016**, *499*, 65 – 79.

[9] O. Shekhah, J. Liu, R. A. Fischer, C. Wöll, *Chem. Soc. Rev.* **2011**, *40*, 1081 – 1106.

[10] a) S. M. Saufi, A. F. Ismail, *Carbon* **2004**, *42*, 241 – 259; b) M. Rungta, G. B. Wenz, C. Zhang, L. Xu, W. Qiu, J. S. Adams, W. J. Koros, *Carbon* **2017**, *115*, 237 – 248.

[11] a) A. F. Ismaila, P. S. Goha, S. M. Sanipa, M. Aziz, *Sep. Purif. Technol.* **2009**, *70*, 12 – 26; b) D. Mattia, H. Leese, K. P. Lee, *J. Membr. Sci.* **2015**, *475*, 266 – 272.

[12] a) G. Liu, W. Jin, N. Xu, *Chem. Soc. Rev.* **2015**, *44*, 5016 – 5030; b) H. Huang, Y. Ying, X. Peng, *J. Mater. Chem. A* **2014**, *2*, 13772 – 13782.

[13] T. S. Chung, L. Y. Jiang, Y. Li, S. Kulprathipanja, *Prog. Polym. Sci.* **2007**, *32*, 483 – 507.

[14] a) J. Caro, *Curr. Opin. Chem. Eng.* **2011**, *1*, 77 – 83; b) H. Bux, F. Liang, Y. Li, J. Cravillon, M. Wiebcke, J. Caro, *J. Am. Chem. Soc.* **2009**, *131*, 16000 – 16001.

[15] S. R. Venna, M. A. Carreon, *Chem. Eng. Sci.* **2015**, *124*, 3 – 19.

[16] a) B. Zornoza, A. Martinez-Joaristi, P. Serra-Crespo, C. Tellez, J. Coronas, J. Gascon, F. Kapteijn, *Chem. Commun.* **2011**, *47*, 9522 – 9524; b) O. G. Nik, X. Y. Chen, S. Kaliaguine, *J. Membr. Sci.* **2012**, *413 – 414*, 48 – 61; c) H. B. T. Jeazet, C. Staudt, C. Janiak, *Dalton Trans.* **2012**, *41*, 14003 – 14027; d) K. Hunger, N. Schmeling, H. B. Jeazet, C. Janiak, C. Staudt, K. Kleinermanns, *Membranes* **2012**, *2*, 727 – 763; e) H. B. T. Jeazet, C. Janiak in *Metal-Organic Framework Materials* (Eds.: L. R. MacGillivray, C. Lukehart), Wiley, Chichester, **2014**, pp. 1 – 15; f) B. Zornoza, C. Tellez, J. Coronas, J. Gascon, F. Kapteijn, *Microporous Mesoporous Mater.* **2013**, *166*, 67 – 78; g) D. Bastani, N. Esmaeili, M. Asadollahi, *J. Ind. Eng. Chem.* **2013**, *19*, 375 – 393; h) G. Dong, H. Li, V. Chen, *J. Mater. Chem. A* **2013**, *1*, 4610 – 4630; i) M. J. C. Ordoñez, K. J. Balkus, Jr., J. P. Ferraris, I. H. Musselman, *J. Membr. Sci.* **2010**, *361*, 28 – 37; j) Y. Dai, J. R. Johnson, O. Karvan, D. S. Sholl, W. J. Koros, *J. Membr. Sci.* **2012**, *401 – 402*, 76 – 82; k) D. Zheng, X. Liu, D. Hu, M. Li, J. Zhang, G. Zeng, Y. Zhang, Y. Sun, *RSC Adv.* **2014**, *4*, 10140 – 10143; l) M. G. Buonomenna, W. Yave, G. Golemme, *RSC Adv.* **2012**, *2*, 10745 – 10773; m) X. Y. Chen, H. Vinh-Thang, D. Rodrigue, S. Kaliaguine, *RSC Adv.* **2014**, *4*, 12235 – 12244; n) S. Sorribas, B. Zornoza, C. Téllez, J. Coronas, *J. Membr. Sci.* **2014**, *452*, 184 – 192; o) P. Burmann, B. Zornoza, C. Téllez, J. Coronas, *Chem. Eng. Sci.* **2014**, *107*, 66 – 75; p) X. Y. Chen, H. Vinh-Thang, D. Rodrigue, S. Kaliaguine, *Ind. Eng. Chem. Res.* **2012**, *51*, 6895 – 6906; q) B. Seoane, J. M. Zamaro, C. Tellez, J. Coronas, *RSC Adv.* **2011**, *1*, 917 – 922; r) X. Y. Chen, V.-T. Hoang, D. Rodrigue, S. Kaliaguine, *RSC Adv.* **2013**, *3*, 24266 – 24279.

[17] a) G. Rebollar-Perez, E. Carretier, N. Lesage, P. Moulin, *Membranes* **2011**, *1*, 80 – 90; b) L. Dumee, L. Velleman, K. Sears, M. Hill, J. Schutz, N. Finn, M. Duke, S. Gray, *Membranes* **2010**, *1*, 25 – 36.

[18] a) B. Seoane, J. Coronas, I. Gascon, M. E. Benavides, O. Karvan, J. Caro, F. Kapteijn, J. Gascon, *Chem. Soc. Rev.* **2015**, *44*, 2421 – 2454; b) R. D. Noble, *J. Membr. Sci.* **2011**, *378*, 393 – 397.

[19] a) H. Furukawa, K. E. Cordova, M. O'Keeffe, O. M. Yaghi, *Science* **2013**, *341*, 1230444; b) C. Janiak, J. K. Vieth, *New J. Chem.* **2010**, *34*, 2366 – 2388.

[20] a) T. Rodenas, I. Luz, G. Prieto, B. Seoane, H. Miro, A. Corma, F. Kapteijn, F. X. Llabrés i Xamena, J. Gascon, *Nat. Mater.* **2015**, *14*, 48 – 55; b) J. B. DeCoste, J. M. S. Denny, G. W. Peterson, J. J. Mahle, S. M. Cohen, *Chem. Sci.* **2016**, *7*, 2711 – 2716.

[21] a) F. Jeremias, D. Frohlich, C. Janiak, S. K. Henninger, *New J. Chem.* **2014**, *38*, 1846 – 1852; b) C. Janiak, S. K. Henninger, *Chimia* **2013**, *67*, 419 – 424; c) J. J. Low, A. I. Benin, P. Jakubczak, J. F. Abrahamian, S. A. Faheem, R. R. Willis, *J. Am. Chem. Soc.* **2009**, *131*, 15834 – 15842.

[22] a) J. Ehrenmann, S. K. Henninger, C. Janiak, *Eur. J. Inorg. Chem.* **2011**, 471 – 474; b) A. Khutia, H. U. Rammelberg, T. Schmidt, S. Henninger, C. Janiak, *Chem. Mater.* **2013**, *25*, 790 – 798; c) S. Karmakar, J. Dechnik, C. Janiak, S. De, *J. Hazard. Mater.* **2016**, *303*, 10 – 20; d) F. Jeremias, D. Frohlich, C. Janiak, S. K. Henninger, *RSC Adv.* **2014**, *4*, 24073 – 24082; e) D. Fröhlich, S. K. Henninger, C. Janiak, *Dalton Trans.* **2014**, *43*, 15300 – 15304; f) P. Küsgens, M. Rose, I. Senkovska, H. Fröde, A. Henschel, S. Siegle, S. Kaskel, *Microporous Mesoporous Mater.* **2009**, *120*, 325 – 330; g) T. Wu, L. Shen, M. Luebbers, C. Hu, Q. Chen, Z. Ni, R. I. Masel, *Chem. Commun.* **2010**, *46*, 6120 – 6122.

[23] a) N. Stock, S. Biswas, *Chem. Rev.* **2012**, *112*, 933 – 969; b) S. L. James, C. J. Adams, C. Bolm, D. Braga, P. Collier, T. Friščić, F. Grepioni, K. D. M. Harris, G. Hyett, W. Jones, A. Krebs, J. Mack, L. Maini, A. G. Orpen, I. P. Parkin, W. C. Shearouse, J. W. Steed, D. C. Waddell, *Chem. Soc. Rev.* **2012**, *41*, 413 – 447; c) M. Rubio-Martinez, M. P. Batten, A. Polyzos, K.-C. Carey, J. I. Mardel, K.-S. Lim, M. R. Hill, *Sci. Rep.* **2014**, 5443.

[24] See, for example a) Z. Kang, Y. Peng, Y. Qian, D. Yuan, M. A. Addicoat, T. Heine, Z. Hu, L. Tee, Z. Guo, D. Zhao, *Chem. Mater.* **2016**, *28*, 1277 – 1285; b) B. Biswal, H. D. Chaudhari, R. Banerjee, U. K. Kharul, *Chem. Eur. J.* **2016**, *22*, 4695 – 4699; c) M. Shan, B. Seoane, E. Rozhko, A. Dikhtiarenko, G. Clet, F. Kapteijn, J. Gascon, *Chem. Eur. J.* **2016**, *22*, 14467 – 14470.

[25] See, for examples a) C. H. Lau, P. T. Nguyen, M. R. Hill, A. W. Thornton, K. Konstas, C. M. Doherty, R. J. Mulder, L. Bourgeois, A. C. Y. Liu, D. J. Sprouster, J. P. Sullivan, T. J. Bastow, A. J. Hill, D. L. Gin, R. D. Noble, *Angew. Chem. Int. Ed.* **2014**, *53*, 5322 – 5326; *Angew. Chem.* **2014**, *126*, 5426 – 5430; T. Mitra, R. S. Bhavsar, D. J. Adams, P. M. Budd, A. I. Cooper, *Chem. Commun.* **2016**, *52*, 5581 – 5584.

[26] P. J. Waller, F. Gándara, O. M. Yaghi, *Acc. Chem. Res.* **2015**, *48*, 3053 – 3063.

[27] T. Ben, H. Ren, S. Ma, D. Cao, J. Lan, X. Jing, W. Wang, J. Xu, F. Deng, J. M. Simmons, S. Qiu, G. Zhu, *Angew. Chem. Int. Ed.* **2009**, *48*, 9457 – 9460; *Angew. Chem.* **2009**, *121*, 9621 – 9624.

[28] S. Chandra, S. Kandambeth, B. P. Biswal, B. Lukose, S. M. Kunjir, M. Chaudhary, R. Babarao, T. Heine, R. Banerjee, *J. Am. Chem. Soc.* **2013**, *135*, 17853 – 17861.

[29] a) G. Zhang, M. Mastalerz, *Chem. Soc. Rev.* **2014**, *43*, 1934 – 1947; b) A. G. Slater, A. I. Cooper, *Science* **2015**, *348*, aaa8075; c) J. D. Evans, C. J. Sumby, C. J. Doonan, *Chem. Lett.* **2015**, *44*, 582 – 588; d) T. Hasell, A. I. Cooper, *Nat. Rev. Mater.* **2016**, *1*, 16053.

[30] D. J. Tranchemontagne, Z. Ni, M. O'Keeffe, O. M. Yaghi, *Angew. Chem. Int. Ed.* **2008**, *47*, 5136 – 5147; *Angew. Chem.* **2008**, *120*, 5214 – 5225.

[31] See, for examples: a) E. V. Perez, K. J. Balkus, Jr., J. P. Ferraris, I. H. Musselman, *J. Membr. Sci.* **2014**, *463*, 82 – 93; b) M.

Kitchin, J. Teo, K. Konstas, C. H. Lau, C. J. Sumby, A. W. Thornton, C. J. Doonan, M. R. Hill, *J. Mater. Chem. A* **2015**, *3*, 15241 – 15247; c) A. F. Bushell, P. M. Budd, M. P. Attfield, J. T. A. Jones, T. Hasell, A. I. Cooper, P. Bernardo, F. Bazzarelli, G. Clarizia, J. C. Jansen, *Angew. Chem. Int. Ed.* **2013**, *52*, 1253 – 1256; *Angew. Chem.* **2013**, *125*, 1291 – 1294; d) H. Mao, S. Zhang, *J. Colloid Interface Sci.* **2017**, *490*, 29 – 36.

[32] a) A. Avellaneda, P. Valente, A. Burgun, J. D. Evans, A. W. Markwell-Heys, M. R. Hill, D. J. Nielsen, C. J. Sumby, C. J. Doonan, *Angew. Chem. Int. Ed.* **2013**, *52*, 3746 – 3749; *Angew. Chem.* **2013**, *125*, 3834 – 3837; b) M. Kitchin, K. Konstas, C. J. Sumby, M. Czyz, P. Valente, M. R. Hill, A. Polyzos, C. J. Doonan, *Chem. Commun.* **2015**, *51*, 14231 – 14234.

[33] a) Y. Zhang, X. Feng, S. Yuan, J. Zhou, B. Wang, *Inorg. Chem. Front.* **2016**:■■pages or article number?■■ b) W. Li, Y. Zhang, Q. Li, G. Zhang, *Chem. Eng. Sci.* **2015**, *135*, 232 – 257; c) N. Rangnekar, N. Mittal, B. Elyassi, J. Caro, M. Tsapatsis, *Chem. Soc. Rev.* **2015**, *44*, 7128 – 7154.

[34] G. E. Cmarik, M. Kim, S. M. Cohen, K. S. Walton, *Langmuir* **2012**, *28*, 15606 – 15613.

[35] C. Zlotea, D. Phanon, M. Mazaj, D. Heurtaux, V. Guillerm, C. Serre, P. Horcajada, T. Devic, E. Magnier, F. Cuevas, G. Ferey, P. L. Llewellyn, M. Latroche, *Dalton Trans.* **2011**, *40*, 4879 – 4881.

[36] M. G. Goesten, J. Juan-Alcañiz, E. V. Ramos-Fernandez, K. B. S. S. Gupta, E. Stavitski, H. van Bekkum, J. Gascon, F. Kapteijn, *J. Catal.* **2011**, *281*, 177 – 187.

[37] A. Torrisi, C. Mellot-Draznieks, R. G. Bell, *J. Chem. Phys.* **2010**, *132*, 044705.

[38] a) B. Seoane, C. Téllez, J. Coronas, C. Staudt, *Sep. Purif. Technol.* **2013**, *111*, 72 – 81; b) T. Rodenas, M. van Dalen, P. Serra-Crespo, F. Kapteijn, J. Gascon, *Microporous Mesoporous Mater.* **2014**, *192*, 35 – 42.

[39] X. Guo, H. Huang, Y. Ban, Q. Yang, Y. Xiao, Y. Li, W. Yang, C. Zhong, *J. Membr. Sci.* **2015**, *478*, 130 – 139.

[40] M. W. Anjum, B. Bueken, D. De Vos, I. F. J. Vankelecom, *J. Membr. Sci.* **2016**, *502*, 21 – 28.

[41] K. Vanherck, P. Vandezande, S. O. Aldea, I. F. J. Vankelecom, *J. Membr. Sci.* **2008**, *320*, 468 – 476.

[42] A. L. Khan, C. Klaysom, A. Gahlaut, X. Li, I. F. J. Vankelecom, *J. Mater. Chem.* **2012**, *22*, 20057 – 20064.

[43] Z. Li, G. He, Y. Zhao, Y. Cao, H. Wu, Y. Li, Z. Jiang, *J. Power Sources* **2014**, *262*, 372 – 379.

[44] Q. Xin, T. Liu, Z. Li, S. Wang, Y. Li, Z. Li, J. Ouyang, Z. Jiang, H. Wu, *J. Membr. Sci.* **2015**, *488*, 67 – 78.

[45] a) A. Umemura, S. Diring, S. Furukawa, H. Uehara, T. Tsuruoka, S. Kitagawa, *J. Am. Chem. Soc.* **2011**, *133*, 15506 – 15513; b) C. V. McGuire, R. S. Forgan, *Chem. Commun.* **2015**, *51*, 5199 – 5217.

[46] a) A. Schaate, P. Roy, A. Godt, J. Lippke, F. Waltz, M. Wiebcke, P. Behrens, *Chem. Eur. J.* **2011**, *17*, 6643 – 6651; b) Q. Liu, L.-N. Jin, W.-Y. Sun, *CrystEngComm* **2013**, *15*, 8250 – 8254; c) G. Wißmann, A. Schaate, S. Lilienthal, I. Bremer, A. M. Schneider, P. Behrens, *Microporous Mesoporous Mater.* **2012**, *152*, 64 – 70.

[47] F. Vermoortele, B. Bueken, G. Le Bars, B. Van de Voorde, M. Vandichel, K. Houthoofd, A. Vimont, M. Daturi, M. Waroquier, V. Van Speybroeck, C. Kirschhock, D. E. De Vos, *J. Am. Chem. Soc.* **2013**, *135*, 11465 – 11468.

[48] M. W. Anjum, F. Vermoortele, A. L. Khan, B. Bueken, D. E. De Vos, I. F. J. Vankelecom, *ACS Appl. Mater. Interfaces* **2015**, *7*, 25193 – 25201.

[49] K. S. Park, Z. Ni, A. P. Côté, J. Y. Choi, R. Huang, F. J. Uribe-Romo, H. K. Chae, M. O'Keeffe, O. M. Yaghi, *Proc. Natl. Acad. Sci. USA* **2006**, *103*, 10186 – 10191.

[50] D. Fairen-Jimenez, S. A. Moggach, M. T. Wharmby, P. A. Wright, S. Parsons, T. Düren, *J. Am. Chem. Soc.* **2011**, *133*, 8900 – 8902.

[51] M. Hasib-ur-Rahman, M. Siaj, F. Larachi, *Chem. Eng. Process.* **2010**, *49*, 313 – 322.

[52] Y. Ban, Z. Li, Y. Li, Y. Peng, H. Jin, W. Jiao, A. Guo, P. Wang, Q. Yang, C. Zhong, W. Yang, *Angew. Chem.* **2015**, *127*, 15703 – 15707.

[53] a) S. M. Cohen, *Chem. Rev.* **2012**, *112*, 970 – 1000; b) Y.-F. Song, L. Cronin, *Angew. Chem. Int. Ed.* **2008**, *47*, 4635 – 4637; *Angew. Chem.* **2008**, *120*, 4713 – 4715; c) K. K. Tanabe, S. M. Cohen, *Chem. Soc. Rev.* **2011**, *40*, 498 – 519; d) Z. Wang, S. M. Cohen, *Chem. Soc. Rev.* **2009**, *38*, 1315 – 1329; e) J. D. Evans, C. J. Sumby, C. J. Doonan, *Chem. Soc. Rev.* **2014**, *43*, 5933 – 5951.

[54] L. Cao, F. Lv, Y. Liu, W. Wang, Y. Huo, X. Fu, R. Sun, Z. Lu, *Chem. Commun.* **2015**, *51*, 4364 – 4367.

[55] T. Ahnfeldt, N. Guillou, D. Gunzelmann, I. Margiolaki, T. Loiseau, G. Férey, J. Senker, N. Stock, *Angew. Chem. Int. Ed.* **2009**, *48*, 5163 – 5166; *Angew. Chem.* **2009**, *121*, 5265 – 5268.

[56] S. R. Venna, M. Lartey, T. Li, A. Spore, S. Kumar, H. B. Nulwala, D. R. Luebke, N. L. Rosi, E. Albenze, *J. Mater. Chem. A* **2015**, *3*, 5014 – 5022.

[57] a) Z. Zhang, H. T. H. Nguyen, S. A. Miller, S. M. Cohen, *Angew. Chem. Int. Ed.* **2015**, *54*, 6152 – 6157; *Angew. Chem.* **2015**, *127*, 6250 – 6255; b) Z. Zhang, H. T. H. Nguyen, S. A. Miller, A. M. Ploskonka, J. B. DeCoste, S. M. Cohen, *J. Am. Chem. Soc.* **2016**, *138*, 920 – 925; c) Y. Zhang, X. Feng, H. Li, Y. Chen, J. Zhao, S. Wang, L. Wang, B. Wang, *Angew. Chem. Int. Ed.* **2015**, *54*, 4259 – 4263; *Angew. Chem.* **2015**, *127*, 4333 – 4337.

[58] a) G. R. Whittell, I. Manners, *Adv. Mater.* **2007**, *19*, 3439 – 3468; b) J.-C. Eloi, L. Chabanne, G. R. Whittell, I. Manners, *Mater. Today* **2008**, *11*, 28 – 36.

[59] T. Ishiwata, Y. Furukawa, K. Sugikawa, K. Kokado, K. Sada, *J. Am. Chem. Soc.* **2013**, *135*, 5427 – 5432.

[60] G. Distefano, H. Suzuki, M. Tsujimoto, S. Isoda, S. Bracco, A. Comotti, P. Sozzani, T. Uemura, S. Kitagawa, *Nat. Chem.* **2013**, *5*, 335 – 341.

[61] a) H. Li, M. Eddaoudi, M. O'Keeffe, O. M. Yaghi, *Nature* **1999**, *402*, 276 – 279; b) D. J. Tranchemontagne, J. R. Hunt, O. M. Yaghi, *Tetrahedron* **2008**, *64*, 8553 – 8557.

[62] D. Saha, Z. Bao, F. Jia, S. Deng, *Environ. Sci. Technol.* **2010**, *44*, 1820 – 1826.

[63] E. V. Perez, K. J. Balkus, Jr., J. P. Ferraris, I. H. Musselman, *J. Membr. Sci.* **2009**, *328*, 165 – 173.

[64] a) C. A. Allen, J. A. Boissonnault, J. Cirera, R. Gulland, F. Paesani, S. M. Cohen, *Chem. Commun.* **2013**, *49*, 3200 – 3202; b) C. A. Allen, S. M. Cohen, *Inorg. Chem.* **2014**, *53*, 7014 – 7019.

[65] P. Nugent, Y. Belmabkhout, S. D. Burd, A. J. Cairns, R. Luebke, K. Forrest, T. Pham, S. Ma, B. Space, L. Wojtas, M. Eddaoudi, M. J. Zaworotko, *Nature* **2013**, *495*, 80 – 84.

[66] a) S. Henke, A. Schneemann, S. Kapoor, R. Winter, R. A. Fischer, *J. Mater. Chem.* **2012**, *22*, 909 – 918; b) S. Henke, R. A. Fischer, *J. Am. Chem. Soc.* **2011**, *133*, 2064 – 2067; c) S. Henke, A. Schneemann, A. Wütscher, R. A. Fischer, *J. Am. Chem. Soc.* **2012**, *134*, 9464 – 9474.

[67] A. Bhattacharya, B. N. Misra, *Prog. Polym. Sci.* **2004**, *29*, 767 – 814.

[68] N. Tien-Binh, H. Vinh-Thang, X. Y. Chen, D. Rodrigue, S. Kaliaguine, *J. Mater. Chem. A* **2015**, *3*, 15202 – 15213.

[69] a) S. Furukawa, J. Reboul, S. Diring, K. Sumida, S. Kitagawa, *Chem. Soc. Rev.* **2014**, *43*, 5700 – 5734; b) R. Ricco, C. Pfeiffer, K. Sumida, C. J. Sumby, P. Falcaro, S. Furukawa, N. R. Champness, C. J. Doonan, *CrystEngComm* **2016**, *18*, 6532 – 6542.

[70] B. Seoane, S. Castellanos, A. Dikhtiarenko, F. Kapteijn, J. Gascon, *Coord. Chem. Rev.* **2016**, *307*, 147 – 187.

[71] T.-H. Bae, J. S. Lee, W. Qiu, W. J. Koros, C. W. Jones, S. Nair, *Angew. Chem. Int. Ed.* **2010**, *49*, 9863 – 9866; *Angew. Chem.* **2010**, *122*, 10059 – 10062.

[72] T. C. Merkel, H. Q. Lin, X. T. Wei, R. Baker, *J. Membr. Sci.* **2010**, *359*, 126 – 139.

[73] T. Li, Y. Pan, K.-V. Peinemann, Z. Lai, *J. Membr. Sci.* **2013**, *425 – 426*, 235 – 242.

[74] S. Konduri, S. Nair, *J. Phys. Chem. C* **2007**, *111*, 2017 – 2024.

[75] S. Choi, J. Coronas, E. Jordan, W. Oh, S. Nair, F. Onorato, D. F. Shantz, M. Tsapatsis, *Angew. Chem. Int. Ed.* **2008**, *47*, 552 – 555; *Angew. Chem.* **2008**, *120*, 562 – 565.

[76] Z. Kang, Y. Peng, Z. Hu, Y. Qian, C. Chi, L. Y. Yeo, L. Tee, D. Zhao, *J. Mater. Chem. A* **2015**, *3*, 20801 – 20810.

[77] A. Sabetghadam, B. Seoane, D. Keskin, N. Duim, T. Rodenas, S. Shahid, S. Sorribas, C. Le Guillouzer, G. Clet, C. Tellez, M. Daturi, J. Coronas, F. Kapteijn, J. Gascon, *Adv. Funct. Mater.* **2016**, *26*, 3154 – 3163.

[78] G. Zhu, H. Ren, *Porous Organic Frameworks, Design, Synthesis and Their Advanced Applications*, Springer, Berlin, **2015**.

[79] N. B. McKeown, P. M. Budd, *Chem. Soc. Rev.* **2006**, *35*, 675 – 683.

[80] C. H. Lau, K. Konstas, C. M. Doherty, S. Kanehashi, B. Ozcelik, S. E. Kentish, A. J. Hill, M. R. Hill, *Chem. Mater.* **2015**, *27*, 4756 – 4762.

[81] C. H. Lau, X. Mulet, K. Konstas, C. M. Doherty, M.-A. Sani, F. Separovic, M. R. Hill, C. D. Wood, *Angew. Chem. Int. Ed.* **2016**, *55*, 1998 – 2001; *Angew. Chem.* **2016**, *128*, 2038 – 2041.

[82] R. Dawson, A. I. Cooper, D. J. Adams, *Prog. Polym. Sci.* **2012**, *37*, 530 – 563.

[83] M. Jung, H. Kim, K. Baek, K. Kim, *Angew. Chem. Int. Ed.* **2008**, *47*, 5755 – 5757; *Angew. Chem.* **2008**, *120*, 5839 – 5841.

[84] J. Ma, Y. Ying, Q. Yang, Y. Ban, H. Huang, X. Guo, Y. Xiao, D. Liu, Y. Li, W. Yang, C. Zhong, *Chem. Commun.* **2015**, *51*, 4249 – 4251.

[85] a) K. Nagai, T. Masuda, T. Nakagawa, B. D. Freeman, I. Pinnau, *Prog. Polym. Sci.* **2001**, *26*, 721 – 798; b) H. B. Park, C. H. Jung, Y. M. Lee, A. J. Jill, S. J. Pas, S. T. Mudie, E. V. Wagner, B. D. Freeman, D. J. Cookson, *Science* **2007**, *318*, 254 – 258.

[86] C. Zhao, N. Wang, L. Wang, S. Sheng, H. Fan, F. Yang, S. Ji, J.-R. Li, J. Yu, *AIChE J.* **2016**, *62*, 3706 – 3716.

[87] C. Zhao, N. Wang, L. Wang, H. Huang, R. Zhang, F. Yang, Y. Xie, S. Ji, J.-R. Li, *Chem. Commun.* **2014**, *50*, 13921 – 13923.

[88] Q. Song, S. Jiang, T. Hasell, M. Liu, S. Sun, A. K. Cheetham, E. Sivaniah, A. I. Cooper, *Adv. Mater.* **2016**, *28*, 2629 – 2637.

[89] a) L. Liu, Z. Jiang, F. Pan, F. Peng, H. Wu, *J. Membr. Sci.* **2006**, *279*, 111 – 119; b) P. P. Chapala, M. V. Bermeshev, L. E. Starannikova, V. P. Shantarovich, N. N. Gavrilova, V. G. Avakyan, M. P. Filatova, Yu. P. Yampolskii, E. S. Finkelshtein, *J. Membr. Sci.* **2015**, *474*, 83 – 91.

[90] a) L. Y. Jiang, T. S. Chung, *J. Membr. Sci.* **2009**, *327*, 216 – 225; b) P. P. Chapala, M. V. Bermeshev, L. E. Starannikova, V. P. Shantarovich, N. N. Gavrilova, Yu. P. Yampolskii, E. S. Finkelshtein, *Polym. Compos.* **2015**, *36*, 1029 – 1038.

[91] See, for example: a) H. L. Chen, L. G. Wu, J. Tan, C. L. Zhu, *Chem. Eng. J.* **2000**, *78*, 159 – 164; b) A. Yamasaki, K. Mizoguchi, *J. Appl. Polym. Sci.* **1994**, *53*, 1669 – 1674; c) S. J. Lue, S. H. Peng, *J. Membr. Sci.* **2003**, *222*, 203 – 210.

[92] J. D. Evans, D. M. Huang, M. R. Hill, C. J. Sumby, A. W. Thornton, C. J. Doonan, *J. Phys. Chem. C* **2014**, *118*, 1523 – 1529.

[93] T. Tozawa, J. T. A. Jones, S. I. Swamy, S. Jiang, D. J. Adams, S. Shakespeare, R. Clowes, D. Bradshaw, T. Hasell, S. Y. Chong, C. Tang, S. Thompson, J. Parker, A. Trewin, J. Bacsa, A. M. Z. Slawin, A. Steiner, A. I. Cooper, *Nat. Mater.* **2009**, *8*, 973 – 978.

[94] M. W. Schneider, I. M. Oppel, H. Ott, L. G. Lechner, H. J. S. Hauswald, R. Stoll, M. Mastalerz, *Chem. Eur. J.* **2012**, *18*, 836 – 847.

[95] H. Kudo, R. Hayashi, K. Mitani, T. Yokozawa, N. C. Kasuga, T. Nishikubo, *Angew. Chem. Int. Ed.* **2006**, *45*, 7948 – 7952; *Angew. Chem.* **2006**, *118*, 8116 – 8120.

[96] J. Tian, P. K. Thallapally, S. J. Dalgarno, P. B. McGrail, J. L. Atwood, *Angew. Chem. Int. Ed.* **2009**, *48*, 5492 – 5495; *Angew. Chem.* **2009**, *121*, 5600 – 5603.

[97] S. Jiang, L. Chen, M. E. Briggs, T. Hasell, A. I. Cooper, *Chem. Commun.* **2016**, *52*, 6895 – 6898.

[98] M. Benzaqui, R. Semino, N. Menguy, F. Carn, T. Kundu, J.-M. Guigner, N. B. McKeown, K. J. Msayib, M. Carta, R. Malpass-Evans, C. Le Guillouzer, G. Clet, N. A. Ramsahye, C. Serre, G. Maurin, N. Steunou, *ACS Appl. Mater. Interfaces* **2016**, *8*, 27311 – 27321.

[99] a) S. Kanehashi, G. Q. Chen, C. A. Scholes, B. Ozcelik, C. Hua, L. Ciddor, P. D. Southon, D. M. D'Alessandro, S. E. Kentish, *J. Membr. Sci.* **2015**, *482*, 49 – 55; b) S. Kanehashi, G. Q. Chen, L. Ciddor, A. Chaffee, S. E. Kentish, *J. Membr. Sci.* **2015**, *492*, 471 – 477.

[100] A. Sabetghadam, B. Seoane, D. Keskin, N. Duim, T. Rodenas, S. Shahid, S. Sorribas, C. L. Guillouzer, G. Clet, C. Tellez, M. Daturi, J. Coronas, F. Kapteijn, J. Gascon, *Adv. Funct. Mater.* **2016**, *26*, 3154 – 3163.

[101] T. Rodenas, M. van Dalen, E. García-Pérez, P. Serra-Crespo, B. Zornoza, F. Kapteijn, J. Gascon, *Adv. Funct. Mater.* **2014**, *24*, 249 – 256.

[102] S. J. D. Smith, C. H. Lau, J. I. Mardel, M. Kitchin, K. Konstas, B. P. Ladewig, M. R. Hill, *J. Mater. Chem. A* **2016**, *4*, 10627 – 10634.

[103] M. Eddaoudi, J. Kim, J. B. Wachter, H. K. Chae, M. O'Keeffe, O. M. Yaghi, *J. Am. Chem. Soc.* **2001**, *123*, 4368 – 4369.

[104] a) H. Furukawa, J. Kim, K. E. Plass, O. M. Yaghi, *J. Am. Chem. Soc.* **2006**, *128*, 8398 – 8399; b) J. J. Perry, V. C. Kravtsov, M. J. Zaworotko, R. W. Larsen, *Cryst. Growth Des.* **2011**, *11*, 3183 – 3189; c) M. Tonigold, J. Hitzbleck, S. Bahnmuller, G. Langstein, D. Volkmer, *Dalton Trans.* **2009**, 1363 – 1371.

[105] a) Y. Ke, D. J. Collins, H.-C. Zhou, *Inorg. Chem.* **2005**, *44*, 4154 – 4156; b) S. Furukawa, N. Horike, M. Kondo, Y. Hijikata, A. Carné-Sánchez, P. Larpent, N. Louvain, S. Diring, H. Sato, R. Matsuda, R. Kawano, S. Kitagawa, *Inorg. Chem.* **2016**, *55*, 10843 – 10846.

[106] J. M. Teo, C. J. Coghlan, J. D. Evans, E. Tsivion, M. Head-Gordon, C. J. Sumby, C. J. Doonan, *Chem. Commun.* **2016**, *52*, 276 – 279.

[107] J.-R. Li, H.-C. Zhou, *Nat. Chem.* **2010**, *2*, 893 – 898.

[108] N. Hosono, M. Gochomori, R. Matsuda, H. Sato, S. Kitagawa, *J. Am. Chem. Soc.* **2016**, *138*, 6525 – 6531.

[109] S. Horike, S. Shimomura, S. Kitagawa, *Nat. Chem.* **2009**, *1*, 695 – 704.

[110] L. Diestel, N. Wang, B. Schwiedland, F. Steinbach, U. Giese, J. Caro, *J. Membr. Sci.* **2015**, *492*, 181 – 186.

[111] R. W. Baker, *Membrane Technology and Applications, 2nd ed.*, Wiley, Chichester, **2004**.

[112] a) M. F. A. Wahab, A. F. Ismail, S. J. Shilton, *Sep. Purif. Technol.* **2012**, *86*, 41 – 48; b) S. Husain, W. J. Koros, *J. Membr. Sci.* **2007**, *288*, 195 – 207; c) N. Peng, N. Widjojo, P. Sukitpaneenit, M. M. Teoh, G. G. Lipscomb, T.-S. Chung, J.-Y. Lai, *Prog. Polym. Sci.* **2012**, *37*, 1401 – 1424.

[113] a) S. Basu, A. Cano-Odena, I. F. J. Vankelecom, *J. Membr. Sci.* **2010**, *362*, 478 – 487; b) S. Basu, A. Cano-Odena, I. F. J. Vankelecom, *Sep. Purif. Technol.* **2011**, *81*, 31 – 40; c) H. Ren, J. Jin, J. Hu, H. Liu, *Ind. Eng. Chem. Res.* **2012**, *51*, 10156 – 10164; d) N. Nordin, A. Ismail, A. Mustafa, *J. Teknol.* **2014**, *69*, 73 – 76.

[114] S. Loeb, S. Sourirajan in *Saline Water Conversion-II*, *Vol. 38*, ACS, Washington, DC, **1963**, Chap. 9, pp. 117 – 132.

[115] C. Zhang, K. Zhang, L. Xu, Y. Labreche, B. Kraftschik, W. J. Koros, *AIChE J.* **2014**, *60*, 2625 – 2635.

[116] a) M. S. Denny, S. M. Cohen, *Angew. Chem. Int. Ed.* **2015**, *54*, 9029 – 9032; *Angew. Chem.* **2015**, *127*, 9157 – 9160; b) J. C. Moreton, M. S. Denny, Jr., S. M. Cohen, *Chem. Commun.* **2016**, *52*, 14376 – 14379.
[117] I. N. Odeh, Y. Liu (Sabic Global Technologies B.V.), WO2017003661, **2017**.
[118] C. Li, B. McCulloch, S. T. Wilson, A. I. Benin, M. E. Schott, (UOP LLC), US 7,637,983 B1, **2009**.
[119] R. R. Willis, (UOP LLC), US 2011/0138999 A1, **2011**.
[120] T. C. Merkel, B. D. Freeman, R. J. Spontak, Z. He, I. Pinnau, P. Meakin, A. J. Hill, *Science* **2002**, *296*, 519 – 522.

Manuscript received: January 31, 2017
Revised manuscript received: April 3, 2017
Accepted manuscript online: April 4, 2017
Version of record online: ■■ ■■, ■■■■

Supporting Information for:

Mixed-Matrix Membranes

Janina Dechnik,[a] Jorge Gascon,[b] Christian J. Doonan,[c] Christoph Janiak*[a] and Christopher J. Sumby*[c]

[a] J. Dechnik, Prof. Dr C. Janiak, Institut für Anorganische Chemie und Strukturchemie, Universität Düsseldorf, Düsseldorf, Germany. E-mail: janiak@uni-duesseldorf.de

[b] Prof. Dr J. Gascon, Department of Chemical Engineering, Technical University Delft Delft, The Netherlands.

[c] Prof. C. J. Doonan, Prof. C. J. Sumby, Department of Chemistry and the Centre for Advanced Nanomaterials, University of Adelaide, Adelaide, Australia. E-mail: christopher.sumby@adelaide.edu.au

SI 1. General considerations about membrane performance

Permeability, officially the permeability coefficient, $\boldsymbol{P}_i$, gives the normalized productivity of a specific gas and is defined (Eq. 1) as the diffusive *Flux* of gas *i* through the membrane (flow per unit membrane area *A*) normalized by the partial pressure difference of that component across the membrane per unit thickness of the membrane (*l*):

$$\boldsymbol{P}_i = \frac{Flux_i \cdot \ell}{\Delta p_i}$$

$$Flux_i = \frac{Flow_i}{A} \qquad \text{(Eq. 1)}$$

Permeability values are typically reported in Barrer units (1 Barrer = $1 \cdot 10^{-10}$ cm^3 (STP)·cm·cm^{-2}·s^{-1}·$cmHg^{-1}$ = $3.344 \cdot 10^{-16}$ mol·m·m^{-2}·Pa^{-1}·s^{-1}).

The separation factor or permselectivity reflects the capability of a membrane to separate one gas from another. If the permeabilities of two individual components are known, the ideal selectivity, S_{ij} (Eq. 2), is given by their ratio:

$$S_{ij} = \frac{\boldsymbol{P}_i}{\boldsymbol{P}_j} \qquad \text{(Eq. 2)}$$

For permeation of actual *i*/*j* mixtures, the mixed gas selectivity, also called separation factor (α_{ij}), is calculated from composition analysis as the ratio of the mole fractions, *X,* of the components in the permeate stream, and the retentate stream (Eq. 3). In the case where the gases do not interact strongly with each other or with the membrane material, the ideal selectivity is equal to the actual separation factor, but often this is not the case.[S1]

$$\alpha_{ij} = \frac{\left(X_i / X_j\right)_{permeate}}{\left(X_i / X_j\right)_{retentae}} \qquad \text{(Eq. 3)}$$

SI 2. Structures of some polymers and fillers discussed in the review

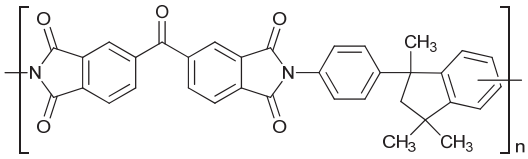

Matrimid®

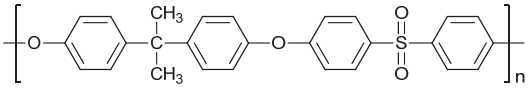

Polysulfone (PSF)

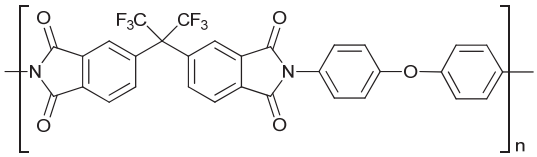

6FDA/ODA polyimide

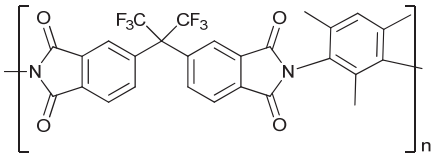

6FDA/DAM polyimide

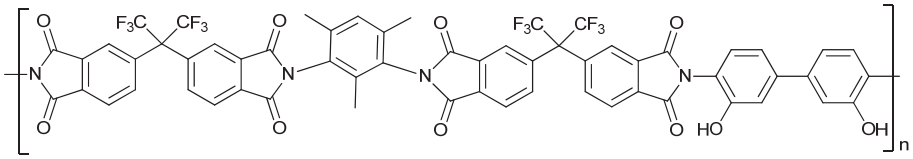

6FDA-DAM-HAB (1:1) polyimide

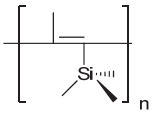

poly(1-trimethylsilyl-1)propyne (PTMSP)

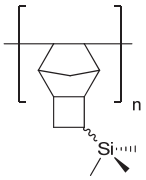

poly(3-trimethylsilyltricyclononene-7) (PTCNSi1)

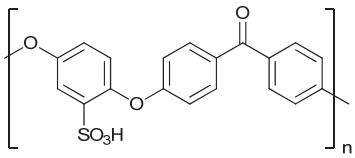

sulfonated poly(ether ether ketone) (SPEEK)

Figure SI 1. Organic polymers used for the continuous phase, which are depicted by their repeat unit.

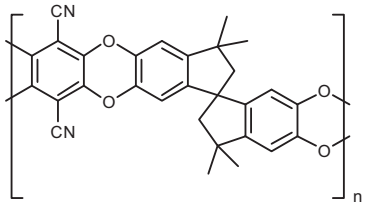

Polymer of Intrinsic Microporosity 1 (PIM-1)

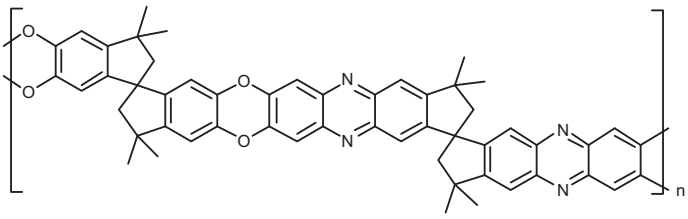

Polymer of Intrinsic Microporosity 7 (PIM-7)

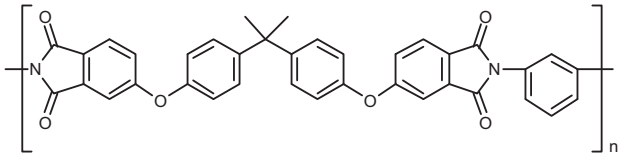

Ultem®

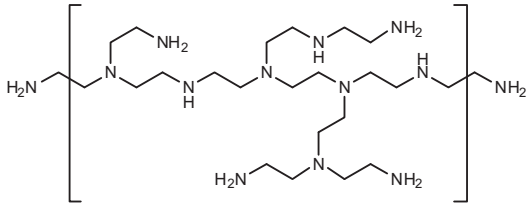

polyethyleneimine (PEI)

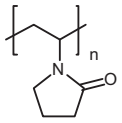

polyvinylpyrrolidone (PVP)

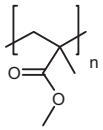

poly(methyl methacrylate) (PMMA)

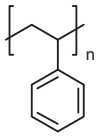

polystyrene (PS)

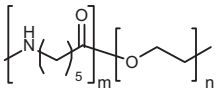

poly(amide-b-ethylene oxide) (Pebax®$_{1657}$)

Figure SI 1 (cont'd). Organic polymers used for the continuous phase, which are depicted by their repeat unit.

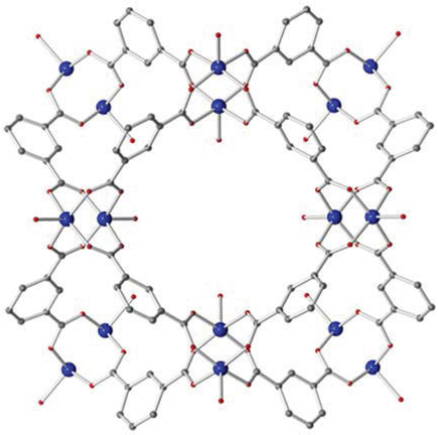

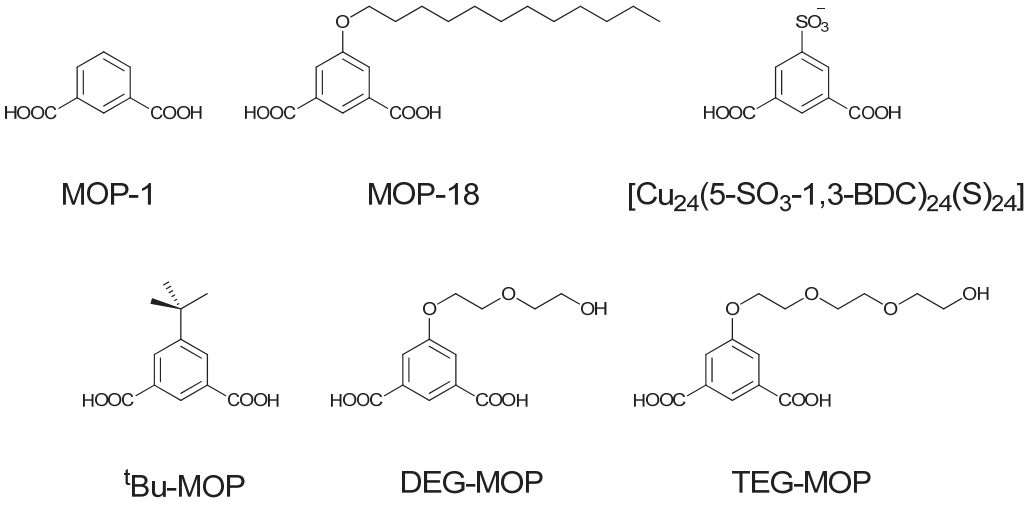

Figure SI 2. A representation of the structure of MOP-1 (top) and the ligands used to form the various MOP structures discussed in the review.

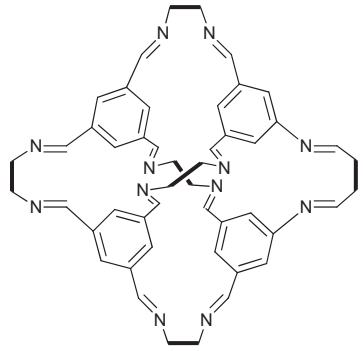

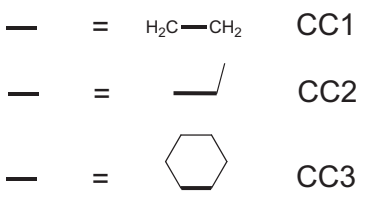

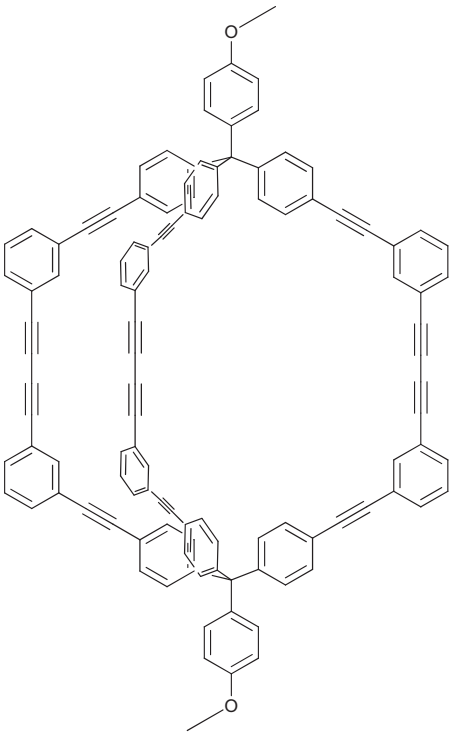

DC1

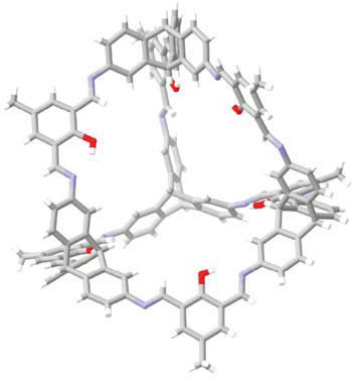

MC1

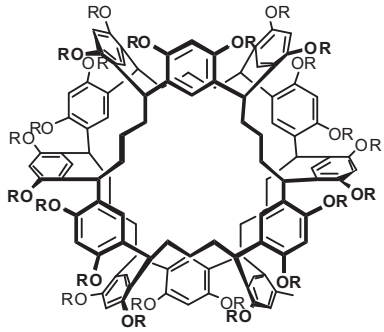

Noria R = H

Noria-BOC R = $COOC(CH_3)_3$

Noria-CO^{t}Bu R = $COC(CH_3)_3$

Figure SI 3. The structures of some of the POC materials discussed in the review. Top: Representatives of the family of tetrahedral imine cages prepared by Cooper (CC1, CC2 and CC3) and the elongated dipyramidal cage of Doonan (called DC1 in this review). Bottom left: A representation of the adamantoid imine cage of Mastalerz (called MC1 in this review). Bottom right: The structure of Noria and its derivatives.

Table SI 1. Polymers and additives of the highlighted MOF-MMMs and the gas separation problems addressed.

Additive	Polymer	X/Y Gas separation	Ref.
MIL-125(Ti)-NH_2	PSF	CO_2/CH_4	Guo 2015 [S2]
MIL-125(Ti), MIL-125(Ti)-NH_2	Matrimid® 9725	CO_2/CH_4	Waqas Anjum 2016 [S3]
MIL-101(Cr), MIL-101(Cr)-SO_3H	SPEEK	CO_2/CH_4, CO_2/N_2	Xin 2015 [S4]
UiO-66(Zr), UiO-66(Zr)-NH_2 (functionalization: benzoic acid and 4-aminobenzoic acid)	Matrimid® 9725	CO_2/CH_4	Anjum 2015 [S5]
ZIF-8, IL@ZIF-8	PSF (asymmetric)	CO_2/CH_4, CO_2/N_2	Ban 2015 [S6]
CAU-1-NH_2, CAU-1-NH_2@PDA	PMMA	O_2/N_2, O_2/CO_2	Cao 2015 [S7]
UiO-66(Zr)-NH_2 (functionalization: phenyl acetyl, decanoyl, succinic acid)	Matrimid® 5218	CO_2/N_2	Venna 2015 [S8]
MIL-53(Al), MIL-53(Al)-NH_2	6FDA–ODA	CO_2/CH_4	Chen 2012 [S9]
MIL-53(Al), MIL-53(Al)-NH_2	6FDA–DAM	CO_2/CH_4	Tien-Binh 2015 [S10]
MIL-53(Al), MIL-53(Al)-NH_2	6FDA–DAM–HAB	CO_2/CH_4	Tien-Binh 2015 [S10]
ZIF-90	6FDA–DAM	CO_2/CH_4	Bae 2010 [S11]
ZIF-7	Pebax®1657	CO_2/CH_4, CO_2/N_2	Li 2013 [S12]
CuBDC (morphology: bulk and nanosheets)	Matrimid® 5218	CO_2/CH_4	Rodenas 2015 [S13]
$[Cu_2(ndc)_2(dabco)]$ (morphology: bulk, nanocubes and nanosheets)	PBI	H_2/CO_2	Kang 2015 [S14]
MIL-53(Al)-NH_2 (morphology: nanoparticles, nanorods, and microneedles)	Matrimid®5218	CO_2/CH_4	Sabetghadam 2016 [S15]
MIL-53(Al)-NH_2 (morphology: nanoparticles, nanorods, and microneedles)	6FDA-DAM	CO_2/CH_4	Sabetghadam 2016 [S15]

Table SI 2. Polymers and additives of the highlighted COF/POF-MMMs and molecular additive MMMs and the gas separation problems addressed.

Additive	Polymer	X/Y Gas separation	Ref.
POF/COF additives			
PAF-1	PTMSP, PIM-1, poly(4-methyl-2-pentyne) (PMP)	CO_2/N_2	Lau 2014 [S16]
PAF-1, PAF-1-NH_2, PAF-1-SO_3H, PAF-1-C_{60}, PAF-1-Li_6C_{60}	PTMSP	CO_2/CH_4	Lau 2015 [S17]
Hypercrosslinked nanoparticle α,α'-dichloro-p-xylene (*p*-DCX)	PTMSP	CO_2/N_2	Mitra 2016 [S18]
NUS-2, NUS-3	poly(ether imide) (Ultem) or polybenzimidazole (PBI)	H_2/CO_2	Kang 2016 [S19]
TpPa-1, TpBD	polybenzimidazole (PBI)	CO_2/N_2, CO_2/CH_4	Biswal 2016 [S20]
ACOF-1	Matrimid	CO_2/CH_4	Shan 2016 [S21]
MOP additives			
MOP-18	Matrimid	O_2/N_2, H_2/CO_2, CH_4/N_2, C_3H_8/N_2, C_3H_6/N_2, C_3H_6/C_3H_8, H_2/CH_4, H_2/N_2, CO_2/CH_4, H_2/O_2	Perez 2014 [S22]
Na_6H_{18}-[Cu_{24}(5-SO_3-1,3-BDC)$_{24}$($S)_{24}$]·xS	PSF	CO_2/CH_4	Ma 2015 [S23]
^{t}Bu-MOP, DEG MOP, TEG MOP, MOP-18	PTMSP	CO_2/CH_4	Kitchin 2015 [S24]
POC and related additives			
β-cyclodextrin	Matrimid	O_2/N_2	Jiang 2009 [S25]
Me- and Me_3Si-substituted α,β,γ-cyclodextrin	PTCNSi1	O_2/N_2, CO_2/O_2, CO_2/CH_4, H_2/N_2, H_2/CH_4, He/N_2	Chapala 2015 [S26]
Various substituted calixarenes	PTCNSi1	O_2/N_2, CO_2/O_2, CO_2/CH_4, H_2/N_2, H_2/CH_4, He/N_2, C_4/C_1	Chapala 2015 [S27]
CC3	PIM-1	CO_2/N_2, CO_2/CH_4	Bushell 2013 [S28]
Noria, Noria-CO^{t}Bu	6FDA-DAM	O_2/N_2, CO_2/CH_4	Mao 2017 [S29]
Scrambled POCs	Polyethyleneimine (PEI), polyvinylpyrrolidone (PVP), poly(methyl methacrylate) (PMMA), and polystyrene (PS)	CO_2/N_2	Jiang 2016 [S30]

SI 3. References

[S1] W. Koros, Y. H. Ma and T. Shimidzu, *Pure Appl. Chem.* **1996**, *68*, 1479-1489.

[S2] X. Guo, H. Huang, Y. Ban, Q. Yang, Y. Xiao, Y. Li, W. Yang, C. Zhong, *J. Membr. Sci.* **2015**, *478*, 130-139.

[S3] M. Waqas Anjum, B. Bueken, D. De Vos, I. F. J. Vankelecom, *J. Membr. Sci.* **2016**, *502*, 21-28.

[S4] Q. Xin, T. Liu, Z. Li, S. Wang, Y. Li, Z. Li, J. Ouyang, Z. Jiang, H. Wu, *J. Membr. Sci.* **2015**, *488*, 67-78.

[S5] M. W. Anjum, F. Vermoortele, A. L. Khan, B. Bueken, D. E. De Vos, I. F. J. Vankelecom, *ACS Appl. Mater. Interfaces* **2015**, *7*, 25193-25201.

[S6] Y. Ban, Z. Li, Y. Li, Y. Peng, H. Jin, W. Jiao, A. Guo, P. Wang, Q. Yang, C. Zhong, W. Yang, *Angew. Chem.* **2015**, *127*, 15703-15707.

[S7] L. Cao, F. Lv, Y. Liu, W. Wang, Y. Huo, X. Fu, R. Sun, Z. Lu, *Chem. Commun.* **2015**, *51*, 4364-4367.

[S8] S. R. Venna, M. Lartey, T. Li, A. Spore, S. Kumar, H. B. Nulwala, D. R. Luebke, N. L. Rosi, E. Albenze, *J. Mater. Chem. A* **2015**, *3*, 5014-5022.

[S9] X. Y. Chen, H. Vinh-Thang, D. Rodrigue, S. Kaliaguine, *Ind. Eng. Chem. Res.* **2012**, *51*, 6895-6906.

[S10] N. Tien-Binh, H. Vinh-Thang, X. Y. Chen, D. Rodrigue, S. Kaliaguine, *J. Mater. Chem. A* **2015**, *3*, 15202-15213.

[S11] T. H. Bae, J. S. Lee, W. Qiu, W. J. Koros, C. W. Jones, S. Nair, *Angew. Chem., Int. Ed.* **2010**, *49*, 9863-9866.

[S12] T. Li, Y. Pan, K.-V. Peinemann, Z. Lai, *J. Membr. Sci.* **2013**, *425–426*, 235-242.

[S13] T. Rodenas, I. Luz, G. Prieto, B. Seoane, H. Miro, A. Corma, F. Kapteijn, F. X. Llabrés i Xamena, J. Gascon, *Nat. Mater.* **2015**, *14*, 48-55.

[S14] Z. Kang, Y. Peng, Z. Hu, Y. Qian, C. Chi, L. Y. Yeo, L. Tee, D. Zhao, *J. Mater. Chem. A* **2015**, *3*, 20801-20810.

[S15] A. Sabetghadam, B. Seoane, D. Keskin, N. Duim, T. Rodenas, S. Shahid, S. Sorribas, C. L. Guillouzer, G. Clet, C. Tellez, M. Daturi, J. Coronas, F. Kapteijn, J. Gascon, *Adv. Funct. Mater.* **2016**, *26*, 3154-3163.

[S17] C. H. Lau, P. T. Nguyen, M. R. Hill, A. W. Thornton, K. Konstas, C. M. Doherty, R. J. Mulder, L. Bourgeois, A. C. Y. Liu, D. J. Sprouster, J. P. Sullivan, T. J. Bastow, A. J. Hill, D. L. Gin, R. D. Noble, *Angew. Chem. Int. Ed.* **2014***, 53,* 5322 –5326.

[S17] C. H. Lau, K. Konstas, C. M. Doherty, S. Kanehashi, B. Ozcelik, S. E. Kentish, A. J. Hill, M. R. Hill, *Chem. Mater*. **2015**, *27*, 4756**-**4762.

[S18] T. Mitra, R. S. Bhavsar, D. J. Adams, P. M. Budd, A. I. Cooper, *Chem. Commun*. **2016**, *52*, 5581-5584.

[S19] Z. Kang, Y. Peng, Y. Qian, D. Yuan, M. A. Addicoat, T. Heine, Z. Hu, L. Tee, Z. Guo, D. Zhao, *Chem. Mater.* **2016**, *28*, 1277-1285.

[S20] B. Biswal, H. D. Chaudhari, R. Banerjee, U. K. Kharul, *Chem. Eur. J.* **2016**, 22, 4695-4699.

[S21] M. Shan, B. Seoane, E. Rozhko, A. Dikhtiarenko, G. Clet, F. Kapteijn, J. Gascon, *Chem. Eur. J.* **2016**, *22*, 14467-14470.

[S22] E. V. Perez, K. J. Balkus Jr., J. P. Ferraris, I. H. Musselman, *J. Membr. Sci.* **2014**, *463*, 82-93.

[S23] J. Ma, Y. Ying, Q. Yang, Y. Ban, H. Huang, X. Guo, Y. Xiao, D. Liu, Y. Li, W. Yang, C. Zhong, *Chem. Commun*. **2015**, *51*, 4249-4251.

[S24] M. Kitchin, J. Teo, K. Konstas, C. Hon Lau, C. J. Sumby, A. W. Thornton, C. J. Doonan, M. R. Hill, *J. Mater. Chem. A* **2015**, *3*, 15241-15247.

[S25] L. Y. Jiang, T. S. Chung, *J. Membr. Sci*. **2009**, *327*, 216-225.

[S26] P. P. Chapala, M. V. Bermeshev, L. E. Starannikova, V. P. Shantarovich, N. N. Gavrilova, Yu. P. Yampolskii, E. Sh. Finkelshtein, *Polym. Compos*. **2015**, *36*, 1029-1038.

[S27] P. P. Chapala, M. V. Bermeshev, L. E. Starannikova, V. P. Shantarovich, N. N. Gavrilova, V. G. Avakyan, M. P. Filatova, Yu. P. Yampolskii, E. Sh. Finkelshtein, *J. Membr. Sci*. **2015**, *474*, 83-91.

[S28] A. F. Bushell, P. M. Budd, M. P. Attfield, J. T. A. Jones, T. Hasell, A. I. Cooper, P. Bernardo, F. Bazzarelli, G. Clarizia, J. C. Jansen, *Angew. Chem. Int. Ed.* **2013**, *52*, 1253-1256.

[S29] H. Mao, S. Zhang, *J. Colloid Interface Sci*. **2017**, *490*, 29-36.

[S30] S. Jiang, L. Chen, M. E. Briggs, T. Hasell, A. I. Cooper, *Chem. Commun*. **2016**, *52*, 6895-6898.

3.2 Mixed-Matrix Membranes of the Air-Stable MOF-5 Analogue [$Co_4(\mu_4$-$O)(Me_2pzba)_3$] with a Mixed-Functional Pyrazolate-Carboxylate Linker for CO_2/CH_4 Separation

Janina Dechnik, Alexander Nuhnen, Christoph Janiak

Cryst. Growth Des. **2017**, in press.
DOI: 10.1021/acs.cgd.7b0020, Quelle[217]

Die Synthese des isostrukturellen MOF-5-Analogons [$Co_4(\mu_4$-$O)(Me_2pzba)_3$] mit dem bifunktionellen Liganden 4-(3,5-Dimethyl-1H-pyrazol-4-yl)benzoesäure (H_2Me_2pzba) konnte im Vergleich zur Solvothermalsynthese durch eine mikrowellenunterstützte Synthese verbessert werden und ermöglichte so eine höhere Ausbeute, deutlich kürzere Reaktionszeiten, eine nahezu verdoppelte BET-Oberfläche, kleinere Partikelgrößen und weniger Aggregation. Die signifikant erhöhte Feuchtigkeitsstabilität von [$Co_4(\mu_4$-$O)(Me_2pzba)_3$] im Vergleich zu MOF-5 [$Zn_4(\mu_4$-$O)(1,4\text{-}BDC)_3$] (1,4-H_2BDC = Terephthalsäure) prädestinierte dieses MOF für die Herstellung von feuchtigkeitstoleranten Matrimid MMMs ohne die Verwendung von inerten Bedingungen. Ein gleichmäßiges Einbetten der MOF-Partikel wurde im Polymer ohne Aggregation und mit guter MOF-Polymer-Kompatibilität erreicht. Die [$Co_4(\mu_4$-$O)(Me_2pzba)_3$]/Matrimid-MMMs zeigten eine verbesserte CO_2/CH_4-Trennleistung gegenüber reinen Matrimid-Membranen mit einer Erhöhung der Gemischtgasselektivität von 41 für Matrimid auf 60 für die 24 Gew.-% MMM bei 3 bar Druckdifferenz, welche auch höher ist, als für feuchtigkeitsempfindliche MOF-5/Matrimid-MMMs (maximal S = 45).

Anteil an der Veröffentlichung:

- Konzept, synthetische Arbeiten und Analytik der Verbindungen und Materialien. Entwicklung und Modifikation der Permeationsapparatur für Gemischtgasmessungen, Schreiben des Manuskripts und Bearbeitung der Abbildungen und Tabellen sowie Auswertung der Ergebnisse. Bearbeitung des Manuskripts nach Revision.
- Korrekturen wurden durch Christoph Janiak vorgenommen.
- Alexander Nuhnen hat einen Teil der synthetischen Arbeit und der MOF-Analytik im Rahmen seiner Bachelorarbeit angefertigt und war bei den Permeationsmessungen der Membranen beteiligt.

CRYSTAL GROWTH & DESIGN

Article

pubs.acs.org/crystal

Mixed-Matrix Membranes of the Air-Stable MOF-5 Analogue $[Co_4(\mu_4\text{-}O)(Me_2pzba)_3]$ with a Mixed-Functional Pyrazolate-Carboxylate Linker for CO_2/CH_4 Separation

Published as part of a Crystal Growth and Design virtual special issue on Crystal Engineering of Nanoporous Materials for Gas Storage and Separation

Janina Dechnik, Alexander Nuhnen, and Christoph Janiak*

Institut für Anorganische Chemie und Strukturchemie, Heinrich-Heine Universität Düsseldorf, 40204 Düsseldorf, Germany

Supporting Information

ABSTRACT: The synthesis of the isostructural MOF-5 analogue 3D-$[Co_4(\mu_4\text{-}O)(Me_2pzba)_3]$ with the bi- or mixed-functional was improved by the use of microwave heating instead of previously described conventional thermal heating, giving a higher yield at drastically shorter reaction time with nearly doubled BET surface area, smaller size, and less aggregation. The significantly increased air/moisture stability of $[Co_4(\mu_4\text{-}O)(Me_2pzba)_3]$ compared to MOF-5 made the Co-MOF amenable for the preparation of moisture-tolerant $[Co_4(\mu_4\text{-}O)(Me_2pzba)_3]$/Matrimid mixed-matrix membranes (MMMs) without the use of inert conditions. Uniformly embedding of the small metal−organic framework (MOF) particles was achieved in the polymer, without aggregation and with good MOF−polymer compatibility. $[Co_4(\mu_4\text{-}O)(Me_2pzba)_3]$/Matrimid MMMs exhibited an improved CO_2/CH_4 separation performance over neat Matrimid membranes with an increase in mixed-gas selectivity from 41 for Matrimid to 60 for the 24 wt % MMM at 3 bar transmembrane pressure, which is also higher than reported for moisture-sensitive MOF-5/Matrimid MMMs (maximal $S = 45$).

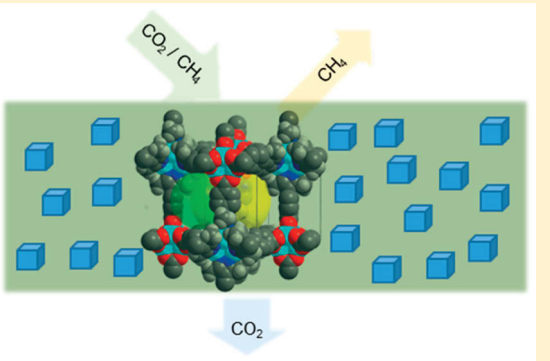

INTRODUCTION

Energy savings of up to 50% of the production costs can be achieved by applying membrane technology in industry in the separation of mixtures.[1] Membrane processes proved to be advantageous over separations that had been carried out with conventional methods, such as distillation, crystallization, or adsorption. Lower costs, reduced power consumption, and simpler process conditions make membrane separation techniques the preferred technology for the separation of mixtures.[2,3] Efficient processes for the removal of carbon dioxide from industrial gas streams (biogas and natural gas) are of current interest.[4]

Membranes are characterized by their permeability and selectivity to assess their efficiency. In current membrane preparations, organic polymers are the preferred material because of their general advantages like modest costs, high flexibility, high mechanical and chemical resistance, low energy consumption, and their versatile use. However, polymer membranes show a trade-off or inverse relation between gas permeability and selectivity, which is described by the so-called Robeson upper bound, the performance limit of polymer membranes known in the literature.[5,6] Mixed-matrix membranes (MMMs) are an alternative to pure polymer membranes, as MMMs can exhibit markedly better selectivity combined with good permeability. MMMs consist of organic polymers and inorganic or inorganic−organic hybrid particles, which are embedded as functional fillers in the polymer matrix. A variety of materials impermeable and permeable have been used as filler materials.[6−32]

Metal−organic frameworks (MOFs) are potentially porous three-dimensional (3D) network materials with often selective adsorption properties. They consist of inorganic metal clusters which are coordinatively linked by organic molecules.[33,34] Because of their high surface area, defined pore size, crystallinity, and structural diversity, MOFs have attracted tremendous interest in various fields for potential applications.[35−39] MOF fillers in MMMs may have the potential to improve membrane gas separation performance to a commercially attractive region.[3,8,17,40,41] MOFs are hybrid materials and offer various advantages over other, e.g., purely inorganic fillers materials, like good compatibility with the organic polymer composite.[8−13]

Pure MOF-5 membranes as well as MOF-5 MMMs with various polymer materials have already shown good separation properties for CO_2/CH_4 gas mixtures.[42−46] Yet, the strong water sensitivity of MOF-5 is a considerable problem for

Received: February 9, 2017
Revised: June 19, 2017
Published: June 23, 2017

DOI: 10.1021/acs.cgd.7b00202
Cryst. Growth Des. XXXX, XXX, XXX−XXX

possible industrial applications. Because of the influence of humidity, an initial decomposition of MOF-5 can be observed after just 10 min. After 24 h, the decomposition of the MOF-5 network is complete, and the material shows no more porosity, which is a fundamental requirement for MOF fillers in MMMs in separation processes.[47]

The introduction of linkers with donor groups of stronger basicity such as imidazolates or pyrazolates can result in a higher covalency of the metal−ligand bonds and thus contribute to markedly increased water stability. In metal-azolate frameworks (MAFs), including zeolitic-imidazolate frameworks (ZIFs), the metal centers are coordinated by linkers from imidazolate, pyrazolate, triazolate, or tetrazolate derivatives. MAFs can show high thermal and chemical stability, which results from the more covalent coordination of the nitrogen atoms to the metal ions. In addition, the substituents on the linkers often form highly hydrophobic MAFs causing a low affinity for the adsorption of water and thus also lead to better water stability.[48,49]

Recently MOF-5 analogous structures with a mixed- or bifunctional pyrazolate-carboxylate ligand, 4-(3,5-dimethyl-1*H*-pyrazol-4-ate)benzoate (Me_2pzba^{2-}), were reported (Figure 1).

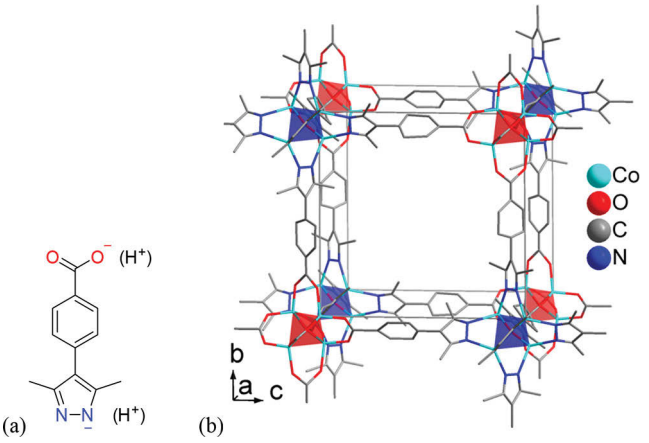

Figure 1. (a) Mixed-functional pyrazolate-carboxylate linker 4-(3,5-dimethyl-1*H*-pyrazol-4-ate)benzoate (Me_2pzba^{2-})/4-(3,5-dimethyl-1*H*-pyrazol-4-yl)benzoic acid (H_2Me_2pzba) and (b) wire-frame model (no H atoms shown for clarity) with an idealized pyrazolate-only (blue) and carboxylate-only (red tetrahedra) coordination for $\{Co_4(\mu_4\text{-}O)\}$.

These 3D-$[M_4(\mu_4\text{-}O)(Me_2pzba)_3]$ MOFs with accessible porosity (Figure S1) were prepared for M = Co and Zn and were characterized regarding their crystal structures and sorption properties.[50−52]

The $[M_4(\mu_4\text{-}O)(Me_2pzba)_3]$ networks show the same topology as MOF-5 with the identical $[M_4(\mu_4\text{-}O)L_3]$ sum formula (M = Zn, L = terephthalate^{2-} for MOF-5). The pyrazolate and carboxylate groups from the Me_2pzba^{2-} linker coordinate statistically to the metal centers, and each ligand bridges between two $\{M_4(\mu_4\text{-}O)\}$ metal clusters (Figure 1). Herein, we report an improved and scaled-up synthesis of the MOF-5 analog $[Co_4(\mu_4\text{-}O)(Me_2pzba)_3]$ using microwave heating. Unlike MOF-5 the isostructural MOF 3D-$[Co_4(\mu_4\text{-}O)(Me_2pzba)_3]$ does not degrade in humid air. The MOF-microcrystals were incorporated into MMMs with the commercial polymer Matrimid for the separation of carbon dioxide from methane.

EXPERIMENTAL SECTION

All starting materials and solvents were obtained from commercial sources and used without further purification unless otherwise mentioned in the experimental description. Cobalt nitrate hexahydrate ($Co(NO_3)_2\cdot 6H_2O$, 99%), potassium carbonate (99%) and copper(I) iodide (99%) were obtained from Sigma-Aldrich. 4-Iodobenzoic acid (98%) was received from Acros Organics, and 2,4-pentanedione (99%) and L-proline (98%) were acquired from Merck. Dichloromethane (99%), *N*,*N*-dimethylformamide (99.99%), and dimethyl sulfoxide (99%) were purchased from Fisher Chemical. Hydrazine monohydrate was obtained from Alfa-Aesar. 4-(3,5-Dimethyl-1*H*-pyrazol-4-yl)benzoic acid (H_2Me_2pzba) has been synthesized from 4-iodobenzoic acid according to a previously reported[53] but modified procedure (details in Supporting Information). The polymer Matrimid 5218 was kindly supplied by Huntsman Advanced Materials. For comparison, a sample of MOF-5 was prepared according to a literature procedure.[54] Details for the microwave-heating assisted synthesis of 3D-$[Co_4(\mu_4\text{-}O)(Me_2pzba)_3]$, the synthesis of MOF-5, and characterization of these MOFs are given in the Supporting Information

Preparation of MMMs. Matrimid was dried at 120 °C for 24 h under a vacuum to remove the adsorbed moisture. The MMMs were prepared using a priming protocol.[23] Priming of the MOF particle suspension with part of the polymer solution reduces the stress at the particle−polymer interface and reduces also potential agglomeration of the filler material.[55] MMMs with 8 wt % of $[Co_4(\mu_4\text{-}O)(Me_2pzba)_3]$ were prepared by dissolving Matrimid (400 mg) in dichloromethane (3.5 mL) followed by stirring for 24 h. Simultaneously $[Co_4(\mu_4\text{-}O)(Me_2pzba)_3]$ (35 mg) was suspended in dichloromethane (4.5 mL) and was also stirred for 24 h. Afterward the MOF suspension was homogenized by using an ultrasonic liquid processor (VCX 750 Sonics, Microtip 630-0419). The suspension was treated for 15 min with an amplitude of 20% and was stirred for additional 45 min. The homogenization step was repeated three times. Subsequently 0.31 mL of the Matrimid solution was added to the MOF suspension to achieve an equal polymer/MOF mass ratio in the priming mixture. This mixture was stirred for an additional 24 h followed by repeating the homogenization steps. Afterward, the remaining polymer solution was added to the mixture and was stirred for one additional hour. This mixture was cast into a metal ring (7.5 cm diameter) which was placed on a flat glass plate. The metal rings were covered with funnels to protect the membranes from dust, but at the same time allow the solvent to evaporate slowly. The membranes were left to dry overnight at room temperature and were then peeled off from the glass plate and dried under a vacuum at 120 °C for 24 h. The MMMs with 16 and 24 wt % were prepared following the synthetic procedure for 8 wt % MMM using 76 mg and 126 mg MOF, respectively. Also, the added Matrimid solution in the priming step was varied to 0.67 and 1.11 mL, respectively.

CHARACTERIZATION

General Methods. Electron impact (EI) mass spectra were obtained on a Finnigan Trace GC Ultra. ^1H NMR and ^{13}C NMR spectra were recorded with a Bruker Avance III-600 at 290 K at 600 MHz. Thermogravimetric analyses (TGA) were done with a Netzsch TG 209 F3 Tarsus in the range 25 to 1000 °C, equipped with Al_2O_3-crucibles and applying a heating rate of 5 K·min^{-1} under nitrogen flow.

Powder X-ray diffraction (PXRD) patterns were collected on a Bruker D2 Phaser powder diffractometer equipped with a flat silicon, low background sample holder using Cu−K_α radiation (λ = 1.5418 Å, 30 kV, 10 mA, ambient temperature). With this sample holder at 2θ < ~10° the beam spot is strongly broadened so that only a fraction of the reflected radiation reaches the detector; hence lower relative intensities are measured in this range. The sample of MOF-5 was measured with a scan speed of 1 s/step and a step size of 0.15° (2θ) at 290 K in the range of 2θ = 5−70°. The Co(II)-compound

DOI: 10.1021/acs.cgd.7b00202
Cryst. Growth Des. XXXX, XXX, XXX−XXX

$[Co_4(\mu_4\text{-}O)(Me_2pzba)_3]$ was measured with a scan speed of 2 s/step and a step size of 0.028° (2θ), and the lower discriminative of the detector was raised from 0.1 to 0.2 V to avoid reduced resolution by cobalt X-ray florescence. Simulated PXRD patterns were calculated with CCDC Mercury 3.7 program using the single-crystal data of MOF-5[56] and $[Co_4(\mu_4\text{-}O)(Me_2pzba)_3]$.[50] A Jeol JSM-6510LV QSEM Advanced scanning electron microscope (SEM) with wolfram (W) cathode (5−20 keV) was used for acquiring images. The microscope was equipped with a Bruker Xflash 410 silicon drift detector and Bruker ESPRIT software for energy-dispersive X-ray spectroscopic (EDX) analysis. The membrane cross sections for SEM imaging were prepared through freeze-fracturing after immersion in liquid nitrogen and coating with gold using a Jeol JFC 1200 fine-coater (20 mA for 20 s).

Gas adsorption and permeation experiments were carried out to characterize the gas uptake of $[Co_4(\mu_4\text{-}O)(Me_2pzba)_3]$ and the separation performance of the MMMs. See Supporting Information for a detailed description of the experiments.

RESULTS AND DISCUSSION

Microwave Synthesis vs Conventional Solvothermal Method. The heating method in MOF preparation has been extensively shown to be crucial for the resulting morphology and especially for the particle size.[57] These properties are of importance for the preparation of MOF samples for MMMs, as the particle size influences the distribution of the filler particles within the polymer matrix and the interactions between filler and matrix. The synthesis by microwave heating has been reported as an effective method to prepare small and uniformly sized MOF particles as suitable fillers in MMMs.[58] The previously published synthesis procedure for $[Co_4(\mu_4\text{-}O)(Me_2pzba)_3]$ required 5 days of heating at 130 °C under solvothermal conditions. A reduction of synthesis time would represent a remarkable improvement in order to address a large scale production of this material for applications. The reaction time with conventional heating can be reduced from several days to about 1 h by using microwave heating. The conversion of microwave radiation into heat is very effective and occurs uniformly throughout the sample. As a result, no heat transfer from outside into the sample is required, which is particularly important for larger batches.[59]

In order to achieve a uniform distribution of the embedded MOF particles in the polymer matrix, it is advantageous if the MOF particles exhibit nanoparticle morphology, little aggregation, and have a small size distribution. Rapid heating during a microwave-assisted synthesis decreased the particle size of a MOF material in comparison with conventional heating, and also a smaller size distribution was achieved.[60] In this study we report for the first time the synthesis of $[Co_4(\mu_4\text{-}O)(Me_2pzba)_3]$ by microwave heating with good yields of up to 95%, and we were able to scale up the syntheses to 1.34 g in a single batch. Optimization concerning reaction time, temperature, and molar ratio showed nearly quantitative yields for reaction times of 1 h at 150 °C and a molar ratio of metal salt to linker of 1.5 to 1. This is far better than the average yield of 70% in the conventional solvothermal reaction.[50] The characterization of the particle morphology and size by SEM revealed that $[Co_4(\mu_4\text{-}O)(Me_2pzba)_3]$ from microwave heating is composed mostly of cubic-shaped particles with a size of 3−11 μm with little aggregation (Figure S3a,b). Conventional solvothermal heating yielded particles of 100−300 μm which were highly aggregated (Figure S3 in Supporting Information).[50] Thus, microwave heating gave particles with much less aggregation and considerably reduced particle size (Figure S3 and Figure S7). A low degree of aggregation and small particle size is important for the intended use of the material as additive in MMMs in order to achieve a uniform distribution of the MOF particles in the MMMs with no sedimentation.

The material $[Co_4(\mu_4\text{-}O)(Me_2pzba)_3]$ is stable until about 350 °C from thermogravimetric analysis, irrespective of preparation method. Up to 400 °C a slight weight loss was observed, and an abrupt weight loss occurs above 480 °C, corresponding to the decomposition of the compound (cf. Figure 6). These data are in good agreement with the earlier reported TG analysis of the solvothermal product.[50] It is known that the final decomposition of cobalt compounds with organic ligands occurs at higher temperatures up to 900 °C.[61]

The nitrogen adsorption isotherm for $[Co_4(\mu_4\text{-}O)(Me_2pzba)_3]$ is of type I (Figure S4a), typical for microporous materials.[62] The calculated Brunauer, Emmett and Teller (BET) surface area for the microwave-synthesized material is 1850 m^2/g (measured 1 day after activation), which is substantially higher than the reported value for the solvothermal product (~1070 m^2/g).[50] We trace this to an improvement in the synthesis and activation protocol. We had changed the activating solvent from ethanol to the more volatile dichloromethane (DCM) in combination with an elongated solvent equilibration time (24 h in DCM, instead of 2 h in ethanol). DFT calculations based on nitrogen adsorption measurements show two pore diameter (Figure S4b). The larger one of 14 Å matches the value for the pore size, which was determined by single-crystal diffraction.[50] The smaller value of ~6 Å corresponds to the pore windows, which also can contribute in the adsorption process (cf. Figure S1). To estimate if activation was complete, the theoretical surface area was calculated using the program CrystalExplorer[63] (see Supporting Information for details). The experimental surface area estimates are still only about half the theoretical value for the BET model and Langmuir model. Experimental N_2 sorption isotherms and BET or Langmuir surface areas derived therefrom will always suffer from defects, incomplete ligand or solvent removal, partial framework collapse or distortion, inaccessible void space, etc. Also concave bends of the inner surface will be probed incompletely by N_2 adsorption as its bent end-on adsorption will shield the nearby concave surface part from further N_2 adsorption. For example, the surface area around the pore window with a diameter of about 8.5 Å (0.002 au) or 5.5 Å (0.0003 au) (Figure S8) will be probed by a N_2 molecule at 77 K with an excepted diameter of 4.32 Å at this temperature. Thus, it is evident that only a fraction of the surface around the pore window will be covered by an N_2 molecule, while the remaining surface area will be blocked from the approach of another N_2 molecule.

In MMMs selectivity of the filler materials in gas uptake is essential to raise the selectivity above the level of the neat polymer matrix. The reported CO_2 and CH_4 adsorption isotherms of solvothermal $[Co_4(\mu_4\text{-}O)(Me_2pzba)_3]$ yielded a selectivity of 3:1.[50] CO_2 and CH_4 adsorption measurements with the microwave-synthesized compound affirm this ratio (Figure S9): The uptake at 820 mmHg of carbon dioxide (58 cm^3/g) was three times higher than the methane value (21 cm^3/g). A selectivity for CO_2 over CH_4 of 3.5:1 was determined by Henry plots of the adsorption isotherms (Figure S10 in Supporting Information). The pore diameter (14 Å) and the pore aperture size (<10 Å) in 3D-$[Co_4(\mu_4\text{-}O)(Me_2pzba)_3]$

DOI: 10.1021/acs.cgd.7b00202
Cryst. Growth Des. XXXX, XXX, XXX−XXX

(Figure S1) together with the polarizability of CO_2 and the kinetic diameters of CO_2 (3.3 Å) and CH_4 (3.8 Å) affect the gas selectivity.

For water-stability testing, especially in comparison to MOF-5, we exposed $[Co_4(\mu_4\text{-}O)(Me_2pzba)_3]$ to ambient air for 24 h and checked the crystallinity by PXRD (Figure 2). As the

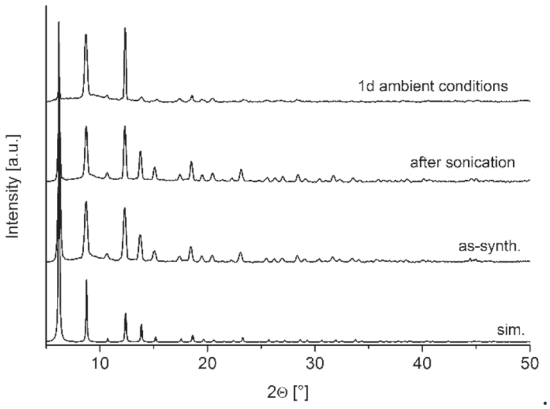

Figure 2. Powder X-ray diffractograms for $[Co_4(\mu_4\text{-}O)(Me_2pzba)_3]$ of the microwave-synthesized (as-synth.) compound, after sonication in a dichloromethane dispersion as for the MMM preparation and after exposure to ambient air conditions for 1 day with air humidity of about 50−60% in comparison with simulated diffractogram (sim., based on the X-ray data refinement, CCDC number: 937763).

porosity can be more affected by hydrolysis than the crystallinity, we also repeated the initial nitrogen sorption study the porosity characteristics after 3 weeks where the sample had been stored in a closed vessel under ambient air. We also note that samples of $[Co_4(\mu_4\text{-}O)(Me_2pzba)_3]$ were routinely handled in ambient air without special precautions. After 3 weeks in ambient air, the BET surface area was 1985 m^2/g (versus 1858 m^2/g after 1 day) and the specific pore volume was 0.73 cm^3/g (versus 0.67 cm^3/g) (Table S1, Figure S12), which can be considered identical within experimental error.

To ensure no degradation during MMM fabrication, a dispersion of $[Co_4(\mu_4\text{-}O)(Me_2pzba)_3]$ in dichloromethane was treated by sonication in the same way as for the preparation of the membrane casting mixture only without the polymer. From PXRD no change in crystallinity was apparent (Figure 2), and the BET surface area of the sonicated sample was only slightly reduced to 1777 m^2/g (Figure S12). The activation of the sonicated MOF was also carried out the same way as the activation of the MOF/polymer MMM, that is, heating to 120 °C overnight.

The hydrolytic stability of $[Co_4(\mu_4\text{-}O)(Me_2pzba)_3]$ is far better than for MOF-5. Stability investigations by Tranchemontagne et al. showed a beginning degeneration of MOF-5 within 10 min after exposure to ambient air.[54]

The classification of hydrolytic stability can be done in various ways. To prove strong hydrolytic stability, the most stressful case for MOFs is to load the degassed material with water vapor by repeated, cycling water sorption and concomitant cyclic thermal stress, e.g., by exposure to a humidified gas flow, with a partial water vapor pressure of 5.6 kPa using argon as a carrier gas, with sample temperatures varying between 40 and 140 °C for at least 40 cycles[64−68] up to several thousand cycles.[67,69] Also the material is often stirred in water for a chosen time. For $[Co_4(\mu_4\text{-}O)(Me_2pzba)_3]$, a water sorption isotherm and stirring in water for 1 h results in an amorphous material with no crystallinity. A milder way is to stir the material for 1 h in a water/DMF 1:2 mixture and to increase the amount of water by adding defined aliquots of deionized water sequentially.[70] For $[Co_4(\mu_4\text{-}O)(Me_2pzba)_3]$ the water/DMF method revealed a higher water stability in comparison to MOF-5 (Figure S11).[50,70] Tests in a 1:2 water/DMF mixture for 1 h did not show significant structural changes by PXRD but a decrease in BET surface area to 715 m^2/g occurred. For the crystallinity, pronounced decomposition is visible after 1 h in a 1:1 water/DMF mixture (Figure S11). For MOF-5, a ratio of 1:4 (water/DMF) already induces hydrolysis.[50]

The hydrothermal stability of $[Co_4(\mu_4\text{-}O)(Me_2pzba)_3]$ makes this analogue of MOF-5 more suitable for embedding in MMMs for gas separation processes.

$[Co_4(\mu_4\text{-}O)(Me_2pzba)_3]$/Matrimid MMMs. Matrimid 5218 was chosen as polymer due to its high selectivity, high thermal, and chemical resistance and commercial availability. Martimid is a well investigated polymer matrix in MMMs with MOFs as a filler material[71−73] and serves as a model polyimide to study the enhancement of separation properties upon addition of porous fillers in polyimides. The polyimide carries polar functional groups (imide, carbonyl) (Figure 3) which are good interaction sites with the surface of the MOF crystallites.

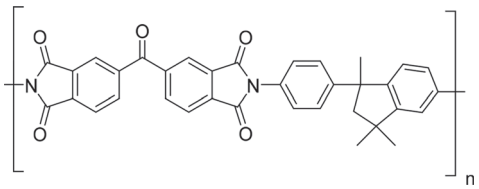

Figure 3. Structure of Matrimid.

MMMs from Matrimid and MOF-5 which were synthesized under inert conditions were reported by Perez et al. and exhibited favorable separation properties.[44] Still, the MOF-5/MMMs had to be stored under nitrogen to preserve the MOF-5 crystallinity. Unfortunately Perez et al. did not examine the stability of MOF-5 or MOF-5-MMMs regarding moisture.[44] Previous work by Tranchemontagne et al. showed degradation of MOF-5 within 10 min after expose to (humid) air.[54]

The microwave-synthesized MOF $[Co_4(\mu_4\text{-}O)(Me_2pzba)_3]$ was used to prepare MMMs with Matrimid using a priming protocol.[74] The membranes were characterized by SEM, PXRD, thermogravimetric analysis (TGA) and gas permeation. The prepared MMMs (with 8 and 16 and 24 wt % $[Co_4(\mu_4\text{-}O)(Me_2pzba)_3]$) were tested in the separation of CO_2 from mixtures of CO_2 and CH_4.

SEM images in Figure 4 and Figure 5 show the cross sections of the $[Co_4(\mu_4\text{-}O)(Me_2pzba)_3]$/Matrimid MMMs at 8, 16, and 24 wt % of the MOF in the polymer matrix. The SEM images of all membranes even with 24 wt % loading show a uniform MOF dispersion in the polymer matrix. An energy-dispersive X-ray spectroscopic (EDX) cobalt element mapping confirms the uniform distribution of the MOF particles in the MMMs (Figure 5). Particles with the element Co are evenly distributed throughout the MMM cross sections. A slight MOF sedimentation at the "bottom" of the casted membranes is revealed, shown by locally increased intensity of the mapped cobalt. There is no significant interfacial void formation around the incorporated filler particles. No MOF particles separated

DOI: 10.1021/acs.cgd.7b00202
Cryst. Growth Des. XXXX, XXX, XXX−XXX

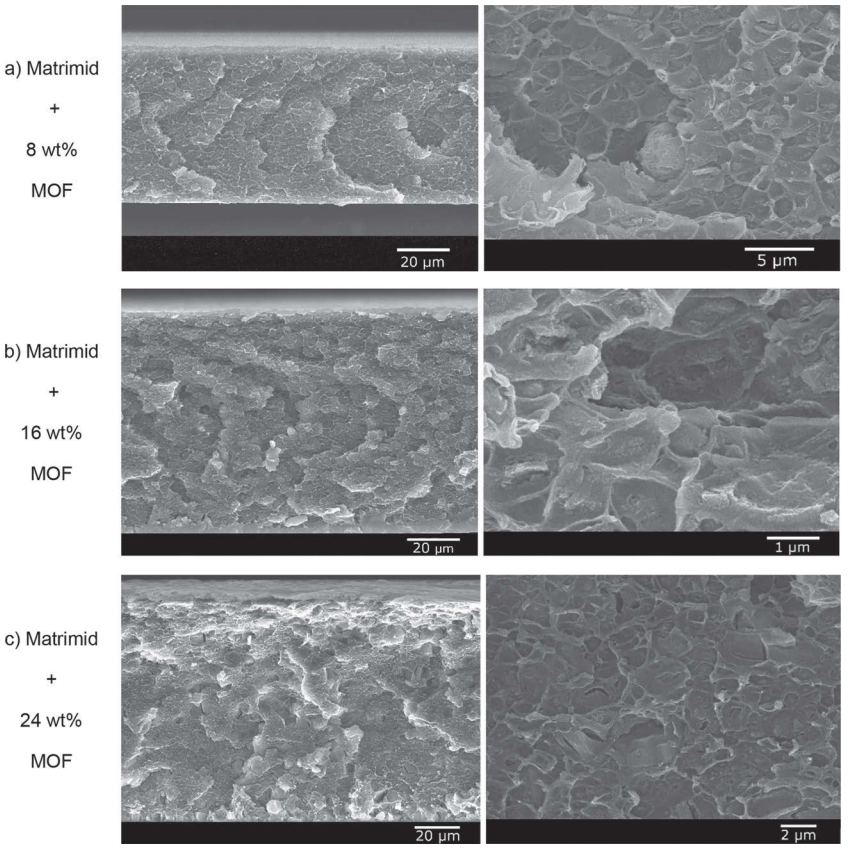

Figure 4. SEM images of cross-section of Matrimid with different loadings of $[Co_4(\mu_4\text{-}O)(Me_2pzba)_3]$ as filler (a) 8 wt %, (b) 16 wt %, (c) 24 wt %.

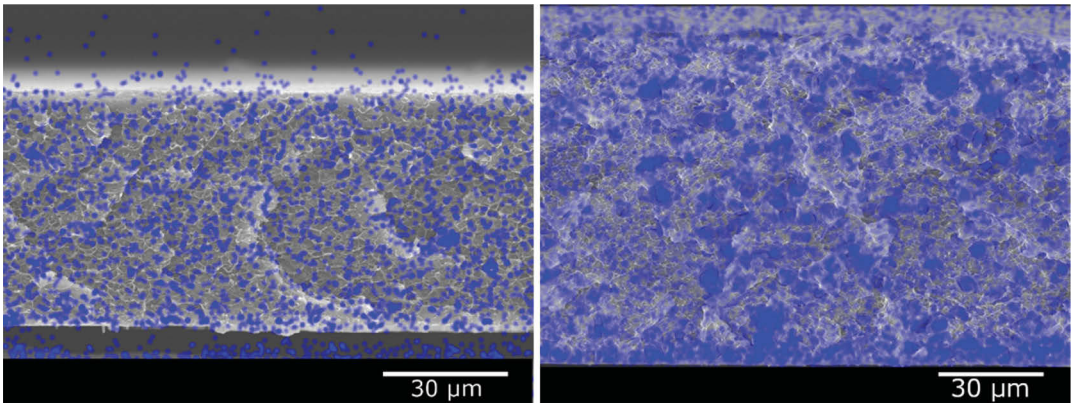

Figure 5. EDX-mapping of cobalt (blue) in MMM cross sections (left: 8 wt %, right: 24 wt % $[Co_4(\mu_4\text{-}O)(Me_2pzba)_3]$). Some detection of Co is found outside of the membrane cross section due to reflection of the electron beam on the sample holder. The bottom of the images corresponds to the bottom of the membrane when casted.

from the polymer can be seen in the cross sections which were prepared by freeze-fracturing of the membrane samples (Figure 4). This is an indicator for high affinity between MOF particles and polymer, which results in increased interfacial tension at the particle/polymer interface.[23,75]

TGA of $[Co_4(\mu_4\text{-}O)(Me_2pzba)_3]$/Matrimid indicates a good thermal stability for the prepared membranes following the average of the degradation curve of the pure MOF and pure Matrimid (Figure 6a).

The crystallinity of $[Co_4(\mu_4\text{-}O)(Me_2pzba)_3]$ is maintained during the membrane preparation procedure, as depicted in Figure 6b. The sonication and stirring steps in the priming protocol did not affect the MOF stability. Even after a 2 month exposure to ambient conditions the distinct reflections of $[Co_4(\mu_4\text{-}O)(Me_2pzba)_3]$ in the MMM are still visible. For direct comparison to the stability of a MOF-5/Matrimid MMM the compound MOF-5 was synthesized,[54] and Matrimid MMMs were prepared the exact same way as with $[Co_4(\mu_4\text{-}O)(Me_2pzba)_3]$. The as-synthesized MOF-5 product was identified by PXRD (with good agreement to the simulated pattern from single crystal data, Figure 7)[76] and a BET surface area of 3600 m^2/g (in agreement with literature values of a Langmuir surface area of 3900 m^2/g[54]). However, after incorporation of MOF-5 into Matrimid MMMs using the priming protocol under noninert conditions, degradation occurred, as depicted in Figure 7. The air stability makes the

DOI: 10.1021/acs.cgd.7b00202
Cryst. Growth Des. XXXX, XXX, XXX−XXX

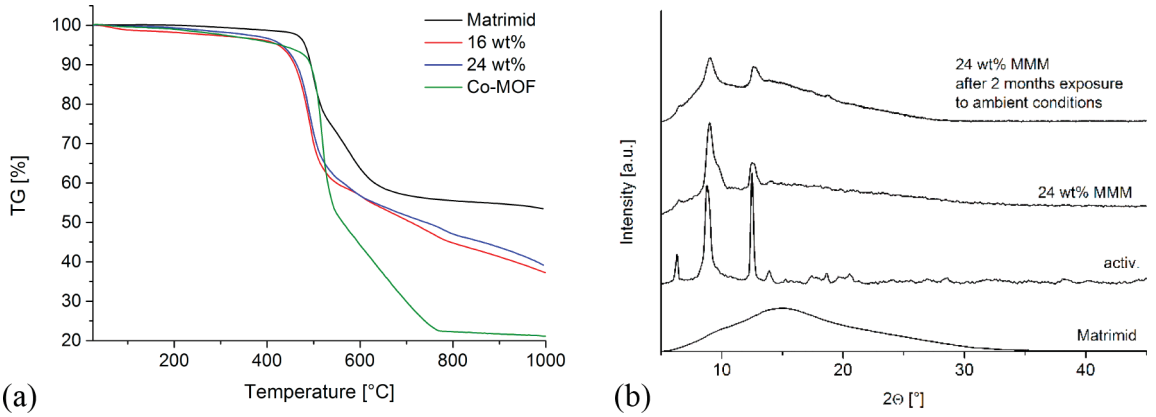

Figure 6. (a) Thermogravimetric analysis (TGA) curves of neat Matrimid, MMMs with 16 and 24 wt % and neat $[Co_4(\mu_4\text{-}O)(Me_2pzba)_3]$ (Co-MOF) under nitrogen flow at a heating rate of 5 K/min. (b) Powder X-ray diffractograms for neat Matrimid membrane, neat $[Co_4(\mu_4\text{-}O)(Me_2pzba)_3]$ (activ.), the MMM with 24 wt % of Co-MOF and after exposure to ambient air for about two months.

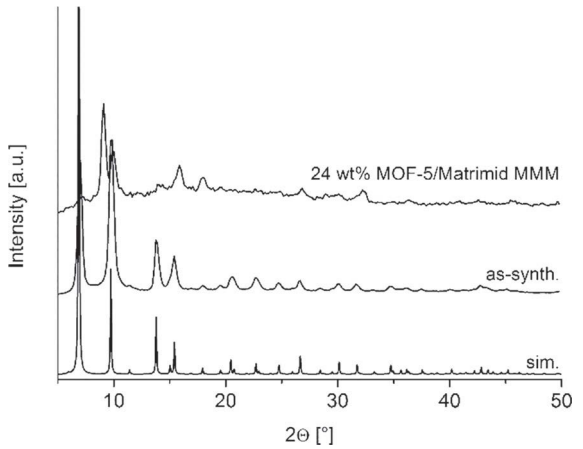

Figure 7. PXRD patterns of simulated (CCDC number: 256965), as-synthesized MOF-5 (as-synth.) and MOF-5 embedded in Matrimid under noninert conditions for stability comparison with $[Co_4(\mu_4\text{-}O)(Me_2pzba)_3]$/MMM. Clear degradation is visible after preparation of MOF-5 MMMs.

structural MOF-5 analogue $[Co_4(\mu_4\text{-}O)(Me_2pzba)_3]$ a more suitable filler for MMMs than MOF-5 itself.

Permeation Results. Single gas permeation was carried with CO_2 and CH_4 to test the intrinsic gas transport properties of the MMMs and to investigate the influence of $[Co_4(\mu_4\text{-}O)(Me_2pzba)_3]$ loadings on permeability and selectivity of the MMMs. The measurements include pure Matrimid and MMMs with 8 and 16 and 24 wt % $[Co_4(\mu_4\text{-}O)(Me_2pzba)_3]$. As shown in Table 1, all $[Co_4(\mu_4\text{-}O)(Me_2pzba)_3]$/Matrimid mixed-matrix membranes exhibited performance superior to the unfilled neat Matrimid membrane even when used two months after preparation and storage under ambient air conditions. The single gas permeation experiments were always repeated under the same conditions (30 °C, 3 bar transmembrane pressure difference), to ensure reproducibility of the results. A strong increase in CO_2 permeability and a lesser increase in CH_4 permeability with MOF loading leads to an enhanced ideal CO_2/CH_4 selectivity with increasing MOF content reaching a separation factor $S_{ij,ideal}$ of 60 ± 4 for CO_2/CH_4 at 24 wt % MOF loading. The CO_2 permeability of 22.8 ± 0.2 Barrer for the 24 wt % MMM is more than a 2-fold increase compared to the unfilled neat Matrimid membrane.

To evaluate the practical separation performance of the MMMs, mixed-gas permeation tests for the separation of CO_2 from a 50:50 v:v CO_2/CH_4 mixture at 25 °C and a transmembrane pressure of 3 bar were performed. CO_2 permeability and CO_2/CH_4 mixed-gas selectivity results for the prepared membranes are displayed in Figure 8 and Table 2. The mixed-gas CO_2 permeability of the membranes was slightly reduced compared to their corresponding single gas permeability. This is due to the effect of permeate competition from the competitive sorption and diffusion of both gases.[77] We can rule out plastization. Plastization is the phenomenon that the

Table 1. Single Gas Permeabilities of $[Co_4(\mu_4\text{-}O)(Me_2pzba)_3]$/Matrimid MMMs[a]

MOF-loading [wt %]	P (CO_2)[b] [Barrer]	P (CH_4)[b] [Barrer]	S_{ideal} (CO_2/CH_4)[c]
0	9.9 ± 0.1	0.28 ± 0.01	36 ± 1
8	15.4 ± 0.1	0.40 ± 0.03	38 ± 3
16	18.5 ± 0.1	0.45 ± 0.03	41 ± 3
24	22.8 ± 0.2	0.38 ± 0.04	60 ± 4

[a]Measured at 30 °C and 3 bar transmembrane pressure. [b]Permeability. [c]Selectivity.

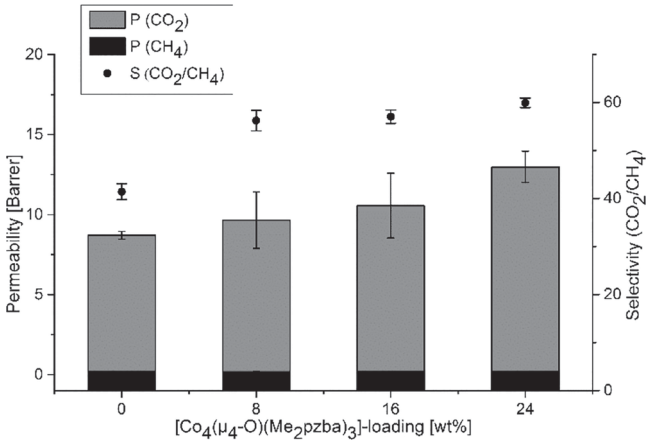

Figure 8. Performance of $[Co_4(\mu_4\text{-}O)(Me_2pzba)_3]$/Matrimid MMMs with different $[Co_4(\mu_4\text{-}O)(Me_2pzba)_3]$ loadings in the separation of CO_2 from a 50:50 v:v CO_2/CH_4 mixture at 25 °C and a transmembrane pressure of 3 bar. Error bars correspond to standard deviations. P = Permeability. S = Selectivity.

DOI: 10.1021/acs.cgd.7b00202
Cryst. Growth Des. XXXX, XXX, XXX−XXX

Table 2. Summary of $[Co_4(\mu_4\text{-}O)(Me_2pzba)_3]$/Matrimid MMM Performance for the CO_2 Separation of a CO_2/CH_4 50:50 v:v Mixture at 25 °C[a]

membrane					
MOF-loading [wt %]	membrane thickness [μm]	P (CO_2)[b] [Barrer]	P (CH_4)[b] [Barrer]	S_{real}[c] (CO_2/CH_4)	α (CO_2/CH_4)[d]
0	59−61	8.7 ± 0.2	0.21 ± 0.00	41 ± 2	42 ± 2
8	59−74	9.7 ± 1.8	0.17 ± 0.03	56 ± 2	57 ± 2
16	65−85	10.6 ± 2.0	0.18 ± 0.03	57 ± 1	58 ± 1
24	90−74	13.0 ± 1.0	0.22 ± 0.01	60 ± 1	61 ± 1

[a]The data were obtained with a pressure difference (transmembrane pressure) of 3 bar. Permeate side at atmospheric pressure with helium as sweep gas. [b]Permeability. [c]Selectivity. [d]Separation factor.

permeability of both components increases and the selectivity decreases caused by an increase in the segmental motion of polymer chains at high feed pressures due to the presence of one or more sorbates.[78] Plasticization of Matrimid occurs above a feed pressure of 12 bar, which is clearly higher than the feed pressures used in this report.[77] Up to a plastization pressure of 12 bar the reverse happens, with the permeability being reduced with rising feed pressure.[79]

Also the mixed-gas selectivity of the $[Co_4(\mu_4\text{-}O)(Me_2pzba)_3]$/Matrimid MMMs increased with filler loading to a selectivity of 60 for CO_2/CH_4 with a CO_2 permeability of 13 Barrer for MMMs with 24 wt % of $[Co_4(\mu_4\text{-}O)(Me_2pzba)_3]$. This confirms the cumulative effect of $[Co_4(\mu_4\text{-}O)(Me_2pzba)_3]$ by selective adsorption of CO_2 over CH_4 in the MMMs during the separation process, thereby enhancing the solubility of CO_2 in the membrane material and increasing its permeability.

The performance of polymer membranes, pure MOF membranes, and MMMs depends to a considerable extent on the sorption selectivity of the materials used. For the MOFs used in pure MOF membranes or MMMs, the sorption selectivity can be determined by means of sorption measurements of the different gases. For the separation problem of carbon dioxide and methane, MOF-5 proves to be an excellent separating agent due to its very high adsorption selectivity of $S(CO_2/CH_4)$ = 16. Additionally single gas permeation experiments through MOF-5/poly(ether imide) MMMs revealed that concomitant with the increase in CO_2 and CH_4 permeability with MOF loading the solubility coefficient increased more than did the diffusivity coefficient of the gas through the MMM. At the same time the gas solubility was higher for CO_2 than for CH_4.[46] Experiments with pure MOF-5 membranes which were synthesized on macroporous support material and characterized by single gas permeation experiments showed Knudsen diffusion behavior; that is, the diffusion properties were based on the pore size of MOF-5. A slight deviation from the ideal Knudsen behavior was detected, which was traced to microdefects in the membranes.[42,43] MMMs from 30 wt % MOF-5 in Matrimid showed an increased permeability of about 120% for carbon dioxide compared to pure Matrimid membranes with constant selectivity for CO_2/CH_4 in gas separation processes.[44] MOF-5/Ultem 1000 MMMs exhibited an increased carbon dioxide permeability by 50% with a mass fraction of 20 wt % of MOF-5, and slightly decreased selectivity.[45] MMMs with 25 wt % MOF-5 in a poly(ether imide) matrix show an increased permeability of carbon dioxide by more than 300% with simultaneous increase in selectivity for CO_2/CH_4 separation from 18 for pure PEI to 23.[46]

A summary of the separation characteristics of the $[Co_4(\mu_4\text{-}O)(Me_2pzba)_3]$/Matrimid with 3D-MOF/Matrimid MMMs from the literature compared to the Robeson upper bound of 2008 is shown in Figure 9 and Table 3.

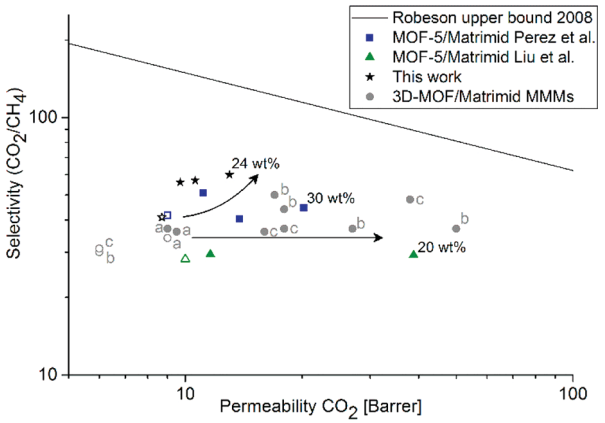

Figure 9. Comparative plot of permeabilities and selectivities of MOF-5-type/Matrimid MMMs and other MOF MMMs relative to the Robeson upper bound of 2008. Data obtained for MOF-5/Matrimid Liu et al. from ref 45 and MOF-5/Matrimid Perez et al. from ref 44, both from single-gas measurements. The mixed gas permeation data for other MOF MMMs is obtained for NH_2-MIL-53 and NH_2-MIL-101 (a) from ref 80, for MIL-125 and NH_2-MIL125 (b) from ref 71, for UiO-66 and derivatives (c) from ref 72. Data from this work is from mixed-gas measurements. Filled symbols correspond to MMMs, unfilled symbols to neat Matrimid membranes.

The $[Co_4(\mu_4\text{-}O)(Me_2pzba)_3]$/Matrimid MMMs showed an improved selectivity over MOF-5/Matrimid MMMs in the direction of the upper bound compared to the pure polymer; thus the separation properties were improved. The selectivity and separation potential of $[Co_4(\mu_4\text{-}O)(Me_2pzba)_3]$/Matrimid MMMs increased with the MOF mass fractions. The real selectivity for CO_2/CH_4 separation from mixed-gas measurements increased by 46% in $[Co_4(\mu_4\text{-}O)(Me_2pzba)_3]$/Matrimid MMMs for 3 bar transmembrane pressure and CO_2 permeability increased by 49% compared to the neat Matrimid membrane. The MMM from 24 wt % $[Co_4(\mu_4\text{-}O)(Me_2pzba)_3]$ and Matrimid has moved into the direction of the Robeson upper bound.

Other 3D-MOFs as fillers in Matrimid MMMs are also well investigated for the separation of CO_2/CH_4 mixtures. NH_2-MIL-53 and NH_2-MIL-101 give moderate improvement with respect to the neat Matrimid membrane at similar operating conditions.[80] On the other hand the mixed gas selectivity and permeability are significantly increased when the membrane is filled with NH_2-MIL-125. At 15 wt % loading a selectivity of 50 is reached, higher loadings further increase permeability but lose some selectivity.[71] The incorporation of UiO-66 in Matrimid results both in better permeation rates and separation factors. This is slightly more pronounced for the use of the amine functionalized UiO-66 and can be further increased when 4-aminobenzoic acid (ABA) is used as a modulator

DOI: 10.1021/acs.cgd.7b00202
Cryst. Growth Des. XXXX, XXX, XXX−XXX

Table 3. Comparison of MOF/Matrimid MMMs

filler	MOF-loading (wt %)	P^a (CO_2) [Barrer]	P^a (CH_4) [Barrer]	S^b (CO_2/CH_4)	temp [°C]	pressure diff^c [bar]	ref
none (neat Matrimid)	0	9.0	0.22	42	35	2	44
MOF-5[d]	10	11.1	0.22	51			
MOF-5[d]	20	13.8	0.34	41			
MOF-5[d]	30	20.2	0.45	45			
none (neat Matrimid)	0	10.0	0.36	28	50	7	45
nano-MOF-5[e]	20	11.6	0.39	29			
MOF-5[e]	20	38.8	1.33	29			
none (neat Matrimid)	0	9	n.a.	34	35	3	80
NH_2-MIL-53	25	9	n.a.	37			
NH_2-MIL-101	25	9.5	n.a.	36			
none (neat Matrimid)	0	6	n.a.	30	35	9	71
MIL-125	15	18	n.a.	44			
MIL-125	30	27	n.a.	37			
NH_2-MIL-125	15	17	n.a.	50			
NH_2-MIL-125	30	50	n.a.	37			
none (neat Matrimid)	0	6	n.a.	31	35	9	72
UiO-66	30	16	n.a.	36			
NH_2-UiO-66	30	18	n.a.	37			
NH_2-UiO-66-ABA	30	38	n.a.	48			
none (neat Matrimid)	0	8.7	0.21	41	25	3	this work
$[Co_4(\mu_4\text{-}O)(Me_2pzba)_3]$	8	9.7	0.17	56			
$[Co_4(\mu_4\text{-}O)(Me_2pzba)_3]$	16	10.6	0.18	57			
$[Co_4(\mu_4\text{-}O)(Me_2pzba)_3]$	24	13.0	0.22	60			

[a]Permeability. [b]Selectivity. [c]Transmembrane pressure. [d]MMM preparation under inert conditions, single gas permeability and ideal selectivity. [e]MMM preparation specified with dry MOF-material, single gas permeability and ideal selectivity.

during the NH_2-UiO-66 synthesis to prepare NH_2-UiO-66-ABA/Matrimid MMMs.[72]

Higher selectivities can be achieved for Matrimid-based MMMs (up to 80 at low filler loadings), when the morphology of the MOF is engineered toward "two-dimensional (2D)" nanosheets to function as 2D sieve sheets. Such was shown for the MOF of Cu-benzene dicarboxylate where the 2D sheets were at the same time oriented perpendicular to the direction of diffusion, which results in repeated gas discrimination events by the MOF nanosheets, contributing to higher separation selectivity.[81]

High performing MMMs can be produced when polymers with better intrinsic CO_2 separation properties are used as membrane matrix, with the potential to surpass the Robeson upper bound.[8,82] Examples are MOF MMMs from 4,4′-(hexafluoroisopropylidene)diphthalic anhydride (6FDA) containing polyimides,[32,83] PIM-1[84,85] (polymer with intrinsic microporosity), and Pebax[86] (poly(amide-*b*-ethylene oxide)).

CONCLUSIONS

In summary the synthesis of the MOF-5 analogue 3D-$[Co_4(\mu_4\text{-}O)(Me_2pzba)_3]$ was improved by microwave heating over conventional hydrothermal synthesis concerning yield, reaction time, BET surface area, smaller size, and less aggregation. The control of the particle size and shape of MOF fillers has been shown to be crucial for the preparation of MOF MMMs with improved separation properties.[81,87] Thereby the choice of the MOF preparation method gives the possibility to access the full potential of a MOF material by preventing MOF particle aggregation and improve distribution and orientation of the filler. In this work the choice of microwave heating could generate nonaggregated MOF particles compared to the conventional solvothermal synthesis method. Microwave-assisted heating also proved to be a powerful tool for the preparation of smaller MOF particles and the upscaling of the MOF synthesis. Synthesis methods to influence the growth and porosity of MOFs have been the subject of recent reviews.[88] The use of these methods to produce application-adapted particles should have great potential to optimize the morphology of MOF fillers in MMMs regarding performance and applicability.

Further $[Co_4(\mu_4\text{-}O)(Me_2pzba)_3]$ showed a significantly increased moisture stability compared to MOF-5. In $[Co_4(\mu_4\text{-}O)(Me_2pzba)_3]$/Matrimid MMMs the SEM images in combination with EDX cobalt element mapping showed that the MOF particles were uniformly embedded in the polymer, with good MOF−polymer compatibility which was affirmed by the improved CO_2/CH_4 separation performance of the MMMs over neat Matrimid membranes. The $[Co_4(\mu_4\text{-}O)(Me_2pzba)_3]$ containing membranes show an increase of more than 46% in CO_2/CH_4 selectivity for 24 wt % filler loading and 3 bar transmembrane pressure relative to the pure Matrimid membrane, together with an enhanced permeability of 49% for CO_2.

For moisture-sensitive MOFs with labile metal−ligand bonds, an intensive characterization of the filler material is necessary to ascertain whether the permselectivity effect of the MOF material is indeed due to its still existing porosity. Therefore, it is important to ensure whether the MOF characteristics, especially porosity, are maintained in the final MMM material by treating the MOF in the absence of polymer identical to the MMM formation and verifying retention of its properties.

ASSOCIATED CONTENT

Supporting Information

The Supporting Information is available free of charge on the ACS Publications website at DOI: 10.1021/acs.cgd.7b00202.

DOI: 10.1021/acs.cgd.7b00202
Cryst. Growth Des. XXXX, XXX, XXX−XXX

Synthesis of 3,5-dimethyl-4-(4-carboxyphenyl)-1*H*-pyrazole; synthesis and characterization of $[Co_4(\mu_4\text{-}O)(Me_2pzba)_3]$ and MOF-5, SEM and particle size histogram of $[Co_4(\mu_4\text{-}O)(Me_2pzba)_3]$ from microwave and conventional synthesis, details of gas adsorption and permeation experiments, gas selectivity from CO_2 and CH_4 adsorption isotherms, calculation of theoretical surface area (PDF)

AUTHOR INFORMATION

Corresponding Author

*E-mail: janiak@hhu.de.

ORCID

Christoph Janiak: 0000-0002-6288-9605

Notes

The authors declare no competing financial interest.

ACKNOWLEDGMENTS

Support of the work by BMBF Project OptiMat 03SF0492C and from the Anton-Betz foundation is gratefully acknowledged.

REFERENCES

(1) Buonomenna, M. G. *RSC Adv.* **2013**, *3*, 5694−5740.
(2) Strathmann, H. *AIChE J.* **2001**, *47*, 1077−1087.
(3) Koros, W. J.; Mahajan, R. *J. Membr. Sci.* **2000**, *175*, 181−196.
(4) D'Alessandro, D. M.; Smit, B.; Long, J. R. *Angew. Chem.* **2010**, *122*, 6194−6219.
(5) Robeson, L. M. *J. Membr. Sci.* **1991**, *62*, 165−185.
(6) Robeson, L. M. *J. Membr. Sci.* **2008**, *320*, 390−400.
(7) Shan, M.; Seoane, B.; Rozhko, E.; Dikhtiarenko, A.; Clet, G.; Kapteijn, F.; Gascon, J. *Chem. - Eur. J.* **2016**, *22*, 14467−14470.
(8) Seoane, B.; Coronas, J.; Gascon, I.; Benavides, M. E.; Karvan, O.; Caro, J.; Kapteijn, F.; Gascon, J. *Chem. Soc. Rev.* **2015**, *44*, 2421−2454.
(9) Noble, R. D. *J. Membr. Sci.* **2011**, *378*, 393−397.
(10) Li, J.-R.; Ma, Y.; McCarthy, M. C.; Sculley, J.; Yu, J.; Jeong, H.-K.; Balbuena, P. B.; Zhou, H.-C. *Coord. Chem. Rev.* **2011**, *255*, 1791−1823.
(11) Liu, D.; Zhong, C. *J. Mater. Chem.* **2010**, *20*, 10308−10318.
(12) Meek, S. T.; Greathouse, J. A.; Allendorf, M. D. *Adv. Mater.* **2011**, *23*, 249−267.
(13) Bae, T. H.; Lee, J. S.; Qiu, W.; Koros, W. J.; Jones, C. W.; Nair, S. *Angew. Chem., Int. Ed.* **2010**, *49*, 9863−9866.
(14) Rebollar-Perez, G.; Carretier, E.; Lesage, N.; Moulin, P. *Membranes* **2011**, *1*, 80−90.
(15) Dumee, L.; Velleman, L.; Sears, K.; Hill, M.; Schutz, J.; Finn, N.; Duke, M.; Gray, S. *Membranes* **2011**, *1*, 25−36.
(16) Chung, T.-S.; Jiang, L. Y.; Li, Y.; Kulprathipanja, S. *Prog. Polym. Sci.* **2007**, *32*, 483−507.
(17) Tanh Jeazet, H. B.; Staudt, C.; Janiak, C. *Dalton Trans.* **2012**, *41*, 14003−14027.
(18) Hunger, K.; Schmeling, N.; Tanh Jeazet, H. B.; Janiak, C.; Staudt, C.; Kleinermanns, K. *Membranes* **2012**, *2*, 727−763.
(19) Tanh Jeazet, H. B.; Janiak, C. Metal-Organic Frameworks in Mixed-Matrix Membranes. In *Metal-Organic Framework Materials*; MacGillivray, L. R., Lukehart, C., Eds.; John Wiley & Sons: Chichester UK, 2014; pp 1−15.
(20) Zornoza, B.; Téllez, C.; Coronas, J.; Gascon, J.; Kapteijn, F. *Microporous Mesoporous Mater.* **2013**, *166*, 67−78.
(21) Bastani, D.; Esmaeili, N.; Asadollahi, M. *J. Ind. Eng. Chem.* **2013**, *19*, 375−393.
(22) Dong, G.; Li, H.; Chen, V. *J. Mater. Chem. A* **2013**, *1*, 4610−4630.
(23) Ordoñez, M. J. C.; Balkus, K. J., Jr; Ferraris, J. P.; Musselman, I. H. *J. Membr. Sci.* **2010**, *361*, 28−37.
(24) Dai, Y.; Johnson, J. R.; Karvan, O.; Sholl, D. S.; Koros, W. J. *J. Membr. Sci.* **2012**, *401−402*, 76−82.
(25) Zheng, D.; Liu, X.; Hu, D.; Li, M.; Zhang, J.; Zeng, G.; Zhang, Y.; Sun, Y. *RSC Adv.* **2014**, *4*, 10140−10143.
(26) Buonomenna, M. G.; Yave, W.; Golemme, G. *RSC Adv.* **2012**, *2*, 10745−10773.
(27) Chen, X. Y.; Vinh-Thang, H.; Rodrigue, D.; Kaliaguine, S. *RSC Adv.* **2014**, *4*, 12235−12244.
(28) Sorribas, S.; Zornoza, B.; Téllez, C.; Coronas, J. *J. Membr. Sci.* **2014**, *452*, 184−192.
(29) Burmann, P.; Zornoza, B.; Téllez, C.; Coronas, J. *Chem. Eng. Sci.* **2014**, *107*, 66−75.
(30) Chen, X. Y.; Vinh-Thang, H.; Rodrigue, D.; Kaliaguine, S. *Ind. Eng. Chem. Res.* **2012**, *51*, 6895−6906.
(31) Seoane, B.; Zamaro, J. M.; Téllez, C.; Coronas, J. *RSC Adv.* **2011**, *1*, 917−922.
(32) Chen, X. Y.; Hoang, V.-T.; Rodrigue, D.; Kaliaguine, S. *RSC Adv.* **2013**, *3*, 24266−24279.
(33) Batten, S. R.; Champness, N. R.; Chen, X.-M.; Garcia-Martinez, J.; Kitagawa, S.; Öhrström, L.; O'Keeffe, M.; Paik Suh, M.; Reedijk, J. *Pure Appl. Chem.* **2013**, *85*, 1715.
(34) Batten, S. R.; Champness, N. R.; Chen, X.-M.; Garcia-Martinez, J.; Kitagawa, S.; Öhrström, L.; O'Keeffe, M.; Suh, M. P.; Reedijk, J. *CrystEngComm* **2012**, *14*, 3001−3004.
(35) Lee, J.; Farha, O. K.; Roberts, J.; Scheidt, K. A.; Nguyen, S. T.; Hupp, J. T. *Chem. Soc. Rev.* **2009**, *38*, 1450−1459.
(36) Horcajada, P.; Gref, R.; Baati, T.; Allan, P. K.; Maurin, G.; Couvreur, P.; Férey, G.; Morris, R. E.; Serre, C. *Chem. Rev.* **2012**, *112*, 1232−1268.
(37) Long, J. R.; Yaghi, O. M. *Chem. Soc. Rev.* **2009**, *38*, 1213−1214.
(38) Janiak, C. *Dalton Trans.* **2003**, 2781−2804.
(39) Janiak, C.; Vieth, J. K. *New J. Chem.* **2010**, *34*, 2366−2388.
(40) Zhang, Z.; Zhao, Y.; Gong, Q.; Li, Z.; Li, J. *Chem. Commun.* **2013**, *49*, 653−661.
(41) Kitagawa, S.; Kitaura, R.; Noro, S.-i. *Angew. Chem., Int. Ed.* **2004**, *43*, 2334−2375.
(42) Yoo, Y.; Lai, Z.; Jeong, H.-K. *Microporous Mesoporous Mater.* **2009**, *123*, 100−106.
(43) Liu, Y.; Ng, Z.; Khan, E. A.; Jeong, H.-K.; Ching, C.-b.; Lai, Z. *Microporous Mesoporous Mater.* **2009**, *118*, 296−301.
(44) Perez, E. V.; Balkus, K. J., Jr; Ferraris, J. P.; Musselman, I. H. *J. Membr. Sci.* **2009**, *328*, 165−173.
(45) Liu, C.; McCulloch, B.; Wilson, S. T.; Benin, A. I.; Schott, M. E. Metal organic framework—polymer mixed matrix membranes. US 7.637.983 B1, December 29, 2009.
(46) Arjmandi, M.; Pakizeh, M. *J. Ind. Eng. Chem.* **2014**, *20*, 3857−3868.
(47) Kaye, S. S.; Dailly, A.; Yaghi, O. M.; Long, J. R. *J. Am. Chem. Soc.* **2007**, *129*, 14176−14177.
(48) Zhang, J.-P.; Zhang, Y.-B.; Lin, J.-B.; Chen, X.-M. *Chem. Rev.* **2012**, *112*, 1001−1033.
(49) Zhu, A.-X.; Lin, R.-B.; Qi, X.-L.; Liu, Y.; Lin, Y.-Y.; Zhang, J.-P.; Chen, X.-M. *Microporous Mesoporous Mater.* **2012**, *157*, 42−49.
(50) Heering, C.; Boldog, I.; Vasylyeva, V.; Sanchiz, J.; Janiak, C. *CrystEngComm* **2013**, *15*, 9757−9768.
(51) Padial, N. M.; Quartapelle Procopio, E.; Montoro, C.; López, E.; Oltra, J. E.; Colombo, V.; Maspero, A.; Masciocchi, N.; Galli, S.; Senkovska, I.; Kaskel, S.; Barea, E.; Navarro, J. A. R. *Angew. Chem.* **2013**, *125*, 8448−8452.
(52) Montoro, C.; Linares, F.; Quartapelle Procopio, E.; Senkovska, I.; Kaskel, S.; Galli, S.; Masciocchi, N.; Barea, E.; Navarro, J. A. R. *J. Am. Chem. Soc.* **2011**, *133*, 11888−11891.
(53) Bryant, M. R.; Burrows, A. D.; Fitchett, C. M.; Hawes, C. S.; Hunter, S. O.; Keenan, L. L.; Kelly, D. J.; Kruger, P. E.; Mahon, M. F.; Richardson, C. *Dalton Trans.* **2015**, *44*, 9269−9280.
(54) Tranchemontagne, D. J.; Hunt, J. R.; Yaghi, O. M. *Tetrahedron* **2008**, *64*, 8553−8557.
(55) Hillock, A. M. W.; Miller, S. J.; Koros, W. J. *J. Membr. Sci.* **2008**, *314*, 193−199.

DOI: 10.1021/acs.cgd.7b00202
Cryst. Growth Des. XXXX, XXX, XXX−XXX

(56) Eddaoudi, M.; Kim, J.; Rosi, N.; Vodak, D.; Wachter, J.; O'Keeffe, M.; Yaghi, O. M. *Science* **2002**, *295*, 469−472.
(57) Stavitski, E.; Goesten, M.; Juan-Alcañiz, J.; Martinez-Joaristi, A.; Serra-Crespo, P.; Petukhov, A. V.; Gascon, J.; Kapteijn, F. *Angew. Chem., Int. Ed.* **2011**, *50*, 9624−9628.
(58) Zornoza, B.; Martinez-Joaristi, A.; Serra-Crespo, P.; Téllez, C.; Coronas, J.; Gascon, J.; Kapteijn, F. *Chem. Commun.* **2011**, *47*, 9522−9524.
(59) Taddei, M.; Dau, P. V.; Cohen, S. M.; Ranocchiari, M.; van Bokhoven, J. A.; Costantino, F.; Sabatini, S.; Vivani, R. *Dalton Trans.* **2015**, *44*, 14019−14026.
(60) Liu, B.; Zou, R.-Q.; Zhong, R.-Q.; Han, S.; Shioyama, H.; Yamada, T.; Maruta, G.; Takeda, S.; Xu, Q. *Microporous Mesoporous Mater.* **2008**, *111*, 470−477.
(61) Tang, C.-W.; Wang, C.-B.; Chien, S.-H. *Thermochim. Acta* **2008**, *473*, 68−73.
(62) Thommes, M.; Kaneko, K.; Neimark, A. V.; Olivier, J. P.; Rodriguez-Reinoso, F.; Rouquerol, J.; Sing, K. S. W. *Pure Appl. Chem.* **2015**, *87*, 1051−1069.
(63) Turner, M. J.; McKinnon, J. J.; Jayatilaka, D.; Spackman, M. A. *CrystEngComm* **2011**, *13*, 1804−1813.
(64) Jeremias, F.; Khutia, A.; Henninger, S. K.; Janiak, C. *J. Mater. Chem.* **2012**, *22*, 10148−10151.
(65) Jeremias, F.; Lozan, V.; Henninger, S. K.; Janiak, C. *Dalton Trans.* **2013**, *42*, 15967−15973.
(66) Jeremias, F.; Fröhlich, D.; Janiak, C.; Henninger, S. K. *New J. Chem.* **2014**, *38*, 1846−1852.
(67) Jeremias, F.; Fröhlich, D.; Janiak, C.; Henninger, S. K. *RSC Adv.* **2014**, *4*, 24073−24082.
(68) Fröhlich, D.; Henninger, S. K.; Janiak, C. *Dalton Trans.* **2014**, *43*, 15300−15304.
(69) Fröhlich, D.; Pantatosaki, E.; Kolokathis, P. D.; Markey, K.; Reinsch, H.; Baumgartner, M.; van der Veen, M. A.; De Vos, D. E.; Stock, N.; Papadopoulos, G. K.; Henninger, S. K.; Janiak, C. *J. Mater. Chem. A* **2016**, *4*, 11859−11869.
(70) Cychosz, K. A.; Matzger, A. J. *Langmuir* **2010**, *26*, 17198−17202.
(71) Waqas Anjum, M. W.; Bueken, B.; De Vos, D.; Vankelecom, I. F. J. *J. Membr. Sci.* **2016**, *502*, 21−28.
(72) Anjum, M. W.; Vermoortele, F.; Khan, A. L.; Bueken, B.; De Vos, D. E.; Vankelecom, I. F. J. *ACS Appl. Mater. Interfaces* **2015**, *7*, 25193−25201.
(73) Venna, S. R.; Lartey, M.; Li, T.; Spore, A.; Kumar, S.; Nulwala, H. B.; Luebke, D. R.; Rosi, N. L.; Albenze, E. *J. Mater. Chem. A* **2015**, *3*, 5014−5022.
(74) Mahajan, R.; Koros, W. J. *Ind. Eng. Chem. Res.* **2000**, *39*, 2692−2696.
(75) Naseri, M.; Mousavi, S. F.; Mohammadi, T.; Bakhtiari, O. *J. Ind. Eng. Chem.* **2015**, *29*, 249−256.
(76) Li, H.; Eddaoudi, M.; O'Keeffe, M.; Yaghi, O. M. *Nature* **1999**, *402*, 276−279.
(77) Dong, G.; Li, H.; Chen, V. *J. Membr. Sci.* **2011**, *369*, 206−220.
(78) Wind, J. D.; Staudt-Bickel, C.; Paul, D. R.; Koros, W. J. *Ind. Eng. Chem. Res.* **2002**, *41*, 6139−6148.
(79) Bos, A.; Pünt, I. G. M.; Wessling, M.; Strathmann, H. *J. Membr. Sci.* **1999**, *155*, 67−78.
(80) Rodenas, T.; van Dalen, M.; Serra-Crespo, P.; Kapteijn, F.; Gascon, J. *Microporous Mesoporous Mater.* **2014**, *192*, 35−42.
(81) Rodenas, T.; Luz, I.; Prieto, G.; Seoane, B.; Miro, H.; Corma, A.; Kapteijn, F.; Llabrés i Xamena, F. X.; Gascon, J. *Nat. Mater.* **2015**, *14*, 48−55.
(82) Dechnik, J.; Gascon, J.; Doonan, C.; Janiak, C.; Sumby, C. J. *Angew. Chem., Int. Ed.* **2017**, http://dx.doi.org/10.1002/anie.201701109.
(83) Tien-Binh, N.; Vinh-Thang, H.; Chen, X. Y.; Rodrigue, D.; Kaliaguine, S. *J. Mater. Chem. A* **2015**, *3*, 15202−15213.
(84) Bushell, A. F.; Attfield, M. P.; Mason, C. R.; Budd, P. M.; Yampolskii, Y.; Starannikova, L.; Rebrov, A.; Bazzarelli, F.; Bernardo, P.; Carolus Jansen, J.; Lanč, M.; Friess, K.; Shantarovich, V.; Gustov, V.; Isaeva, V. *J. Membr. Sci.* **2013**, *427*, 48−62.
(85) Khdhayyer, M. R.; Esposito, E.; Fuoco, A.; Monteleone, M.; Giorno, L.; Jansen, J. C.; Attfield, M. P.; Budd, P. M. *Sep. Purif. Technol.* **2017**, *173*, 304−313.
(86) Li, T.; Pan, Y.; Peinemann, K.-V.; Lai, Z. *J. Membr. Sci.* **2013**, *425-426*, 235−242.
(87) Sabetghadam, A.; Seoane, B.; Keskin, D.; Duim, N.; Rodenas, T.; Shahid, S.; Sorribas, S.; Guillouzer, C. L.; Clet, G.; Téllez, C.; Daturi, M.; Coronas, J.; Kapteijn, F.; Gascon, J. *Adv. Funct. Mater.* **2016**, *26*, 3154−3163.
(88) Seoane, B.; Castellanos, S.; Dikhtiarenko, A.; Kapteijn, F.; Gascon, J. *Coord. Chem. Rev.* **2016**, *307*, 147−187.

DOI: 10.1021/acs.cgd.7b00202
Cryst. Growth Des. XXXX, XXX, XXX−XXX

Supporting Information for

Mixed-matrix membranes of the air-stable MOF-5 analog $[Co_4(\mu_4\text{-}O)(Me_2pzba)_3]$ with mixed-functional pyrazolate-carboxylate linker for CO_2/CH_4 separation

Janina Dechnik, Alexander Nuhnen, Christoph Janiak*

Institut für Anorganische Chemie und Strukturchemie, Heinrich-Heine Universität Düsseldorf, 40204 Düsseldorf, Germany,

J. Dechnik Janina.Dechnik@hhu.de

A. Nuhnen Alexander.Nuhnen@hhu.de

C. Janiak janiak@hhu.de

Content

1. Structural details of $[Co_4(\mu_4\text{-}O)(Me_2pzba)_3]$

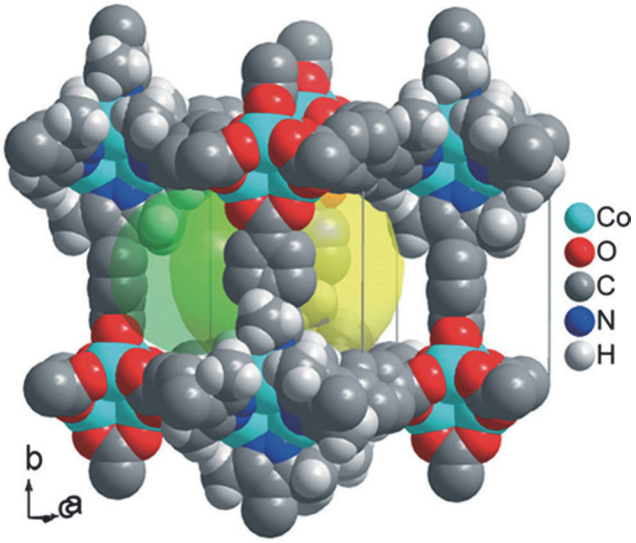

Figure S1. Space-filling plot of 3D-$[Co_4(\mu_4\text{-}O)(Me_2pzba)_3]$ showing the large cavity (yellow transparent sphere, Ø = 14 Å) and one of the pore apertures (green transparent sphere, Ø = ~10 Å). Figures reproduced with permission from ref.[1] Copyright The Royal Society of Chemistry.

2. Synthesis of 3,5-dimethyl-4-(4-carboxyphenyl)-1H-pyrazole.

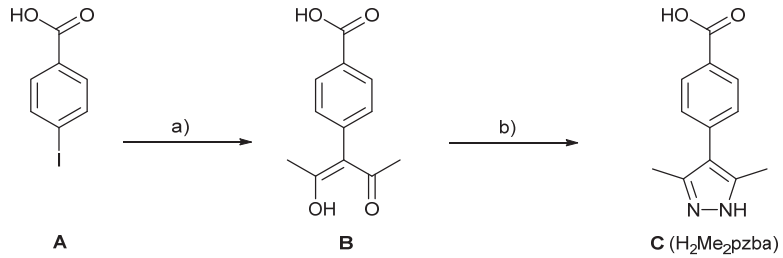

Scheme S1 Synthesis of H_2Me_2pzba: a) CuI, 2,4-pentanedione, DMSO, 90 °C, 24 h; b) hydrazine monohydrate, EtOH, 90 °C, 3 h.

H_2Me_2pzba was synthesized according to a known but modified literature procedure.[2]

- Synthesis of the intermediate 3-(4-carboxyphenyl)-2,4-pentanedione, B. 4-Iodobenzoic acid (9.92 g, 40 mmol) A, copper(I) iodide (0.762 g, 4 mmol), L-proline (0.921 g, 8 mmol) and K_2CO_3 (22.20 g, 160 mmol) were suspended in dry dimethyl sulfoxide (190 mL) and stirred for 10 minutes at room temperature. 2,4-Pentanedione (12.4 mL, 120 mmol) was added dropwise to this mixture and the initially blue mixture turned green within five minutes. The suspension was heated to 90 °C and stirred for 24 hours. After cooling to room temperature the mixture was transferred slowly and with vigorous stirring into hydrochloric acid (3 mol/L, 500 mL). An additional 300 mL of water was added and the suspension was cooled down in an ice bath. Below 8 °C a solid precipitated. After filtration and washing with ice-cooled water (3x 100 mL) the filter cake was dried over night at 60 °C in vacuum to afford the desired intermediate **B** (6.48 g, 30 mmol, 74 % based on 4-iodobenzoic acid) as off-white solid. ^{1}H-NMR (600 MHz, DMSO-D_6): δ/ppm 1.87 (s, 6H, -CH_3OH), 2.17 (s, 6H, -CH_3OH), 5.50 (s, 1H, acidic H –CO-CH-CO), 7.42 & 7.98 (d, 4H, -C_6H_4-), 13.0 (s, 1H, -COOH). ^{13}C-NMR (600 MHz, DMSO-D_6): δ/ppm 24.5 (s, CH_3); 114.5 (s, -CO-*C*H-CO-); 130-139 (aromatic C); 167.5 (s, COOH); 191 (s, CO). MS (EI): *m/z* 220 ($[M]^+$, 93%); 205 ($[M - CH_3]^+$ 100%).

- Synthesis of 3,5-dimethyl-4-(4-carboxyphenyl)-1*H*-pyrazole (**H_2Me_2pzba**), **C**. A solution of compound **B** (6.48 g, 30 mmol) in ethanol (70 mL) was added dropwise to a solution of hydrazine monohydrate (1.75 g, 35 mmol) in ethanol (10 mL) while stirring and upon complete addition the combined solution was then refluxed for 3 h. After cooling to room temperature the solution was concentrated under reduced pressure to one third of the original volume. With addition of water (200 mL) and cooling to 0 °C the product was precipitated. The precipitate was filtered and washed three times with ice-cooled water (100 mL each) and dried in vacuum over night at 80 °C to afford compound **C** (5.59 g, 26 mmol, 86 % based on 3-(4-carboxyphenyl)-2,4-pentanedione) as a white solid. ^{1}H-NMR (600 MHz, DMSO-D_6): δ/ppm 2.24 (s, 6H, -CH_3), 7.42 & 7.97 (d, 4H, -C_6H_4-), 12.6 (s, 1H, -COOH). ^{13}C-NMR (600 MHz, DMSO-D_6): δ/ppm 11.6 (s, CH_3); 127-130 (aromatic C); 138.8 (s, C-N); 167.5 (s, COOH). MS (EI): *m/z* 216 ($[M]^+$, 100 %); 215 ($[M - H]^+$ 32 %).

3. Preparation of $[Co_4(\mu_4\text{-}O)(Me_2pzba)_3]$

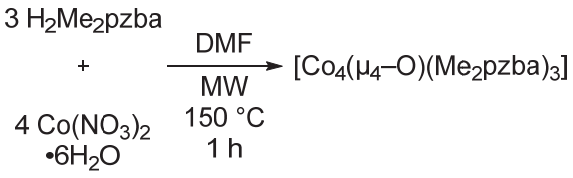

Scheme S2. Microwave-assisted synthesis of 3D-$[Co_4(\mu_4\text{-}O)(Me_2pzba)_3]$.

To a stirred solution of H_2Me_2pzba (1.02 g, 4.72 mmol) in dimethylformamide (120 mL) $Co(NO_3)_2{\cdot}6H_2O$ (1.83 g, 6.30 mmol) was added in small portions. This mixture was transferred to eight Teflon microwave vessels in portions of 15 mL and was heated from room temperature to 150 °C within 20 minutes in a CEM Mars 6 with a gradual rise to 300 W heating power. After reaching 150 °C the mixture was kept at 150 °C with a frequent gradual regulation of the temperature by a heating power of 150-250 W. After cooling to room temperature, the obtained blue solid was separated by centrifugation at 10.000 rpm for 20 min. After decanting of the liquid phase the precipitate was immersed for 2 h in dimethylformamide (150 mL), giving the as-synthesized material. The solvent was decanted off and the solid was re-immersed in dry dichloromethane (150 mL) under nitrogen atmosphere for 24 h. A blue crystalline solid of $[Co_4(\mu_4\text{-}O)(Me_2pzba)_3]$ was obtained after drying at 150 °C overnight with a Pfeiffer *MVP 015 T* turbomolecular pump in vacuum at $5{\cdot}10^{-6}$ mbar to give the activated material. Yield: 1.34 g, 1.50 mmol (95 % based on H_2Me_2pzba). The phase purity of the bulk product was confirmed by positively matching the experimental powder pattern of the as-synthesized material, before activation, the activated material and the simulated powder pattern of the previously reported crystal structure of $[Co_4(\mu_4\text{-}O)(Me_2pzba)_3]$ (**Figure S2**).[1]

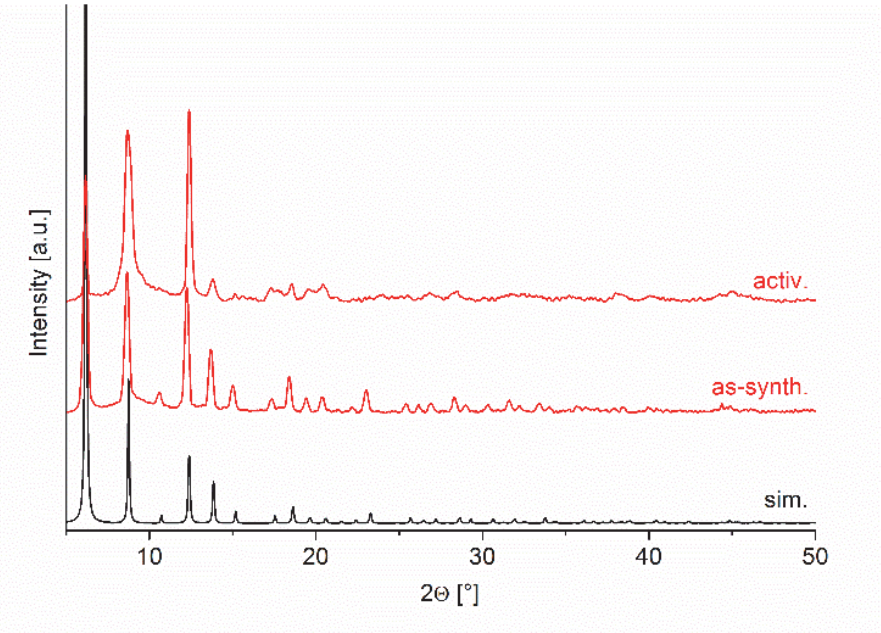

Figure S2. Experimental powder X-ray diffractogram (PXRD) pattern of the microwave-synthesized (as-synth.) and activated compound $[Co_4(\mu_4\text{-}O)(Me_2pzba)_3]$ (activ.), in comparison to the simulated diffractogram (sim.) from the single-crystal X-ray data set (CCDC-number: 937763).[1] For the flat silicon sample holder the beam spot is strongly broadened at low angles (and $2\theta < \sim 10°$) so that only a fraction of the reflected radiation reaches the detector, hence lower relative intensities are measured in this range.

(a) 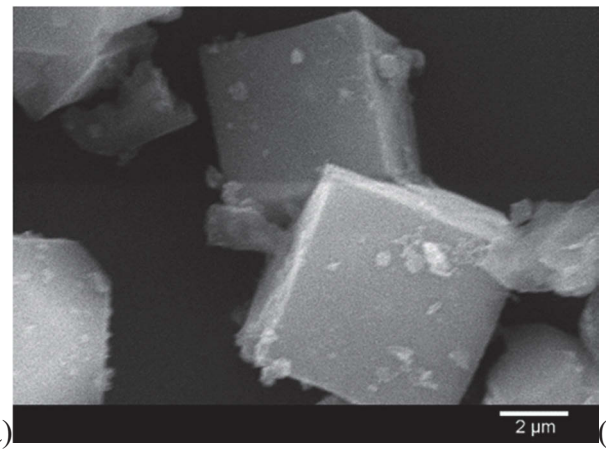

(b) 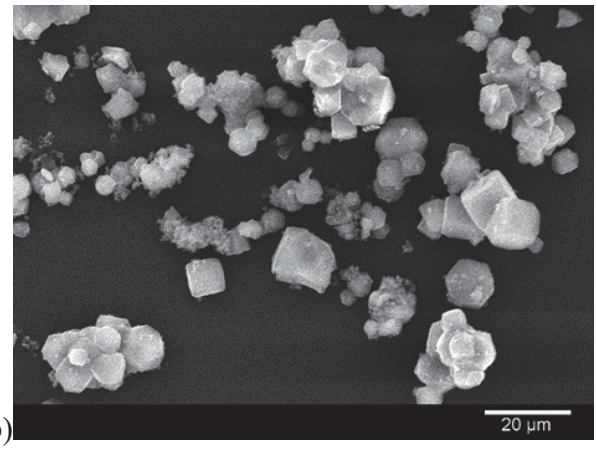

(c) 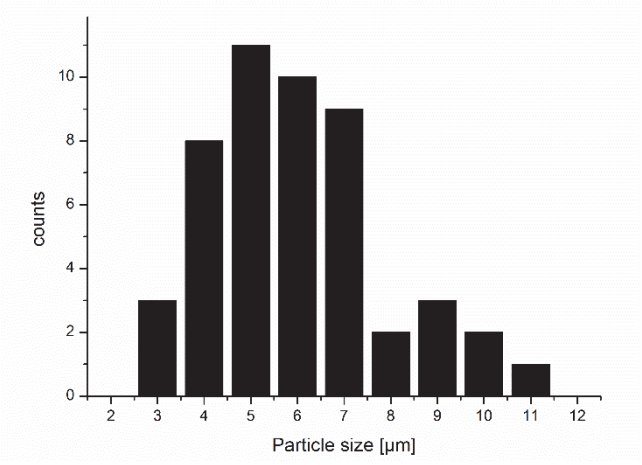

Figure S3. (a,b) Scanning electron microscopy (SEM) images and (c) histogram of particle size (diameter) from SEM-image of $[Co_4(\mu_4\text{-}O)(Me_2pzba)_3]$ (50 particles measured) from microwave synthesis.

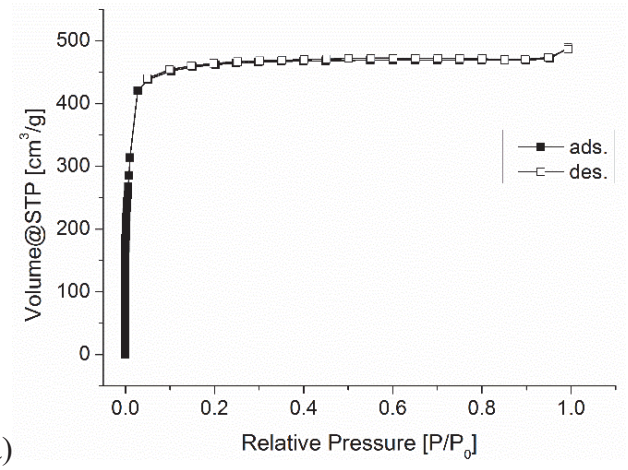

(a)

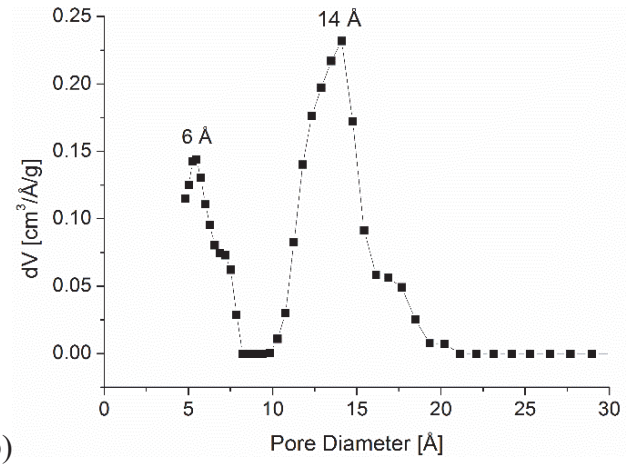

(b)

Figure S4. (a) Nitrogen adsorption isotherm of $[Co_4(\mu_4\text{-}O)(Me_2pzba)_3]$ from microwave synthesis measured at 77 K; (b) plot of the differential volume from DFT calculation. Calculated from the data of nitrogen sorption measurement using the equilibrium model for nitrogen at 77 K on carbon, slit pore and NLDFT.

4. Synthesis of MOF-5.

MOF-5 was synthesized according to a known literature procedure.[3]

Under inert atmosphere a solution of terephthalic acid (1.27 g, 7.62 mmol) in dry dimethylformamide (100 mL) and triethylamine (2.13 mL, 1.54 g, 15.2 mmol) was added dropwise under stirring to an inert solution of zinc acetate dehydrate (4.25 g, 19.3 mmol) in dry dimethylformamide (125 mL). The mixture became turbid immediately and was stirred for an additional 3 hours. Afterwards the solid was filtered using a glass frit under nitrogen atmosphere and was immersed in dry dimethylformamide (75 mL) overnight. The solvent was separated by filtration under nitrogen atmosphere and the solid was re-immersed in dry dichloromethane (100 mL). The separation of the solvent by filtration and re-immersion in dry dichloromethane (100 mL) under nitrogen atmosphere was repeated on the third and seventh day. After an additional three days of immersion in dichloromethane the solvent was decanted off and the remaining solid was dried in a nitrogen stream at room temperature. Yield: 1.37 g, 1.78 mmol (70 % based on terephthalic acid) as white fine powder.

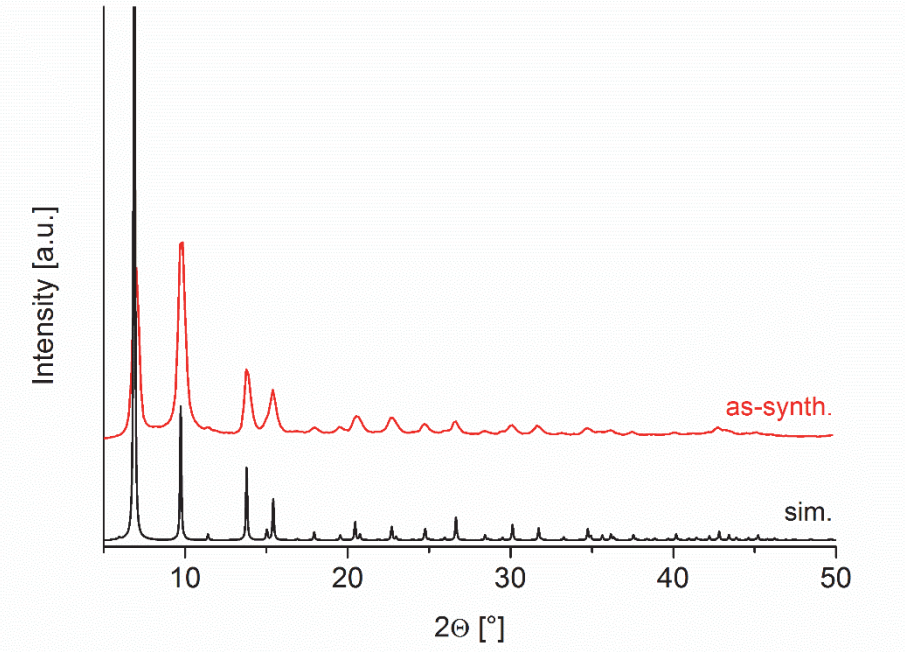

Figure S5. Powder X-ray diffractograms for MOF-5 as synthesized (as-synth.) in comparison with simulated diffractogram (sim.). The simulated diffractogram (sim.) is based on the X-ray data refinement (CCDC number: 256965).

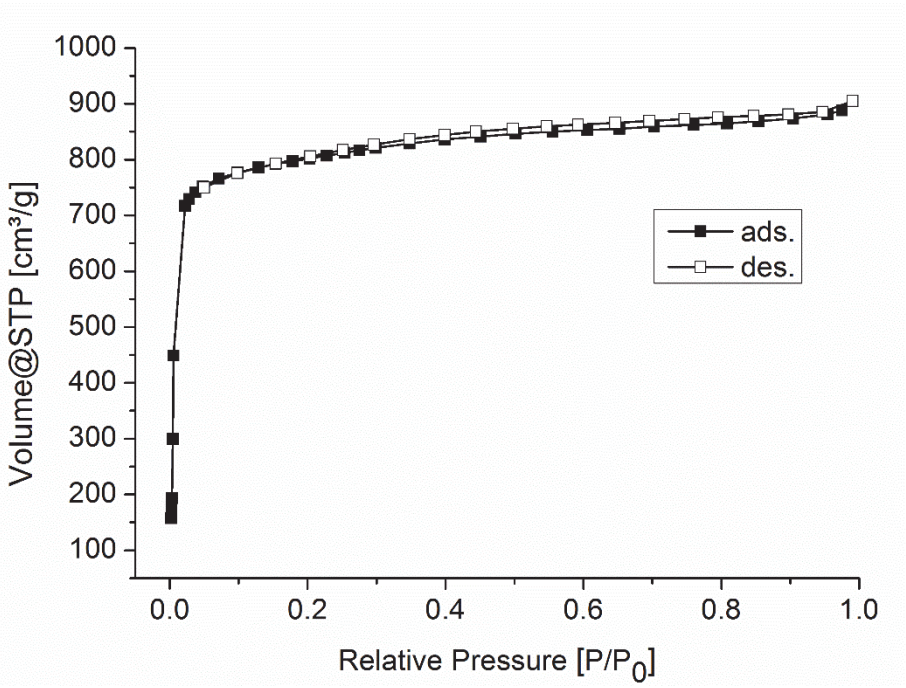

Figure S6. Nitrogen adsorption isotherm of MOF-5 at 77 K.

5. Gas Adsorption and Permeation Experiments

Prior to the gas sorption measurements, the samples were degassed at 160 °C for 2 h at 10^{-5} mbar. Nitrogen physisorption isotherms (0 to 1 bar) for Brunauer-Emmett-Teller (BET) surface area determination were measured with a Quantachrome Autosorb iQ MP automated gas sorption analyzer at 77 K. The BET surface areas were calculated from nitrogen adsorption isotherms in the P/P_0-range of 0.006-0.050. Total pore volumes were calculated from nitrogen sorption isotherms at $P/P_0 = 0.95$. DFT calculations for the pore size distribution were done with the ASiQwin 3 software using the equilibrium model for nitrogen at 77 K on carbon, slit pore and NLDFT. Additionally samples were characterized with a Quantachrome NOVA 4200e in the P/P_0-range of 0.006-0.050 and processed with the software Quantachrome NovaWin. Adsorption isotherms for $[Co_4(\mu_4\text{-}O)(Me_2pzba)_3]$ with CO_2 and CH_4 were recorded on a Micromeritics ASAP 2020 gas sorption analyzer equipped with oil-free vacuum pumps (ultimate vacuum $<10^{-8}$ mbar) and valves, which guaranteed contamination free measurements. Helium gas was used for the determination of the cold and warm free space of the sample tubes. CO_2 and CH_4 sorption isotherms were measured at 0 °C (ice/deionized water bath). All gases were of ultra-pure grades (99.999 %), supplied by Air Liquide Germany and used as received.

Single-gas permeabilities were evaluated with a permeation cell described earlier.[4] The membrane thicknesses were measured by using a micrometer as an average value over 10 random spots. The permeation measurements were performed by using the pressure-rise method under steady-state conditions at 30 °C. After placing the membranes into the sample cell at first the permeate side was evacuated to 10^{-2} mbar followed by evacuation of the feed side. At the feed side a gas pressure of 3.0 bar were set. The linear pressure increased upon permeation from the feed to the permeate side was recorded and used to calculate the permeability P in Barrer units [1 Barrer = 1×10^{-10} cm^3 (STP) cm/(cm^2 s cmHg) or 7.5005×10^{-18} m^2 s^{-1} Pa^{-1} in SI units].

Mixed-gas permeation experiments were conducted with a continuous flow permeation system with helium as sweep gas and an Agilent 490μGC gas chromatograph to measure the permeate gas concentration and composition in the sweep gas stream. Round membrane sheets were cut from the casted films and were placed in a permeation module (4.5 cm diameter) which allows an effective membrane diameter of 3.6 cm with an area of 11.3 cm^2 (restricted compared to the total area of the membrane sheet due to the *o*-ring). The module is surrounded by a temperature controlled chamber, so the membranes could be investigated at 25 °C to separate CO_2/CH_4 gas mixtures using the gas permeation setup presented in **Scheme S3**. The feed gases are mixed with a setup provided by Convergence Industry B.V., 7532 SM Enschede, The Netherlands, which contains two Bronkhorst Coriolis-flow controllers and a pressure controller to adjust the transmembrane pressure to 3 bar, while a 50/50 volume flow mixture of CO_2 and CH_4 with a total flow of 160 mL·min^{-1} is provided in the upstream. The downstream side of the membranes was swept with helium at 1 mL·min^{-1} at atmospheric pressure. The gas concentrations were analyzed by an on-line gas chromatograph (Agilent 490μGC equipped with thermal conductivity detector, TCD and Pora PLOT Q column) every 30 min over a period of 6 hours. After steady state was achieved the average of all measurements was used to calculate permeability and selectivity. Each membrane sample was fabricated twice and measured under the same conditions to ensure reproducibility. Permeability P_i was calculated from the molar flow rate of compound *i*, the membrane thickness, membrane area and the partial pressure difference of component *i* across the membrane. The molar flow rate of compound *i* in the mixed-gas measurement was derived from the concentration of i in the sweep gas stream and the sweep gas flow (at a given transmembrane pressure). The separation factor was calculated as the ratio of the

permeability of the more permeable compound (i, CO_2) to the permeability of the less permeable compound (j, CH_4), separately for single-gas ($S_{ij,ideal}$) and mixed-gas measurements ($S_{ij,real}$) (Eq. 1).[5] In the case where the gases do not interact strongly with each other or with the membrane material, the ideal and real selectivity is the same and is also equal to the separation factor α_{ij} (Eq. 2), but often this is not the case.

$$S_{ij} = \frac{P_i}{P_j} \qquad \text{(Eq. 1)}$$

For permeation of gas mixtures, the mixed-gas selectivity, also called separation factor (α_{ij}), can in addition be calculated from composition analysis as the ratio of the mole fractions, X of the components i and j in the permeate and the retentate stream (Eq. 2).[6]

$$\alpha_{ij} = \frac{\left(X_i / X_j\right)_{permeate}}{\left(X_i / X_j\right)_{retentate}} \qquad \text{(Eq. 2)}$$

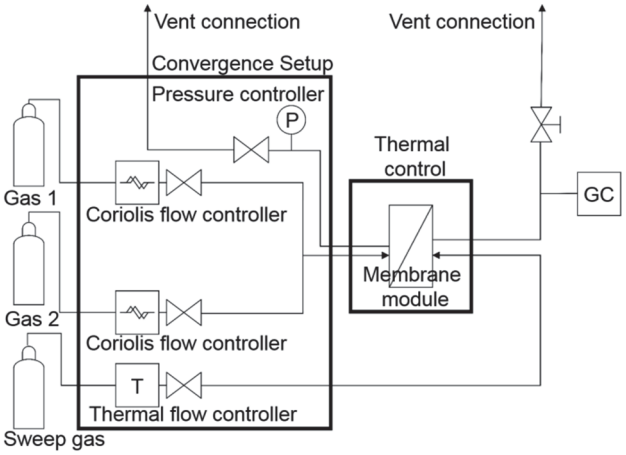

Scheme S3. Simplified scheme of the experimental setup of the gas permeation system based on the OSMO inspector instrument by Convergence Industry B.V., 7532 SM Enschede, The Netherlands.

6. SEM and size histogram of [$Co_4(\mu_4\text{-}O)(Me_2pzba)_3$] from conventional synthesis

(a)

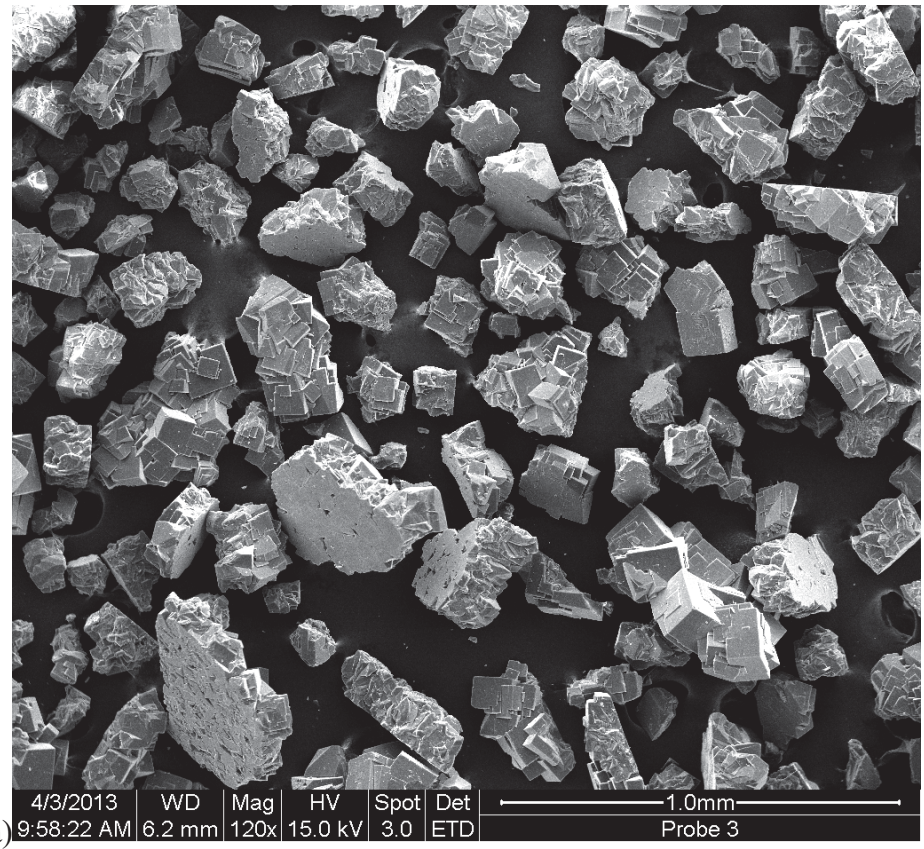

(b)

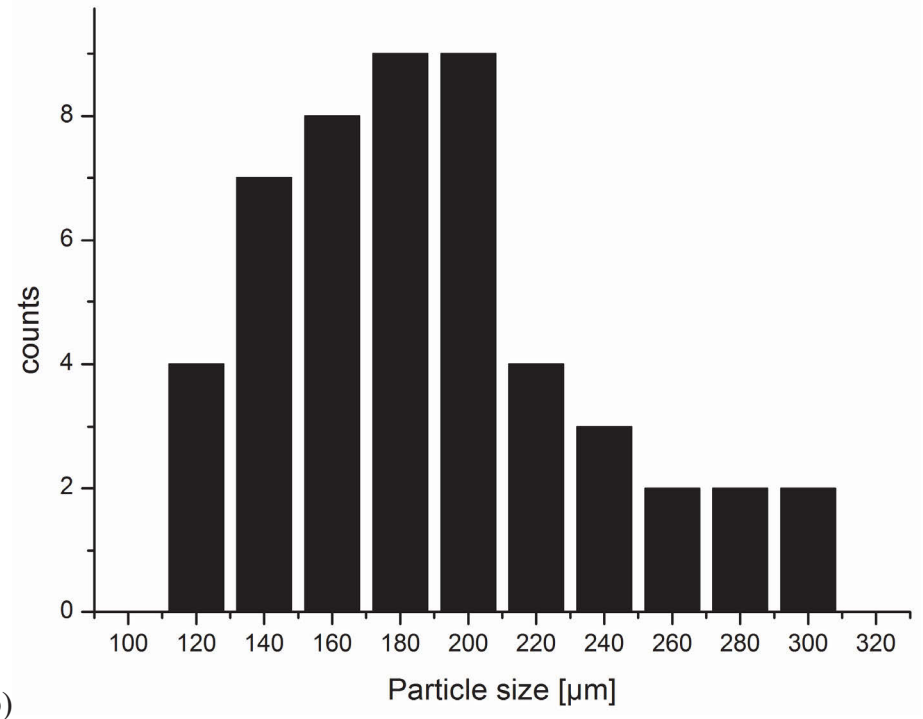

Figure S7. (a) SEM image and (b) analysis of particle size (diameter) from SEM-image of [$Co_4(\mu_4\text{-}O)(Me_2pzba)_3$] synthesized by conventional solvothermal method and reported previously.[1] SEM image reproduced with permission from ref.[1]. Copyright The Royal Society of Chemistry.

7. Theoretical surface area

The theoretical surface area and pore volume of [$Co_4(\mu_4\text{-}O)(Me_2pzba)_3$] was calculated using the program CrystalExplorer[7], following the methodology outlined in ref.[8]. The values for the crystal voids defined by both 0.002 and 0.0003 au procrystal isosurfaces are listed in Table S1.

Table S1. Surface areas ($m^2\ g^{-1}$) and pore volumes ($cm^3\ g^{-1}$) for [$Co_4(\mu_4\text{-}O)(Me_2pzba)_3$].

	CrystalExplorer theoretical values		experimental results from N_2 sorption data	
	procrystal isosurface definition			
	0.002 au	0.0003 au	BET experiment [c]	Langmuir [c]
surface area				
- unit cell ($Å^2$)	566.3	548.4		
- specific ($m^2\ g^{-1}$) [a]	3857	3734	1858,[e] 1985[f]	1938, 2124
pore volume				
- unit cell ($Å^3$)	2023.3	1717.4		
- specific ($cm^3\ g^{-1}$) [b,d]	1.378	1.169	0.67,[e] 073[f]	

[a] Calculated according to $(S_{unit\ cell} \times N_A)/(Z \times M_{asym\ unit})$.

[b] Calculated according to $(V_{unit\ cell} \times N_A)/(Z \times M_{asym\ unit})$; N_A = Avogadro's constant, $6.022 \cdot 10^{23}\ mol^{-1}$, Z = number of asymmetric formula units, $M_{asym\ unit}$ = molecular weight of asymmetric formula unit (in $g\ mol^{-1}$).

[c] Measurements on two different samples from two different batches; sample 1 on a Quantachrome NOVA 4200e, sample 2 on a Quantachrome Autosorb iQ MP

[d] Total pore volume at $P/P_0 = 0.95$ for pores ≤ 40 nm diameter (sample 1) or for pores ≤ 20 nm (sample 2).

[e] Sample measured 1 d after activation.

[f] Sample measured after 3 week storage in a closed vessel under ambient air.

The 0.0003 au calculated surface area is seen as a better choice for estimating the internal surface area in porous materials.[8] **Figure S8** illustrates the surface area at 0.0002 au and 0.0003 au around a pore window (cf. **Figure S1**). The mean diameter of this pore window is about 8.5 and 5.5 Å, respectively (cf. **Figure S4b**). The value of 0.002 au corresponds approximately to a smoothed van der Waals surface and 0.0003 au seems to be most appropriate for mapping "empty" space in molecular crystals.[8] The calculated pore volumes derived from both isosurface definitions differ by the typical 0.1–0.2 $cm^3\ g^{-1}$ as seen with other MOF structures, and they surround the experimental pore volume in most other studied MOF cases.[8]

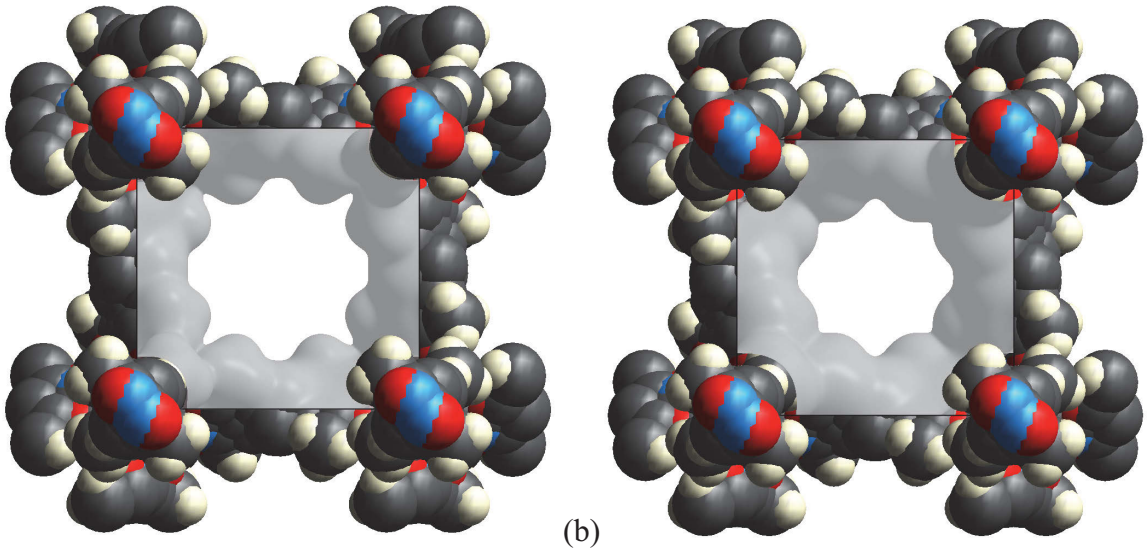

Figure S8. Void surfaces (a) 0.002 au and (b) 0.0003 au around a pore window in [$Co_4(\mu_4$-O)$(Me_2pzba)_3$] superimposed on space-filling representations of the unit cell content. The view is down the a axis. From the b and c length of the unit cell of 14.278(3) Å and 14.332(4) Å, respectively, the pore diameter is measured to about 8.5 Å (0.002 au) and 5.5 Å (0.0003 au).

On the other hand, the presence of disorder is suggested to have little effect on the calculated surface area[8] and, if any, removal of the crystallographically-induced disorder in [$Co_4(\mu_4$-O)$(Me_2pzba)_3$] will lead to an even larger calculated surface area. Clearly, the calculated surface area presents an upper bound which can be approached but it will be physically unrealistic to expect that the experimental measurements will surpass the calculated value.

8. Gas selectivity from CO_2 and CH_4 adsorption isotherms of $[Co_4(\mu_4\text{-}O)(Me_2pzba)_3]$

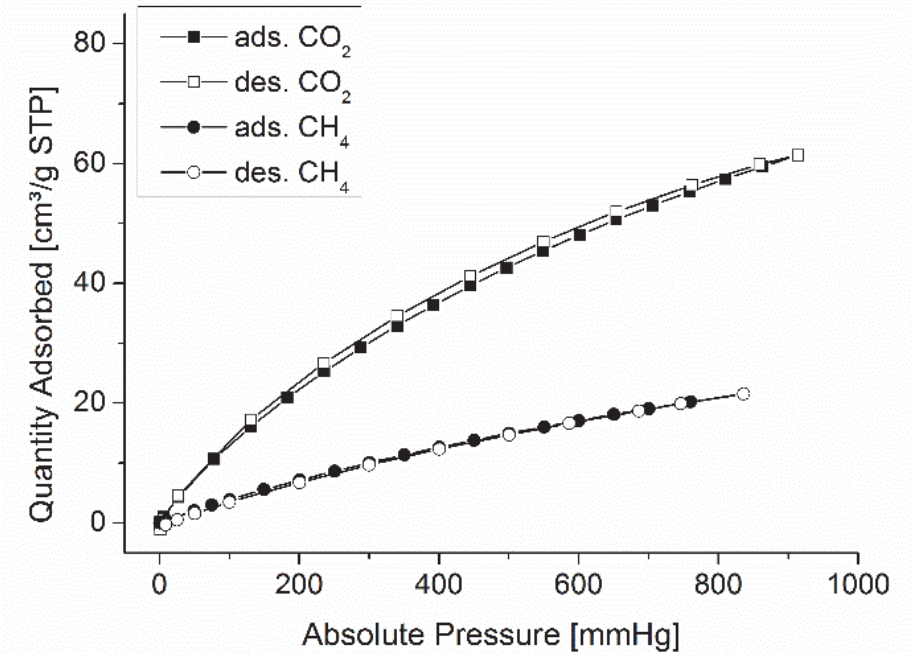

Figure S9. CO_2 and CH_4 sorption isotherms of $[Co_4(\mu_4\text{-}O)(Me_2pzba)_3]$ at 273 K.

The ratio of the initial slopes, 0.14 (CO_2) and 0.04 (CH_4) in the Henry region of the adsorption isotherms determines the selectivities exhibited by $[Co_4(\mu_4\text{-}O)(Me_2pzba)_3]$ for adsorption of CO_2 over CH_4. $[Co_4(\mu_4\text{-}O)(Me_2pzba)_3]$ shows a selectivity ratio for CO_2:CH_4 of 3.5:1 at 273 K.

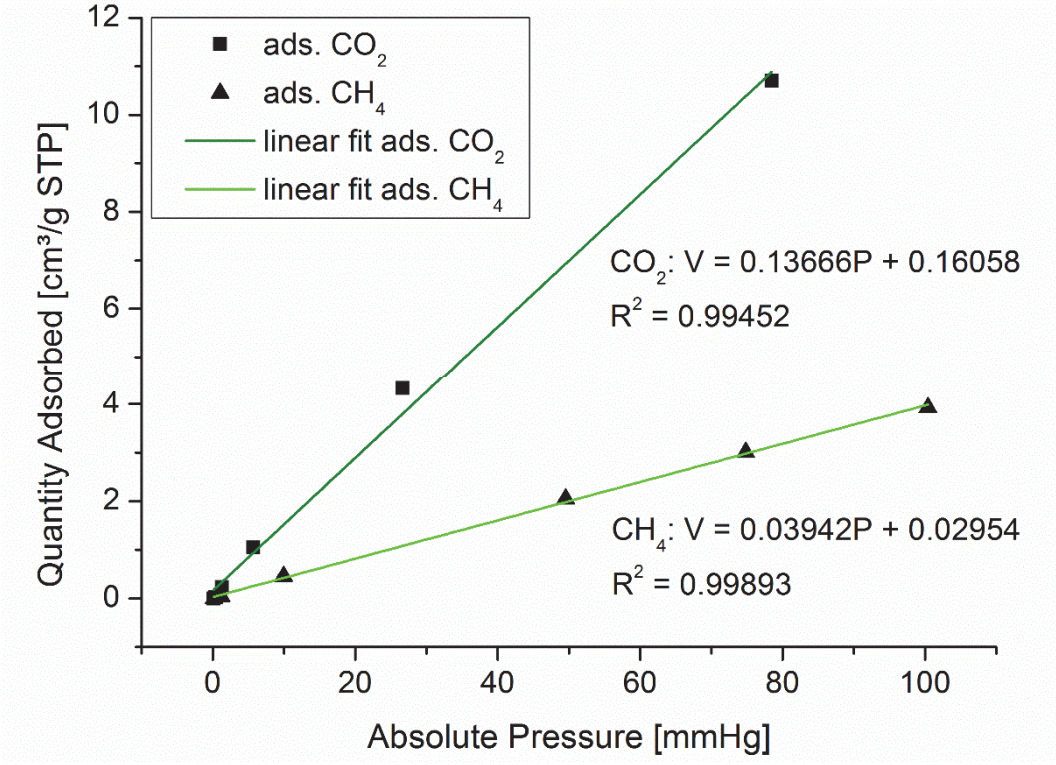

Figure S10. The initial slope in the Henry region of the sorption isotherms of CO_2 and CH_4 of $[Co_4(\mu_4\text{-}O)(Me_2pzba)_3]$ at 273 K

9. Water stability testing of $[Co_4(\mu_4\text{-}O)(Me_2pzba)_3]$

The water stability test performed here followed the procedure by *Cychosz et. al.*[9] The activated $[Co_4(\mu_4\text{-}O)(Me_2pzba)_3]$ was placed in DMF and deionized water was added to achieve a (v : v) water:DMF ratio of 1 : 2 and the mixture was stirred at RT for 1 h. Then a small amount of the sample was extracted to be analyzed using powder X-ray diffraction. Afterwards the mixture was diluted with water to prepare a (v : v) water–DMF ratio of 1 : 1 and again analysis was done after stirring at RT.

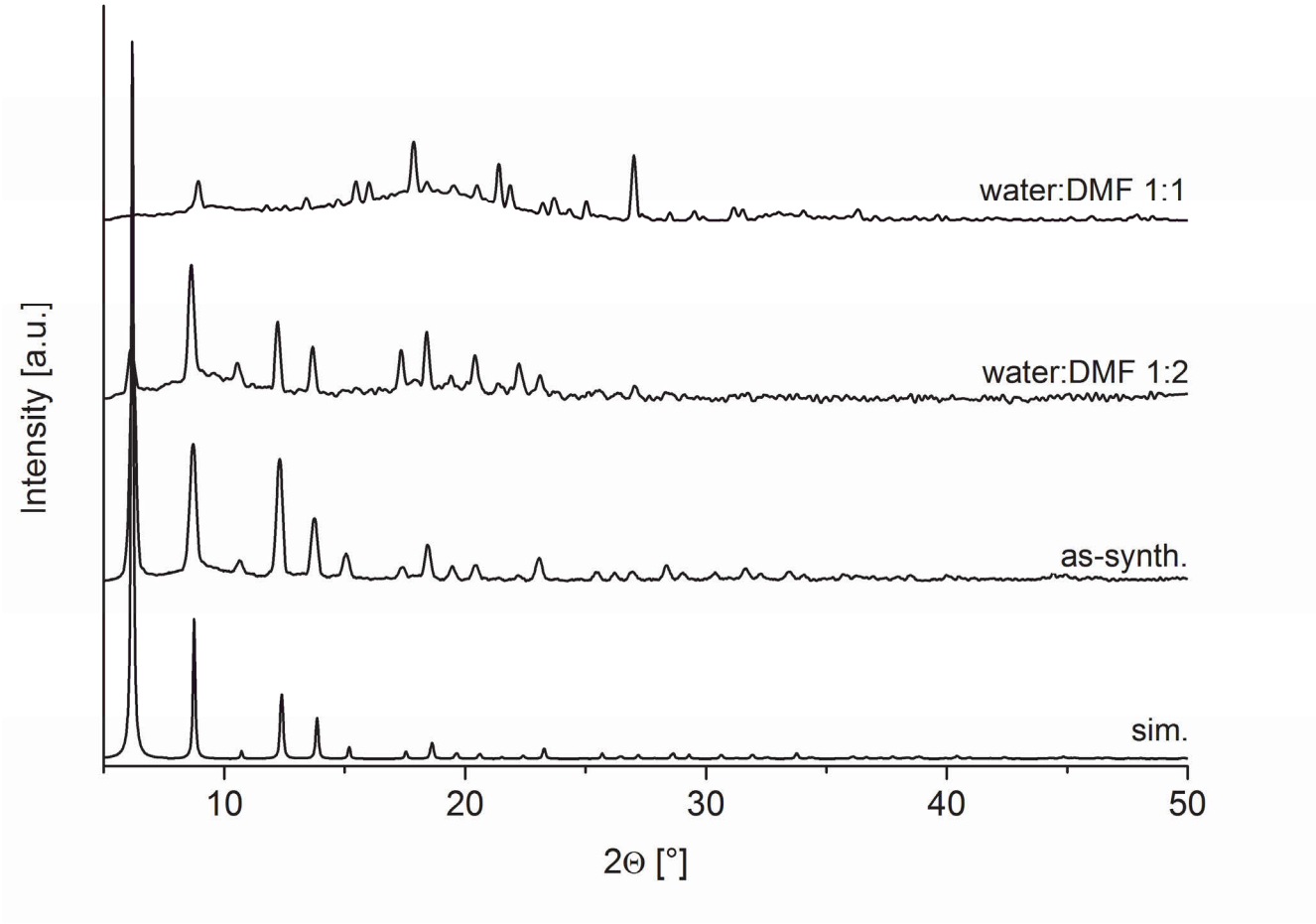

Figure S11. Water stability tests by comparison of powder X-ray diffractograms of $[Co_4(\mu_4\text{-}O)(Me_2pzba)_3]$ before (as-synth.) and after exposure (for 1 h) to mixtures of water:DMF at different v : v ratios in comparison with simulated diffractogram (sim., based on the X-ray data refinement, CCDC number: 937763).

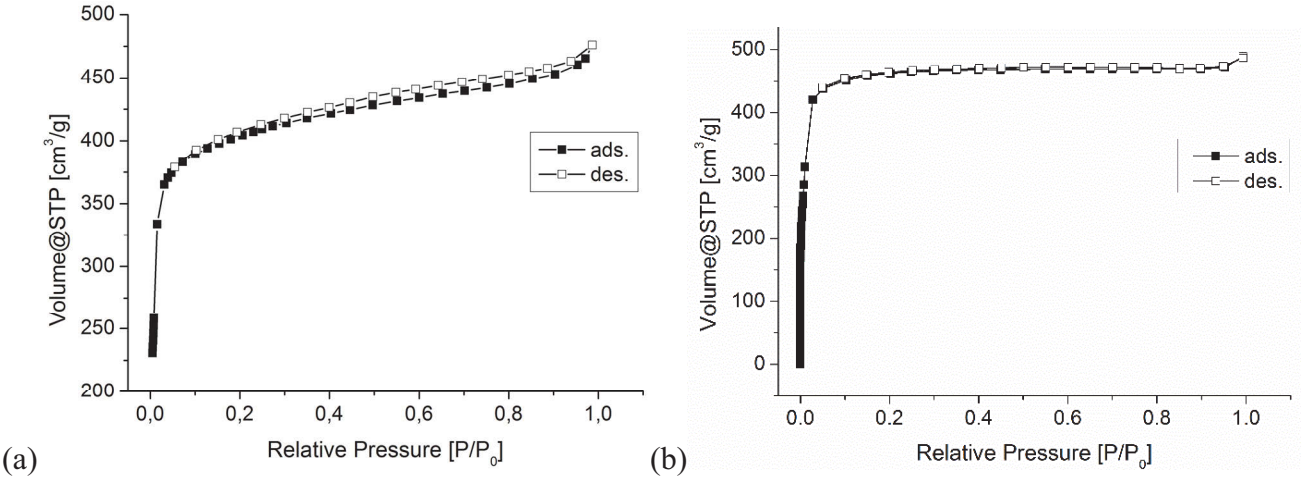

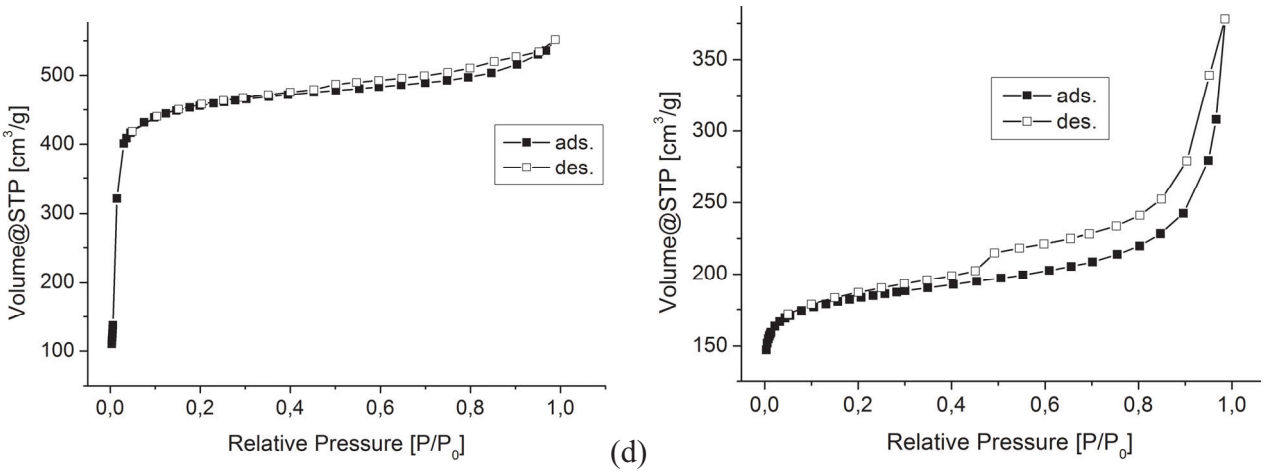

Figure S12. Nitrogen adsorption isotherm of $[Co_4(\mu_4\text{-}O)(Me_2pzba)_3]$ from microwave synthesis measured at 77 K (a) after 1 day of activation and storage in a closed vessel under ambient air (corresponding to Fig. S4a (BET: 1858 $m^2\ g^{-1}$); (b) after 3 weeks of synthesis and storage in a closed vessel under ambient air (BET: 1985 $m^2\ g^{-1}$); (c) after repeated sonication in a dichloromethane dispersion as described for the MMM preparation (BET: 1777 $m^2\ g^{-1}$); (d) after exposure (for 1h) to a 1:2 water:DMF at mixture (BET: 715 $m^2\ g^{-1}$).

(1) Heering, C.; Boldog, I.; Vasylyeva, V.; Sanchiz, J.; Janiak, C. *CrystEngComm* **2013**, *15*, 9757-9768.
(2) Bryant, M. R.; Burrows, A. D.; Fitchett, C. M.; Hawes, C. S.; Hunter, S. O.; Keenan, L. L.; Kelly, D. J.; Kruger, P. E.; Mahon, M. F.; Richardson, C. *Dalton Trans.* **2015**, *44*, 9269-9280.
(3) Tranchemontagne, D. J.; Hunt, J. R.; Yaghi, O. M. *Tetrahedron* **2008**, *64*, 8553-8557.
(4) Wieneke, J. U.; Staudt, C. *Polym. Degrad. Stab.* **2010**, *95*, 684-693.
(5) Wiederhorn, S.; Fields, R.; Low, S.; Bahng, G.-W.; Wehrstedt, A.; Hahn, J.; Tomota, Y.; Miyata, T.; Lin, H.; Freeman, B.; Aihara, S.; Hagihara, Y.; Tagawa, T. Mechanical Properties. In *Springer Handbook of Materials Measurement Methods*; Czichos, H.; Saito, T.; Smith, L., Eds.; Springer: Berlin, Heidelberg, 2006; Chapter 7, pp 283-397.
(6) Koros, W. J.; Ma, Y. H.; Shimidzu, T. *Pure Appl. Chem.* **1996**, *68*, 1479-1489.
(7) *CrystalExplorer17*, Version 3.1; Turner, M. J.; McKinnon, J. J.; Wolff, S. K.; Grimwood, D. J.;Spackman, P. R.; Jayatilaka, D. and Spackman, M. A.: University of Western Australia, 2017. http://hirshfeldsurface.net
(8) Turner, M. J.; McKinnon, J. J.; Jayatilaka, D.; Spackman, M. A. *CrystEngComm* **2011**, *13*, 1804-1813.
(9) Cychosz, K. A.; Matzger, A. J. *Langmuir* **2010**, *26*, 17198-17202.

3.3 HKUST-1 coatings on laser-microperforated brass supports for water adsorption

Adelaida Perea-Cachero, Janina Dechnik, Ruth Lahoz, Christoph Janiak, Carlos Téllez and Joaquin Coronas

CrystEngComm, **2017**, *19*, 1470-1478.
DOI: 10.1039/C6CE02490D, Quelle[218]

Diese Arbeit beschreibt die Herstellung von HKUST-1 Schichten auf Messingträgern durch ein Temperaturgradienten Verfahren. Die Messingbleche wurden mittels Laserbestrahlung perforiert, um 30-50 µm große Mikrolöcher zu erzeugen. Die Perforation verbesserte die Haftung und Beladung des MOFs auf dem Trägermaterial. Die bei der Laserbehandlung erzeugte Mikrolochumgebung führte zu einer gut angebundenen Beschichtung. Zwei verschiedene Proben wurden mit Reaktionstemperaturen von 100 bzw. 150°C synthetisiert. Eine kontinuierliche HKUST-1-Beschichtung wurde nur bei der höheren Temperatur beobachtet. In beiden Fällen wurden die Mikrolöcher vollständig mit Kristallen gefüllt, und so konnten Massenanteile von 2,4 und 6,6 Gew.-% des kristallinen Materials auf dem Träger erreicht werden. PXRD und N_2-Sorptionsmessungen bestätigten die Bildung von HKUST-1-Kristallen mit hoher Qualität (S_{BET} = 1105 m^2 g^{-1}). Wassersorptionsisothermen zeigen mit dem Hauptschritt der Wasseraufnahme unterhalb von einem relativen Druck von 0,4 und einer Wasseraufnahmekapazität (0,48 und 0,45 g g-1 bei 293 K und p / p0 = 0,9), dass im Bereich der für HKUST-1 typischen Werte erreicht werden können. Diese Eigenschaften und die verbesserte Wechselwirkung der MOF-Schicht mit dem Trägermaterial machen diese Beschichtungen zu einem interessanten Materialien für den Einsatz in wasserbasierten Adsorptionsanwendungen für Kältemaschinen oder Wärmepumpen.

Anteil an der Veröffentlichung

- Konstruktion und Planung des Aufbaus für das Temperaturgradienten-Verfahren und Analytik der Proben. Synthetische Arbeiten wurden in Zusammenarbeit mit Adelaida Perea-Cachero am Institut für Anorganische Chemie und Strukturchemie in Düsseldorf durchgeführt.
- Schreiben des Manuskripts und Erstellen der Abbildungen und Tabellen erfolgte durch Adelaida Perea Cachero in Kooperation mit Janina Dechnik.
- Ruth Lahoz stellte die laser-perforierten Messingbleche her.
- Korrekturen wurden durch Christoph Janiak, Carlos Téllez und Joaquin Coronas vorgenommen

CrystEngComm

PAPER

View Article Online
View Journal | View Issue

Cite this: *CrystEngComm*, 2017, **19**, 1470

HKUST-1 coatings on laser-microperforated brass supports for water adsorption†

Adelaida Perea-Cachero,‡[a] Janina Dechnik,‡[b] Ruth Lahoz,[c] Christoph Janiak,*[b] Carlos Téllez[a] and Joaquín Coronas*[a]

Received 1st December 2016,
Accepted 10th January 2017

DOI: 10.1039/c6ce02490d

rsc.li/crystengcomm

This work describes the preparation of HKUST-1 layers on brass supports by a thermal gradient approach. Supports were perforated using laser irradiation to create 30–50 μm microholes. Perforation improved the adhesion and loading of the MOF. The microhole environment generated during the laser treatment led to well-anchored coatings. Two distinct samples were synthesized with the reaction temperature (100 and 150 °C) as the main difference. A continuous HKUST-1 coating was only achieved with the higher temperature of 150 °C. However, the microholes were totally filled with crystals in both samples reaching weight fractions of crystallized material of 2.4 and 6.6 wt%. PXRD and N_2 physisorption studies confirmed the formation of HKUST-1 crystals with high quality (S_{BET} = 1105 m^2 g^{-1}). Water adsorption was performed on both samples, showing the main sorption event below a relative pressure of 0.4 and obtaining uptakes (0.48 and 0.45 g g^{-1} at 293 K and p/p_0 = 0.9) among the reported values for HKUST-1 powder. The HKUST-1 properties and the enhanced MOF–support interaction make these coatings candidates for use in gas storage and separation, sensing and water-based adsorption applications, such as chillers or heat pumps.

Introduction

The global warming phenomenon has attracted much attention in recent years. Many efforts are aimed at mitigating the effects of anthropogenic actions of emitting and distorting the presence of greenhouse gases in the atmosphere. In particular, the contribution of chlorofluorocarbon (CFC) and hydrochlorofluorocarbon (HCFC) gases to climate change is estimated to be roughly 12% of the total impact from greenhouse gases.[1] In addition, stratospheric accumulation of CFCs and HCFCs, having long atmospheric lifetimes, causes ozone layer depletion.[1] Environmental concerns about the use of CFCs and HCFCs as refrigerants have provoked the search for harmless working fluids.[2] Adsorption technology employs more environmentally friendly refrigerants such as water, ammonia, methanol and ethanol.[3,4] Despite the problems arising from its low vapour pressure, water is the preferable refrigerant owing to its non-toxicity and high latent heat of vaporization.[3,5,6] Adsorption cycle systems can operate using efficient energy resources, such as waste heat and solar energy.[3,7] Active carbons, silica gels and zeolites are the adsorbents usually employed.[3] Recent studies have focused on metal–organic frameworks (MOFs) as adsorbents for efficient sorption-based heating and cooling systems with water as the refrigerant.[8–17] The increasing interest in MOFs as water adsorbents is due to the wide variety of available organic and inorganic moieties affording tunable pore sizes, shapes and chemical surfaces, thus tailoring their adsorption and chemical properties.[14,17–21] MOFs, also known as porous coordination polymers (PCPs), are highly porous compounds consisting of metal ions or clusters coordinated by organic linkers leading to one-, two- or three-dimensional networks.[22] MOFs have emerged as intriguing materials for a number of applications, such as catalysis,[23,24] encapsulation,[25] gas separation[26] and storage,[23,27] drug delivery,[23] sensor technology,[28] *etc.*

HKUST-1 (also named Cu-BTC or MOF-199, $[Cu_3(BTC)_2(H_2O)_3]_n$) is a MOF with an open framework composed of Cu^{2+} cations as metal nodes and benzene-1,3,5-tricarboxylate (BTC) anions as organic connectors.[29] The pseudo-octahedral coordination sphere of HKUST-1 includes paddle-wheel clusters formed by dinuclear cupric tetracarboxylate units ($Cu_2(OOC–)_4$).[29–31] Cu^{2+} ions are coordinated by four oxygen

[a] *Chemical and Environmental Engineering Department and Instituto de Nanociencia de Aragón (INA), Universidad de Zaragoza, 50018 Zaragoza, Spain. E-mail: coronas@unizar.es; Tel: +34 976762471*
[b] *Institut für Anorganische Chemie und Strukturchemie, Heinrich-Heine Universität Düsseldorf, 40204 Düsseldorf, Germany. E-mail: janiak@uni-duesseldorf.de; Tel: +49 2118111580*
[c] *Centro de Química y Materiales de Aragón (CEQMA), CSIC-Universidad de Zaragoza, 50018 Zaragoza, Spain*

† Electronic supplementary information (ESI) available. See DOI: 10.1039/c6ce02490d

‡ These two authors contributed equally.

atoms from BTC and one oxygen atom in the axial position from a water ligand.[29] HKUST-1 comprises two kinds of pores and windows. Larger cuboctahedral pores (11 Å), delimited by 12 paddle-wheel subunits, are accessible through square-shaped windows (9 Å) (Fig. 1).[29,32,33] Octahedral side cavities (5 Å) are connected to the main channels by triangular windows (3.5 Å) (see also Fig. 1).[32–34] The inner surface of the smaller pockets comprises four benzene rings from BTC resulting in a more hydrophobic character.[35] Upon activation, water ligands are removed from the HKUST-1 structure creating coordinatively unsaturated metal sites (CUS).[30] Thereby, coordinative vacancies on Cu^{2+} cations could bind to distinct guests, such as water molecules, among others.[36]

In this work, HKUST-1 layers were prepared on microperforated brass supports following a thermal gradient synthesis.[37] The thermal gradient synthesis allows better control of MOF deposition on the supports[38] and renders mechanically and thermally stable coatings.[37–39] Perforations of metal substrates were carried out by laser irradiation to promote the formation of HKUST-1. For many years, laser technology has been widely applied in common metal drilling and machining processes.[40,41] But laser processing has also been used in the so-called surface activation and surface engineering for numerous purposes. For instance, laser surface engineering afforded the development of controllable wettability on distinct materials[42] and preservation of functional properties under abrasive wear and cavitation loads.[43] In addition, chemical surface activation enhanced the biocompatibility in implants and controlled the cell growth,[44,45] as well as improved the bonding in metal–ceramic joints.[46] Previously in our group, laser microperforation was used to activate silicalite-1 and ZIF-8 growth on stainless steel[47] and brass sheets,[48] respectively, for micromembrane preparation. In this case, the process also profited from the chemical surface activation of brass due to the melting and spallation phenomena related to laser ablation during the drilling process. Therefore, two distinct HKUST-1–brass samples were synthesized by changing the reaction temperature to form a uniform HKUST-1 layer on the laser-perforated support. Characterization by different techniques (optical microscopy, OM; scanning electron microscopy, SEM; energy-dispersive X-ray spectroscopy, EDX; powder X-ray diffraction, PXRD; N_2 physisorption) and water sorption isotherms of both samples are presented and discussed. Upon demonstration of adsorbate access to the microporosity of the MOF present in the MOF–metal composite, supporting HKUST-1 on microperforated metal sheets could provide advantages in adsorption-based applications taking into account the MOF properties along with the water sorption uptakes in accordance with values from the bulk powder. The highly porous coatings obtained in this work could increase the efficiency of adsorption systems by reducing the heat and mass transfer limitations.[38]

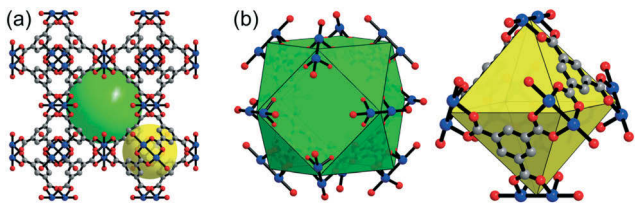

Fig. 1 (a) Representation of the bimodal pore system of HKUST-1 viewed along the (1 0 0) direction. Green and yellow spheres are depicted filling the larger cuboctahedral (11 Å) and smaller octahedral cavities (5 Å). (b) Details of the cuboctahedral (left) and octahedral (right) pores. Cu, O and C atoms are coloured in blue, red and grey, respectively. H atoms are omitted for clarity.

Experimental section

General methods and materials

Copper(II) nitrate hemi(pentahydrate) ($Cu(NO_3)_2{\cdot}2.5H_2O$, >99.99%, Aldrich), benzene-1,3,5-tricarboxylic acid (H_3BTC, $C_6H_3(CO_2H)_3$, 98%, Alfa Aesar), and *N*,*N*-dimethylformamide (DMF, $HCON(CH_3)_2$, 99.99%, Fisher Chemical) were obtained commercially and used without further purification.

Perforation of brass supports

The laser used was a commercial diode-pumped Yb:YAG fiber laser device emitting at 1050 nm (Easy Mark 20, Jeanologia) with a 100 ns pulse width and the beam was deflected by a pair of galvanometric mirrors controlled by CAD software. The laser CAD software allows generating a predefined pattern of spots onto a given material surface with any geometrical design by combining the laser repetition rate and the scanning speed. The pattern may be repeated as many times as required assuring exactly coincidence in position so that, in principle, sheets of any thickness can be drilled by just varying the number of laser cycles. In this case, brass sheets of 75 μm thickness were drilled with a 4 kHz repetition rate and a 500 mm s^{-1} scanning speed that yielded a pattern of holes with 125 μm of separation between centres. For this sheet thickness, 50 cycles were needed to complete drilling the material. The energy parameter applied was 150 J cm^{-2}. According to energy-dispersive X-ray spectroscopy, brass sheets were composed of 68, 30 and 2 atomic% Cu, Zn and O, respectively, thus the Cu/Zn ratio was 2.3. Square sheets, 5 × 5 cm^2, were employed and irradiated generating a dot linear pattern of 4.5 × 4.5 cm^2.

Synthesis of HKUST-1 coatings on microperforated brass sheets

After perforation, supports were washed twice with water and acetone for 15 min in an ultrasonic bath to remove impurities. The supports were dried at 100 °C overnight. HKUST-1 was formed on the perforated brass supports by means of the thermal gradient approach reported by Jeremias *et al.*[37] and following their synthesis conditions. Sample 1 and sample 2 were prepared from a solution of 8.17 g of $Cu(NO_3)_2{\cdot}2.5H_2O$ and 4.21 g of H_3BTC in 250 mL of DMF. The synthesis was carried out using a heating block (Fig. S1a†). The heating

block consists of a rectangular prism made of brass. The block has 6 bores: one for mounting purposes, one for temperature control by a thermocouple and four for insertion of the heating cartridges. The support was grabbed with clips on the heating block in such a way that its non-irradiated side was in contact with the block surface and not with the solution. Consequently, crystals were only formed on the irradiated surface of the substrate. The block with the brass sheet attached was placed into the reactant solution. The glass beaker containing the solution and the heating block was immersed in a cooling thermostatic bath (Fig. S1b†). The temperatures on the block surface and near the beaker wall (at the interface between the cooling bath and the synthesis solution) were continuously monitored. The heating power was adjusted in such a way that the surface temperature was 100 and 150 °C for sample 1 and sample 2. The temperature of the cooling bath was set at 10 and 75 °C for sample 1 and sample 2, respectively. After a reaction time of 2 h, the setup was cooled down to room temperature. Blue HKUST-1 crystals covered the perforated sheets. The sheets were rinsed twice with DMF and dried under ambient conditions. Table S1† shows the synthesis parameters and MOF weight fractions of both sample 1 and sample 2.

Characterization

Optical microscopy (OM) images were taken with a Leica M80 reflected-light microscope. Powder X-ray diffraction (PXRD) patterns were obtained at ambient temperature on a Bruker D2 Phaser equipped with a Lynx-Eye detector in reflection geometry. Samples for PXRD were prepared on a flat sample holder with a Si-wafer platform using Cu-Kα radiation (λ = 1.54182 Å). Molecular graphics of HKUST-1 were obtained with Diamond[49] using the cif file from Yakovenko *et al.* (CCDC 943009).[50] Scanning electron microscopy (SEM) images were recorded with a Jeol JSM-6510LV QSEM advanced electron microscope with a LAB-6 cathode at 5–20 keV. The microscope was equipped with a Bruker XFlash 410 silicon drift detector and Bruker ESPRIT software for energy-dispersive X-ray spectroscopy (EDX) analysis. Cu, Zn, C and O atomic composition maps were obtained by EDX. Atomic percentages were calculated as an average of measurements on two distinct spots. Cross-sections were prepared by cutting the samples with conventional scissors along the perforation of the support and then coated with gold by a Jeol JFC 1200 fine-coater (at an approximate current of 20 mA for 20–30 s). N_2 physisorption isotherms were acquired on a Nova 4000e from Quantachrome at 77 K. Brunauer–Emmett–Teller (BET) surface areas were calculated from the N_2 sorption isotherms. Water physisorption isotherms were measured volumetrically on a Quantachrome Autosorb iQ MP at 293 K. For measuring the isotherms, samples were loaded into glass tubes capped with septa. The weighed tubes were attached to the corresponding degassing port of the sorption analyzer, degassed under vacuum at 160 °C for 2 h, weighed again and then transferred to the analysis port of the sorption analyzer. The adsorption phenomenon is only due to the MOF because the metal substrate does not show sorption features. For this reason, the N_2 and water isotherms were corrected by dividing the adsorption data by the MOF weight fraction of the corresponding sample.

Results and discussion

Microperforated brass sheets

The goals of using laser irradiation to perforate brass sheets were to achieve a high (through the filling of the support microperforations) and uniform loading of MOF material and to improve the MOF–support attachment through the created roughness. Laser irradiation produced truncated cone-shaped holes with the largest and smallest diameters of *ca.* 50 and 30 μm, respectively. The higher diameter corresponds to the irradiated side of the support. On this side, the surface became rough and craters appeared around holes (Fig. 2a and b). EDX analysis at the area between holes gave an atomic composition of 31, 32 and 37% Cu, Zn and O, respectively (see Table S2†). However, these values were 49, 35 and 16% at the crater rims. The resulting atomic Cu/Zn ratios, therefore, decreased to 1.0 and 1.4 for the non-perforated surface and crater rims, respectively, in comparison with the value from the bare metal sheet (2.3). According to the work reported by Navarro *et al.*, one could expect an increment instead of a reduction in the ratio of the laser-affected zones due to higher volatilization of Zn (lower vaporization temperature), giving rise to Cu enrichment.[48] In our case and probably due to a smaller diameter of the inlet microperforations (50 μm *vs.* 72 and 59 μm for Navarro *et al.*[48]), after laser ablation, Zn recondensed and was deposited on the surface between craters. The evaporated material inside the holes was unable to leave the craters and was deposited on the hole walls and crater peripheries.[51] Both facts resulted in Zn enrichment in the non-perforated areas and crater rims, as compared to the bare sheet, decreasing the Cu/Zn ratio. On the other hand, the atomic content of O was moderately raised from 2 to 16% for the crater rims while it was substantially increased from 2 to 37% for the surface between holes, so the metallic oxides were preferentially formed at the non-irradiated zones, more exposed to the surrounding atmosphere. As seen in Fig. 2b, the non-perforated areas are partially covered with particles deposited during irradiation as a result of the ablation and oxidation of the brass sheet. Smaller particles are generated by nucleation and condensation of vapour and are placed away from craters.[51,52] Bigger particles are ejected from the melted liquid remaining at the craters' surroundings.[51,52] Several authors have related the particle size with the composition, determining that the larger particles are mainly composed of Cu, whereas the smaller particles are rich in Zn.[52,53] Liu *et al.*[52] supported that vaporized atoms and ions condense on the ejected droplets creating an outer layer. Thus, vaporized Zn is supposed to condense as ZnO, forming small particles and covering large ejected Cu droplets. The lower standard reduction

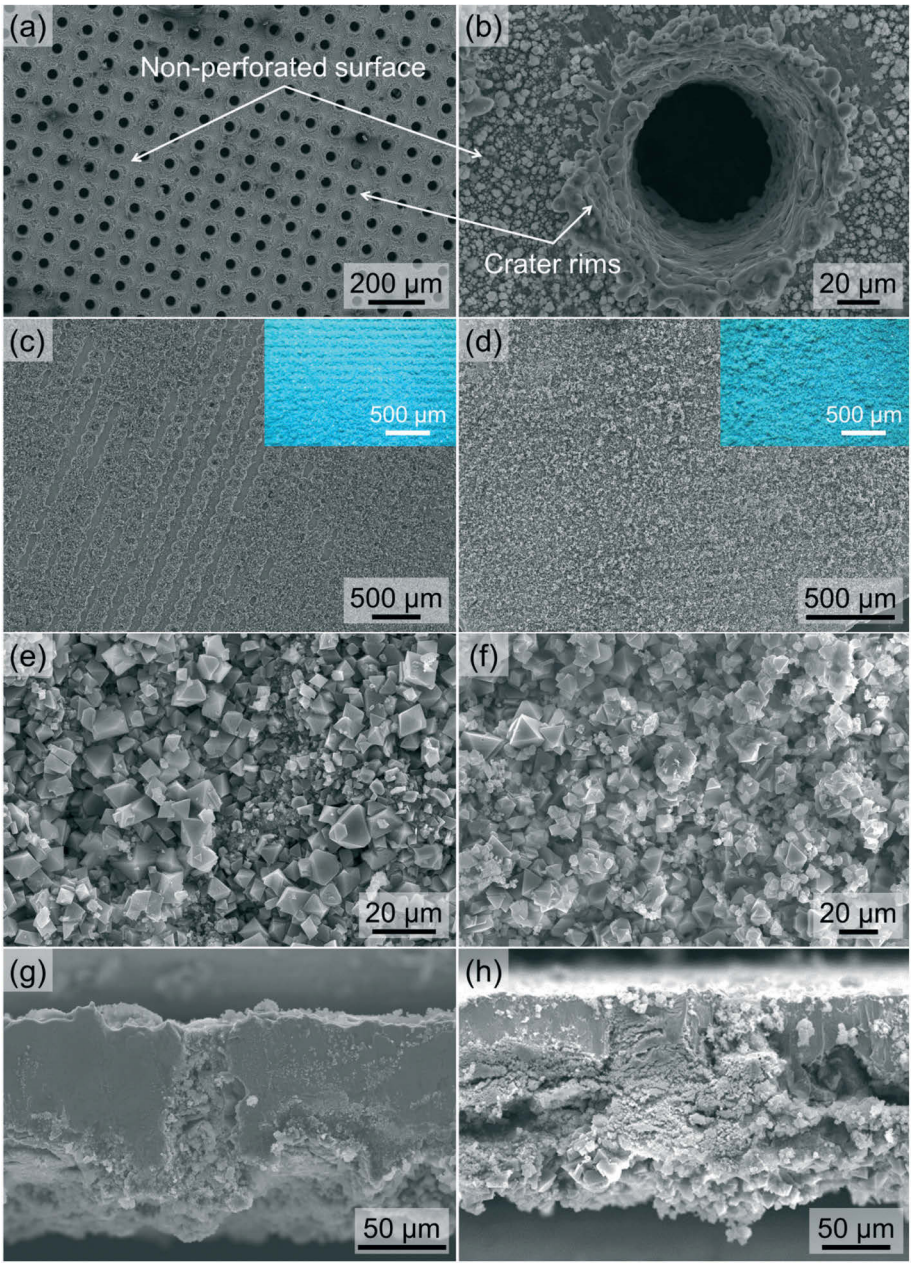

Fig. 2 Top view SEM images of (a) linear patterns and (b) a microhole detail from the laser-irradiated side of the brass support, (c and e) sample 1 and (d and f) sample 2. Insets in images (c) and (d) are the corresponding optical images. Cross-sectional SEM images of (g) sample 1 and (h) sample 2.

potential of Zn in comparison to that of Cu facilitates the formation of ZnO instead of CuO. Although HKUST-1 is not constituted by Zn, ZnO could affect and assist the formation of the MOF acting as heterogeneous nucleation sites.[54] On the other hand, the higher content of Cu species in the crater rims may facilitate the growth of HKUST-1 crystals on them.

Characterization of HKUST-1 coatings on microperforated brass supports

The thermal gradient approach was developed by Jeremias and co-workers in 2012.[37] They used the thermal gradient synthesis to grow a dense HKUST-1 layer on a copper substrate. Conductivity tests were carried out, determining good heat transfer between the MOF and the metallic sheet. A similar procedure was reported by Tatlier and Erdem-Senatalar in 1999.[38] They prepared zeolite 4A coatings on stainless steel substrates to enhance the mass and heat transfer in adsorption heat pumps. Here, HKUST-1 coatings were synthesized on laser-microperforated brass supports instead of bare substrates to improve the MOF–metal interaction, as mentioned above, and water sorption studies were carried out (see below). HKUST-1 was selected as the adsorbent because it is one of the most investigated hydrophilic MOFs, thus its properties

such as thermal and chemical stabilities and high surface area are well-known. Concerning its water vapour stability, Low *et al.*[55] placed HKUST-1 in the moderate steam stability region. In contrast, the studies of Küsgens *et al.*[35] and Henninger *et al.*[9] concluded that this MOF degrades upon vapour exposure and under hydrothermal conditions, respectively.

Sample 1 and sample 2 were prepared following conditions similar to those used by Jeremias *et al.*,[37] but the heating block surface (100 and 150 °C) and cooling bath (10 and 75 °C) temperatures were different (Table S1†). As a result, sample 1 achieved a 2.4 wt% MOF loading, whereas sample 2 achieved a 6.6 wt% MOF loading. The increase in the block surface temperature for sample 2 led to a higher reaction rate, resulting in the formation of more MOF material. OM images reveal that both sheets were completely coated with blue crystals (see insets in Fig. 2). The PXRD patterns of sample 1 and sample 2 are in good agreement with the simulated pattern of HKUST-1,[50] confirming that the blue crystals were HKUST-1 (Fig. 3). No peaks related to ZnO or CuO are observable. In contrast, contributions of Cu_2O and a rouaite phase from $Cu_2NO_3(OH)_3$ are present (denoted in Fig. 3 by black rhombi and circles), as reported in the article by Jeremias *et al.*[37] Sample 1 is mostly composed of HKUST-1, with only weak intensities coming from the abovementioned impurities. On the other hand, the stronger intensities of peaks in sample 2 related to Cu_2O and rouaite phases denote a higher content of impurities. Sample 1 was not uniformly coated with MOF crystals, as observed in Fig. 2c. HKUST-1 principally adhered to the rough edges and not to the non-perforated surface. Thus, MOF formation was benefited from a larger amount of Cu on crater rims and the creation of roughness in spite of the higher presence of metallic oxides on the surface between holes. Unlike sample 1, sample 2 was completely covered by crystals (Fig. 2d), thus the higher temperature synthesis favoured the formation of a continuous coating. Microholes were blocked with crystals for both samples (Fig. 2g and h). The crystals exhibit an octahedral shape typical for HKUST-1 (Fig. 2e and f). The crystal size distribution for both samples is heterogeneous with sizes ranging from 1 to 15 μm and from 2 to 30 μm for sample 1 and sample 2, respectively. The thicknesses of the HKUST-1 layers are about 26 for sample 1 and 42 μm for sample 2, as seen in Fig. 4. The larger size of the crystals and layer thickness in sample 2 are due to the higher reaction temperature of 150 °C used in its synthesis. The existence of Zn deposits on the brass substrates after laser irradiation could have brought about the appearance of Zn–HKUST-1, a polymorph of HKUST-1 with Zn^{2+} as the metal cation.[56,57] However, Zn–HKUST-1 crystals are colourless and cubic. If the Zn analogue had been formed in large amounts, its presence would have been identified through SEM, PXRD and OM characterization.

EDX analysis was performed on the cross-sections of both samples in order to visualize the deposition of the MOF (Fig. 4). The different elemental mappings show areas where the Cu and Zn concentrations are higher corresponding to the brass support while higher O and C concentrations indicate the MOF. In the Zn + O + C-overlaid images, the thorough hole-filling is clearly visualized. Some MOF crystals were also deposited on the laser-irradiated side of the support, where the C and O density is higher. The N_2 physisorption isotherm at 77 K of sample 2 and its corresponding correction using the MOF weight fraction are displayed in Fig. S2.† As the metal substrate does not exhibit any adsorption, isotherm data were divided by the actual MOF weight fraction (wt%) to correct the uptake values, referencing them to the amount of MOF. The N_2 isotherms are a combination of types I and IV, typical for microporous and mesoporous materials. This implies the presence of hierarchical porosity,[58] with some mesoporosity coming from intercrystalline voids, in accordance with a thin hysteresis loop from p/p_0 = 0.4. The BET specific surface area for the corrected sample 2 (1105 $m^2\ g^{-1}$) is found among the values reported in the literature for HKUST-1 powder (Table S3†). This is consistent with the formation of high-quality MOF crystals.

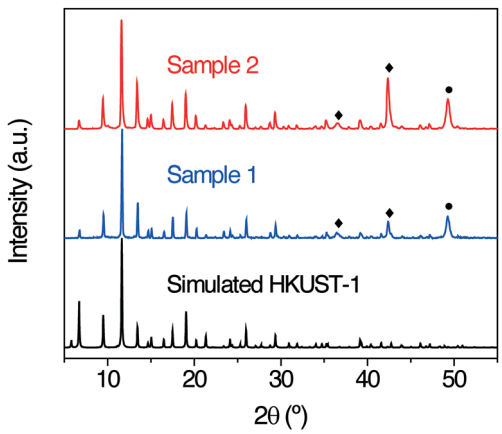

Fig. 3 PXRD patterns of sample 1 and sample 2 in comparison with that of simulated HKUST-1 (CCDC 943009).[50] Symbols denote peaks assignable to: ♦, Cu_2O and ●, rouaite $Cu_2NO_3(OH)_3$.

Water adsorption of HKUST-1 coatings

Water adsorption was carried out on sample 1 and sample 2 at 293 K. Besides the adsorption data for the composite sample, isotherms obtained through the correction with the MOF weight percent are also depicted in Fig. 5. Water adsorption occurs in a two-step fashion. According to the work developed by Küsgens *et al.*,[35] the first step (p/p_0 = 0.04–0.16) corresponds to the filling of more hydrophilic (cuboctahedral, 11 Å) pores *via* interaction of water with CUS. The second step (p/p_0 = 0.16–0.4) is related to either total filling of cuboctahedral pores or filling of less hydrophilic (octahedral, 5 Å) cages.[35] Water adsorption on HKUST-1 pores is a controversial issue since it has also been suggested that the filling of water could take place first on the octahedral micropores with the consecutive adsorption on the cuboctahedral cavities.[59] The slight increase in adsorption above p/p_0 = 0.8

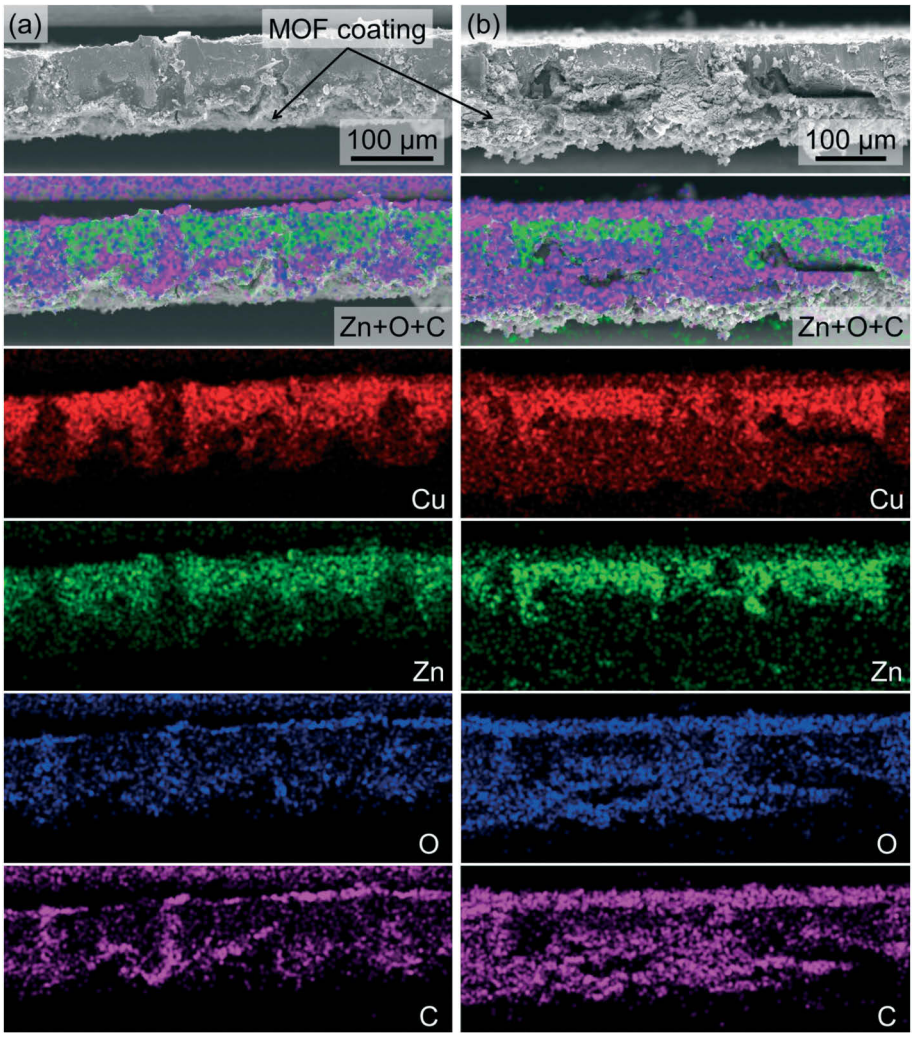

Fig. 4 Cross-sectional EDX mapping images of (a) sample 1 and (b) sample 2. Cu, Zn, O and C are represented in red, green, blue and pink, respectively. The laser-irradiated sides of the supports are facing down. In the Zn + C + O-overlaid images (second row from the top), Cu has been omitted for better contrast as it is part of both HKUST-1 and the perforated brass support. The crystalline non-coloured part of the sample at the bottom of the layered image is the surface of the MOF layer which is not part of the elemental map because it is located in a further distance from the electron beam compared to the cross-section of the sample. Zn and Cu are also detected outside the sample cross-sections because the sample holder is made from brass.

indicates water condensation in voids between MOF particles.[35] Hysteresis is promoted due to the strong hydrogen bonds between water molecules.[35] Furthermore, the chemisorption of water molecules by copper sites caused an open hysteresis loop, denoting an irreversible process.[35] It is worth mentioning that the adsorption phenomenon takes place mainly at a low relative pressure range, being of great interest for thermally driven chillers or adsorption-based heat pumps, where the working relative pressure region is p/p_0 = 0.05–0.32.[17] When comparing water adsorption capacities with HKUST-1 powder data from other studies (Table 1), the corrected uptakes for sample 1 and sample 2 (at 293 K) are observed within the range of the reported values (at 298 K). Although the uptake of sample 2 was slightly lower than that of sample 1, both capacities were similar. The presence of Cu_2O and rouaite $Cu_2NO_3(OH)_3$ impurities could explain the difference in the water uptake. Concerning HKUST-1 thin films, the corrected values for sample 1 and sample 2 also fall between the uptakes for an HKUST-1 coating on a QCM-gold electrode (at 294 K and p/p_0 = 0.8)[60] and a 60 layer HKUST-1 film on a hydroxylated SiO_2 support (at 298 K).[61] The advantage of MOF attachment on microperforated metal sheets is the improvement of both high adsorbent loading (*ca.* 66 mg of MOF per g of support) with more uniform crystal coatings and MOF–support interaction. Besides, water adsorption could be favoured due to a better MOF distribution on the substrate and the presence of accessible intercrystalline voids (external surface area). This would enhance the contact and interaction between water molecules and HKUST-1 crystals, thus improving the mass and heat transfer. The benefits originating from growing HKUST-1 coatings on microperforated brass sheets as well as the remarkable water adsorption capacity of samples may promote their use in applications such as heat pumps and adsorption chillers.

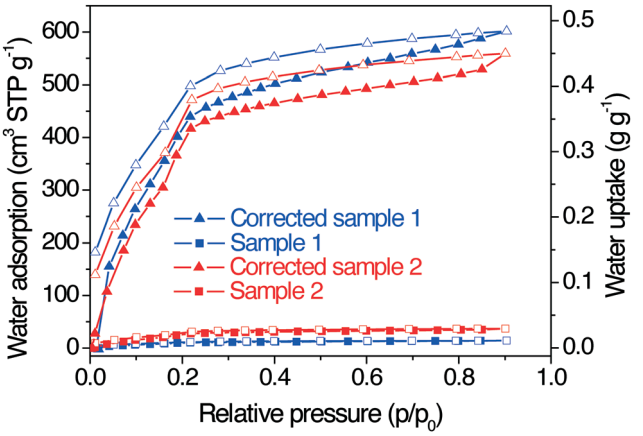

Fig. 5 Water adsorption and desorption isotherms at 293 K of sample 1 and sample 2 and the corresponding corrected ones (values divided by the MOF weight fraction of 2.4 and 6.6 wt% for sample 1 and sample 2, respectively). Full and empty symbols for adsorption and desorption branches, respectively.

Table 1 Water adsorption capacities of different HKUST-1 powder and thin films at p/p_0 = 0.9 and 298 K (unless specified)

Sample	Water uptake (g g^{-1} MOF)	Ref.
HKUST-1	0.51[a]	35
HKUST-1	~0.52[a,b]	64
HKUST-1	~0.40[a]	65
HKUST-1	0.58	12
HKUST-1	0.46[a]	66
Basolite C300 (commercial HKUST-1)	0.55	16
HKUST-1/QCM-gold electrode	0.26[b,c]	60
HKUST-1 (60 layers)/SiO_2	0.61	61
Corrected sample 1	0.48[d]	This work
Corrected sample 2	0.45[d]	This work

[a] Data obtained from water isotherms of the corresponding references. [b] Value at p/p_0 = 0.8 because of condensation at higher relative pressures. [c] Measured at 294 K. [d] At 293 K.

Although the insufficient water vapour stability of HKUST-1 could be a barrier for further development, it can be obviated by using other working fluids such as methanol.[15,62,63] HKUST-1 features a type-I adsorption isotherm for MeOH and exhibits a methanol loading lift of *ca.* 0.5 g g^{-1}, and it turned out that it retains its crystallinity even after several thousands of methanol adsorption–desorption cycles.[15] HKUST-1 layers on microperforated supports may also be employed in catalysis, membrane reactors, gas separation and storage, and sensor technology.

Conclusions

This work deals with MOF HKUST-1 layers on laser-microperforated brass sheets synthesized according to the thermal gradient procedure. The formation of HKUST-1 on the supports was confirmed by PXRD patterns where the presence of phases as Cu_2O and rouaite $Cu_2NO_3(OH)_3$ was also observed. High-quality crystals were produced, as demonstrated by PXRD and N_2 physisorption characterization. The coating thickness and crystal size depended on the reaction temperature. Microholes were completely filled by HKUST-1 crystals. Creation of roughness after laser irradiation and a larger Cu content on crater rims caused crystal growth to take place at the channel edges preferentially. The use of a higher reaction temperature (150 °C) ensured that the brass substrate was totally covered with MOF crystals. Corrected water capacities and the BET surface area values fell within the reported values for HKUST-1 powder, demonstrating full adsorbate access to the supported HKUST-1 crystals, for which then also other gas storage applications could be envisioned. Corrected water adsorption isotherms showed that the main adsorption step occurred at a low relative pressure. The benefits of perforating brass supports with laser irradiation include an improvement of MOF attachment and a better arrangement of crystals all over the surface, giving rise to strongly and uniformly adhered coatings without the use of any organic binder which might alter the adsorption capacity of the active MOF material in the MOF–metal composite. These properties could result in faster water uptake in the MOF due to improved mass and heat transfer, aided by the presence of accessible intercrystalline spaces (which suggests the formation of a hierarchical porous structure). Consequently, and considering the features of the target MOF, the HKUST-1 coatings prepared here could be used in a number of applications related to separation and storage, sensing and catalysis, among others.

Acknowledgements

The authors thank the financial support from the Spanish Ministry of Economy and Competitiveness (MAT2013-40556-R, PRI-PIMNIN-2011-1478) as well as the European Social Fund (ESF) through the Aragón Government (DGA, T05). A. P.-C. acknowledges a Ph.D. grant from DGA. Support of the work of C. J. by the BMBF project OptiMat 03SF0492C is gratefully acknowledged. The New INDIGO platform from FP7 (INDIGO-DST1-014) is also thanked.

References

1 R. K. de Richter, T. Z. Ming, S. Caillol and W. Liu, *Int. J. Greenhouse Gas Control*, 2016, **49**, 449–472.
2 J. Deng, R. Z. Wang and G. Y. Han, *Prog. Energy Combust. Sci.*, 2011, **37**, 172–203.
3 R. E. Critoph and Y. Zhong, *Proc. Inst. Mech. Eng., Part E*, 2005, **219**, 285–300.
4 K. Habib, B. B. Saha, A. Chakraborty, S. T. Oh and S. Koyama, *Appl. Therm. Eng.*, 2013, **50**, 1582–1589.
5 A. M. W. Wojcik, J. C. Jansen and T. Maschmeyer, *Microporous Mesoporous Mater.*, 2001, **43**, 313–317.
6 M. Wickenheisser, T. Paul and C. Janiak, *Microporous Mesoporous Mater.*, 2016, **220**, 258–269.
7 R. Z. Wang and R. G. Oliveira, *Prog. Energy Combust. Sci.*, 2006, **32**, 424–458.

8 S. K. Henninger, H. A. Habib and C. Janiak, *J. Am. Chem. Soc.*, 2009, **131**, 2776–2777.
9 S. K. Henninger, F. P. Schmidt and H. M. Henning, *Appl. Therm. Eng.*, 2010, **30**, 1692–1702.
10 J. Ehrenmann, S. K. Henninger and C. Janiak, *Eur. J. Inorg. Chem.*, 2011, 471–474.
11 S. K. Henninger, F. Jeremias, H. Kummer and C. Janiak, *Eur. J. Inorg. Chem.*, 2012, 2625–2634.
12 J. B. DeCoste, G. W. Peterson, B. J. Schindler, K. L. Killops, M. A. Browe and J. J. Mahle, *J. Mater. Chem. A*, 2013, **1**, 11922–11932.
13 M. Wickenheisser, F. Jeremias, S. K. Henninger and C. Janiak, *Inorg. Chim. Acta*, 2013, **407**, 145–152.
14 D. Fröhlich, S. K. Henninger and C. Janiak, *Dalton Trans.*, 2014, **43**, 15300–15304.
15 F. Jeremias, D. Fröhlich, C. Janiak and S. K. Henninger, *New J. Chem.*, 2014, **38**, 1846–1852.
16 H. Furukawa, F. Gandara, Y. B. Zhang, J. Jiang, W. L. Queen, M. R. Hudson and O. M. Yaghi, *J. Am. Chem. Soc.*, 2014, **136**, 4369–4381.
17 J. Canivet, A. Fateeva, Y. Guo, B. Coasne and D. Farrusseng, *Chem. Soc. Rev.*, 2014, **43**, 5594–5617.
18 C. Serre, F. Millange, C. Thouvenot, M. Noguès, G. Marsolier, D. Louer and G. Férey, *J. Am. Chem. Soc.*, 2002, **124**, 13519–13526.
19 S. Kitagawa, R. Kitaura and S. Noro, *Angew. Chem., Int. Ed.*, 2004, **43**, 2334–2375.
20 S. L. Qiu and G. S. Zhu, *Coord. Chem. Rev.*, 2009, **253**, 2891–2911.
21 A. Perea-Cachero, B. Seoane, B. Diosdado, C. Téllez and J. Coronas, *RSC Adv.*, 2016, **6**, 260–268.
22 P. Amo-Ochoa and F. Zamora, *Coord. Chem. Rev.*, 2014, **276**, 34–58.
23 D. Y. Hong, Y. K. Hwang, C. Serre, G. Férey and J. S. Chang, *Adv. Funct. Mater.*, 2009, **19**, 1537–1552.
24 W. Xuan, C. Zhu, Y. Liu and Y. Cui, *Chem. Soc. Rev.*, 2012, **41**, 1677–1695.
25 N. Liédana, A. Galve, C. Rubio, C. Téllez and J. Coronas, *ACS Appl. Mater. Interfaces*, 2012, **4**, 5016–5021.
26 H. J. Park, D. W. Lim, W. S. Yang, T. R. Oh and M. P. Suh, *Chem. – Eur. J.*, 2011, **17**, 7251–7260.
27 L. M. Huang, H. T. Wang, J. X. Chen, Z. B. Wang, J. Y. Sun, D. Y. Zhao and Y. S. Yan, *Microporous Mesoporous Mater.*, 2003, **58**, 105–114.
28 O. K. Farha and J. T. Hupp, *Acc. Chem. Res.*, 2010, **43**, 1166–1175.
29 S. S. Y. Chui, S. M. F. Lo, J. P. H. Charmant, A. G. Orpen and I. D. Williams, *Science*, 1999, **283**, 1148–1150.
30 K. Schlichte, T. Kratzke and S. Kaskel, *Microporous Mesoporous Mater.*, 2004, **73**, 81–88.
31 P. Krawiec, M. Kramer, M. Sabo, R. Kunschke, H. Frode and S. Kaskel, *Adv. Eng. Mater.*, 2006, **8**, 293–296.
32 Q. Yang, C. Xue, C. Zhong and J. F. Chen, *AIChE J.*, 2007, **53**, 2832–2840.
33 J. A. Mason, M. Veenstra and J. R. Long, *Chem. Sci.*, 2014, **5**, 32–51.
34 A. Tahli, R. F. M. Elshaarawy, Ü. Köc, A. C. Kautz and C. Janiak, *Polyhedron*, 2016, **117**, 579–584.
35 P. Küsgens, M. Rose, I. Senkovska, H. Fröde, A. Henschel, S. Siegle and S. Kaskel, *Microporous Mesoporous Mater.*, 2009, **120**, 325–330.
36 S. Loera-Serna, M. A. Oliver-Tolentino, M. de Lourdes López-Núñez, A. Santana-Cruz, A. Guzmán-Vargas, R. Cabrera-Sierra, H. I. Beltrán and J. Flores, *J. Alloys Compd.*, 2012, **540**, 113–120.
37 F. Jeremias, S. K. Henninger and C. Janiak, *Chem. Commun.*, 2012, **48**, 9708–9710.
38 M. Tatlier and A. Erdem-Senatalar, Studies in Surface Science and Catalysis, in *Porous Materials in Environmentally Friendly Processes*, ed. I. Kiricsi, G. PalBorbely, J. B. Nagy and H. G. Karge, Elsevier Science B. V., Amsterdam, The Netherlands, 1st edn, 1999, vol. 125, pp. 101–108.
39 F. Jeremias, D. Fröhlich, C. Janiak and S. K. Henninger, *RSC Adv.*, 2014, **4**, 24073–24082.
40 M. R. H. Knowles, G. Rutterford, D. Karnakis and A. Ferguson, *Int. J. Adv. Des. Manuf. Technol.*, 2007, **33**, 95–102.
41 A. Weck, T. H. R. Crawford, D. S. Wilkinson, H. K. Haugen and J. S. Preston, *Appl. Phys. A: Mater. Sci. Process.*, 2008, **90**, 537–543.
42 F. Chen, D. Zhang, Q. Yang, J. Yong, G. Du, J. Si, F. Yun and X. Hou, *ACS Appl. Mater. Interfaces*, 2013, **5**, 6777–6792.
43 A. M. Emelyanenko, F. M. Shagieva, A. G. Domantovsky and L. B. Boinovich, *Appl. Surf. Sci.*, 2015, **332**, 513–517.
44 E. Rebollar, I. Frischauf, M. Olbrich, T. Peterbauer, S. Hering, J. Preiner, P. Hinterdorfer, C. Romanin and J. Heitz, *Biomaterials*, 2008, **29**, 1796–1806.
45 A. Kurella and N. B. Dahotre, *J. Biomater. Appl.*, 2005, **20**, 5–50.
46 K. Kordas, A. E. Pap, J. Saavalainen, H. Jantunen, P. Moilanen, E. Haapaniemi and S. Leppavuori, *IEEE Trans. Adv. Packag.*, 2005, **28**, 259–263.
47 E. Mateo, R. Lahoz, G. F. de la Fuente, A. Paniagua, J. Coronas and J. Santamaría, *Chem. Mater.*, 2004, **16**, 4847–4850.
48 M. Navarro, B. Seoane, E. Mateo, R. Lahoz, G. F. de la Fuente and J. Coronas, *J. Mater. Chem. A*, 2014, **2**, 11177–11184.
49 H. Putz and K. Brandenburg, *Diamond - Crystal and Molecular Structure Visualization*, Brandenburg GbR, Bonn, Germany, 2016.
50 A. A. Yakovenko, J. H. Reibenspies, N. Bhuvanesh and H. C. Zhou, *J. Appl. Crystallogr.*, 2013, **46**, 346–353.
51 D. N. Patel, R. P. Singh and R. K. Thareja, *Appl. Surf. Sci.*, 2014, **288**, 550–557.
52 C. Y. Liu, X. L. Mao, S. S. Mao, R. Greif and R. E. Russo, *Anal. Chem.*, 2005, **77**, 6687–6691.
53 H. R. Kuhn and D. Gunther, *Anal. Chem.*, 2003, **75**, 747–753.
54 S. M. Meckler, C. Y. Li, W. L. Queen, T. E. Williams, J. R. Long, R. Buonsanti, D. J. Milliron and B. A. Helms, *Chem. Mater.*, 2015, **27**, 7673–7679.
55 J. J. Low, A. I. Benin, P. Jakubczak, J. F. Abrahamian, S. A. Faheem and R. R. Willis, *J. Am. Chem. Soc.*, 2009, **131**, 15834–15842.

56 J. I. Feldblyum, M. Liu, D. W. Gidley and A. J. Matzger, *J. Am. Chem. Soc.*, 2011, **133**, 18257–18263.
57 M. K. Bhunia, J. T. Hughes, J. C. Fettinger and A. Navrotsky, *Langmuir*, 2013, **29**, 8140–8145.
58 J. Huo, M. Brightwell, S. El Hankari, A. Garai and D. Bradshaw, *J. Mater. Chem. A*, 2013, **1**, 15220–15223.
59 D. Wu, X. Guo, H. Sun and A. Navrotsky, *J. Phys. Chem. C*, 2016, **120**, 7562–7567.
60 E. Biemmi, A. Darga, N. Stock and T. Bein, *Microporous Mesoporous Mater.*, 2008, **114**, 380–386.
61 N. Nijem, K. Fürsich, S. T. Kelly, C. Swain, S. R. Leone and M. K. Gilles, *Cryst. Growth Des.*, 2015, **15**, 2948–2957.
62 M. F. de Lange, B. L. van Velzen, C. P. Ottevanger, K. Verouden, L. C. Lin, T. J. H. Vlugt, J. Gascón and F. Kapteijn, *Langmuir*, 2015, **31**, 12783–12796.
63 B. T. Nguyen, H. L. Nguyen, T. C. Nguyen, K. E. Cordova and H. Furukawa, *Chem. Mater.*, 2016, **28**, 6243–6249.
64 P. M. Schoenecker, C. G. Carson, H. Jasuja, C. J. J. Flemming and K. S. Walton, *Ind. Eng. Chem. Res.*, 2012, **51**, 6513–6519.
65 M. Gaab, N. Trukhan, S. Maurer, R. Gummaraju and U. Müller, *Microporous Mesoporous Mater.*, 2012, **157**, 131–136.
66 A. Rezk, R. Al-Dadah, S. Mahmoud and A. Elsayed, *Int. J. Heat Mass Transfer*, 2012, **55**, 7366–7374.

Electronic Supplementary Material (ESI) for CrystEngComm.

Supporting Information

HKUST-1 coatings on laser microperforated brass supports for water adsorption

Adelaida Perea-Cachero,[a†] Janina Dechnik,[b†] Ruth Lahoz,[c] Christoph Janiak,[b*] Carlos Téllez[a] and Joaquín Coronas[a*]

aChemical and Environmental Engineering Department and Instituto de Nanociencia de Aragón (INA), Universidad de Zaragoza, 50018 Zaragoza, Spain

bInstitut für Anorganische Chemie und Strukturchemie, Heinrich-Heine Universität Düsseldorf, 40204 Düsseldorf, Germany

cCentro de Química y Materiales de Aragón (CEQMA), CSIC-Universidad de Zaragoza, 50018 Zaragoza, Spain

*J. Coronas, e-mail: coronas@unizar.es, Tel: (+34) 976762471; C. Janiak, e-mail: janiak@uni-duesseldorf.de, Tel: (+49) 2118111580.

† These two authors contributed equally.

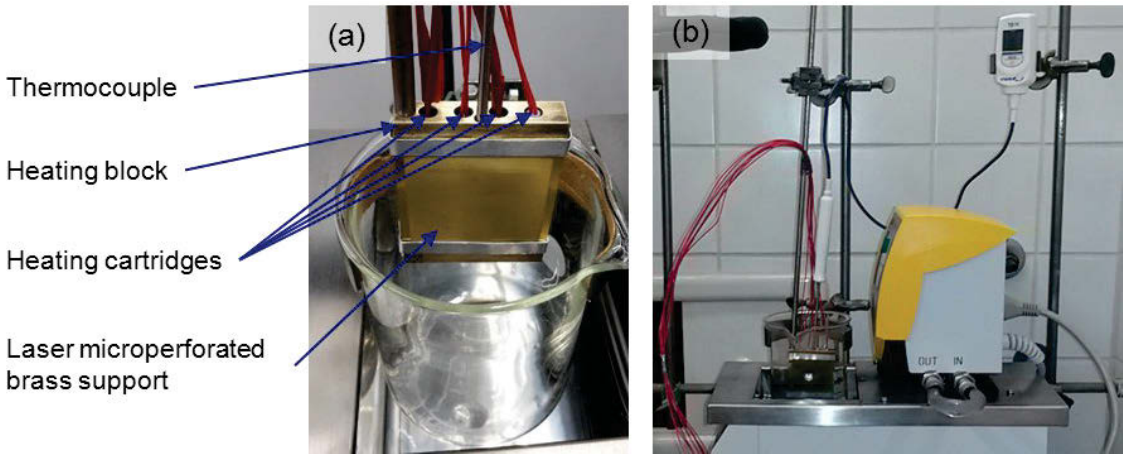

Figure S1. (a) Thermal gradient setup used in this work. (b) Heating block assembly.

Table S1. Parameters in the synthesis of sample 1 and sample 2

Sample	Synthesis conditions			Support mass (before synthesis) (mg)	Support + MOF loading (after synthesis) (mg)	MOF weight fraction (wt%)[a]
	$T_{surface}$ (°C)	T_{bath} (°C)	t (h)			
Sample 1	100	10	2	353.7	362.2	2.35
Sample 2	150	75	2	407.0	435.9	6.63

[a] The MOF weight fraction was calculated as the percentage of deposited mass of MOF after synthesis divided by the sum of the mass of MOF and the perforated metallic support.

Table S2. Composition of brass supports by EDX analysis

	Atomic %			Cu/Zn ratio
	Cu	Zn	O	
Before perforation	68	30	2	2.3
Crater rim (after perforation)	49	35	16	1.4
Non-perforated surface (after perforation)	31	32	37	1.0

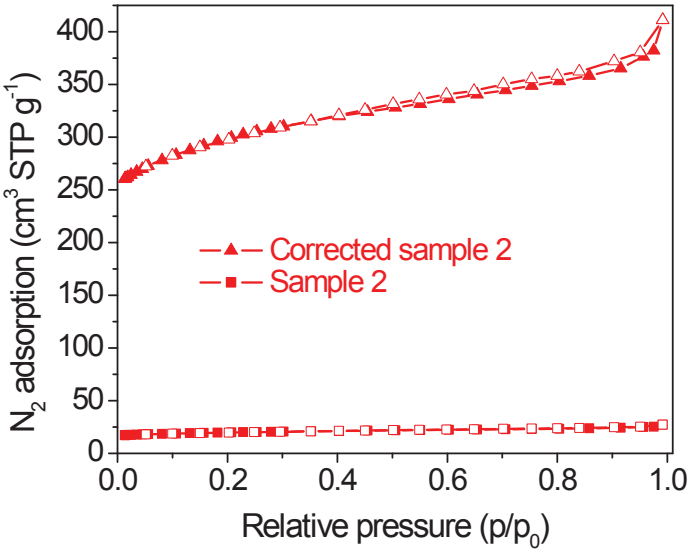

Figure S2. N_2 physisorption isotherms measured at 77 K of sample 2 and corrected sample 2 (calculated by dividing the isotherm data of sample 2 by the MOF weight fraction of 6.63 wt%). Full and empty symbols indicate adsorption and desorption data, respectively.

Table S3. BET surface area comparison for some HKUST-1 materials

Sample	S_{BET} (m^2 g^{-1})	Reference
HKUST-1	692-1944	[1-3]
Sample 2	73	This work
Corrected sample 2	1105[a]	This work

[a] Value achieved from N_2 isotherms (adsorption branch) when dividing the sorption data of sample 2 by the MOF weight fraction of 6.63 wt%.

References

1. S. S. Y. Chui, S. M. F. Lo, J. P. H. Charmant, A. G. Orpen and I. D. Williams, *Science*, 1999, **283**, 1148-1150.
2. A. G. Wong-Foy, A. J. Matzger and O. M. Yaghi, *J. Am. Chem. Soc.*, 2006, **128**, 3494-3495.
3. M. Klimakow, P. Klobes, K. Rademann and F. Emmerling, *Microporous Mesoporous Mater.*, 2012, **154**, 113-118.

3.4 Luminescent Metal-Organic Framework Mixed-Matrix Membranes from Lanthanide Metal-Organic Frameworks in Polysulfone and Matrimid

Janina Dechnik, Friedrich Mühlbach, Dennis Dietrich, Tobias Wehner, Marcus Gutmann, Tessa Lühmann, Lorenz Meinel, Christoph Janiak und Klaus Müller-Buschbaum

Eur. J. Inorg. Chem. **2016**, *27*, 4408-4415.

DOI: 10.1002/ejic.201600235, Quelle[219]

MOF-MMMs wurden durch Einbettung lumineszierender Lanthanoid (Ln) MOFs 3D-$[Sr_{0.9}Eu_{0.1}Im_2]$ und 2D-$[Tb_2Cl_6(bipy)_3]\cdot 2bipy$ (Im^- = Imidazolat, Bipy = 4,4'-Bipyridin) in Polysulfon (PSF) und Matrimid-Polymerfilme hergestellt. Die erfolgreiche Einbettung der MOFs wurde für beide Matrix-Polymere erreicht und die ursprüngliche MOF-Lumineszenz wurde beibehalten. Die defektfreie Natur der Membranen wurde durch die verringerte Gaspermeation der MMMs mit den nicht porösen Füllstoffpartikeln nachgewiesen. Für das Tb-bipy-MOF ist eine erfolgreiche Einbettung nur mit Polysulfon möglich. Zur Herstellung der MOF-Polymermembranen wurde der Einfluss unterschiedlicher Massenanteile der lumineszierenden MOFs von 8-16 Gew.-% und die Herstellung aus Suspensionen mit und ohne Ultraschallbehandlung untersucht. Der Einfluss der MOF-Anteile ist für beide Membranmaterialien unterschiedlich. Für PSF sind niedrigere Mengen an MOF von Vorteil und führen zu einer Erhöhung der Gesamtlumineszenzintensität, während das Gegenteil für Matrimid beobachtet wurde. Insgesamt ist die Emission der Eu^{2+}-Ionen stärker als die Tb^{3+}-Emission und führt zu Membranen mit starker Emission, die bei normalem Tageslicht für das bloße Auge sichtbar ist. Damit öffnen die Ln-MOF-Polymermembranen neue Möglichkeiten für die Handhabung von lumineszierenden MOFs.

Anteil an der Veröffentlichung

- Herstellung und grundlegende Analytik der Ln-MOF-MMMs. Durchführung der O_2-Permeationsmessungen.
- Dennis Dietrich war ebenfalls an der Herstellung der Ln-MOF-MMMs beteiligt und fertigte die REM-Aufnahmen an.
- Die Synthese der MOFs und die Fluoreszenzspektroskopie wurden von Friedrich Mühlbach, Tobias Wehner und Klaus Müller Buschbaum durchgeführt.
- Lorenz Meinel, Tessa Lühmann und Marcus Gutmann waren für die Fluoreszenzmikroskopischen Untersuchungen zuständig.
- Korrekturen wurden durch Christoph Janiak und Klaus Müller-Buschbaum vorgenommen.

ChemPubSoc Europe

DOI: 10.1002/ejic.201600235

EurJIC European Journal of Inorganic Chemistry

Full Paper

MOF Polymer Membranes

CLUSTER ISSUE

Luminescent Metal–Organic Framework Mixed-Matrix Membranes from Lanthanide Metal–Organic Frameworks in Polysulfone and Matrimid

Janina Dechnik,[a] Friedrich Mühlbach,[b] Dennis Dietrich,[a] Tobias Wehner,[b] Marcus Gutmann,[c] Tessa Lühmann,[c] Lorenz Meinel,[c] Christoph Janiak,*[a] and Klaus Müller-Buschbaum*[b]

Abstract: Metal–organic framework/polymer (MOF–polymer) mixed-matrix membranes (MMMs) have been prepared by embedding the luminescent lanthanide (Ln) MOFs $^{3}_{\infty}[Sr_{0.9}Eu_{0.1}Im_2]$ and $^{2}_{\infty}[Tb_2Cl_6(bipy)_3]\cdot 2bipy$ (Im^- = imidazolate, bipy = 4,4′-bipyridine) into polysulfone (PSF, Ultrason® S) and Matrimid® polymer films. The successful embedding of the Sr and Eu MOFs has been achieved for both matrixes, and the original MOF luminescence is maintained. The defect-free nature of the membranes was proven by the slightly lower gas permeation of the MMMs with the dense filler particles. For the Tb–bipy MOF, successful embedding is possible for polysulfone only. For the preparation of the MOF polymer membranes, the influence of different mass fractions of the luminescent MOFs ranging from 8–16 wt.-% and preparation from suspensions with and without ultrasonic radiation were studied. The influence of the MOF fraction is different for both membrane materials. For the polysulfone, lower amounts of MOF are preferable and lead to an increase of the overall luminescence intensity, whereas the opposite was observed for Matrimid. Altogether, the parity-allowed emission of the Eu^{2+} ions is apparently stronger than the Tb^{3+} emission and leads to membranes with strong emission that is visible to the naked eye under normal daylight. Thereby, the Ln MOF polymer membranes open new options for the handling of luminescent MOFs.

Introduction

Coordination polymers and metal–organic frameworks (MOFs) are a high research priority in coordination chemistry.[1] These hybrid materials exhibit a broad variety of physical properties,[2] and photoluminescence[3] and sensing are current focusses.[4] For the application of MOFs, as well as the availability of pure bulk materials, stability and processability play important roles. For technical applications, MOFs have to be formulated,[5] for example, as layers,[6] pressed into tablets,[7] fabricated into monolithic structures[8] or used as composite materials.[9] MOFs can also be luminescent as nanoparticles[10] or in thin films.[11]

MOF–polymer mixed-matrix membranes (MMMs) are established composites and have been investigated widely for gas separations.[12–15]

Among luminescent MOFs and coordination polymers, lanthanide-containing (Ln containing) compounds[16] are of special interest for photoluminescence owing to their beneficial photophysical properties through suitable metal–ligand combinations.[17] Effective Ln^{3+} luminescence is achieved by circumventing the low light-absorption coefficients of the 4f–4f transitions through the combination of the Ln^{3+} ions with suitable organic light-harvesting ligands that work as sensitizers for the metal emission (the so-called "antenna effect")[18] by transferring excitation energy from the ligand to the metal centers. MOFs with N-donor ligands, such as the series $^{2}_{\infty}[Ln_2Cl_6(bipy)_3]\cdot 2bipy$[19] (bipy = 4,4′-bipyridine), show effective antenna effects, as the energetic position of the singlet and triplet states[20] of the ligand in the coordination polymer matches with suitable excited metal states.[21] For example, the linker 1,2-di(4-pyridyl)ethylene exhibits both structural and electronic properties for the formation of coordination polymers with effective photoluminescence. In principle, the energetic positions of the involved excited ligand states[22] are exactly in the range for the possible sensitization of the lanthanide ions for visible or near-infrared emission.[23] Another option, although much less frequent for MOFs, is the use of the divalent Eu^{2+} ion, which utilizes 5d–4f transitions. These transitions are parity-allowed and strong; therefore, they do not require ligand sensitization, as the series $^{3}_{\infty}[Sr_{1-x}Eu_xIm_2]$ shows (Im^- = imidazolate).[24]

As a proof-of-principle, we show here that it is possible to embed luminescent MOFs into organic polysulfone (PSF) Ultrason® S 6010 and Matrimid® 5218 polymers and generate, to the best of our knowledge, the first luminescent MOF mixed-matrix

[a] Institut für Anorganische Chemie und Strukturchemie, Universität Düsseldorf, Universitätsstraße 1, 40225 Düsseldorf, Germany
E-mail: Christoph.Janiak@uni-duesseldorf.de
http://www.janiak.hhu.de/
[b] Institut für Anorganische Chemie, Universität Würzburg, Am Hubland, 97074 Würzburg, Germany
E-mail: k.mueller-buschbaum@uni-wuerzburg.de
[c] Institut für Pharmazie und Lebensmittelchemie, Universität Würzburg, Am Hubland, 97074 Würzburg, Germany

Supporting information and ORCID(s) from the author(s) for this article are available on the WWW under http://dx.doi.org/10.1002/ejic.201600235.

membranes (see Figure 1). The LnMOF@MMMs have been characterized by photoluminescence spectroscopy, X-ray powder diffraction, electron microscopy, energy-dispersive X-ray (EDX) analysis, gas permeation, and fluorescence microscopy.

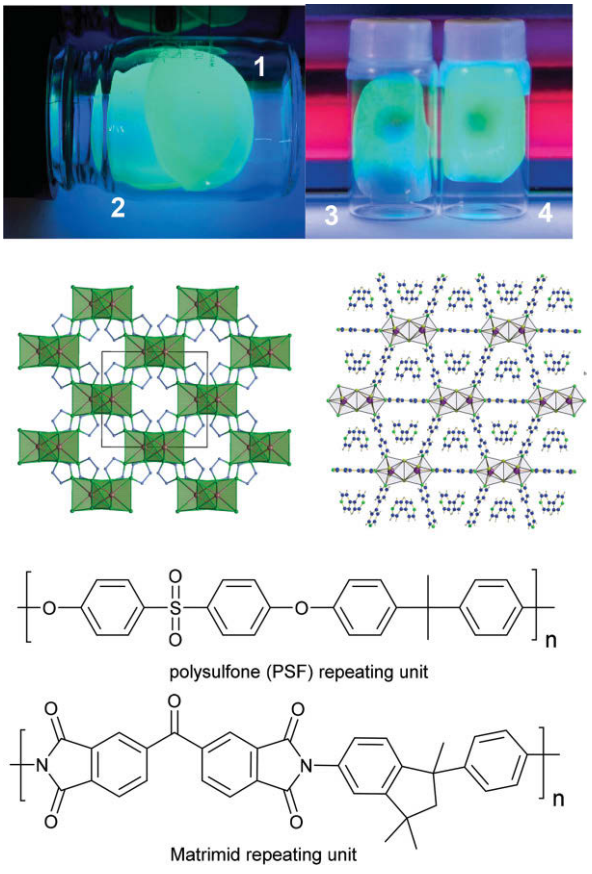

Figure 1. Top: The luminescent MOF MMMs $^3_\infty[Sr_{0.9}Eu_{0.1}Im_2]$@PSF (**1**: 8 wt.-% MOF; **2**: 16 wt.-% MOF) and $^3_\infty[Sr_{0.9}Eu_{0.1}Im_2]$@Matrimid (**3**: 8 wt.-% MOF; **4**: 16 wt.-% MOF). Center: The structures of the MOFs $^3_\infty[Sr_{0.9}Eu_{0.1}Im_2]$ (left) and $^2_\infty[Ln_2Cl_6(bipy)_3]$·2bipy (right), adapted from ref.[3f] with permission of the Royal Society of Chemistry, 2013. Bottom: PSF Ultrason® S and Matrimid®.

PSF[25] and Matrimid[26] are low-flux glassy polymers for gas-separation applications. Both polymers were chosen because of their good mechanical properties and availability. They are well-known to have good film-formation properties and are suitable matrixes for MMMs with MOFs as filler materials.[13]

The fillers are sensitive to hydrolysis and oxidation, which results in the loss of luminescence. To expand their processability for practical applications through embedding in or coating with a convenient polymer, the moisture stability of these compounds is expected to be enhanced.[27]

Results and Discussion

Preparation of LnMOF@polysulfone and LnMOF@Matrimid MMMs

For membrane preparation, the chosen amounts of MOF and polymer were combined under nitrogen in dichloromethane (DCM) and treated (by stirring or ultrasound) to form homogeneous dispersions (see Exp. Sect. for details). The dispersion was cast into metal rings on a flat glass surface in a desiccator filled with nitrogen gas and a desiccant. The conditions for film formation were chosen in terms of polymer concentration to influence the viscosity of the casting solution and time of stirring to form a homogeneous dispersion of the fillers in the casting solution. These factors are essential in the formation of defect-free MMMs with good filler dispersion. The solvent was evaporated overnight with a slight stream of predried nitrogen gas. The membrane was finally dried at 25 °C under reduced pressure. Eight different membranes of 5 cm diameter with 8 and 16 wt.-% MOF in ca. 200 mg of polymer were prepared this way (Table 1; see also Figure 1).

Table 1. Overview of prepared membranes.[a]

MOF@polymer	8 wt.-%	16 wt.-%
$^3_\infty[Sr_{0.9}Eu_{0.1}Im_2]$@PSF	**1**	**2**
$^3_\infty[Sr_{0.9}Eu_{0.1}Im_2]$@Matrimid	**3**	**4**
$^3_\infty[Sr_{0.9}Eu_{0.1}Im_2]$@Matrimid with ultrasound	**5**[b]	–
$^2_\infty[Tb_2Cl_6(bipy)_3]$·2bipy @PSF	**6**	**7**
$^2_\infty[Tb_2Cl_6(bipy)_3]$·2bipy @Matrimid	gel formation	gel formation
$^2_\infty[Tb_2Cl_6(bipy)_3]$·2bipy @PSF with ultrasound	**8**[b]	–

[a] Approximately 200 mg of polymer casted into 5 cm diameter membranes from 4 mL of CH_2Cl_2 dispersion. [b] 200 mg of polymer casted from 2 mL of CH_2Cl_2 dispersion.

Characterization of LnMOF@poylsulfone and LnMOF@Matrimid MMMs

Photoluminescence Spectroscopy

For all prepared MOF MMMs, excitation and emission spectra were recorded at room temperature. Both $^3_\infty[Sr_{0.9}Eu_{0.1}Im_2]$@PSF (**1** and **2**) and $^3_\infty[Sr_{0.9}Eu_{0.1}Im_2]$@Matrimid (**3** and **4**) show the typical excitation and emission spectra of their respective frameworks.[19,24] The membrane polymers were selected to allow MOF luminescence without interference with the polymer. For PSF, a weak fluorescence in the blue region is observed, whereas Matrimid does not show any significant luminescence. The combination of $^3_\infty[Sr_{0.9}Eu_{0.1}Im_2]$ with PSF shifts the excitation away from the polymer to the lower energies of the allowed Eu^{2+} excitation (see Figures 2, 3, and S5).

Therefore, the spectra exhibit transitions between the 4f ground state and excited 5d states of the Eu^{2+} ions. The luminescence is turquoise-green and strong, and no participation of the membrane polymer is detected (see Figure 2). Owing to the geometric differences between the ground and excited states, the peaks are broad with half-widths of ca. 75 nm and maxima at λ = 498 nm for **1** and **2** and λ = 500 nm for **3** and **4**.

For Matrimid®, a slight shift is observed for the 5d←4f Eu^{2+} excitation maximum from λ = 315 nm for the pure MOF to λ = 328 nm for the MMMs. This may hint towards an impact of the organic polymer on the Eu 5d states. However, the emission maxima and band profiles are similar within 2 nm. Moreover, the lifetimes of the luminescence processes give Eu^{2+} decay times τ_{obs} = 609(4) and 584(2) ns for the PSF membranes **1** and **2**, respectively, and τ_{obs} = 620(2) and 605(3) ns for the Matrimid membranes **3** and **4**, respectively. The similarities to the proper-

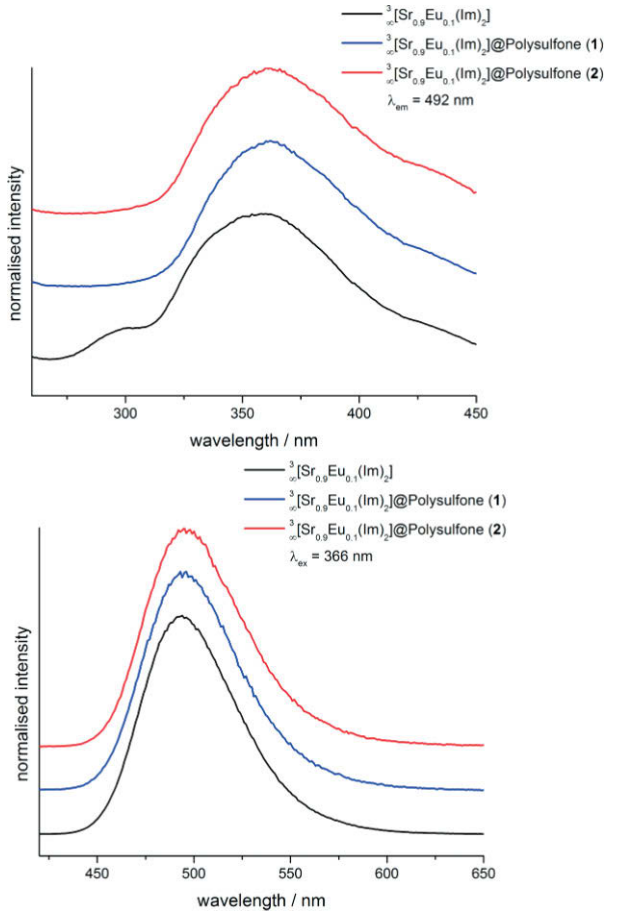

Figure 2. Normalized excitation (top) and emission spectra (bottom) of the framework $^3_\infty[Sr_{0.9}Eu_{0.1}Im_2]$ (black) in comparison with those of $^3_\infty[Sr_{0.9}Eu_{0.1}Im_2]$@PSF (blue: **1**, red: **2**); the MOF luminescence is maintained after the MOF is embedded in the polysulfone membrane.

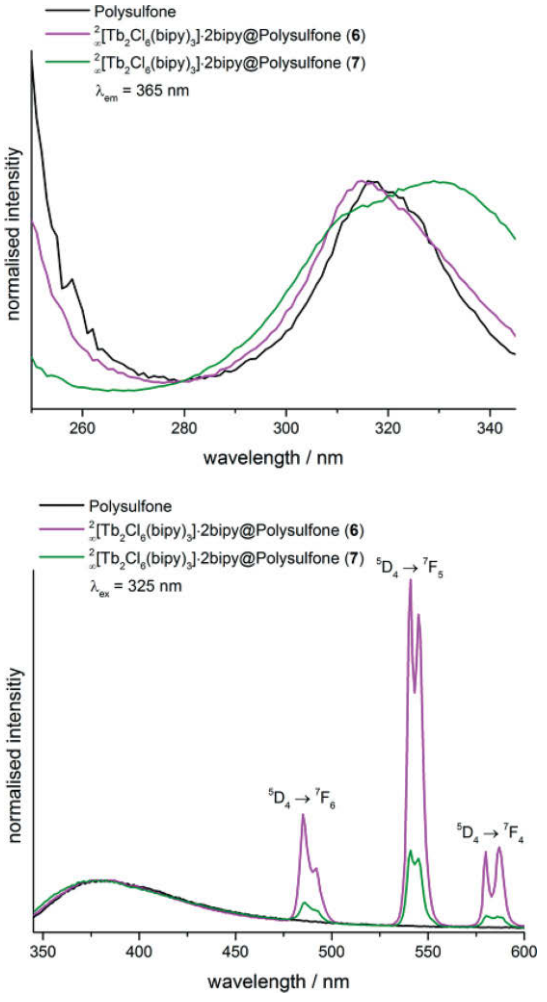

Figure 3. Excitation (top) and emission spectra (bottom) of the MMMs $^2_\infty[Tb_2Cl_6(bipy)_3]$·2bipy@PSF (**6**: purple, **7**: green) normalized for polysulfone and in comparison with those of polysulfone without MOF (black). The emission indicates the dependence of the luminescence intensity on the amount of MOF.

ties of the MOF itself are prominent; therefore, it is clear that the embedded framework is unaltered. This similarity was also present when the membranes were prepared from suspensions with [MMM **5**: τ = 601(3) ns] or without ultrasonic radiation (MMMs **1**–**4**).

It is intriguing that the intensity of the MOF luminescence depends on the amount of MOF and the membrane matrix material. For polysulfone, an inversely proportional behavior is observed, and higher emission intensities are observed for the lower MOF fraction; therefore, the higher amount of 16 wt.-% leads to concentration quenching, whereas the lower MOF fraction of only 8 wt.-% gives a significantly higher luminescence intensity (see also Figure S1). For Matrimid®, the opposite behavior is observed, and the intensity increases as the MOF fraction increases (see Figure S2). Therefore, polysulfone and Matrimid differ in their concentration quenching, which is not reached for 16 wt.-% MOF in Matrimid. A comparison of the absolute intensities is possible on the basis of the otherwise identical sample and instrumentation parameters.

For the MOF $^2_\infty[Tb_2Cl_6(bipy)_3]$·2bipy, the photoluminescence properties were determined for polysulfone membranes only, because of the gel formation of the MOF with Matrimid. For $^2_\infty[Tb_2Cl_6(bipy)_3]$·2bipy@PSF (**6** and **7**), the typical luminescence of the MOF can again be observed.[24] It is attributed to the 4f–4f transitions of the Tb^{3+} ions ($^5D_4 \rightarrow {}^7F_J$, J = 6–0) and leads to a green emission of the MOF. In addition, a broad emission of the PSF matrix is also visible in the blue region with a maximum at λ = 380 nm. This is possible as the Tb^{3+} emission is less intense than the Eu^{2+} emission (see also Figures 3, S3, and S4).

The excitation spectra are again similar to that of the MOF and exhibit light absorption mainly by the 4,4′-bipyridine ligand together with weak excitation of the PSF matrix. A comparison of the excitation and emission spectra of the MMMs **6** and **7** with that of the pure MOF is shown in Figure 3. Again, the lower MOF weight fraction results in higher emission intensity, in agreement with the findings for the polysulfone MMMs **1** and **2**. The lifetimes of the luminescence process reflect the typical long decay times of Tb^{3+} ions; we observed biexponential decay times of 747(37) and 1253(32) µs for **5** and 763(22) and 1650(56) µs for **6**, and these values are again an excellent match with the behavior of the MOF itself.

Powder X-ray Diffraction

The MOF–polymer membranes $^{3}_{\infty}[Sr_{0.9}Eu_{0.1}Im_2]$@PSF (**1**: 8 wt.-% MOF; **2**: 16 wt.-% MOF), $^{3}_{\infty}[Sr_{0.9}Eu_{0.1}Im_2]$@Matrimid (**3**–**5**), and $^{2}_{\infty}[Tb_2Cl_6(bipy)_3]$•2bipy@PSF (**6**–**8**) were investigated by X-ray powder diffraction. The powder pattern for a successfully embedded MOF is expected to show the reflections of the crystalline MOFs together with a slight amorphous background from the polymer matrix.

As Figure 4 shows, the MOFs were indeed embedded successfully and without decomposition, whereas ultrasonication gave an ideal pattern only for $^{3}_{\infty}[Sr_{0.9}Eu_{0.1}Im_2]$@Matrimid (**5**) and induced decomposition for the Tb MMM **8** (see also Figure S13).

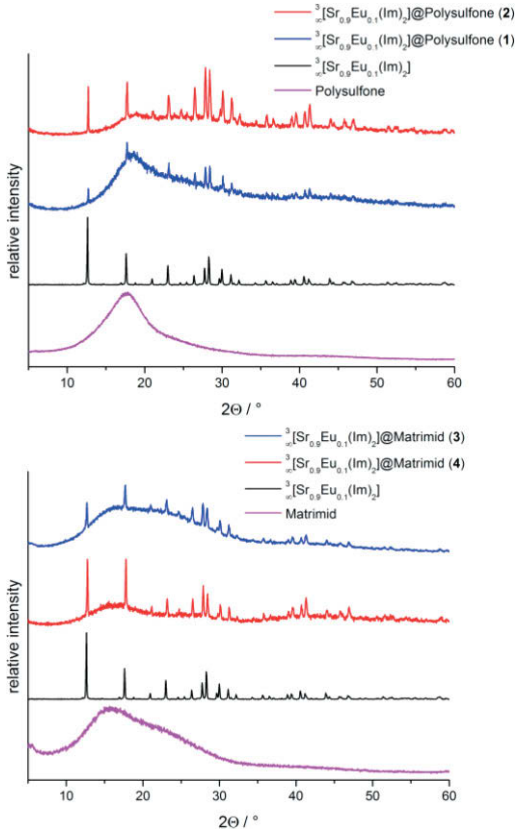

Figure 4. Comparison of the observed powder X-ray diffraction patterns of the mixed MOF membranes **1**–**4** at room temp. with the diffraction patterns of the pure MOF $^{3}_{\infty}[Sr_{0.9}Eu_{0.1}Im_2]$. The reflections of the MOF and the amorphous background of the polymer matrix can be observed.

Hence, the embedding of the MOF without ultrasonic treatment is mild enough to generate luminescent membranes with unaltered MOFs. Although both MOFs have exceptional thermal stabilities,[24,28] ultrasonic treatment provokes decomposition of the MOFs with the exception of the membrane **5**. Altogether, the suspension method without ultrasonication is preferable for stability reasons.

Fluorescence Microscopy, SEM, and EDX

A combination of fluorescence microscopy, scanning electron microscopy (SEM), and element mapping by spatially resolved energy-dispersive X-ray spectroscopy (EDX) was applied for the mixed-matrix membranes **1**–**7** to get information on the distribution of the MOF particles in the membranes. The complimentary character of these methods gives insights into the MOF distribution through their photophysical properties as well as imaging and elemental analysis.

High-resolution fluorescence microscopy was applied to the complete membranes **1**–**8** and the membranes without the MOFs (Figure 5). In addition to the overview, detailed point investigations at a high zoom level were also applied.

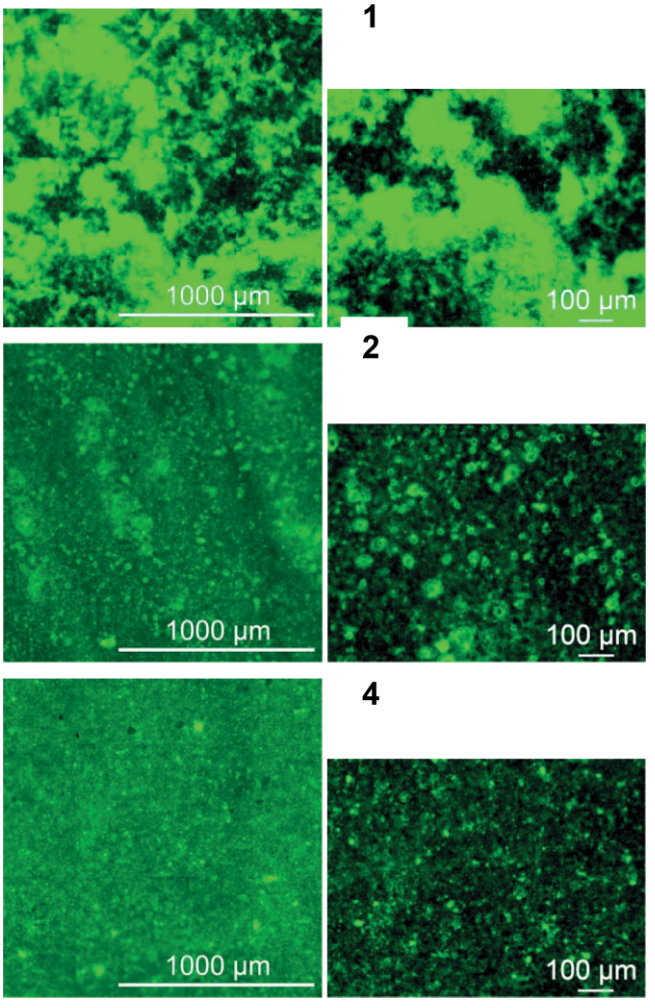

Figure 5. Fluorescence microscopy images of $^{3}_{\infty}[Sr_{0.9}Eu_{0.1}Im_2]$@PSF (**1**, top; **2**, center) and $^{3}_{\infty}[Sr_{0.9}Eu_{0.1}Im_2]$@Matrimid (**4**, bottom) showing the MOF distribution as an overview (left) and microscopic excerpt (right) of the fluorescence intensity (22 ms exposure each; views on membrane top). The images of membrane **1** do not reflect particle aggregation but extraordinarily high luminescence intensity; the particle size is the same as those of the other films. The emission is so bright that even the shortest recording times of 22 ms show an overflow.

Most prominent are the MMMs $^{3}_{\infty}[Sr_{0.9}Eu_{0.1}Im_2]$@PSF (**1** and **2**) as they show the highest fluorescence intensities of all membranes. The intensity reaches the detection maximum of the instrumentation for MMM **1** after an ultrashort exposure time of only 22 ms. In agreement with the photoluminescence spectroscopy observations, a concentration dependence applies

(see also Figures S5–S9 for fluorescence microscopy). The MOF particles are quite evenly distributed within the membrane.

The single MOF crystallites have an average size of 2–20 μm in addition to aggregates of particles larger than 100 μm if no ultrasonic radiation is applied during preparation. The particle size was estimated from a combination of SEM (Figures S11 and S12) and fluorescence microscopy (Figure 5 and S7–9). The impression of further aggregation for membrane **1** can be attributed to the high emission intensity, which reaches the detection limit; it is not a result of real aggregation.

To investigate the effect of the ultrasonic treatment, membrane **5** and the partly decomposed membrane **8** were studied (Figure S8–9). The membranes treated with ultrasound are weaker in luminescence intensity and also show less preferable MOF distribution; therefore, these results stress the importance of mild embedding conditions. The ultrasound-treated membranes show significant MOF degradation and gas inclusion. We are currently investigating the degradation reaction, and we could identify the formation of the hydrate $LnCl_3 \cdot 6H_2O$ from the membranes and LnO(OH) for the bulk MOFs. A further problem could be gel formation, as observed for the Tb–bipy MOF together with Matrimid.

The cross-section SEM images of membranes **1**–**4**, **6**, and **7** show good particle distribution and adhesion on a scale of 10–20 μm for the MOFs with both polysulfone and Matrimid (Figure 6). At higher magnification, slight MOF particle aggregation was detected for membrane **3** (see Figure S10). The good MOF distribution is supported by element mapping through spatially resolved EDX analysis of the MMMs (Figure 7). A slight MOF sedimentation at the "bottom" of the casted membranes is revealed by the locally increased intensity of the mapped metals. Membrane **2** also showed a slight aggregation of MOF particles. Overall, the MOFs were well-distributed along the cross-section in the Eu and Tb MOF MMMs, and the EDX results confirmed the observations from the SEM images.

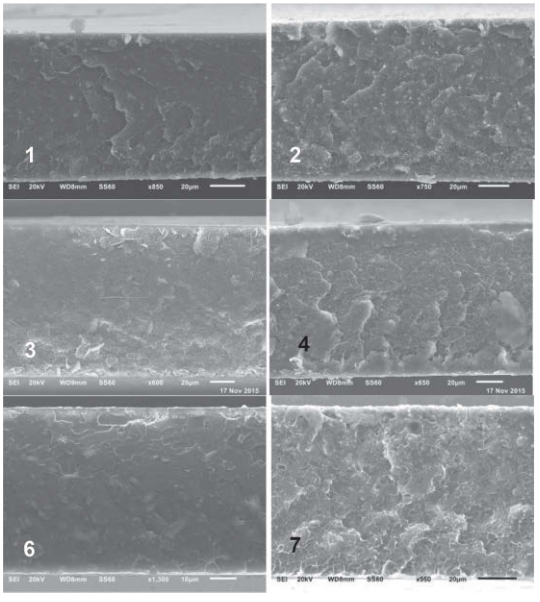

Figure 6. Cross-section SEM images of membranes **1**–**4**, **6**, and **7**.

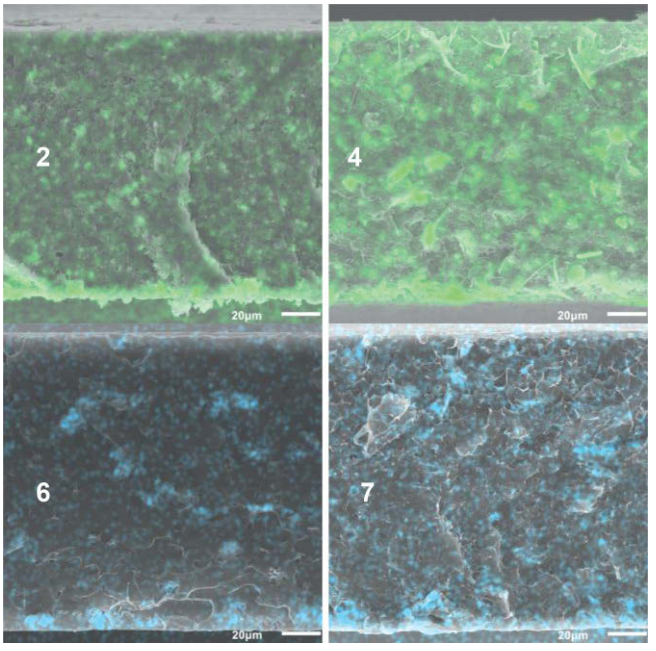

Figure 7. EDX element mapping of membranes **2**, **4**, **6**, and **7** showing the distribution of strontium (green) from $^3_\infty[Sr_{0.9}Eu_{0.1}Im_2]$ and terbium (blue) from $^2_\infty[Tb_2Cl_6(bipy)_3]\cdot 2bipy$. The bottom of the images corresponds to the bottom of the casted membrane.

Gas Permeation

Dioxygen gas-permeation experiments were performed to confirm that the membranes were defect-free and that the morphology at the polymer/particle interface was not defective, as defects would result in much higher gas fluxes compared with those of the pure polymers.[14c] These defects would result in a decrease of the stabilizing properties of the polymer film towards the MOFs. The gas-permeation measurements (Table 2) indicate that the MOF MMMs $^3_\infty[Sr_{0.9}Eu_{0.1}Im_2]$@PSF and $^3_\infty[Sr_{0.9}Eu_{0.1}Im_2]$@Matrimid are defect-free and even have slightly lower permeabilities than those of the pure polymer membranes, as could be expected in view of the dense character of the MOF fillers.[12–14]

Table 2. Gas-permeation results.[a]

Membrane	P (O_2) [Barrer][b]
Pure PSF	1.4
Pure Matrimid	2.1
2	1.0
4	1.4

[a] Permeation experiments performed at 30 °C and 3 bar total feed pressure. [b] 1 Barrer = 1×10^{-10} cm^3(STP) cm/(cm^2 s cmHg) or 7.5005×10^{-18} m^2 s^{-1} Pa^{-1} in SI units.

Conclusions

Luminescent MOF–polymer mixed-matrix membranes have been prepared from the MOFs $^3_\infty[Sr_{0.9}Eu_{0.1}Im_2]$ and $^2_\infty[Tb_2Cl_6(bipy)_3]\cdot 2bipy$ together with the polysulfone Ultrason® S and Matrimid®. For the MMMs $^3_\infty[Sr_{0.9}Eu_{0.1}Im_2]$@PSF (**1** and **2**), $^3_\infty[Sr_{0.9}Eu_{0.1}Im_2]$@Matrimid (**3**–**5**), and $^2_\infty[Tb_2Cl_6(bipy)_3]\cdot$

2bipy@PSF (**6** and **7**), the luminescence of the MOF could be maintained. The luminescence is especially strong for **1** and **2**. The membrane polymers influence the luminescence intensity: in the polysulfone membranes, both MOFs show higher emission intensity for lower MOF concentrations, whereas Matrimid® shows the opposite behavior. This indicates a different concentration quenching depending on the membrane polymer. The distribution of the MOFs in the membranes has been investigated by SEM, EDX, and fluorescence microscopy. Except for some sedimentation, the MOFs were distributed evenly within the membranes without significant aggregation. The use of ultrasonication proved less beneficial, as the resulting membranes showed inferior luminescence properties. Gas-permeation measurements proved that the MOF MMMs $^{3}_{\infty}[Sr_{0.9}Eu_{0.1}Im_2]$@PSF and $^{3}_{\infty}[Sr_{0.9}Eu_{0.1}Im_2]$@Matrimid were defect-free, as they exhibit slightly lower permeabilities than those of the pure polymer membranes. To the best of our knowledge, these are the first examples of luminescent MMMs. Altogether, these examples show that the concept of MOF mixed-matrix membranes can be expanded from gas permeation to new applications. The fabrication of membranes can be an option to increase the stabilities and processabilities of the bulk MOFs.

Experimental Section

General: All experiments were performed under inert conditions (argon or nitrogen atmosphere) through vacuum-line, Schlenk, and glovebox (MBraun, LabMaster SP and Innovative technology, Pure Lab) techniques with DURAN™ ampoules. The MOFs were prepared in heating furnaces with Al_2O_3 tubes, a Kanthal resistance heating wire, and NiCr/Ni temperature elements controlled by Eurotherm 2416 control units together with sealed glass ampoules. Anhydrous terbium chloride was synthesized by the ammonium halide route[29,30] from Tb_4O_7 (99.9 %, Auer-Remy), HCl solution (10 mol L^{-1}, reagent grade) and NH_4Cl (99.9 %, Fluka). The intermediate trivalent terbium ammonium chloride was decomposed and further purified by sublimation under vacuum. Strontium and europium metal (Smart Elements, 99.99 %), bipy (Sigma–Aldrich 98 %), and 1*H*-imidazole (HIm, Sigma–Aldrich 99.5 %) were applied as purchased. The solvent DCM (>99.9 %) was purchased from Fisher Chemicals and dried with an MBraun solvent purification system. O_2 gas for the gas-permeation experiments was supplied by Air Liquide (Germany) and used as received (purity 99.998 %).

$^{3}_{\infty}[Sr_{0.9}Eu_{0.1}(Im)_2]$ and $^{2}_{\infty}[Tb_2Cl_6(bipy)_3]\cdot 2bipy$: $^{3}_{\infty}[Sr_{0.9}Eu_{0.1}(Im)_2]$ was synthesized by a modification of the method reported in ref.[24] Freshly filed europium metal (0.1 mmol, 15.2 mg), small pieces of strontium metal (0.9 mmol, 78.9 mg), and 1*H*-imidazole (3.0 mmol, 204.3 mg) were sealed in an evacuated DURAN™ glass ampoule. The ampoule was heated to 186 °C in a tube oven over 2 h. The temperature was kept constant for 48 h. The ampoule was cooled to 66 °C over 6 h and then to room temperature over 1 h. The excess 1*H*-imidazole was removed by sublimation (140 °C, 24 h). The remaining reaction product was a fine yellow powder.

$^{2}_{\infty}[Tb_2Cl_6(bipy)_3]\cdot 2(bipy)$ was synthesized by a modified solvent-free melt reaction according to refs.[19,25] Anhydrous $TbCl_3$ (0.76 mmol, 201.6 mg) and 4,4′-bipyridine (2.28 mmol, 356.1 mg) were homogenized by grinding. The reaction mixture was then sealed in an evacuated DURAN™ glass ampoule, which was heated to 140 °C in a tube oven at a rate of 20 °C h^{-1}. The temperature was kept constant for 168 h, and then the ampoule was cooled to room temperature over 1 h. The excess 4,4′-bipyridine was removed by sublimation (120 °C, 48 h). The collected product was a fine grey powder.

Membrane Preparation (1–4, 6–7) without Ultrasonication: The embedding of MOFs without sonication was achieved with solutions of 3.6 wt.-% polymer in DCM. Portions (200 mg) of the dry polymer, the MOF material (18 or 39 mg), and dry DCM (4 mL) were combined in a 10 mL Schlenk flask to produce MMMs with 8 and 16 wt.-% of MOF. The dispersions were stirred for 2 d in order to achieve homogeneous mixtures. The dispersions were cast into metal rings, 5 cm in diameter, which were placed on a flat glass surface in a desiccator filled with nitrogen gas and a desiccant. The solvent was evaporated overnight by a slight stream of predried nitrogen gas to achieve some control over the evaporation rate. As soon as all of the solvent was evaporated, the membrane was removed from the metal ring and the glass surface. The membrane was finally dried at 25 °C under reduced pressure.

Membrane Preparation (5 and 8) with Ultrasonication: The embedding of MOFs with ultrasonication was achieved as described above with minor alterations. The amount of polymer in DCM was 8.0 wt.-% (200 mg of polymer in 2 mL of DCM), and the dispersion of the MOF in polymer solution was sonicated for 60 min in a ultrasonic bath (ELMA Transsonic 310, 35 Hz) to try to achieve good dispersion of the MOF particles before membrane casting.

Powder X-ray Diffraction: Samples for powder X-ray diffraction were prepared in open-stage sample holders with a poly(methyl methacrylate) (PMMA) cupola and a Si-wafer platform. The diffraction data were collected with a Bruker AXS D8 Discover powder X-ray diffractometer equipped with Lynx-Eye detector in reflection geometry. The X-ray radiation (Cu-$K_{\alpha 1}$; λ = 154.06 pm) was focused with a Goebel mirror, and Cu-$K_{\alpha 2}$ radiation was eliminated by the application of a Ni absorber. The diffraction patterns were recorded and analyzed with the Bruker AXS Diffrac-Suite.[31]

Photoluminescence Spectroscopy: The excitation and emission spectra were recorded with a HORIBA Jobin Yvon Spex Fluorolog 3 spectrometer equipped with a 450-W Xe lamp, double-grated excitation and emission monochromators, and a photomultiplier tube (R928P) at room temp. with the FluorEssence software. The excitation spectra were corrected for the spectral distribution of the lamp intensity by using a photodiode reference detector. Additionally, the excitation and emission spectra were corrected for the spectral responses of the monochromators and the detector by using the correction spectra provided by the manufacturer. All samples were investigated as solids in spectroscopically pure quartz cuvettes in front-face mode at room temperature. Edge filters were applied when appropriate.

The fluorescence lifetimes were obtained with a Horiba Fluoromax FL3-22 spectrophotometer. The samples were prepared in quartz glass cuvettes under an inert-gas atmosphere. The decay times were recorded by time-correlated single-photon counting (TCSPC) with a 375 nm pulsed laser diode or a microsecond flash lamp with an excitation wavelength of 330 nm. The fluorescence emission was collected at right angles to the excitation source, and the emission wavelength was selected with a monochromator and detected by a single-photon avalanche diode (SPAD). The resulting intensity decays were calculated through tail fits.

SEM/EDX: The SEM images were recorded with a Jeol JSM-6510LV QSEM Advanced electron microscope with a LAB-6 cathode at 5–20 keV. The microscope was equipped with a Bruker Xflash 410 silicon drift detector and the Bruker ESPRIT software for EDX analysis. The membrane cross-sections were prepared through freeze-fracturing after immersion in liquid nitrogen and then coated with

gold by a Jeol JFC 1200 fine-coater (at an approximate current of 20 mA for 20–30 s).

Fluorescence Microscopy: The fluorescence microscopy of oxygen-free sealed MOF–membrane preparations was performed with an Axio Observer.Z1 microscope equipped with an A-Plan 10×/0.25 Ph1 objective and an Optovar 1×/1.6× tube lens (Zeiss). The images were recorded with a phase-contrast channel and a 49 DAPI or 38 HE Green Fluorescent Protein Reflector (Zeiss) with excitation wavelength of 450–490 nm and an emission wavelength of 500–550 nm after 22 ms exposure time with a mercury vapor short-arc lamp.

Gas Permeation: The O_2 permeabilities were evaluated with a permeation cell described elsewhere.[32] The membrane thickness was measured as the average over ten different spots with a micrometer screw. The gas-permeation measurements were performed by the pressure-rise method under steady-state conditions at 30 °C. The membrane was placed into the sample cell, the permeate side was evacuated, and then the feed side was evacuated. The feed side was filled with O_2 gas to a pressure of 3.0 bar. The linear pressure increase upon permeation from the feed to the permeate side was recorded and used to calculate the permeability P in Barrer units [1 Barrer = 1×10^{-10} cm^3(STP) cm/(cm^2 s cmHg) or 7.5005×10^{-18} m^2 s^{-1} Pa^{-1} in SI units]. The Permeability P is defined as the gas flow rate J multiplied by the thickness d of the membrane, divided by the area A and by the pressure difference Δp across the material [Equation (1)].

$$P = (Jd)/\Delta pA \quad (1)$$

Acknowledgments

The work was partly supported by the Bundesministeriums für Bildung und Forschung (BMBF), Germany (project "Robust Porous Coordination Polymers for Mixed-Matrix Membranes", grant number 01DK13026).

Keywords: Metal–organic frameworks · Polymers · Mixed-matrix membranes · Luminescence · Lanthanides

[1] a) H.-C. J. Zhou, S. Kitagawa, *Chem. Soc. Rev.* **2014**, *43*, 5415–5418; b) Z.-J. Lin, J. Lü, M. Hong, R. Cao, *Chem. Soc. Rev.* **2014**, *43*, 5867–5895; c) J. R. Long, O. M. Yaghi, *Chem. Soc. Rev.* **2009**, *38*, 1213–1214; d) N. Stock, S. Biswas, *Chem. Rev.* **2012**, *112*, 933–969; e) C. Janiak, J. K. Vieth, *New J. Chem.* **2010**, *34*, 2366–2388.

[2] a) O. K. Farha, J. T. Hupp, *Acc. Chem. Res.* **2010**, *43*, 1166–1175; b) C. Janiak, S. K. Henninger, *Chimia* **2013**, *67*, 419–424; c) S. K. Henninger, F. Jeremias, H. Kummer, C. Janiak, *Eur. J. Inorg. Chem.* **2012**, 2625–2634.

[3] a) M. D. Allendorf, C. A. Bauer, R. K. Bhakta, R. J. T. Houk, *Chem. Soc. Rev.* **2009**, *38*, 1330–1352; b) M. D. Allendorf, C. A. Bauer, R. K. Bhakta, R. J. T. Houk, *Chem. Soc. Rev.* **2009**, *38*, 1330–1352; c) K. Binnemans, *Chem. Rev.* **2009**, *109*, 4283–4374; d) J. Rocha, L. D. Carlos, F. A. A. Paz, D. Ananias, *Chem. Soc. Rev.* **2011**, *40*, 926–940; e) Y. Chen, S. Ma, *Rev. Inorg. Chem.* **2012**, *32*, 81–100; f) J. Heine, K. Müller-Buschbaum, *Chem. Soc. Rev.* **2013**, *42*, 9232–9242.

[4] a) D. Liu, K. Lu, C. Poon, W. Lin, *Inorg. Chem.* **2014**, *53*, 1916–1924; b) Z. Hu, B. J. Deibert, J. Li, *Chem. Soc. Rev.* **2014**, *43*, 5815–5840; c) J. Lei, R. Qian, P. Ling, L. Cui, H. Ju, *TrAC Trends Anal. Chem.* **2014**, *58*, 71–78; d) K. Müller-Buschbaum, F. Beuerle, C. Feldmann, *Microporous Mesoporous Mater.* **2015**, *216*, 171–199.

[5] B. Böhringer, R. Fischer, M. R. Lohe, M. Rose, S. Kaskel, P. Küsgens, *Metal–Organic Frameworks: Applications from Catalysis to Gas Storage* (Ed.: D. Farrusseng), 1st ed., Wiley-VCH, Weinheim, Germany, **2011**, chapter 15, p. 353–381.

[6] a) F. Jeremias, S. K. Henninger, C. Janiak, *Chem. Commun.* **2012**, *48*, 9708–9710; b) F. Jeremias, D. Fröhlich, C. Janiak, S. K. Henninger, *RSC Adv.* **2014**, *4*, 24073–24082.

[7] V. Finsy, L. Ma, L. Alaerts, D. E. De Vos, G. V. Baron, J. F. M. Denayer, *Microporous Mesoporous Mater.* **2009**, *120*, 221–227.

[8] a) R. Zacharia, D. Cossement, L. Lafi, R. Chahine, *J. Mater. Chem.* **2010**, *20*, 2145–2151; b) M. R. Lohe, M. Rose, S. Kaskel, *Chem. Commun.* **2009**, 6056–6058.

[9] a) M. Wickenheisser, T. Paul, C. Janiak, *Microporous Mesoporous Mater.* **2016**, *220*, 258–269; b) M. Wickenheisser, A. Herbst, R. Tannert, B. Milow, C. Janiak, *Microporous Mesoporous Mater.* **2015**, *215*, 143–153; c) M. Wickenheisser, C. Janiak, *Microporous Mesoporous Mater.* **2015**, *204*, 242–250; d) A. Sachse, R. Ameloot, B. Coq, F. Fajula, B. Coasne, D. De Vos, A. Galarneau, *Chem. Commun.* **2012**, *48*, 4749–4751; e) P. Küsgens, A. Zgaverdea, H. Fritz, S. Siegle, S. Kaskel, *J. Am. Ceram. Soc.* **2010**, *93*, 2476–2479; f) M. G. Schwab, I. Senkovska, M. Rose, M. Koch, J. Pahnke, G. Jonschker, S. Kaskel, *Adv. Eng. Mater.* **2008**, *10*, 1151–1155.

[10] A. M. Spokoyny, D. Kim, A. Sumrein, C. A. Mirkin, *Chem. Soc. Rev.* **2009**, *38*, 1218–1227.

[11] a) D. Zacher, O. Shekhah, C. Wöll, R. A. Fischer, *Chem. Soc. Rev.* **2009**, *38*, 1418–1429; b) O. Shekhah, J. Liu, R. A. Fischer, C. Wöll, *Chem. Soc. Rev.* **2011**, *40*, 1081–1106.

[12] a) H. B. Tanh Jeazet, C. Staudt, C. Janiak, *Dalton Trans.* **2012**, *41*, 14003–14027; b) K. Hunger, N. Schmeling, H. B. Tanh Jeazet, C. Janiak, C. Staudt, K. Kleinermanns, *Membranes* **2012**, *2*, 727–763; c) H. B. Tanh Jeazet, C. Janiak, Metal–Organic Frameworks, in: Mixed-Matrix Membranes, in: *Metal–Organic Framework Materials* (Eds.: L. R. MacGillivray, C. Lukehart), John Wiley & Sons, Chichester, UK, **2014**, p. 403–417.

[13] a) B. Seoane, J. Coronas, I. Gascon, M. Etxeberria Benavides, O. Karvan, J. Caro, F. Kapteijn, J. Gascon, *Chem. Soc. Rev.* **2015**, *44*, 2421–2454; b) B. Zornoza, C. Tellez, J. Coronas, J. Gascon, F. Kapteijn, *Microporous Mesoporous Mater.* **2013**, *166*, 67–78.

[14] a) S. R. Venna, M. A. Carreon, *Chem. Eng. Sci.* **2015**, *124*, 3–19; b) W. Li, Y. Zhang, Q. Li, G. Zhang, *Chem. Eng. Sci.* **2015**, *135*, 232–257; c) G. Dong, H. Li, V. Chen, *J. Mater. Chem. A* **2013**, *1*, 4610–4630.

[15] H. B. Tanh Jeazet, T. Koschine, C. Staudt, K. Raetzke, C. Janiak, *Membranes* **2013**, *3*, 331–353; H. B. Tanh Jeazet, C. Staudt, C. Janiak, *Chem. Commun.* **2012**, *48*, 2140–2142.

[16] a) S. Roy, A. Chakraborty, T. K. Maji, *Coord. Chem. Rev.* **2014**, *273*, 139–164; b) L. V. Meyer, F. Schönfeld, K. Müller-Buschbaum, *Chem. Commun.* **2014**, *50*, 8093–8108; c) Y. Cui, B. Chen, G. Qian, *Coord. Chem. Rev.* **2014**, *273*, 76–86; d) L. Ma, O. R. Evans, B. M. Foxman, W. Lin, *Inorg. Chem.* **1999**, *38*, 5837–5840; e) T. M. Reinecke, M. Eddaoudi, M. Fehr, D. Kelly, O. M. Yaghi, *J. Am. Chem. Soc.* **1999**, *121*, 1651–1657; f) Z.-S. Bai, J. Xu, T. Okamura, M.-S. Chen, W.-Y. Sun, N. Ueyama, *Dalton Trans.* **2009**, *14*, 2528–2539.

[17] a) S. V. Eliseeva, J.-C. G. Bünzli, *New J. Chem.* **2011**, *35*, 1165–1176; b) K. Binnemans, *Chem. Rev.* **2009**, *109*, 4283–4374; c) L. Sorace, C. Benelli, D. Gatteschi, *Chem. Soc. Rev.* **2011**, *40*, 3092–3104.

[18] S. I. Weissman, *J. Chem. Phys.* **1942**, *10*, 214–217.

[19] a) C. J. Höller, M. Mai, C. Feldmann, K. Müller-Buschbaum, *Dalton Trans.* **2010**, *39*, 461–468; b) P. R. Matthes, C. J. Höller, M. Mai, J. Heck, S. J. Sedlmaier, S. Schmiechen, C. Feldmann, W. Schnick, K. Müller-Buschbaum, *J. Mater. Chem.* **2012**, *22*, 10179–10187.

[20] G. A. Crosby, R. E. Whan, R. M. Alire, *J. Chem. Phys.* **1961**, *34*, 743–748.

[21] a) L. Armelao, S. Quici, F. Barigelletti, G. Accorsi, G. Bottaro, M. Cavazzini, E. Tondello, *Coord. Chem. Rev.* **2010**, *254*, 487–505; b) P. A. Tanner, C.-K. Duan, *Coord. Chem. Rev.* **2010**, *254*, 3026–3029; c) D. Parker, J. A. G. Williams, *J. Chem. Soc., Dalton Trans.* **1996**, 3613–3628; d) P. Gawryszewska, J. Sokolnicki, J. Legendziewicz, *Coord. Chem. Rev.* **2005**, *249*, 2489–2509.

[22] M. Noda, K. Matsushima, K. Seki, M. Yagi, *Chem. Phys. Lett.* **1998**, *296*, 599–604.

[23] P. Hänninen, H. Härma (Eds.), *Springer Series on Fluorescence Vol 7: Lanthanide Luminescence*, Springer-Verlag, Berlin, **2011**.

[24] a) A. Zurawski, M. Mai, D. Baumann, C. Feldmann, K. Müller-Buschbaum, *Chem. Commun.* **2011**, *47*, 496–498; b) L. V. Meyer, J. Vogt, H. Schäfer, M. Steinhart, R. Böttcher, A. Pöppl, M. Mai, C. Feldmann, K. Müller-Buschbaum, *Inorg. Chem. Front.* **2015**, *2*, 237–245.

[25] a) J. Won, J. S. Seo, J. H. Kim, H. S. Kim, Y. S. Kang, S. J. Kim, Y. Kim, J. Jegal, *Adv. Mater.* **2005**, *17*, 80–84; b) A. Car, C. Stropnik, K.-V. Peinemann,

Desalination **2006**, *200*, 424–426; c) B. Seoane, J. M. Zamaro, C. Téllez, J. Coronas, *RSC Adv.* **2011**, *1*, 917–922; d) B. Zornoza, B. Seoane, J. M. Zamaro, C. Téllez, J. Coronas, *ChemPhysChem* **2011**, *12*, 2781–2785.

[26] a) S. Basu, M. Maes, A. Cano-Odena, L. Alaerts, D. E. De Vos, I. F. J. Vankelecom, *J. Membr. Sci.* **2009**, *344*, 190–198; b) M. J. C. Ordoñez, K. J. Balkus Jr., J. P. Ferraris, I. H. Musselman, *J. Membr. Sci.* **2010**, *361*, 28–37; c) E. V. Perez, K. J. Balkus Jr., J. P. Ferraris, I. H. Musselman, *J. Membr. Sci.* **2009**, *328*, 165–173; d) Y. Zhang, I. H. Musselman, J. P. Ferraris, K. J. Balkus Jr., *J. Membr. Sci.* **2008**, *313*, 170–181.

[27] W. Zhang, Y. Hu, J. Ge, H.-L. Jiang, S.-H. Yu, *J. Am. Chem. Soc.* **2014**, *136*, 16978–16981.

[28] P. R. Matthes, F. Schönfeld, S. H. Zottnick, K. Müller-Buschbaum, *Molecules* **2015**, *20*, 12125–12153.

[29] G. Jantsch, H. Jawurek, N. Skalla, H. Gawalonski, *Z. Anorg. Allg. Chem.* **1932**, *207*, 353–367.

[30] G. Meyer, *Inorg. Synth.* **1989**, *25*, 146.

[31] Bruker, *SMART Apex Suite* **2001**, Bruker AXS Inc., Madison, WI.

[32] J. U. Wieneke, C. Staudt, *Polym. Degrad. Stab.* **2010**, *95*, 684–693.

Received: March 3, 2016
Published Online: May 30, 2016

Eur. J. Inorg. Chem. **2016** · ISSN 1099–0682

SUPPORTING INFORMATION

DOI: 10.1002/ejic.201600235
Title: Luminescent Metal–Organic Framework Mixed-Matrix Membranes from Lanthanide Metal–Organic Frameworks in Polysulfone and Matrimid
Author(s): Janina Dechnik, Friedrich Mühlbach, Dennis Dietrich, Tobias Wehner, Marcus Gutmann, Tessa Lühmann, Lorenz Meinel, Christoph Janiak,* Klaus Müller-Buschbaum*

Photoluminescence spectroscopy

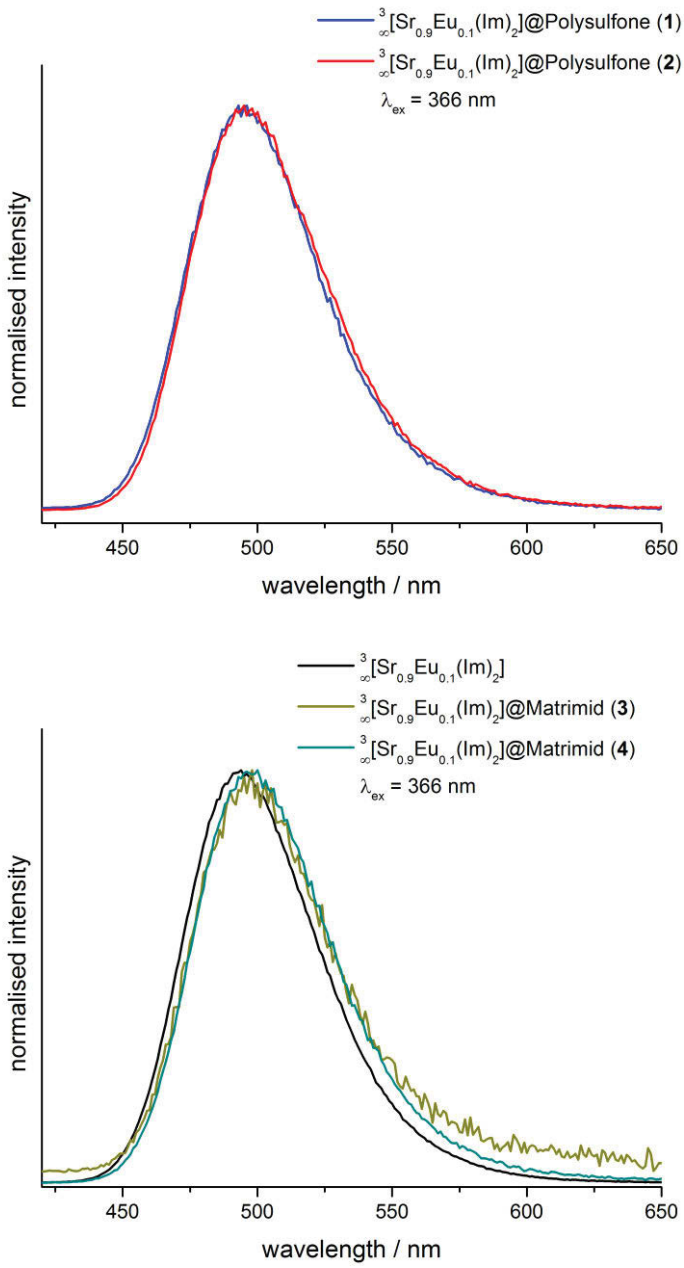

Fig. S1: Normalized emission spectra of $^3_\infty$[$Sr_{0.9}Eu_{0.1}Im_2$]@PSF (blue:**1**, red: **2**) and $^3_\infty$[$Sr_{0.9}Eu_{0.1}Im_2$]@Matrimid (green:**3**, turquoise: **4**) in comparison to the pure MOF (black), indicating the similar emission behavior .

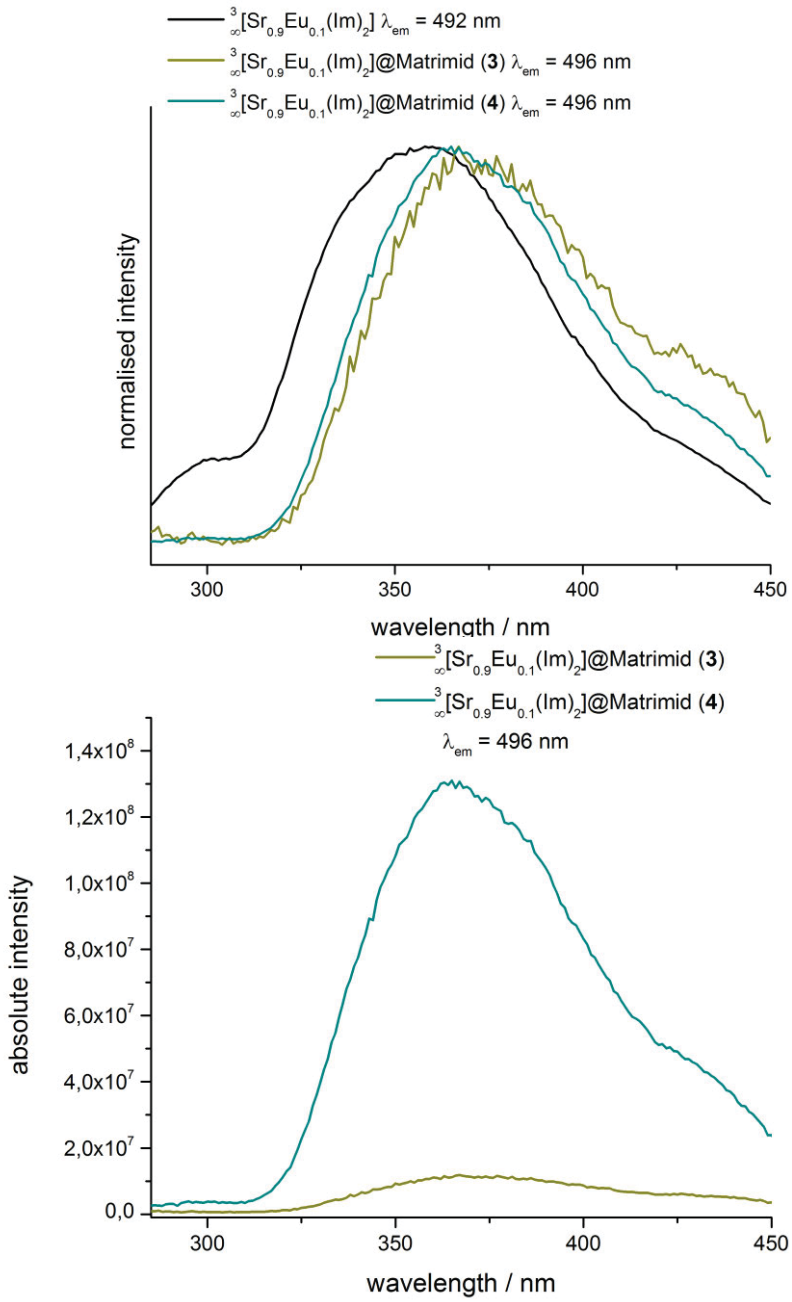

Fig. S2: Normalized excitation spectra of $^3_\infty$[Sr$_{0.9}$Eu$_{0.1}$Im$_2$]@Matrimid (green:**3**, turquoise: **4**) in comparison to the pure MOF and absolute excitation spectra of $^3_\infty$[Sr$_{0.9}$Eu$_{0.1}$Im$_2$]@Matrimid (**3**, **4**), indicating the increase in excitation intensity upon MOF fraction increase.

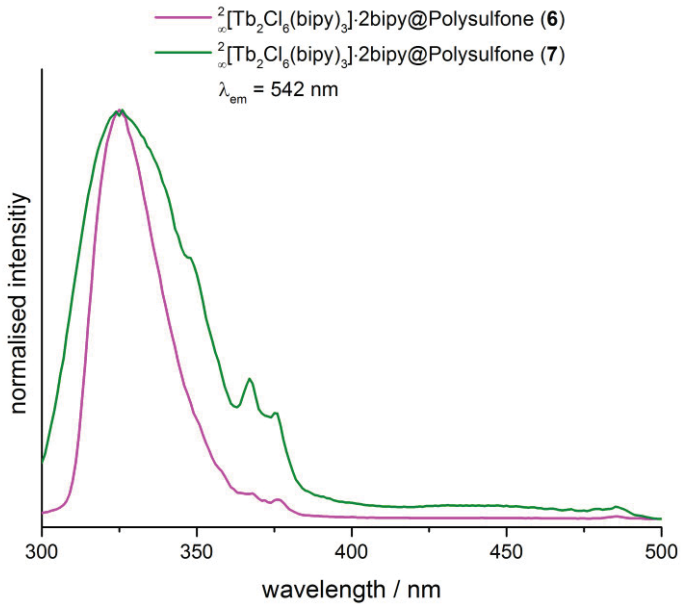

Fig. S3: Normalized excitation spectra of $^2_\infty$[Tb$_2$Cl$_6$(bipy)$_3$]·2bipy@PSF (**6**: purple,**7**: green).

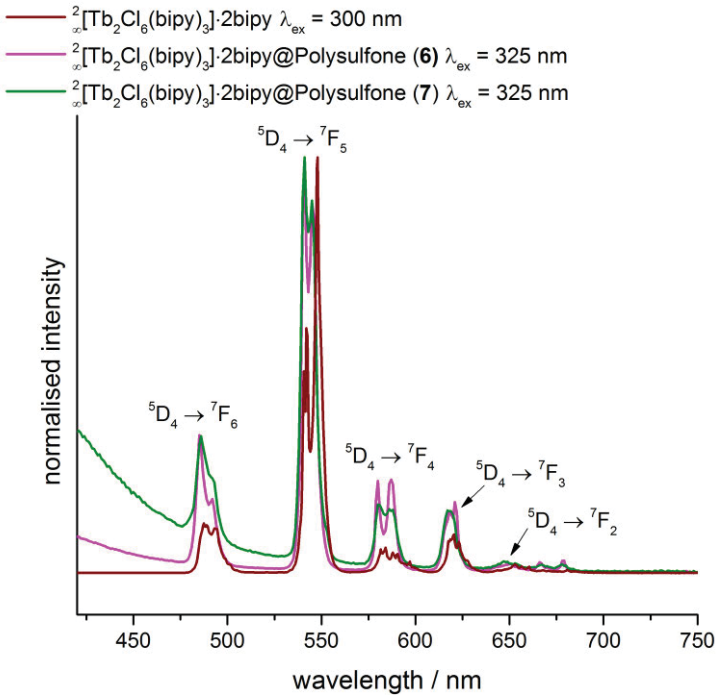

Fig. S4: Normalized emission spectra of $^2_\infty$[Tb$_2$Cl$_6$(bipy)$_3$]·2bipy@PSF (**6**: purple,**7**: green) in comparison to pure MOF (brown).

Fluorescence Microscopy:

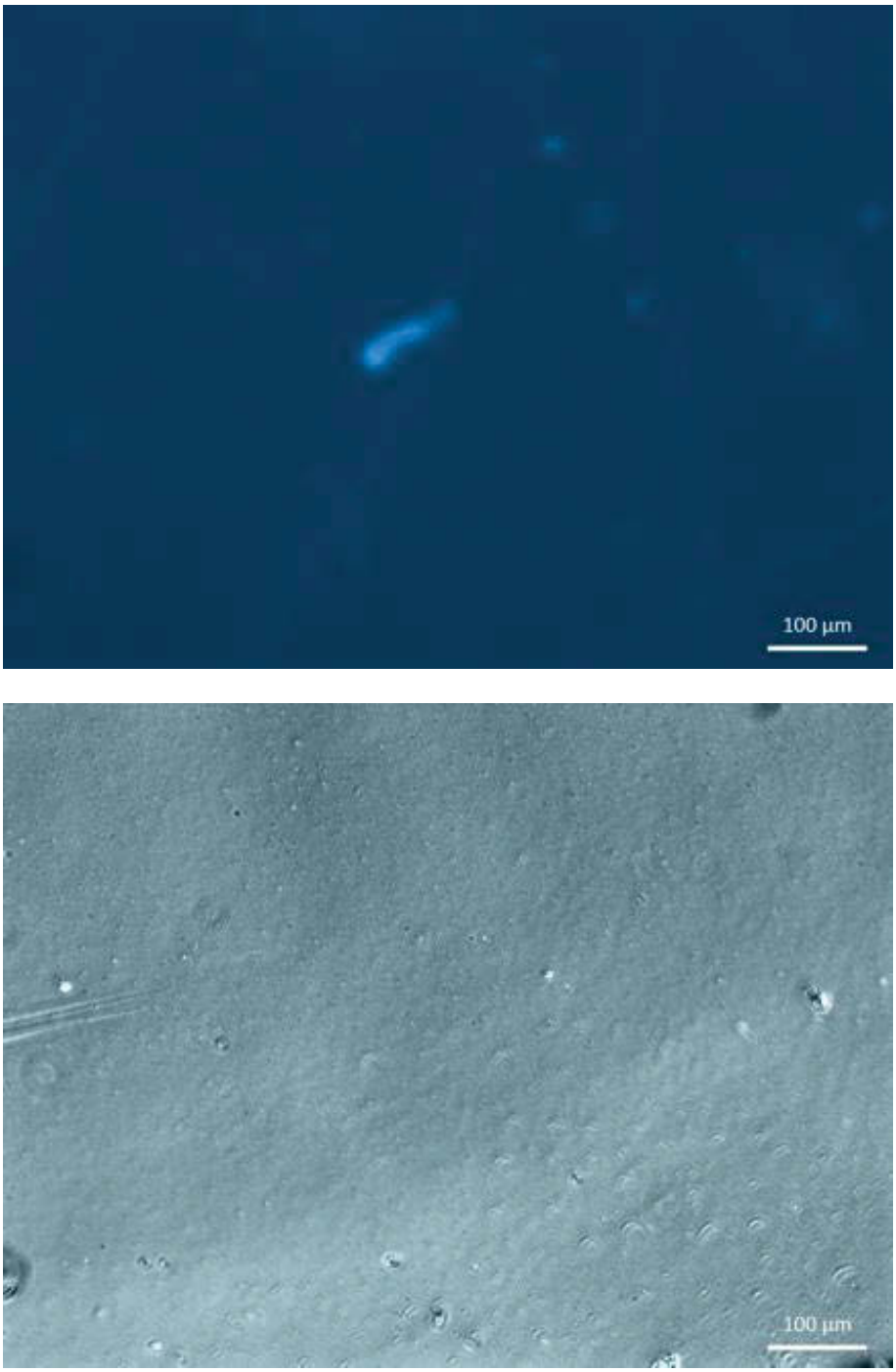

Fig. S5: Fluorescence microscopy images of pure polysulfone (top) and Matrimid (bottom) membranes without MOF participation. Only for PSF, a weak fluorescence in the blue region is observed.

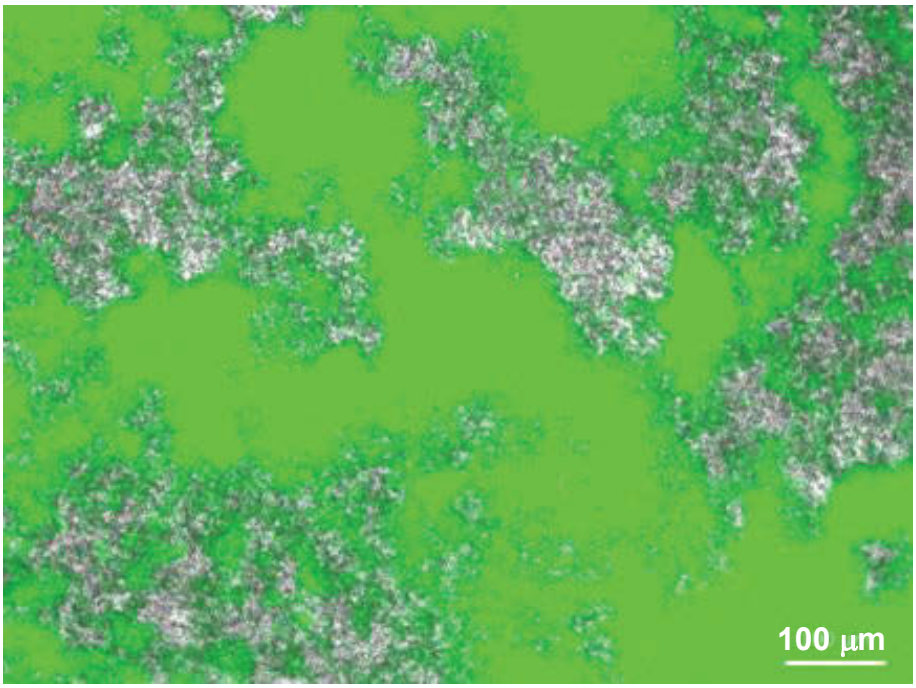

Fig. S6: Fluorescence microscopy image of $^{3}_{\infty}[Sr_{0.9}Eu_{0.1}Im_2]$@PSF (**1**) as complimentary addition of transmission and fluorescence images.

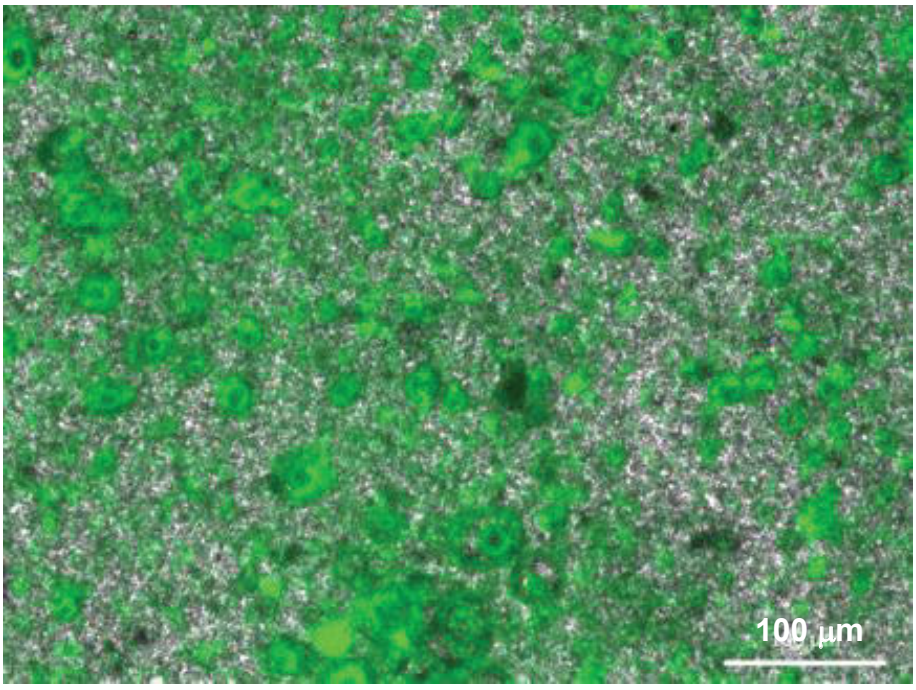

Fig. S7: Fluorescence microscopy image of $^{3}_{\infty}[Sr_{0.9}Eu_{0.1}Im_2]$@PSF (**2**) as complimentary addition of transmission and fluorescence images.

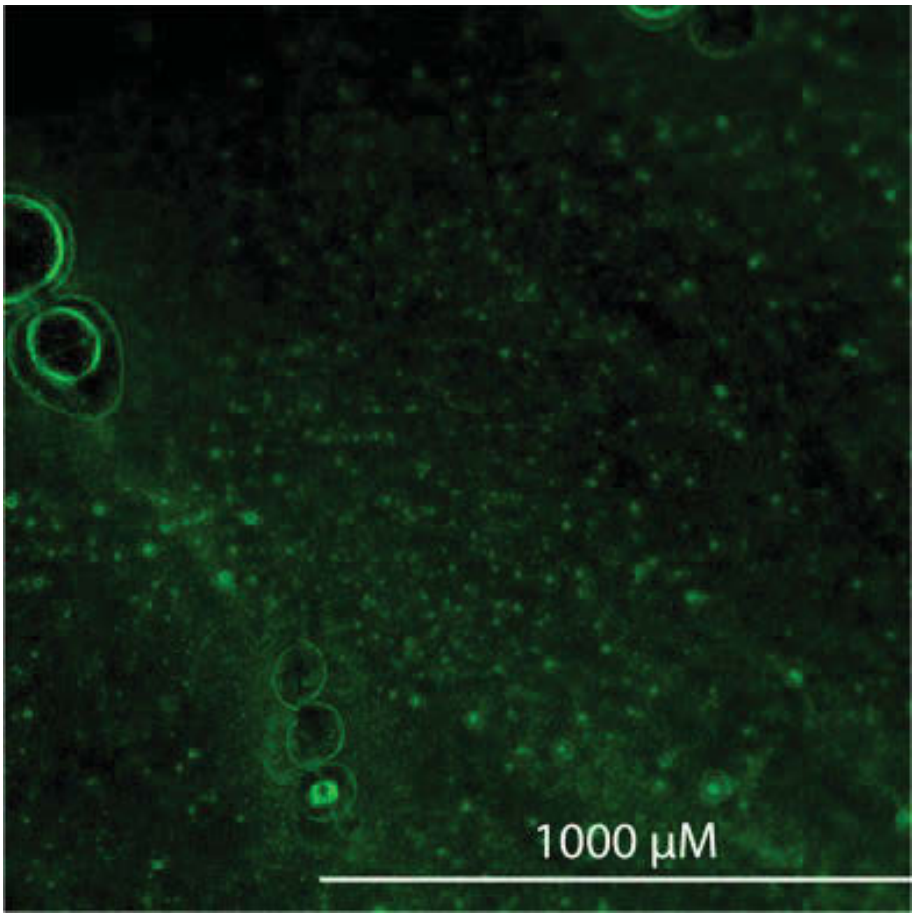

Fig. S8: Fluorescence microscopy image of $^{2}_{\infty}[Tb_2Cl_6(bipy)_3]\cdot 2bipy$@PSF (ultrasonication:**8**), indicating successful incorporation of the MOF in the PSF membrane.

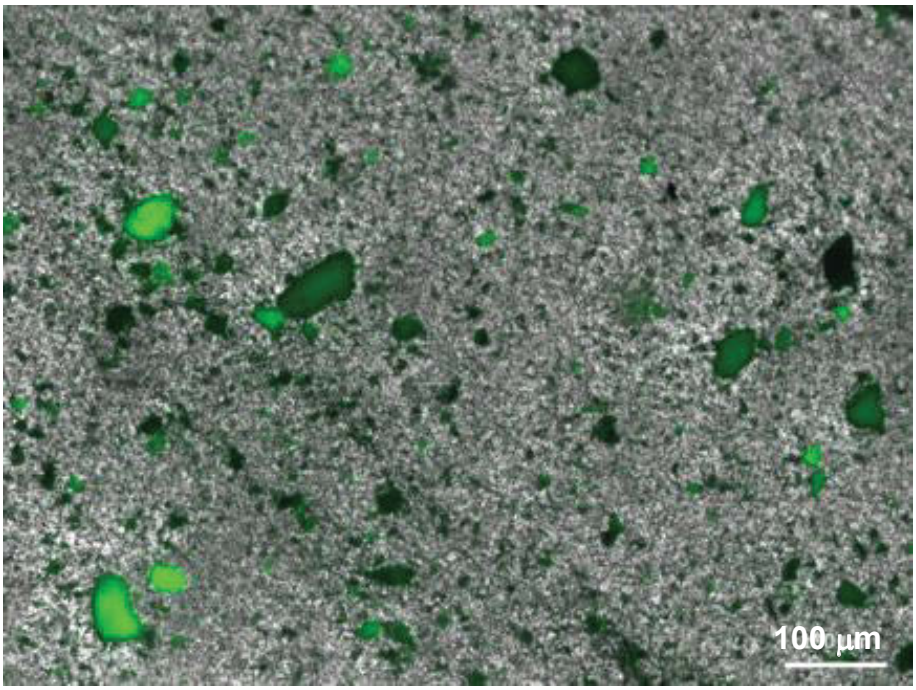

Fig. S9: Fluorescence microscopy image of $^{3}_{\infty}[Sr_{0.9}Eu_{0.1}Im_2]$@Matrimid (ultrasonication: **5**) as complimentary addition of transmission and fluorescence images.

Scanning electron microscopy (SEM)

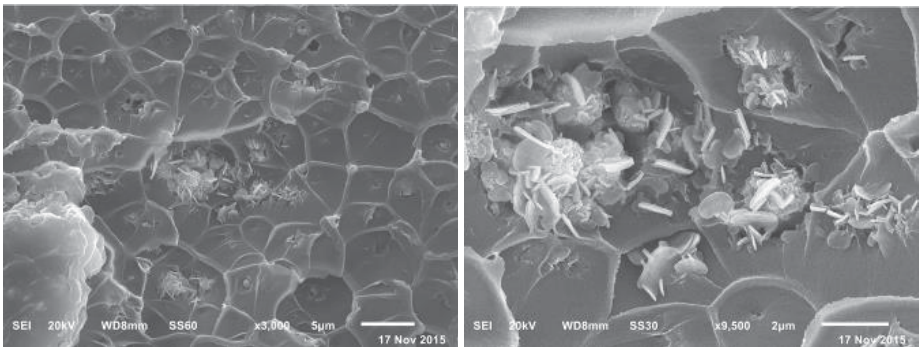

Fig. S10: SEM images of membrane **3** showing minor aggregation of the MOF.

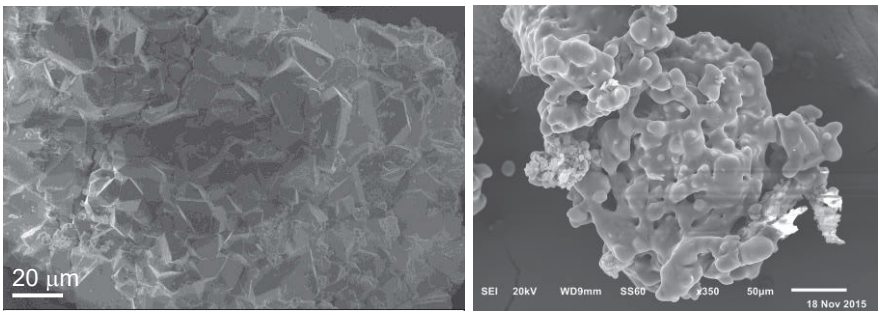

Fig. S11: SEM images of the bulk MOFs $^{3}_{\infty}[Sr_{0.9}Eu_{0.1}Im_2]$ (left) and $^{2}_{\infty}[Tb_2Cl_6(bipy)_3]\cdot 2bipy$ (right).

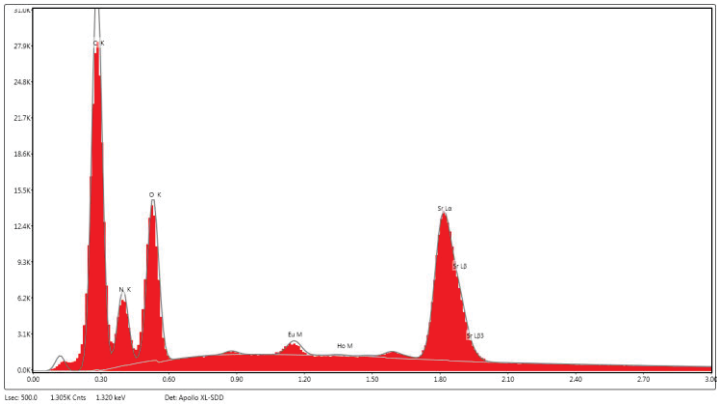

Fig. S12: EDX analysis of bulk MOF $^{3}_{\infty}[Sr_{0.9}Eu_{0.1}Im_2]$.

Powder X-ray diffraction

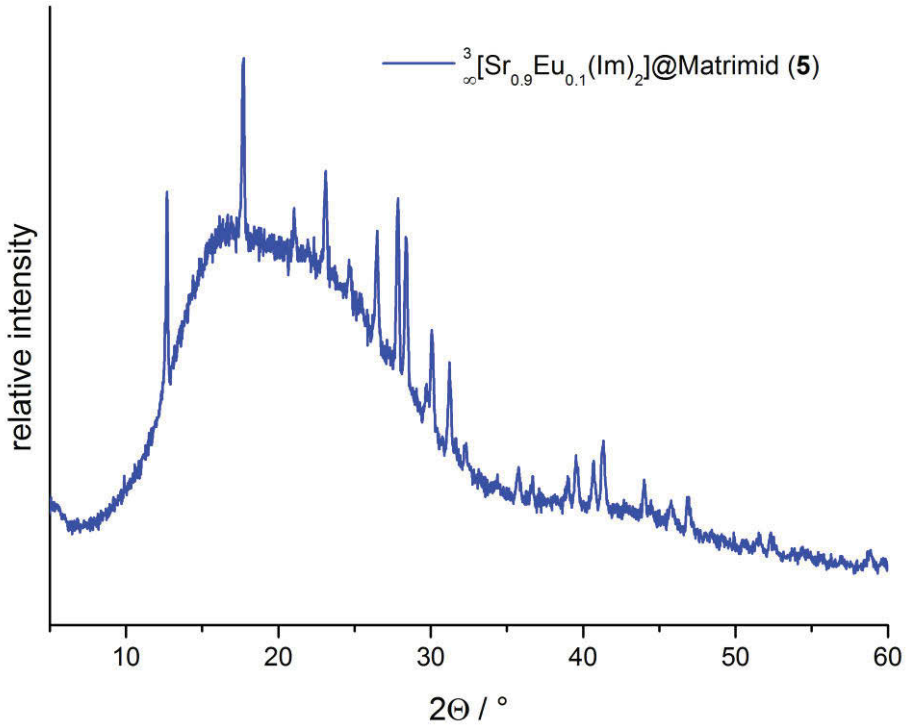

Fig. S13: PXRD pattern of membrane **5** (including ultrsonication) showing the reflections of the MOF.

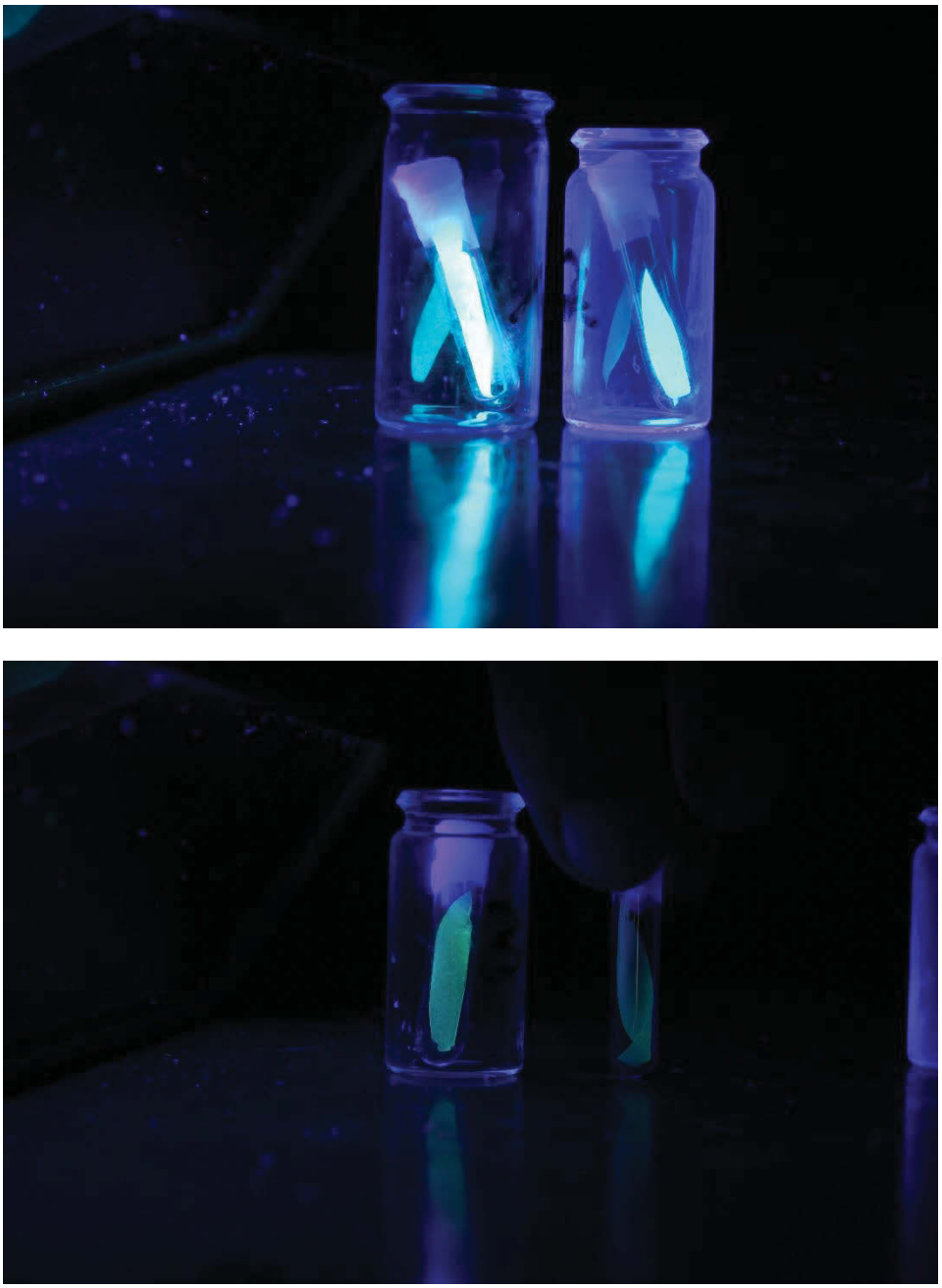

Fig. S14: The emission intensity differences between the stronger, parity allowed Eu^{2+} emission of membranes **1** and **2** (top left and right) compared to the Tb^{3+} emission of **6** and **7** (bottom left and right).

4. Methodenentwicklung zur Charakterisierung von Membranen zur Gastrennung

4.1 Charakterisierung der Separationseigenschaften von Polymer und Polymer-Komposit Filmen in der Gastrennung

Im Rahmen des Aufbaus des Membran-Arbeitsbereichs im Institut für Bioanorganische Chemie und Strukturchemie wird die Trenneigenschaften von dünnen Polymerfilmen oder Polymer-Composite Filmen als Membranmaterial untersucht. Dafür wurden Anlagen für Einzelgasmessungen vom ehemaligen Institut für Polymerchemie/Funktionsmaterialien übernommen, die repariert, erweitert und modernisiert worden sind. Zusätzlich wurde ein neuer Aufbau zur Charakterisierung der Eigenschaften von Membranen zur Trennung von Gasgemischen in Zusammenarbeit mit der Firma Convergence Industry B.V.[ii], als Pilotanlage in der automatisierten Messung der Permeation entworfen, gebaut und so angepasst, dass die Methodik zur zuverlässigen und vergleichbaren und damit publizierbaren Erzeugung von Daten der Permeabilität und Selektivität von Membranmaterialien verwendet werden kann.

Diese Kooperation dient zum einen dazu, der Firma Convergence den Einstieg in die Gastrennungsanlagen zu ermöglichen, da deren vorheriges Spezialgebiet sich auf Mischung und Flussdetektion von Flüssigkeiten beschränkte, und zum anderen in Düsseldorf ein System zur wissenschaftlichen Untersuchung der Materialien zu etablieren, welches ein besseres Verständnis der Wechselwirkungen von verschiedenen permeierenden Komponenten miteinander und mit der Trennschicht im Separationsprozess gewonnen werden solle.

4.1.1 Umbau und Optimierung des Convergence OSMO Inspector

Der ‘Convergence OSMO Inspector‘ ist eine vollständig automatisierte Permeationsanlage zur Untersuchung der Separationseigenschaften von Membranen bei der Trennung von Gemischen aus zwei verschiedenen Gasen.

[ii] Euregioweg 283 7532 SM Enschede The Netherlands

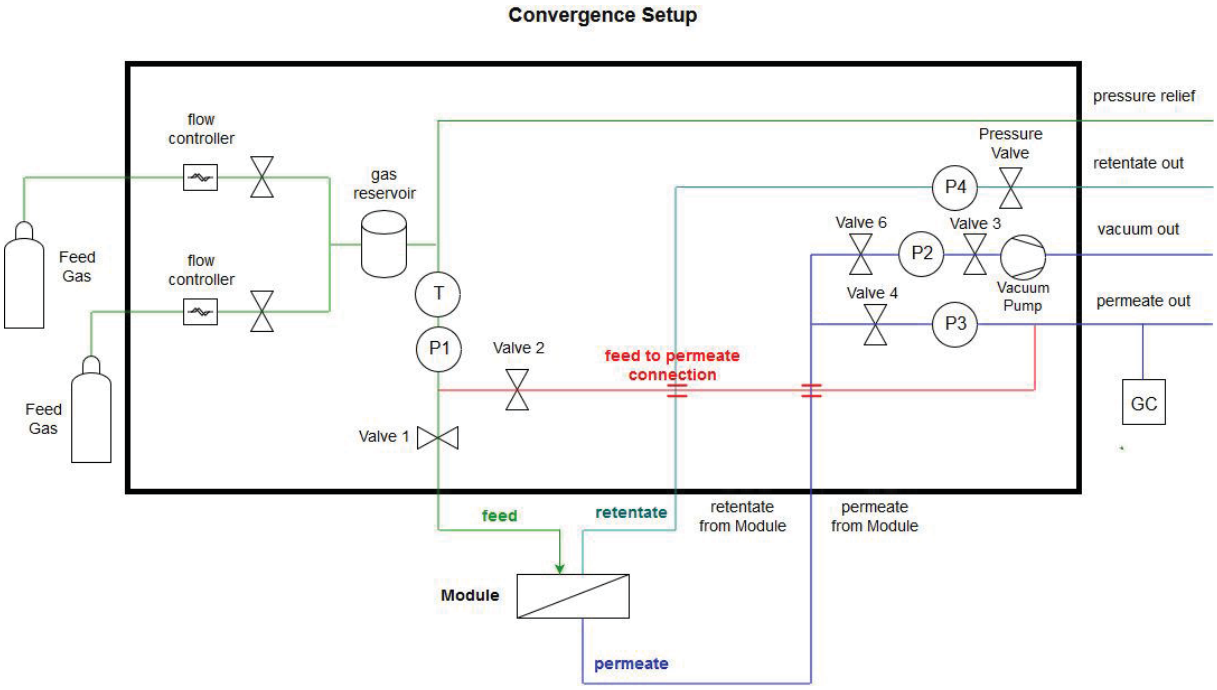

Abbildung 1 Ursprünglicher schematischer Aufbau des OSMO Inspectors

Die Messapparatur ist in eine Feed- (grün) und eine Permeatseite (blau) aufgeteilt, die von einem Membranmodul getrennt werden. Durch Hahn 2 sind der Feed- und Permeatbereich miteinander verbunden. Die Feed-Seite beinhaltet die Gaszufuhr, die den Anschluss zweier verschiedener Messgase ermöglicht. Durch Coriolis-Massendurchflussregler (Bronkhorst M13V10i-MBD-22-K-S, Messbereich: 4-200 g/h) kann bei Gemischtgasexperimenten die Feed-Zusammensetzung gesteuert werden. Um eine Konzentrationspolarisation auf der Membran zu vermeiden, kann durch wechselseitige Regelung der Feed-Massendurchflussregler mit dem Retentat-Drucksensor eine Überströmung der Membran bei höheren Feed-Drücken ermöglicht werden. Außerdem sind ein Drucksensor zur Überprüfung des Feeddrucks und eine Linie zur Entlüftung an den Feedbereich angeschlossen. Der Permeatbereich beinhaltet zum einen eine Linie für Messungen mit der Druckanstiegsmethode (Zugang durch Hahn 6) und zum anderen eine Linie (Zugang durch Hahn 4) für Messungen des Permeatstroms bei Normaldruck mit einem Coriolis-Massendurchflusssensor (Bronkhorst M12P-MBD-22-O-S, Messbereich: 0,2-20 g/h). Die Linie für Messungen mit der Druckanstiegsmethode beinhaltet einen Drucksensor (Messbereich: 0-1 bar) und eine Vakuumpumpe, welche bei Gaspermeationsexperimenten durch Hahn 3 von der Anlage getrennt wird. Alle Sensoren und ein Großteil der Rohrleitungen sind in einem Thermoschrank untergebracht, der konstant temperierbar ist. Die Anschlüsse für externe Zu- und Ableitung der Gasströme sind ‘*Feed 1 in*’ und ‘*Feed 2 in*’ für die beiden Probengase, der Zugang zum Membranmodul ‘*Feed to module*’, ‘*Ret. from module*‘ und ‘*Retentate out*‘ für das Retentat, ‘*Permeate out*“ und

‘*Perm. from module*’ für das Permeat, ‘*Vacuum out*‘ zum Evakuieren der Anlage und ‘*Pressure relief*‘ zum Druckausgleich.

Das Modul liegt außerhalb des Thermoschranks und wird über ein separates Heizband temperiert. Zur besseren Temperaturkontrolle wird das Modul in eine isolierte Box eingebracht, um so isotherme Messbedingungen erreichen zu können (s. Abbildung 2).

Abbildung 2 Membranmodul mit Isolierbox und Stativ

4.1.2 Konstanter Fluss-Methode (Gemischtgaspermeation)

Für Messungen bei konstantem Permeatfluss oder “konstantem Druck/variables Volumen“ wird die Flussrate des Permeats direkt durch Verwendung eines Durchflusssensors bestimmt und anschließend die Zusammensetzung des Permeats durch einen Gaschromatographen ermittelt. Bei sehr geringen Gasflüssen kann eine Spülgasmethode verwendet werden, bei der das Permeat unter konstantem Spülgasfluss von der Membran zur Detektion geleitet wird. Der OSMO-Inspector verwendet ‘miniCORI-FLOW Coriolis-Massedurchflussregler M13V10i‘ von ‘Bronkhorst Cori-Tech‘ zur Mischung der Feed-Gase. Die Massendurchflussregler und -sensoren funktionieren nach dem Coriolis-Betriebsprinzip welches unabhängig von Dichte, Temperatur, Viskosität, Druck und Leitfähigkeit ist. Die Regler erlaubt Flussgeschwindigkeiten zwischen 4 und 200 g/h. Die Durchflussmessung im Permeatbereich erfolgt über einen ‘miniCORI-FLOW Coriolis-Massedurchflussregler M12P‘. Die Sensoren und Regler sind mit ihren Spezifikationen in Tabelle 1 angegeben.

Tabelle 1 Massendurchfluss-Sensoren und -regler im OSMO-Inspector

Nr.	Modell	Arbeitsbereich	Anschluss	Merkmal	Skalierbar	Min. Fluss	Mindest-Obergrenze
F-1	M13V10i-MBD-22-K-S	1 – 2000 g/hr	1/4``	variabel	1:50	1 g/hr	50 g/hr
F-2	M13V10i-MBD-22-K-S	1 – 2000 g/hr	1/4``	variabel	1:50	1 g/hr	50 g/hr
F-3	F-201CV-020-MBD-11-V	0,2 – 10 mL/min	1/8``	nicht variabel	-	-	-
F-4	M12P-MBD-22-O-S	0,4 – 200 g/hr	1/4``	variabel	1:100	0,1 g/hr	5 g/hr

Bei Fehlfunktionen oder Wechsel eines Gases ist es notwendig, den Massenstromregler zunächst mit dem entsprechenden Messgas zu befüllen und anschließend, nachdem der Fluss auf Null gestellt wurde, die Schnellanschlüsse der Gaszufuhr zu entfernen, um zu gewährleisten, dass kein Durchfluss erfolgt. Anschließend werden die Flowcontroller per Software auf null zurückgesetzt (Auto Zero Funktion in Bronkhorst Software).
Bei Ausführung der Auto-Zero Funktion wird eine automatische Nullsetzung auf der Sensorbrückenschaltung durchgeführt. Dabei wird das Potentiometer eingestellt und der Nullskalenfaktor eingestellt, um sicherzustellen, dass das Sensorausgangssignal ohne Strömung Null ausgibt. Bei Anschluss von neuen Messgasen, wird zunächst durch die OSMO-Software mit dem jeweiligen Gas der Feedbereich durchspült und der Ausgang zum Permeat geöffnet. Nach kurzem Spülen mit dem Gas, wird der Contoller durch die „reset to Zero“ Funktion wieder inaktiviert und es wird abgewartet, bis der Fluss wieder den Wert Null annimmt. Anschließend wird die Osmo Software beendet, ohne die manuelle Kontrollfunktion vorher zu beenden, um sicherzustellen dass der Ausgang zum Permeat geöffnet bleibt. Sonst können keine Flusseinstellungen vorgenommen werden, da sich ein zu hoher Druck im Feedbereich aufbaut. Die Schnellanschlüsse zum Feed werden entfernt, um sicherzustellen dass kein Durchfluss erfolgt. Das Programm verbindet sich über Modbus TCP nach Auswahl der Nodes 1-4 mit den Contollern. Die Plotfunktion der Software lässt eine Betrachtung des oszillierenden Sensorausgangssignals zu.
Für optimale Genauigkeit wird eine Aufwärmphase von 30 Minuten nach dem Anschalten benötigt. Der Arbeitsbereich ist anpassbar. Der obere und untere Grenzwert der Massendurchflussregler und Sensoren ist abhängig von der aktuellen Skalierung. Das Stellverhältnis des Flusses ist für die Coriolis-Durchflussmesser 1:50. Dies bedeutet, wenn das Maximum auf X skaliert wird, wird das Minimum (X/50) sein. Es muss allerdings höher als der Mindestdurchfluss sein.
Der thermische Durchflussmesser F-201CV kann nicht skaliert werden (s. Spülgasmessung).
Aus dieser Berechnung ergeben sich die in
Tabelle 2 dargestellten Werte des minimalen und maximalen Durchflusses für die aktuellen Einstellungen der Flowmeter im OSMO.

Tabelle 2 Minimaler und maximaler Durchfluss für die aktuellen Einstellungen der Massendurchflussregler

Bezeichnung	Scale Max (aktuell)	Min Flow (scaled)	Max Flow (scaled)
F-1	200	4	200
F-2	200	4	200
F-3	10	0,2	10
F-4	20	0,2	20

Der Flusssensor im Permeat-Bereich arbeitet im Bereich zwischen 0,2-20 g/h. Für eine typische Membran mit niedriger Permeabilität werden jedoch weit geringere Massenflüsse erwartet. Am Beispiel einer Polysulfonmembran mit der Dicke 34,1 µm und einer Stickstoff-Permeabilität von 0,27 Barrer ist der benötigte Messbereich abzuschätzen. Bei einer Druckdifferenz von 3 bar und bei einer Messtemperatur von 35 °C wird ein Massenfluss von $11{,}7 \cdot 10^{-6}$ g/h erwartet. Dieser Wert stellt die Untergrenze des benötigten Messbereichs dar. Eine direkte Messung von so geringen Flüssen ist nicht möglich. Daher wurde ein zusätzlicher Gasanschluss mit einem thermischen Durchflussregler ergänzt, um Messungen nach der Spülgasmethode zu ermöglichen. Der Umbau beinhaltet auch neue Anschlüsse auf der Permeatseite des Moduls, um ein Unterströmen der Membran mit dem Spülgas Helium zu ermöglichen. In Abbildung 3 ist der Aufbau der Methode schematisch dargestellt.

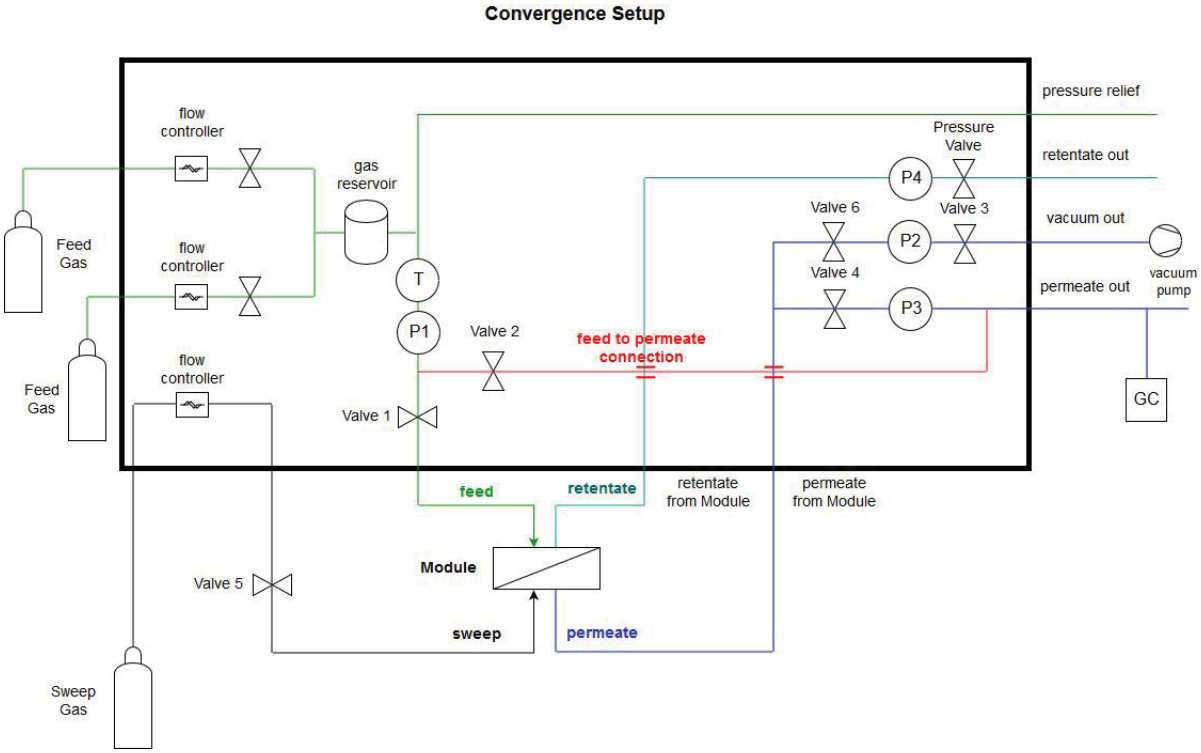

Abbildung 3 Schematischer Aufbau des OSMO Inspectors für Spülgas-Messungen

Zur Detektion der Zusammensetzung des Permeatstroms wird der Agilent 490-GC PRO Micro Gaschromatograph eingesetzt, da dieser kurze Messzyklen erlaubt und als PRO-Station in die Automatisierung des Messprozesses eingebunden werden kann. Der prinzipielle Aufbau besteht aus Trägergas, mikroelektronischer Gaskontrolle, Injektor, Trennsäule im GC-Ofen, Detektor und Signalaufzeichnung. Die Besonderheit der PRO Station Variante der Agilent 490-GC µ-GC ist, dass alle zur Funktionen wie Integration, Identifikation, Quantifizierung, Anwendung sowie Verifizierungs- und Kalibriermöglichkeiten im System des 490-GC PRO (ohne externe Software Steuerung) hinterlegt sind. Grundsätzlich werden über das PROstation Softwarepaket Uploads und Downloads von Konfigurations- und

Methodeneinstellungen und das Sammeln und Anzeigen von Analyseergebnissen durchgeführt.

Als Trägergas wird Helium verwendet. Die **Mikroelektronische Gaskontrolle (EGC)** hat die Aufgabe den Druck der Gase, die durch Injektor, Trennsäule und Detektor strömen einzustellen, wobei 0,5-3,5 bar möglich sind, was eine kontinuierliche Strömgeschwindigkeit des Trägergases von 0,2-4,0 ml/min ermöglicht.

Der **Injektor** ist darauf ausgerichtet aus einem konstant strömenden Gasstrom Proben zu entnehmen. Dabei ist ein maximaler Überdruck von maximal +1 bar möglich. Im Injektor ist eine 10 µl große Schleife eingebaut, die mithilfe einer Vakuumpumpe mit der Probe gefüllt und anschließend in den Gasstrom des Trägergases injiziert wird. Diese Probe sollte einen Druck von 0-1 bar und eine Temperatur von 5-110 °C ± 5 °C aufweisen. Der minimal erforderliche Druck für den Injektor liegt bei 5,5 ± 0,1 bar. Die meistverwendete Injektionszeit beträgt 40 ms, was einem durchschnittlichen Injektionsvolumen von 200 nl entspricht. Weiterhin sind Injektionszeiten von Vielfachen von 5 ms ab 45 ms möglich.

Zum Schutz des Injektionssystems und der Säulen vor möglicherweise vorhandenen Resten von Flüssigkeiten und Partikeln aus dem Probenstrom ist dem GC der Genie 170 Membrane Separator direkt vorgeschaltet. Als Filter dient eine Typ 6/BTU-Membran mit einer effektiven Porengröße kleiner als 1 µm. Sie ist inert und beeinflusst die Zusammensetzung des hindurch strömenden Gases nicht. Die Trennung erfolgt dadurch, dass die Poren der Membran so klein sind, dass es, im Gegensatz zu Gasen, für Flüssigkeiten unmöglich ist diese zu durchdringen, da sie nicht aus einzelnen, sondern mehreren aufgrund von Wechselwirkungen aneinanderhaftenden Molekülen bestehen, die größer sind als die Poren. Gase hingegen strömen unverändert in ihrer Zusammensetzung hindurch. Der maximale Druck, mit dem die Einheit belastet werden sollte, beträgt 35 bar. Die maximal einzusetzende Temperatur für den Filter beträgt 85 °C und die empfohlene maximale Flussrate 300 cm^3/min.

Die enthaltenen kapillaren Trennsäulen sind die Molekularsieb 5A PLOT und die Pora PLOT Q mit jeweils 0,25 mm Innendurchmesser und 10 m Länge. Die beiden Säulen sind jeweils in eigene GC-Kanäle eingebunden und sind separat ansteuerbar. Die Säule Pora PLOT Q ist dazu in der Lage Methan und CO_2 zu trennen und vom Luft-Peak separat aufzulösen. Die Molekularsieb 5A PLOT trennt Sauerstoff von Stickstoff, ist jedoch nicht verwendbar für Gemische die CO_2 enthalten, da durch Adsorption von CO_2 und Wasser ihre Trennleistung abnimmt. Die Säulen werden daher entsprechend der Trennproblematik gewechselt und sollten bei maximal 180 °C Ofentemperatur betrieben werden.

Durch Adsorption von geringen Mengen Wasser oder CO_2 aus dem Probengas können die Peaks von Sauerstoff von Stickstoff mit der Zeit auf dem MS 5A PLOT nicht mehr aufgelöst werden. Zur Regegeneration kann eine Konditionierung der Säulen über Nacht bei maximaler

Ofentemperatur vorgenommen werden. Um während der Messung zu verhindern, dass die entsprechenden Komponenten zur Molekularsieb-Säule gelangen kann das Rückspülsystem des GCs verwendet werden. Dieses Besteht aus einer Vorsäule und einer analytischen Säule. Die beiden Säulen sind mit einem Druckpunkt gekoppelt, der es ermöglicht, die Trägergasströmungsrichtung durch die Vorsäule zu einer voreingestellten Zeit, der "Backflushtime" umzukehren und so zu verhindern, dass später eluierende Komponenten zur analytischen Säule gelangen. Diese Zeit ist entsprechend der gewählten Methode anzupassen. Bei der Pora PLOT Q ist diese Option in der Regel nicht notwendig zu nutzen.
Zur Bestimmung der zu trennenden Komponenten ist das System mit Wärmeleitfähigkeitsdetektoren (TCD) ausgestattet. Dabei wird durch Detektion des Unterschieds der Wärmeleitfähigkeit des Trägergases zu der von Gasproben anhand eines Vergleichs der Wärmeleitfähigkeit des Trägergasstroms mit der Probe und eines konstanten Referenzgasstroms die Konzentration der einzelnen Komponenten der Probe über die direkte Proportionalität von Temperaturänderung in der Messzelle bzw. des elektrischen Wiederstands in Form von Spannungsunterschieden in den Heizdrähten und Probenkonzentration als Signal erfasst. Bei z.B. Kohlenwasserstoffen sind die Wärmeleitfähigkeiten sehr ähnlich und weichen stark ab von den der üblicherweise verwendeten Trägergase, sodass der TCD auch ohne Kalibrierung genutzt werden kann, da die Konzentration eines einzelnen Analyten aus dem Verhältnis zur Summe aller Analyten abgeschätzt werden kann. Aufgrund der unterschiedlichen Wärmeleitfähigkeiten ist bei der Detektion von Komponenten aus Gasströmen die Fläche der Peaks bei gleicher injizierter Stoffmenge jeweils unterschiedlich. Daher muss eine Kalibrierung für jede Substanz erfolgen, die bestimmt werden soll. Es besteht neben der Möglichkeit einer Einzellevelkalibrierung, bei der nur ein Stoff kalibriert wird, auch die Möglichkeit einer Multilevelkalibrierung mit mehreren Stoffen zusammen. Die Kalibrierung erfolgt über Messungen bekannter Probenkonzentrationen, wobei die Ergebnisse in dem ‘PROstation Instrument control’-Programm des GC dargestellt werden.

Die zur Kalibrierung zur Verfügung stehenden Gase sind $He/O_2/N_2$ (99.2/0.4/0.4 Vol. %), $He/CO_2/CH_4$ (99.2/0.4/0.4 Vol. %) und $He/CH_4/H_2$ (70/5 /25 Vol. %). Diese werden zur Kalibrierung mittels der beiden Feed Massendurchflussregler mit Helium weiter verdünnt, um die erwarteten Messbereiche zu erreichen.
Feinkalibrierungen für CO_2 und CH_4 wurden entsprechend vorgenommen. Der einzusetzende Massenstrom an Helium und des Kalibriergases für die zu kalibrierenden Bereiche sind in Tabelle 3 zusammengefasst. Dabei steht Q_g für den Massenstrom, He für Helium, K für das Kalibriergas, x für den Volumenanteil.

Tabelle 3: Vorgaben zur Feinkalibrierung von CO_2 und CH_4

$x_{K,CO2}$ [Vol. %]	$x_{K,CH4}$ [Vol. %]	x_{CO2} [Vol. %]	x_{CH4} [Vol. %]	$Q_{g,K}$ [g/h]	$Q_{g,He}$ [g/h]
0,4	0,4009	0,032	0,032	4	43,7
0,4	0,4009	0,041	0,041	4	33,3
0,4	0,4009	0,049	0,049	4	27,2
0,4	0,4009	0,058	0,058	4	22,4

Die Kalibrierung der Peakfläche gegen Vol% ergibt entsprechend für CO_2 und CH_4 die Ergebnisse aus Tabelle 4 und Tabelle 5 die lineare Korrelation von:

Vol% (CO_2) = 20777 Peakfläche (CO_2)-86,158, R^2 = 0,9999

Vol% (CH_4) = 15520 Peakfläche (CH_4)-6,7954, R^2 = 0,9992

Tabelle 4: Feinkalibrierung von CO_2

Vol. %	Peakfläche (CO_2)
0,032	660,0
0,041	865,9
0,049	1022,8
0,049	1019,7
0,058	1211,0
0,058	1216,6
0,058	1211,5
0,40	8032,3
0,40	8035,8
0,40	8039,8
0,40	8040,2
1,63	33621,6
1,63	34037,7
1,63	33848,7
1,63	33698,3
1,63	33901,8
1,79	36829,1
1,79	37032,1
1,79	37121,9
1,79	36773,9
1,98	40844,7
1,98	41098,3
1,98	40900,9
1,98	41608,7
1,98	41376,4

Tabelle 5: Feinkalibrierung von CH_4

Vol. %	Peakfläche (CH_4)
0,032	488,7
0,032	486,3
0,032	486,8
0,041	641,5
0,049	754,7
0,049	752,5
0,058	890,5
0,058	892,1

Vor Gemischtgasmessungen mit dem OSMO-Inspector muss sichergestellt werden, dass die Menge an Restgasen im System einem Minimum entspricht, da diese sonst die Ergebnisse verfälschen. Diese Restgasentfernung wird vorgenommen, indem abwechselnd der Permeatbereich zwischen Modul und Injektor des GC mit der Vakuumpumpe evakuiert und anschließend mit dem Spülgas befüllt wird. Dazu wurde hinter der Verbindung des GC ein manuell verschließbares Nadelventil eingebaut, um so das Verschließen des Bereichs während der Evakuierung zu ermöglichen (s. relief valve Abbildung 4). Der GC war nach Planung der Spülgasmessungen mittels PET-Schläuchen und Swagelockverbindungen an den OSMO-Inspector angeschlossen. Auch nach mehreren Evakuier- und Spülzyklen zeigte sich, dass Luft und CO_2 in das System eindringen. Daher wurde ein Umbau des außerhalb des OSMO-Inspectors liegenden Anschlusses notwendig. Da sich die PET-Schläuche beim Evakuieren und Befüllen mit Gas ausdehnen und zusammenziehen, können dort Undichtigkeiten entstehen. Daher wurde ein Bypass des Permeatstroms um die Permeationsanlage gebaut, welcher komplett aus Stahlrohrleitungen besteht und entsprechend zum restlichen Messsystem angepasst ist. Durch den Bypass konnte das Volumen des Permeatbereichs auf einen Bruchteil verkleinert werden, da das Permeat nicht wie zuvor erst durch die Anlage hindurch, sondern direkt zum GC strömt. Dies ermöglichte das Erreichen der Messbedingungen und brachte durch das kleinere Volumen verkürzte Evakuierdauer und einen niedrigeren Gasverbrauch mit sich. Über ein T-Stück und einen verschließbaren Hahn erfolgt eine Verbindung des Permeatbereichs des Moduls zum Permeatbereich der Permeationsanlage. Dies ermöglicht einen Einsatz der Vakuumpumpe zum Evakuieren des vollständigen Permeatbereichs. Die Verbindung zu beiden Seiten des „permeate out“ und „permeate from Module“ hat den Sinn dass der externe Aufbau (Memrbanmodul und Gaschromatograph) sich rechts von der Anlage befinden und so ein möglichst kleines Totvolumen zwischen Vakuumpumpe und Permeatbereich gewährleistet werden kann(s. Abbildung 4), gleichzeitig jedoch die Option besteht, dass nach Einbau des weiteren Absperrventils zwischen GC und Membranmodul (s. Kapitel 4.1.4) die Druckanstiegsmethode genutzt werden kann.

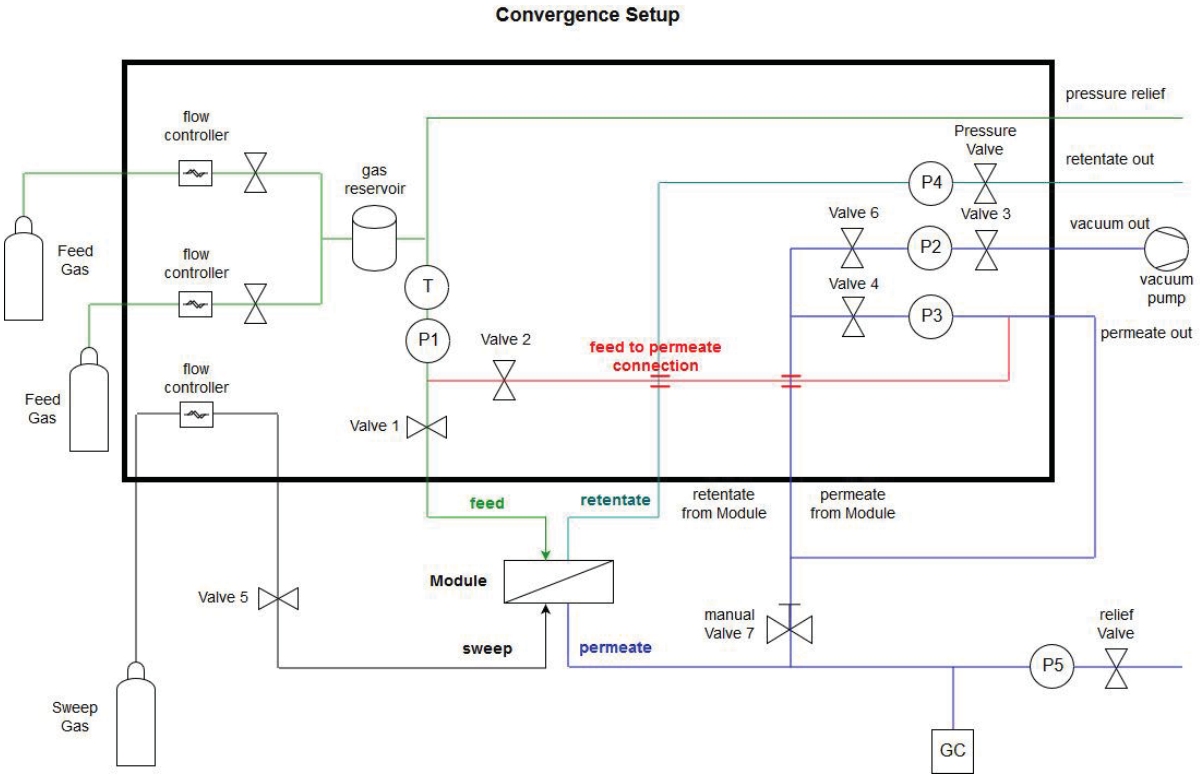

Abbildung 4: Finale schematische Darstellung der Gemischtgaspermeationsanlage

Zur Referenzierung wird mithilfe der kalibrierten Volumenanteile die Gemischtgas-Permeabilitäten von Matrimid für CO_2 und CH_4 bestimmt. Mit einer Permeabilität von 8,7 Barrer für CO_2, einer Permeabilität von 0,21 Barrer für CH_4 und einer Selektivität von 41 stimmen diese gut mit den in der Literatur berichteten Daten von vergleichbaren Gemischtgas-Permeationsexperimenten überein.[60,109,203]

4.1.3 Messmethodik für Gemischtgas-Permeationsmessungen mit dem OSMO-Inspector

Für Permeationsexperimente mit dem OSMO-Inspector wird die zurechtgeschnittene Membran in das Modul eingespannt, das Modul mit einem Heizband umwickelt und auf die gewünschte Temperatur während der gesamten Messzeit temperiert.

Zur möglichst vollständigen Entfernung von Restgasen vor den Messungen wird der Feed- und Permeatbereich zusammen evakuiert und anschließend mit maximalem Heliumfluss gespült. Dazu werden die digital bedienbaren Hähne 1, 2, 3, 4, 6 und der manuell zu bedienende Hahn 7 im Permeatbereich geöffnet und der gesamte Feed-, Permeat- und Retentatbereich der Messapparatur evakuiert. Sobald ein Druck von $1 \cdot 10^{-4}$ mbar erreicht ist, werden der Hahn 3 (Verbindung zur Vakuumpumpe) geschlossen, Hahn 5 geöffnet und die Apparatur mit Helium bei maximaler Flussgeschwindigkeit gespült, bis Atmosphärendruck erreicht ist. Dieser Evakuierungs- und Spülzyklus wird noch zweimal wiederholt.

Anschließend wird unter Atmosphärendruck Hahn 2 geschlossen (Verbindung zwischen Feed-, bzw. Retentatbereich auf der einen Seite und Permeatbereich auf der anderen Seite). Das schlechter durch die Membran permeierende Gas wird mit einem Druck von 1 bar auf den Feedbereich gepresst um die Membran zu fixieren, da abschließend dreimal der oben beschriebene Evakuierungs- und Spülzyklus nur für den Permeatbereich angewendet wird. Dazu wird erneut Hahn 3 geöffnet und der Peremeatbereich durch aktivieren der Vakuumpumpe evakuiert. Um Messbedingungen einzustellen wird bei Atmosphärendruck das Spülgas auf eine Flussmenge von 1 mL pro Minute eingestellt und der manuell zu bedienende Hahn 7 im Permeatbereich geschlossen. Über das Entlastungsventil und mittels eines analogen Manometers (P 5) am Ende des Permeatbereichs, wird über die gesamte Messzeit ein leicht über Atmosphärendruck liegender Permeatdruck eingestellt. Zur Kontrolle der durchgeführten Evakuierungs- und Spülzyklen wird die Gaszusammensetzung im Permeatbereich vor dem Einstellen der Messbedingungen durch eine Messung an dem Gaschromatographen (GC) bestimmt. Im Feedbereich wird ein Druck von 3 bar mit einer 50:50 Vol. % von Methan und Kohlenstoffdioxid eingestellt, was zu einer Druckdifferenz zwischen Feed- und Permeatbereich von 3 bar führt. Die 50:50 Gasmischung entspricht dabei einem Gasfluss von 4.1 $g \cdot h^{-1}$ Methan bzw. 11.4 $g \cdot h^{-1}$ Kohlenstoffdioxid. Alle 30 Minuten wird nun die Gaskonzentration im Permeatbereich über die GC analysiert, bis die Konzentrationen sich zwischen drei Messpunkten nicht mehr signifikant ändern. Bis zum Erreichen des Gleichgewichtszustands wird durchschnittlich eine Messzeit von ca. 6 Stunden benötigt.

Die Permeabilitäten werden auf Basis der vom Gaschromatographen gemessenen Peakbereiche für die verschiedenen Gase berechnet. Aus den durch die die Kalibrierung erhaltenen Volumenkonzentration kann mit Gleichung 7 die Permeabilität in Barrer (1 Barrer = $10^{-10} \cdot cm^3(STP)cm/(cm^2 \cdot s \cdot cmHg)$) errechnet werden.

$$P_A = \frac{x_{1A} \cdot S_{Fl} \cdot d}{x_{He}^{p} \cdot A \cdot (p_2 \cdot x_{2A} - p_1 \cdot x_{1A})} \tag{7}$$

Die Permeabilität P_A des Gases A in Barrer errechnet sich somit aus dem Stoffmengenanteil x_{1A} des Gases A im Permeat multipliziert mit dem Fluss des Spülgases S_{Fl} in $cm^3 \cdot s^{-1}$ und der Dicke der Membran d in cm, dividiert durch den Stoffmengenanteil des Spülgases im Permeat x^p_{He}, die Membranfläche A in cm^2 und den Stoffmengenanteil x_{2A} des Gases A im Feed multipliziert mit dem Feeddruck p_2 in cmHg subtrahiert von dem Stoffmengenanteil x_{1A} des Gases A im Permeat multipliziert mit dem Permeatdruck p_1 in cmHg.

4.1.4 Druckanstiegs-Methode (Einzelgaspermeation)

Bei der Druckanstiegsmethode oder “konstantes Volumen/variabler Druck”-Methode wird die Menge eines durch die Membran permeierten Gases durch den im definiert abgegrenzten Permeatvolumen ansteigenden Druck bestimmt. Dafür ist die Dichtigkeit dieses Volumens essentiell, da das Messsystem durch die Leckrate beeinflusst wird. Besonders bei Messung niedriger Permeabilitäten ist der dadurch verursachte Fehler groß, da der durch die Leckrate bedingte Druckanstieg größer ist als der „reale“ Druckanstieg, welcher durch den Gasfluss durch die Membran entsteht. Bei allen Permeabilitätsmessungen mit der Druckanstiegs-Methode werden daher die Messdaten mit der Leckrate korrigiert.

Für die Messung der Leckrate wird in die Messzelle ein kreisförmiges Stück Aluminiumfolie mit einem Durchmesser von 4,5 cm gelegt. Die Messzelle wird verschraubt und die gesamte Anlage evakuiert. Die Verbindung zwischen Vakuumpumpe, Permeatraum und Feedraum wird getrennt und ein Feeddruck von 3 bar angelegt. Der Druckanstieg im Permeatbereich kann nun nur durch die Leckrate der Anlage verursacht werden, da die Aluminiumfolie dicht ist und keine Gase durch sie permeieren können. Der Druckanstieg wird für 24 h gemessen und der Druckanstieg mit der Zeit bestimmt.

Im ursprünglichen Aufbau (Abbildung 1) war der Permeatbereich zur Bestimmung der Permeabilitäten durch die Druckanstiegsmethode vollständig mit Swagelock-Schraubverbindungen aufgebaut. Starke Unterschiede in der Leckrate vor Auslieferung des Geräts und nach Installation in Düsseldorf zeigten, dass die Schraubverbindungen dem Transport und der Vibration der im OSMO-Inspector verbauten Vakuumpumpe nicht standhalten. Daher wurde durch einen Umbau der komplette Permeatbereich zwischen Hahn 3, Hahn 4 und ‘permeate from module‘ durch Schweißstellen miteinander verbunden und die Vakuumpumpe außerhalb des OSMO-Inpectors verlegt, um mögliche Vibrationen zu vermeiden (Abbildung 3 und Abbildung 4).
Zur Bestimmung des Permeatvolumens wurde von Convergence die Länge der Rohrverbindungen (nach Abbildung 3) ausgemessen und durch Simulation mit Solidworks[220] das interne Volumen mit 27 mL berechnet. Zur Verwendung der Druckanstiegsmethode nach Abbildung 4 muss das Volumen noch angepasst werden und ein weiterer Hahn zwischen GC und dem Membranmodul ergänzt werden.

5. Zusammenfassung und Ausblick

In den folgenden Abschnitten wird jeweils eine Zusammenfassung der verschiedenen Arbeiten dieser Dissertation gegeben und ein kurzer Ausblick gegeben. Kapitel 5.1 fasst die Resultate der in der Fachliteratur dargestellten Entwicklung der neuesten Methoden zum Aufbau von MMMs und die Wirkung der Herstellung und Modifikationsmethoden von MOFs auf Permeabilität und Selektivität zusammen. In Kapitel 5.2 werden die Mikrowellen unterstützte Synthese und Analytik des MOFs $[Co_4(\mu_4\text{-}O)(Me_2pzba)_3]$ als CO_2 selektiver Füllstoff in MMMs beschrieben und die Resultate in der Trennung von CO_2/CH_4 Gasgemischen dargestellt. Kapitel 5.3 zeigt wie die Herstellung von reinen HKUST-1 Schichten auf Laserperforiertem Messing durch ein Temperaturgradienten-Verfahren erreicht werden kann. Kapitel 5.4. zeigt auf, wie durch Einbettung von hydrolyseempfindlichen MOFs in MMMs mit lumineszenten Füllstoffen potentielle Sensormaterialien zur Wasser/Sauerstoffdetektion hergestellt und charakterisiert werden können.

5.1 MOFs als Füllstoffe in Mixed-Matrix Membranen

Die Kombination von MOFs und Polymeren zur Herstellung von MMMs ist eine vielversprechende Strategie, um die Kompromissbeziehung zwischen Permeabilität und Selektivität für organische Polymere zu überwinden und Materialien mit Trennkapazitäten zu realisieren, die die Robeson-„upper-bound“ überschreiten und das Potenzial für industrielle Anwendungen erreichen. Die meisten in der Literatur dargestellten Arbeiten konzentrieren sich auf die Trennung von CO_2/CH_4 für die Aufreinigung von Erdgas oder CO_2/N_2-Trennung zur Reinigung von Rauchgasen. Dabei hängt die Verbesserung der Trennleistung der beschriebenen MMMs vor allem von der optimalen Füllstoffbeladung und der Membranintegrität bei hohen Füllstoffbeladungen oder verbesserter Füllstoffleistung ab. Die Darstellung der Permeationsdaten ermöglicht den systematischen Vergleich eines reinen Polymermaterials und die Wirkung der dargestellten MOF-Füllstoffe auf die Permeabilität und Selektivität. Es existieren viele separate Studien der Trenneigenschaften von MOF-MMMs. Struktur und Leistungsbeziehungen sind daher nicht absolut vergleichbar und lassen aufgrund von Experiment- und Probenunterschieden häufig nur relative Vergleiche zu. Die in Kapitel 1 und 3.1 dargestellten Daten zu MOF-MMMs stammen aus Studien, die eine Vielzahl von Charakterisierungsmethoden für die Gastrennung, aber ähnliche Messbedingungen verwenden. Eine beispielhafte Studie für einen besseren Vergleich der Experimente ist bereits bekannt, so wurden in Ringversuchen ZIF-8 MMMs in drei verschiedenen Laboren getestet und es wurde die Reproduzierbarkeit der Methodik der Permetionsexperimente mit Membranen gezeigt.[210] Insbesondere sollte die Gemischtgaspermeation und der Einfluss von Verunreinigungen auf die Trennleistung quantifiziert werden. Am Beispiel einer SPEEK-

Membran in der Kombination mit sulfoniertem MIL-101(Cr)[114] oder mit funktionalisiertem PEI @ MIL-101[143] als Füllstoff konnte gezeigt werden, dass eine Anwesenheit von Wasser als Verunreinigung im Gasstrom die Trennleistung des Materials erhöht, wodurch die Selektivität und Permeabilität bei 40 Gew.-% Beladung bei der Abtrennung eines CO_2/CH_4-Gasgemisches über die Robeson-„upper-bound“ hinaus drastisch erhöht wurde. Dieses Beispiel zeigt auch, dass Strategien wie die Modulation der MOF-Synthese und die Kontrolle der Partikelgröße entscheidend sind, um Additive für leistungsstarke MMMs zu entwerfen. Die Feinabstimmung der MMM-Eigenschaften durch Nutzung der chemischen Funktionalität des MOF-Linkers[111], oder durch Einführung von funktionellen Gruppen durch post-synthetische Modifikation[126,132] und auch das Design neuer PolyMOFs[156,161-162] die bei der Erzeugung einer neuen Unterkategorie von MOF-Werkstoffen mit großem Potenzial für hochleistungsfähige Membranen zur Gastrennung die hohen Erwartungen an MOFs als multifunktionale Materialien erfolgreich erfüllen. Die hohe Vielseitigkeit der MOF-Chemie ermöglicht es der Forschungsgemeinschaft, auf interessante Effekte zu zielen, wie die Verwendung der chemischen Modifikationen, um nicht nur die Leistung für eine spezifische Anwendung zu erhöhen, sondern auch die Stabilität, was ein wichtiger Schritt für die industrielle Anwendung ist.[216] Eine Ähnliche Rolle spielt dabei das Moduldesign, wobei bei Modulen welche für den industriellen Maßstab geeignet sind die Produktivität einer Membran durch den Einsatz asymmetrischer Membranen erhöht wird. Bei selektiven Schichten von weniger als 1 µm kann die Leistung von Polymeren mit niedrigem Gasfluss verbessert werden, um die Trenneigenschaften in einen kommerziell interessanten Bereich zu bringen. Ein Beispiel ist eine Pebax-MMM mit ZIF-7 Nanopartikeln als Füllstoff, bei welcher eine hohe Trennleistung für CO_2/N_2-Gasgemische erreicht wurde, indem die dünne selektive MMM-Schicht von einem porösen Poly(acrylnitril) Trägermaterial mit einer PTMSP-Zwischenschicht stabilisiert wurde.[178] Asymmetrische Holhfasermembranen in Form von MMMs[52,66-67] oder reine MOF-Membranen, aufgebracht auf polymeren Hohlfasern[211-215] zeigen entsprechende Trends.

5.2 CO_2 selektives [$Co_4(\mu_4\text{-}O)(Me_2pzba)_3$] als Füllstoff in MMMs

Die Synthese des zu MOF-5-Analogen-3D-[$Co_4(\mu_4\text{-}O)(Me_2pzba)_3$] durch Herstellung in der Mikrowelle konnte im Vergleich zur konventionellen solvothermalen Synthese hinsichtlich Ausbeute, Reaktionszeit, BET-Oberfläche, Partikelgrößenverteilung und Aggregation verbessert werden. Die Kontrolle der Partikelgröße und Form von MOF-Füllstoffen hat sich als entscheidend für die Herstellung von MOF-MMMs mit verbesserten Trenneigenschaften erwiesen. Dabei bietet die Wahl des MOF-Herstellungsverfahrens die Möglichkeit, das volle Potential eines MOF-Materials auszuschöpfen, indem die MOF-Partikelaggregation verhindert und die Verteilung und Orientierung des Füllstoffs verbessert wird. In dieser Arbeit konnte

durch die Wahl der Herstellung des MOFs $[Co_4(\mu_4\text{-}O)(Me_2pzba)_3]$ in der Mikrowelle nicht nur die Aggregation der MOF-Partikel verhindert werden, sondern ermöglichte auch die Herstellung größerer Mengen des MOFs was ebenfalls essentiell ist um die Herstellung von anwendungsorientierten Partikeln zur Anpassung der Morphologie hinsichtlich Leistung und Anwendbarkeit zu optimieren. Weiterhin zeigte $[Co_4(\mu_4\text{-}O)(Me_2pzba)_3]$ eine erhöhte Feuchtigkeitsstabilität im Vergleich zum Prototyp MOF-5. Für feuchtigkeitsempfindliche MOFs mit labilen Metall-Ligand Bindungen ist eine intensive Charakterisierung des Füllstoffmaterials notwendig, um zu ermitteln, ob die Permselektivitätswirkung des MOF-Materials tatsächlich auf seine noch vorhandene Porosität zurückzuführen ist. Daher ist es wichtig sicherzustellen, ob die MOF-Eigenschaften, insbesondere die Porosität, im fertigen MMM-Material aufrechterhalten werden, indem das MOF in Abwesenheit von Polymer identisch mit der MMM-Bildung behandelt wird und die Beibehaltung seiner Eigenschaften überprüft wird. Die ausführliche Charakterisierung von $[Co_4(\mu_4\text{-}O)(Me_2pzba)_3]$ bezüglich Feuchtigkeitsstabilität und Erhalt der Sorptionseigenschaften zeigte, dass im Vergleich zur theoretisch berechneten Oberfläche die Aktivierung noch verbessert werden kann. Dennoch wurden BET Oberflächen von 1860-1980 m^2/g erreicht, welche im Gegensatz zu MOF-5 auch nach mehreren Wochen erhalten bleiben. Außerdem erfolgt durch das Membranherstellungsverfahren nur eine leichte Reduzierung der BET-Oberfläche von $[Co_4(\mu_4\text{-}O)(Me_2pzba)_3]$. In $[Co_4(\mu_4\text{-}O)(Me_2pzba)_3]$/Matrimid-MMMs zeigten REM-Aufnahmen der Membranquerschnitte in Kombination mit EDX-Co-Element-Mapping, dass die MOF-Partikel gleichmäßig in das Polymer eingebettet waren, mit guter MOF-Polymer-Kompatibilität, die durch die verbesserte CO_2/CH_4-Trennleistung der MMMs im Vergleich zu reinen Matrimidmembranen bestätigt wurden. Die $[Co_4(\mu_4\text{-}O)(Me_2pzba)_3]$ MMMs zeigen eine Erhöhung von mehr als 46% in der CO_2/CH_4-Selektivität für 24 Gew.-% Füllstoffbeladung und 3 bar Transmembrandruck in Relation zur reinen Matrimid-Membranen zusammen mit einer verbesserter Permeabilität von 49% für CO_2. Im Vergleich zu MOF-5/Matrimid MMMs, welche eine Erhöhung der Permeabilität mit steigenden MOF-Anteilen zeigen, konnte in diesem Fall eine Erhöhung der Selektivität und so eine Annäherung an die Robeson „upper bound“ erreicht werden. Andere MOF/MMMs mit prototypischen MOFs und Derivaten zeigen vergleichbares Verhalten (Abbildung 5)

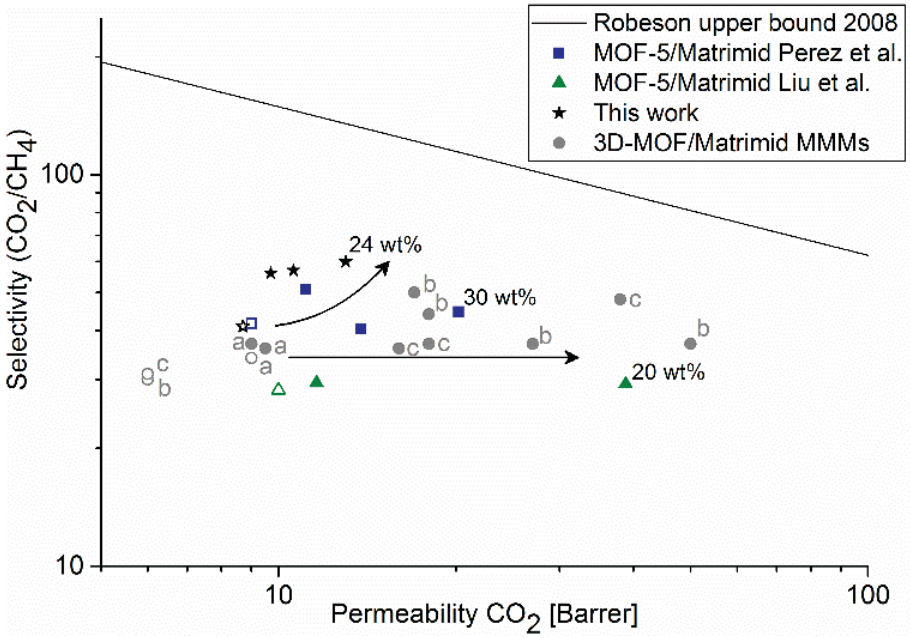

Abbildung 5 Auftragung von Permeabilitäten und Selektivitäten von MOF-5/Matrimid-MMMs und anderen MOF-MMMs in Relation zur Robeson „upper-bound" von 2008. Daten für MOF-5/Matrimid von Liu et al. aus Quelle [221] und für MOF-5/Matrimid von Perez et al. aus Quelle [164], beide aus Einzelgasmessungen. Die Gemischtgaspermeationsdaten für andere MOF-MMMs stammen für NH_2-MIL-53 und NH_2-MIL-101 (a) aus Quelle [109] für MIL-125 und NH_2-MIL125 (b) aus Quelle[111] für UiO- 66 und Derivate (c) aus Quelle[132], Daten aus dieser Arbeit sind aus Gemischtgaspermeationsmessungen. Gefüllte Symbole entsprechen MMMs, ungefüllte Symbole reinen Matrimidmembranen.

5.3 HKUST-1 Schichten auf Laser-microperforiertem Messing durch Temperaturgradienten-Synthese

Diese Arbeit beschäftigt sich mit HKUST-1 Schichten die auf lasermikroperforierten Messing-Blechen mittels eines Temperaturgradienten-Verfahren hergestellt wurden. Die Bildung von HKUST-1 auf den Trägern wurde durch gute Übereinstimmung mit dem simulierten Diffraktogramm mittels Pulverdiffraktometrie bestätigt. Zusätzliche Reflexe zeigen die Anwesenheit von anderen Phasen wie Kupfer(I)-Oxid und der Rouait Phase von basischem Kupfernitrat $Cu_2NO_3(OH)_3$. Zur Herstellung wurde ein Aufbau zur Synthese von MOFs durch einen Temperaturgradienten auf Substraten verwendet. Diese Methode erlaubt eine bessere Kontrolle der MOF-Abscheidung auf den perforierten Messingträgern. Synthesen mit verschiedenen Heiz- und Kühlraten wurden durchgeführt um die Temperatur auf der Oberfläche des Substrats zu steuern. Bei 100 °C und 150 °C Oberflächentemperatur konnte der Messingträger vollständig mit einer einheitlichen Schicht HKUST-1 bedeckt werden. Die Schichtdicke und die Kristallgröße hingegen hängen von der Reaktionstemperatur ab, wobei sich entsprechend die Reaktionsrate und Beladung mit der Temperatur erhöht. In REM-Aufnahmen sind die durch die Perforierung entstandenen Löcher (50µm) mit Kraterrändern erkennbar und die Oberfläche weist eine raue Struktur auf. Untersuchungen mittels EDX

zeigen, dass sich Zn und ZnO bei der Perforierung auf der Oberfläche zwischen den Kratern anreichern und der Cu-Anteil an den Kraterrändern steigt. Beides kann die Kristallisation von HKUST-1 begünstigen, mit den Cu-Spezies als Teil von HKUST-1 und den Oxiden als einheitliche Kristallisationskeime. Im Vergleich der unterschiedlich beladenen Proben ist bei der Probe mit geringerer Beladung das bevorzugte Wachstum an den Kraterrändern zu sehen welches bestätigt, dass die Cu-speziesreichen Bereiche eher das Wachstum von HKUST-1 fördern als die Metalloxide auf der Oberfläche. In den Querschnitten ist eine vollständige Beladung der Mikrolöcher erkennbar die über EDX-Mapping noch besser im Kontrast dargestellt werden können. PXRD- und N_2-Sorptionsmessungen in Kombination zeigen, dass mit dem Temperaturgradienten-Verfahren MOF-Schichten mit guter Kristallinität und hoher Gasaufnahme hergestellt werden konnten. Für die Sorptionsanwendungen ist der Erhalt der Porosität wichtig. Wenn die Stickstoffaufnahme der geträgerten Materialien um den MOF-Anteil korrigiert wird (da das Metallsubstrat keine Mikroporen besitzt), wird eine BET Oberfläche von 1105 m^2/g erreicht. Ebenfalls liegt die Wasser-Aufnahmekapazität bei Relativdücken um 0,8 im Bereich der in der Literatur berichteten typischen Werte sowohl im Vergleich zu dem reinen Bulk-MOF als auch der Wasseraufnahme von HKUST-1-Schichten auf anderen Trägermaterialien und zeigte so einen vollständigen Adsorbatzugang zu den hergestellten geträgerten HKUST-1-Kristallen (s. Tabelle 6).

Tabelle 6: Wasseradsorptionskapazitäten verschiedener HKUST-1-Pulver- und Dünnfilme bei p/p_0 = 0,9 und 298 K (sofern nicht anders angegeben)

Probe	Wasseraufnahme (g/g MOF)	Quelle
HKUST-1	0,51[a]	[99]
HKUST-1	0,52[a,b]	[222]
HKUST-1	0,40[a]	[223]
HKUST-1	0,58	[155]
HKUST-1	0,46[a]	[224]
Basolite C300 (kommerzielles HKUST-1)	0,55	[225]
HKUST-1/ QCM-Gold-Elektrode	0,26[b,c]	[226]
HKUST-1 (60 Schichten)/SiO_2	0,61	[227]
HKUST-1/Messing (100°C)	0,48[d]	Diese Arbeit [218]
HKUST-1/Messing (150°C)	0,45[d]	Diese Arbeit [218]

[a]Daten aus Wassersorptionsisothermen der entsprechenden Quellen. [b]Wert bei p/p_0 = 0,8 wegen Kondensation bei höheren relativen Drücken. [c]gemessen bei 294 K. [d]bei 293 K.

Die Wasseradsorptionsisothermen zeigen den typischen Stufenverlauf für HKUST-1, wobei im ersten Schritt das Besetzen der koordinativ ungesättigten Metallzentren und erst anschließend die vollständige Befüllung der Poren mit Wasser erfolgt. Die Vorteile der Perforierung der Messingträger durch Laserbestrahlung beinhalten eine Verbesserung der

MOF-Anbindung und eine bessere Verteilung der Kristalle auf der Oberfläche der gesamten Probe, wodurch gut und gleichmäßig haftende MOF-Beschichtungen ohne die Verwendung eines organischen Bindemittels erreicht werden können, welches die Adsorptionskapazität des MOFs im MOF-Metall-Verbundwerkstoff verändern könnte. Diese Eigenschaften können aufgrund einer verbesserten Masse- und Wärmeübertragung unterstützt durch das Vorhandensein von zugänglichen interkristallinen Räumen (was auf die Bildung einer hierarchischen porösen Struktur hindeutet) zu einer schnelleren Wasseraufnahme im MOF führen. Infolgedessen und unter Berücksichtigung der Merkmale des Ziel-MOFs, können die hier hergestellten HKUST-1 Beschichtungen potentiell in einer Reihe von Anwendungen verwendet werden, die sich auf Gastrennung und Einlagerung, Sensorik und Katalyse beziehen.

5.4 Hydrolyse empfindliche lumineszierende MOFs in MMMs als Sensormaterialien zur Wasser/Sauerstoffdetektion

Lumineszierende MOF-MMMs wurden aus den MOFs 3D-$[Sr_{0.9}Eu_{0.1}Im_2]$ und 2D-$[Tb_2Cl_6(bipy)_3]\cdot 2bipy$ mit dem Polysulfon Ultrason S und mit dem Polyimid Matrimid als Matrix hergestellt. Für die MMMs aus $[Sr_{0.9}Eu_{0.1}Im_2]$ mit PSF, $[Sr_{0.9}Eu_{0.1}Im_2]$ mit Matrimid und $[Tb_2Cl_6(bipy)_3]\cdot 2bipy$ mit PSF, blieb die Lumineszenz des MOFs auch nach der Filmherstellung erhalten und ist besonders stark für die MMMs aus $[Sr_{0.9}Eu_{0.1}Im_2]$ mit PSF. Die Membranpolymere beeinflussen die Lumineszenzintensität: In den Polysulfonmembranen zeigen beide MOFs eine höhere Emissionsintensität bei niedrigen MOF-Anteilen, während Matrimid als Matrix das entgegengesetzte Verhalten zeigt. Dies deutet darauf hin, dass sich die Polymere in ihrem Konzentrationsquenching unterscheiden. Die Verteilung der MOFs in den Membranen wurde durch REM, EDX und Fluoreszenzmikroskopie untersucht. Außer leichter Sedimentationen, sind die MOFs in den Membranquerschnitten gleichmäßig verteilt ohne signifikante Aggregation. Die Verwendung von Ultraschall erwies sich als unvorteilhaft, da die resultierenden Membranen abgeschwächte oder keine Lumineszenzeigenschaften zeigten. Gapermeationsmessungen zeigten, dass die MOF MMMs aus $[Sr_{0.9}Eu_{0.1}Im_2]$ mit PSF und $[Sr_{0.9}Eu_{0.1}Im_2]$ mit Matrimid keine Mikrodefekte aufwiesen, da sie nur etwas geringere Permeabilitäten aufgrund des nicht porösen Charakters der beiden MOFs aufweisen als die reinen Polymermembranen. Insgesamt zeigen diese Beispiele dass das Konzept der MOF-MMMs von der Gaspermeation auf neue Anwendungen erweitert werden kann. Die Herstellung von MMMs kann dabei eine Option sein, um die Stabilität von labilen Materialien und die Verarbeitbarkeit der Bulk-MOFs zu verbessern.

6. Tabellen- und Abbildungsverzeichnis

7. Literaturverzeichnis

(1) Dechnik, J.; Sumby, C. J.; Janiak, C. *Cryst. Growth Des.* **2017**, in press, http://dx.doi.org/10.1021/acs.cgd.7b00595.

(2) Dechnik, J.; Gascon, J.; Doonan, C.; Janiak, C.; Sumby, C. J. *Angew. Chem., Int. Ed.* **2017**, in press, http://dx.doi.org/10.1002/anie.201701109.

(3) Abetz, V.; Brinkmann, T.; Dijkstra, M.; Ebert, K.; Fritsch, D.; Ohlrogge, K.; Paul, D.; Peinemann, K. V.; Pereira-Nunes, S.; Scharnagl, N.; Schossig, M. *Adv. Eng. Mater.* **2006**, *8*, 328-358.

(4) Koros, W. J.; Mahajan, R. *J. Membr. Sci.* **2000**, *175*, 181-196.

(5) Davis, J.; Valus, R.; Eshraghi, R.; Velikoff, A. *Sep. Sci. Technol.* **1993**, *28*, 463-476.

(6) Buonomenna, M. G. *RSC Adv.* **2013**, *3*, 5694-5740.

(7) He, X.; Hägg, M.-B. *Membranes* **2012**, *2*, 706-726.

(8) Ohlrogge, K.; Stürken, K. The Separation of Organic Vapors from Gas Streams by Means of Membranes. In *Membrane Technology*; Wiley-VCH Verlag GmbH: 2001; pp 69-94.

(9) Baker, R. W. *Ind. Eng. Chem. Res.* **2002**, *41*, 1393-1411.

(10) BORSIG Membrane Technology GmbH. http://www.borsig-china.com/#productrecovery (accessed 2016).

(11) Sulzer Chemtech AG. http://www.sulzer.com/en/Products-and-Services/Separation-Technology/Membrane-Technology/Organic-Solvent-Nanofiltration-OSN (accessed 2016).

(12) Chung, T.-S.; Jiang, L. Y.; Li, Y.; Kulprathipanja, S. *Prog. Polym. Sci.* **2007**, *32*, 483-507.

(13) Seoane, B.; Coronas, J.; Gascon, I.; Benavides, M. E.; Karvan, O.; Caro, J.; Kapteijn, F.; Gascon, J. *Chem. Soc. Rev.* **2015**, *44*, 2421-2454.

(14) Adams, R.; Carson, C.; Ward, J.; Tannenbaum, R.; Koros, W. *Microporous Mesoporous Mater.* **2010**, *131*, 13-20.

(15) Basu, S.; Cano-Odena, A.; Vankelecom, I. F. J. *J. Membr. Sci.* **2010**, *362*, 478-487.

(16) Wiederhorn, S.; Fields, R.; Low, S.; Bahng, G.-W.; Wehrstedt, A.; Hahn, J.; Tomota, Y.; Miyata, T.; Lin, H.; Freeman, B.; Aihara, S.; Hagihara, Y.; Tagawa, T. Mechanical Properties. In *Springer Handbook of Materials Measurement Methods*; Czichos, H.; Saito, T.; Smith, L., Eds.; Springer: Berlin, Heidelberg, 2006; Chapter 7, pp 283-397.

(17) Dong, G.; Li, H.; Chen, V. *J. Membr. Sci.* **2011**, *369*, 206-220.

(18) Merkel, T. C.; Lin, H.; Wei, X.; Baker, R. *J. Membr. Sci.* **2010**, *359*, 126-139.

(19) Huang, Y.; Merkel, T. C.; Baker, R. W. *J. Membr. Sci.* **2014**, *463*, 33-40.

(20) IEA Bioenergy. http://www.iea-biogas.net/files/daten-redaktion/download/publi-task37/Biogas%20upgrading.pdf (accessed 2016).

(21) Basu, S.; Khan, A. L.; Cano-Odena, A.; Liu, C.; Vankelecom, I. F. J. *Chem. Soc. Rev.* **2010**, *39*, 750-768.

(22) Wind, J. D.; Staudt-Bickel, C.; Paul, D. R.; Koros, W. J. *Ind. Eng. Chem. Res.* **2002**, *41*, 6139-6148.

(23) Robeson, L. M. *J. Membr. Sci.* **1991**, *62*, 165-185.

(24) Robeson, L. M. *J. Membr. Sci.* **2008**, *320*, 390-400.

(25) Jessie Lue, S.; Peng, S. H. *J. Membr. Sci.* **2003**, *222*, 203-217.

(26) Qiu, S.; Ben, T. In *Porous polymers: Design, Synthesis and Applications*. RSC Publishing: Cambridge, 2015.

(27) Davis, M. E. *Ind. Eng. Chem. Res.* **1991**, *30*, 1675-1683.

(28) Liu, J.; Yu, J. Chapter 1 - Toward Greener and Designed Synthesis of Zeolite Materials A2 - Sels, Bert F. In *Zeolites and Zeolite-Like Materials*; Kustov, L. M., Ed. Elsevier: Amsterdam, 2016; pp 1-32.

(29) Furukawa, H.; Cordova, K. E.; O'Keeffe, M.; Yaghi, O. M. *Science* **2013**, *341*, 1230444-1-12.

(30) Ryoo, R.; Joo, S. H.; Jun, S. *J. Phys. Chem. B* **1999**, *103*, 7743-7746.

(31) Davis, M. E. *Nature* **2002**, *417*, 813-821.

(32) Harris, P. J. F. In *Carbon nanotube science: synthesis, properties and applications*. Cambridge university press: 2009.

(33) Jiang, L.; Fan, Z. *Nanoscale* **2014**, *6*, 1922-1945.

(34) Tanh Jeazet, H. B.; Staudt, C.; Janiak, C. *Dalton Trans.* **2012**, *41*, 14003-14027.

(35) Caro, J.; Noack, M. *Microporous Mesoporous Mater.* **2008**, *115*, 215-233.

(36) Caro, J.; Noack, M.; Kölsch, P.; Schäfer, R. *Microporous Mesoporous Mater.* **2000**, *38*, 3-24.

(37) Rangnekar, N.; Mittal, N.; Elyassi, B.; Caro, J.; Tsapatsis, M. *Chem. Soc. Rev.* **2015**, *44*, 7128-7154.

(38) Li, W.; Zhang, Y.; Li, Q.; Zhang, G. *Chem. Eng. Sci.* **2015**, *135*, 232-257.

(39) Bux, H.; Chmelik, C.; Krishna, R.; Caro, J. *J. Membr. Sci.* **2011**, *369*, 284-289.

(40) Li, Y.-S.; Liang, F.-Y.; Bux, H.; Feldhoff, A.; Yang, W.-S.; Caro, J. *Angew. Chem.* **2010**, *122*, 558-561.

(41) Bastani, D.; Esmaeili, N.; Asadollahi, M. *J. Ind. Eng. Chem.* **2013**, *19*, 375-393.

(42) Lai, Z.; Bonilla, G.; Diaz, I.; Nery, J. G.; Sujaoti, K.; Amat, M. A.; Kokkoli, E.; Terasaki, O.; Thompson, R. W.; Tsapatsis, M.; Vlachos, D. G. *Science* **2003**, *300*, 456-460.

(43) Venna, S. R.; Carreon, M. A. *Chem. Eng. Sci.* **2015**, *124*, 3-19.

(44) Zhang, Y.; Feng, X.; Yuan, S.; Zhou, J.; Wang, B. *Inorg. Chem. Front.* **2016**, *3*, 896-909.

(45) Zornoza, B.; Martinez-Joaristi, A.; Serra-Crespo, P.; Téllez, C.; Coronas, J.; Gascon, J.; Kapteijn, F. *Chem. Commun.* **2011**, *47*, 9522-9524.

(46) Nik, O. G.; Chen, X. Y.; Kaliaguine, S. *J. Membr. Sci.* **2012**, *413-414*, 48-61.

(47) Hunger, K.; Schmeling, N.; Jeazet, H. B.; Janiak, C.; Staudt, C.; Kleinermanns, K. *Membranes* **2012**, *2*, 727-763.

(48) Jeazet, H. B. T.; Janiak, C. Metal-Organic Frameworks in Mixed-Matrix Membranes. In *Metal-Organic Framework Materials*; MacGillivray, L. R.; Lukehart, C., Eds.; UK: John Wiley & Sons, Ltd: Chichester, 2014; pp 1-15.

(49) Zornoza, B.; Téllez, C.; Coronas, J.; Gascon, J.; Kapteijn, F. *Microporous Mesoporous Mater.* **2013**, *166*, 67-78.

(50) Dong, G.; Li, H.; Chen, V. *J. Mater. Chem. A* **2013**, *1*, 4610-4630.

(51) Ordoñez, M. J. C.; Balkus Jr, K. J.; Ferraris, J. P.; Musselman, I. H. *J. Membr. Sci.* **2010**, *361*, 28-37.

(52) Dai, Y.; Johnson, J. R.; Karvan, O.; Sholl, D. S.; Koros, W. J. *J. Membr. Sci.* **2012**, *401-402*, 76-82.

(53) Zheng, D.; Liu, X.; Hu, D.; Li, M.; Zhang, J.; Zeng, G.; Zhang, Y.; Sun, Y. *RSC Adv.* **2014**, *4*, 10140-10143.

(54) Buonomenna, M. G.; Yave, W.; Golemme, G. *RSC Adv.* **2012**, *2*, 10745-10773.

(55) Chen, X. Y.; Vinh-Thang, H.; Rodrigue, D.; Kaliaguine, S. *RSC Adv.* **2014**, *4*, 12235-12244.

(56) Sorribas, S.; Zornoza, B.; Téllez, C.; Coronas, J. *J. Membr. Sci.* **2014**, *452*, 184-192.

(57) Burmann, P.; Zornoza, B.; Téllez, C.; Coronas, J. *Chem. Eng. Sci.* **2014**, *107*, 66-75.

(58) Chen, X. Y.; Vinh-Thang, H.; Rodrigue, D.; Kaliaguine, S. *Ind. Eng. Chem. Res.* **2012**, *51*, 6895-6906.

(59) Seoane, B.; Zamaro, J. M.; Téllez, C.; Coronas, J. *RSC Adv.* **2011**, *1*, 917-922.

(60) Chen, X. Y.; Hoang, V.-T.; Rodrigue, D.; Kaliaguine, S. *RSC Adv.* **2013**, *3*, 24266-24279.

(61) Rebollar-Perez, G.; Carretier, E.; Lesage, N.; Moulin, P. *Membranes* **2011**, *1*, 80-90.

(62) Dumee, L.; Velleman, L.; Sears, K.; Hill, M.; Schutz, J.; Finn, N.; Duke, M.; Gray, S. *Membranes* **2010**, *1*, 25-36.

(63) Baker, R. W.; Lokhandwala, K. *Ind. Eng. Chem. Res.* **2008**, *47*, 2109-2121.

(64) Wijenayake, S. N.; Panapitiya, N. P.; Versteeg, S. H.; Nguyen, C. N.; Goel, S.; Balkus, K. J.; Musselman, I. H.; Ferraris, J. P. *Ind. Eng. Chem. Res.* **2013**, *52*, 6991-7001.

(65) Wijenayake, S. N.; Panapitiya, N. P.; Nguyen, C. N.; Huang, Y.; Balkus Jr, K. J.; Musselman, I. H.; Ferraris, J. P. *Sep. Purif. Technol.* **2014**, *135*, 190-198.

(66) Zulhairun, A. K.; Fachrurrazi, Z. G.; Nur Izwanne, M.; Ismail, A. F. *Sep. Purif. Technol.* **2015**, *146*, 85-93.

(67) Hu, J.; Cai, H.; Ren, H.; Wei, Y.; Xu, Z.; Liu, H.; Hu, Y. *Ind. Eng. Chem. Res.* **2010**, *49*, 12605-12612.

(68) Noble, R. D. *J. Membr. Sci.* **2011**, *378*, 393-397.

(69) Li, J.-R.; Ma, Y.; McCarthy, M. C.; Sculley, J.; Yu, J.; Jeong, H.-K.; Balbuena, P. B.; Zhou, H.-C. *Coord. Chem. Rev.* **2011**, *255*, 1791-1823.

(70) Liu, D.; Zhong, C. *J. Mater. Chem.* **2010**, *20*, 10308-10318.

(71) Meek, S. T.; Greathouse, J. A.; Allendorf, M. D. *Adv. Mater.* **2011**, *23*, 249-267.

(72) Bae, T. H.; Lee, J. S.; Qiu, W.; Koros, W. J.; Jones, C. W.; Nair, S. *Angew. Chem., Int. Ed.* **2010**, *49*, 9863-9866.

(73) Janiak, C.; Vieth, J. K. *New J. Chem.* **2010**, *34*, 2366-2388.

(74) Czaja, A. U.; Trukhan, N.; Muller, U. *Chem. Soc. Rev.* **2009**, *38*, 1284-1293.

(75) Bloch, E. D.; Queen, W. L.; Krishna, R.; Zadrozny, J. M.; Brown, C. M.; Long, J. R. *Science* **2012**, *335*, 1606-1610.

(76) Chen, B.; Ockwig, N. W.; Millward, A. R.; Contreras, D. S.; Yaghi, O. M. *Angew. Chem., Int. Ed.* **2005**, *44*, 4745-4749.

(77) Mueller, U.; Schubert, M.; Teich, F.; Puetter, H.; Schierle-Arndt, K.; Pastre, J. *J. Mater. Chem.* **2006**, *16*, 626-636.

(78) Li, Y.; Yang, W. *J. Membr. Sci.* **2008**, *316*, 3-17.

(79) Bowen, T. C.; Noble, R. D.; Falconer, J. L. *J. Membr. Sci.* **2004**, *245*, 1-33.

(80) Kosinov, N.; Gascon, J.; Kapteijn, F.; Hensen, E. J. M. *J. Membr. Sci.* **2016**, *499*, 65-79.

(81) NGK INSULATORS, LTD. http://www.ngk.co.jp/english/research/ecology.html (accessed 2016).

(82) Pera-Titus, M. *Chem. Rev.* **2014**, *114*, 1413-1492.

(83) Chen, Y. F.; Babarao, R.; Sandler, S. I.; Jiang, J. W. *Langmuir* **2010**, *26*, 8743-8750.

(84) Denny Jr, M. S.; Moreton, J. C.; Benz, L.; Cohen, S. M. *Nat. Rev. Mater.* **2016**, *1*, 16078.

(85) Jia, Z.; Wu, G. *Microporous Mesoporous Mater.* **2016**, *235*, 151-159.

(86) Sorribas, S.; Gorgojo, P.; Téllez, C.; Coronas, J.; Livingston, A. G. *J. Am. Chem. Soc.* **2013**, *135*, 15201-15208.

(87) Echaide-Gorriz, C.; Navarro, M.; Téllez, C.; Coronas, J. *Dalton Trans.* **2017**, *46*, 6244-6252.

(88) Sorribas, S.; Kudasheva, A.; Almendro, E.; Zornoza, B.; de la Iglesia, Ó.; Téllez, C.; Coronas, J. *Chem. Eng. Sci.* **2015**, *124*, 37-44.

(89) Low, J. J.; Benin, A. I.; Jakubczak, P.; Abrahamian, J. F.; Faheem, S. A.; Willis, R. R. *J. Am. Chem. Soc.* **2009**, *131*, 15834-15842.

(90) Leus, K.; Bogaerts, T.; De Decker, J.; Depauw, H.; Hendrickx, K.; Vrielinck, H.; Van Speybroeck, V.; Van Der Voort, P. *Microporous Mesoporous Mater.* **2016**, *226*, 110-116.

(91) Jeremias, F.; Fröhlich, D.; Janiak, C.; Henninger, S. K. *New J. Chem.* **2014**, *38*, 1846-1852.

(92) Jeremias, F.; Fröhlich, D.; Janiak, C.; Henninger, S. K. *RSC Adv.* **2014**, *4*, 24073-24082.

(93) Janiak, C.; Henninger, S. K. *Chimia* **2013**, *67*, 419-424.

(94) Férey, G.; Mellot-Draznieks, C.; Serre, C.; Millange, F.; Dutour, J.; Surblé, S.; Margiolaki, I. *Science* **2005**, *309*, 2040-2042.

(95) Ehrenmann, J.; Henninger, S. K.; Janiak, C. *Eur. J. Inorg. Chem.* **2011**, *2011*, 471-474.

(96) Khutia, A.; Rammelberg, H. U.; Schmidt, T.; Henninger, S.; Janiak, C. *Chem. Mater.* **2013**, *25*, 790-798.

(97) Karmakar, S.; Dechnik, J.; Janiak, C.; De, S. *J. Hazard. Mater.* **2016**, *303*, 10-20.

(98) Fröhlich, D.; Henninger, S. K.; Janiak, C. *Dalton Trans.* **2014**, *43*, 15300-15304.

(99) Küsgens, P.; Rose, M.; Senkovska, I.; Fröde, H.; Henschel, A.; Siegle, S.; Kaskel, S. *Microporous Mesoporous Mater.* **2009**, *120*, 325-330.

(100) Wu, T.; Shen, L.; Luebbers, M.; Hu, C.; Chen, Q.; Ni, Z.; Masel, R. I. *Chem. Commun.* **2010**, *46*, 6120-6122.

(101) DeCoste, J. B.; Peterson, G. W. *Chem. Rev.* **2014**, *114*, 5695-5727.

(102) Vellingiri, K.; Deep, A.; Kim, K.-H. *ACS Appl. Mater. Interfaces* **2016**, *8*, 29835-29857.

(103) Cmarik, G. E.; Kim, M.; Cohen, S. M.; Walton, K. S. *Langmuir* **2012**, *28*, 15606-15613.

(104) Dan-Hardi, M.; Serre, C.; Frot, T.; Rozes, L.; Maurin, G.; Sanchez, C.; Férey, G. *J. Am. Chem. Soc.* **2009**, *131*, 10857-10859.

(105) Zlotea, C.; Phanon, D.; Mazaj, M.; Heurtaux, D.; Guillerm, V.; Serre, C.; Horcajada, P.; Devic, T.; Magnier, E.; Cuevas, F.; Ferey, G.; Llewellyn, P. L.; Latroche, M. *Dalton Trans.* **2011**, *40*, 4879-4881.

(106) Goesten, M. G.; Juan-Alcañiz, J.; Ramos-Fernandez, E. V.; Sai Sankar Gupta, K. B.; Stavitski, E.; van Bekkum, H.; Gascon, J.; Kapteijn, F. *J. Catal.* **2011**, *281*, 177-187.

(107) Torrisi, A.; Mellot-Draznieks, C.; Bell, R. G. *J. Chem. Phys.* **2010**, *132*, 044705-1-13.

(108) Seoane, B.; Téllez, C.; Coronas, J.; Staudt, C. *Sep. Purif. Technol.* **2013**, *111*, 72-81.

(109) Rodenas, T.; van Dalen, M.; Serra-Crespo, P.; Kapteijn, F.; Gascon, J. *Microporous Mesoporous Mater.* **2014**, *192*, 35-42.

(110) Guo, X.; Huang, H.; Ban, Y.; Yang, Q.; Xiao, Y.; Li, Y.; Yang, W.; Zhong, C. *J. Membr. Sci.* **2015**, *478*, 130-139.

(111) Anjum, M. W.; Bueken, B.; De Vos, D.; Vankelecom, I. F. J. *J. Membr. Sci.* **2016**, *502*, 21-28.

(112) Vanherck, K.; Vandezande, P.; Aldea, S. O.; Vankelecom, I. F. J. *J. Membr. Sci.* **2008**, *320*, 468-476.

(113) Li, Z.; He, G.; Zhao, Y.; Cao, Y.; Wu, H.; Li, Y.; Jiang, Z. *J. Power Sources* **2014**, *262*, 372-379.

(114) Xin, Q.; Liu, T.; Li, Z.; Wang, S.; Li, Y.; Li, Z.; Ouyang, J.; Jiang, Z.; Wu, H. *J. Membr. Sci.* **2015**, *488*, 67-78.

(115) Sijbesma, H.; Nymeijer, K.; van Marwijk, R.; Heijboer, R.; Potreck, J.; Wessling, M. *J. Membr. Sci.* **2008**, *313*, 263-276.

(116) Xin, Q.; Wu, H.; Jiang, Z.; Li, Y.; Wang, S.; Li, Q.; Li, X.; Lu, X.; Cao, X.; Yang, J. *J. Membr. Sci.* **2014**, *467*, 23-35.

(117) Denny, M. S.; Cohen, S. M. *Angew. Chem., Int. Ed.* **2015**, *54*, 9029-9032.

(118) Luan, Y.; Qi, Y.; Gao, H.; Andriamitantsoa, R. S.; Zheng, N.; Wang, G. *J. Mater. Chem. A* **2015**, *3*, 17320-17331.

(119) Wang, Z.; Cohen, S. M. *Chem. Soc. Rev.* **2009**, *38*, 1315-1329.

(120) Yi, X.-C.; Xi, F.-G.; Qi, Y.; Gao, E.-Q. *RSC Adv.* **2015**, *5*, 893-900.

(121) Fei, H.; Pullen, S.; Wagner, A.; Ott, S.; Cohen, S. M. *Chem. Commun.* **2015**, *51*, 66-69.

(122) Karagiaridi, O.; Vermeulen, N. A.; Klet, R. C.; Wang, T. C.; Moghadam, P. Z.; Al-Juaid, S. S.; Stoddart, J. F.; Hupp, J. T.; Farha, O. K. *Inorg. Chem.* **2015**, *54*, 1785-1790.

(123) Song, Y.-F.; Cronin, L. *Angew. Chem., Int. Ed.* **2008**, *47*, 4635-4637.

(124) Tanabe, K. K.; Cohen, S. M. *Chem. Soc. Rev.* **2011**, *40*, 498-519.

(125) Cohen, S. M. *Chem. Rev.* **2012**, *112*, 970-1000.

(126) Venna, S. R.; Lartey, M.; Li, T.; Spore, A.; Kumar, S.; Nulwala, H. B.; Luebke, D. R.; Rosi, N. L.; Albenze, E. *J. Mater. Chem. A* **2015**, *3*, 5014-5022.

(127) Schaate, A.; Roy, P.; Godt, A.; Lippke, J.; Waltz, F.; Wiebcke, M.; Behrens, P. *Chem. Eur. J.* **2011**, *17*, 6643-6651.

(128) Liu, Q.; Jin, L.-N.; Sun, W.-Y. *CrystEngComm* **2013**, *15*, 8250-8254.

(129) Wißmann, G.; Schaate, A.; Lilienthal, S.; Bremer, I.; Schneider, A. M.; Behrens, P. *Microporous Mesoporous Mater.* **2012**, *152*, 64-70.

(130) Valenzano, L.; Civalleri, B.; Chavan, S.; Bordiga, S.; Nilsen, M. H.; Jakobsen, S.; Lillerud, K. P.; Lamberti, C. *Chem. Mater.* **2011**, *23*, 1700-1718.

(131) Vermoortele, F.; Bueken, B.; Le Bars, G.; Van de Voorde, B.; Vandichel, M.; Houthoofd, K.; Vimont, A.; Daturi, M.; Waroquier, M.; Van Speybroeck, V.; Kirschhock, C.; De Vos, D. E. *J. Am. Chem. Soc.* **2013**, *135*, 11465-11468.

(132) Anjum, M. W.; Vermoortele, F.; Khan, A. L.; Bueken, B.; De Vos, D. E.; Vankelecom, I. F. J. *ACS Appl. Mater. Interfaces* **2015**, *7*, 25193-25201.

(133) Cavka, J. H.; Jakobsen, S.; Olsbye, U.; Guillou, N.; Lamberti, C.; Bordiga, S.; Lillerud, K. P. *J. Am. Chem. Soc.* **2008**, *130*, 13850-13851.

(134) Huang, X.-C.; Lin, Y.-Y.; Zhang, J.-P.; Chen, X.-M. *Angew. Chem.* **2006**, *118*, 1587-1589.

(135) Park, K. S.; Ni, Z.; Côté, A. P.; Choi, J. Y.; Huang, R.; Uribe-Romo, F. J.; Chae, H. K.; O'Keeffe, M.; Yaghi, O. M. *Proc. Natl. Acad. Sci.* **2006**, *103*, 10186-10191.

(136) Bux, H.; Liang, F.; Li, Y.; Cravillon, J.; Wiebcke, M.; Caro, J. *J. Am. Chem. Soc.* **2009**, *131*, 16000-16001.

(137) Fairen-Jimenez, D.; Moggach, S. A.; Wharmby, M. T.; Wright, P. A.; Parsons, S.; Düren, T. *J. Am. Chem. Soc.* **2011**, *133*, 8900-8902.

(138) Novaković, S. B.; Bogdanović, G. A.; Heering, C.; Makhloufi, G.; Francuski, D.; Janiak, C. *Inorg. Chem.* **2015**, *54*, 2660-2670.

(139) Ban, Y.; Li, Z.; Li, Y.; Peng, Y.; Jin, H.; Jiao, W.; Guo, A.; Wang, P.; Yang, Q.; Zhong, C.; Yang, W. *Angew. Chem.* **2015**, *127*, 15703-15707.

(140) Hasib-ur-Rahman, M.; Siaj, M.; Larachi, F. *Chem. Eng. Process.* **2010**, *49*, 313-322.

(141) Ahnfeldt, T.; Guillou, N.; Gunzelmann, D.; Margiolaki, I.; Loiseau, T.; Férey, G.; Senker, J.; Stock, N. *Angew. Chem., Int. Ed.* **2009**, *48*, 5163-5166.

(142) Cao, L.; Lv, F.; Liu, Y.; Wang, W.; Huo, Y.; Fu, X.; Sun, R.; Lu, Z. *Chem. Commun.* **2015**, *51*, 4364-4367.

(143) Chiou, J. S.; Paul, D. R. *J. Appl. Polym. Sci.* **1987**, *34*, 1037-1056.

(144) Min, K. E.; Paul, D. R. *J. Polym. Sci., Part B: Polym. Phys.* **1988**, *26*, 1021-1033.

(145) Llewellyn, P. L.; Bourrelly, S.; Serre, C.; Vimont, A.; Daturi, M.; Hamon, L.; De Weireld, G.; Chang, J.-S.; Hong, D.-Y.; Kyu Hwang, Y.; Hwa Jhung, S.; Férey, G. *Langmuir* **2008**, *24*, 7245-7250.

(146) Xin, Q.; Ouyang, J.; Liu, T.; Li, Z.; Li, Z.; Liu, Y.; Wang, S.; Wu, H.; Jiang, Z.; Cao, X. *ACS Appl. Mater. Interfaces* **2015**, *7*, 1065-1077.

(147) Yan, Q.; Lin, Y.; Kong, C.; Chen, L. *Chem. Commun.* **2013**, *49*, 6873-6875.

(148) Hwang, Y. K.; Hong, D.-Y.; Chang, J.-S.; Jhung, S. H.; Seo, Y.-K.; Kim, J.; Vimont, A.; Daturi, M.; Serre, C.; Férey, G. *Angew. Chem., Int. Ed.* **2008**, *47*, 4144-4148.

(149) Hong, D.-Y.; Hwang, Y. K.; Serre, C.; Férey, G.; Chang, J.-S. *Adv. Funct. Mater.* **2009**, *19*, 1537-1552.

(150) Chui, S. S.-Y.; Lo, S. M.-F.; Charmant, J. P. H.; Orpen, A. G.; Williams, I. D. *Science* **1999**, *283*, 1148-1150.

(151) Taylor-Pashow, K. M. L.; Rocca, J. D.; Xie, Z.; Tran, S.; Lin, W. *J. Am. Chem. Soc.* **2009**, *131*, 14261-14263.

(152) Serre, C.; Millange, F.; Thouvenot, C.; Noguès, M.; Marsolier, G.; Louër, D.; Férey, G. *J. Am. Chem. Soc.* **2002**, *124*, 13519-13526.

(153) Millange, F.; Serre, C.; Guillou, N.; Férey, G.; Walton, R. I. *Angew. Chem., Int. Ed.* **2008**, *47*, 4100-4105.

(154) DeCoste, J. B.; Denny, J. M. S.; Peterson, G. W.; Mahle, J. J.; Cohen, S. M. *Chem. Sci.* **2016**, *7*, 2711-2716.

(155) DeCoste, J. B.; Peterson, G. W.; Schindler, B. J.; Killops, K. L.; Browe, M. A.; Mahle, J. J. *J. Mater. Chem. A* **2013**, *1*, 11922-11932.

(156) Zhang, Z.; Nguyen, H. T. H.; Miller, S. A.; Cohen, S. M. *Angew. Chem., Int. Ed.* **2015**, *54*, 6152-6157.

(157) Zhang, Z.; Nguyen, H. T. H.; Miller, S. A.; Ploskonka, A. M.; DeCoste, J. B.; Cohen, S. M. *J. Am. Chem. Soc.* **2016**, *138*, 920-925.

(158) Li, H.; Eddaoudi, M.; O'Keeffe, M.; Yaghi, O. M. *Nature* **1999**, *402*, 276-279.

(159) Tranchemontagne, D. J.; Hunt, J. R.; Yaghi, O. M. *Tetrahedron* **2008**, *64*, 8553-8557.

(160) Eddaoudi, M.; Kim, J.; Rosi, N.; Vodak, D.; Wachter, J.; O'Keeffe, M.; Yaghi, O. M. *Science* **2002**, *295*, 469-472.

(161) Allen, C. A.; Boissonnault, J. A.; Cirera, J.; Gulland, R.; Paesani, F.; Cohen, S. M. *Chem. Commun.* **2013**, *49*, 3200-3202.

(162) Allen, C. A.; Cohen, S. M. *Inorg. Chem.* **2014**, *53*, 7014-7019.

(163) Saha, D.; Bao, Z.; Jia, F.; Deng, S. *Environ. Sci. Technol.* **2010**, *44*, 1820-1826.

(164) Perez, E. V.; Balkus Jr, K. J.; Ferraris, J. P.; Musselman, I. H. *J. Membr. Sci.* **2009**, *328*, 165-173.

(165) Nugent, P.; Belmabkhout, Y.; Burd, S. D.; Cairns, A. J.; Luebke, R.; Forrest, K.; Pham, T.; Ma, S.; Space, B.; Wojtas, L.; Eddaoudi, M.; Zaworotko, M. J. *Nature* **2013**, *495*, 80-84.

(166) Henke, S.; Schneemann, A.; Kapoor, S.; Winter, R.; Fischer, R. A. *J. Mater. Chem.* **2012**, *22*, 909-918.

(167) Henke, S.; Fischer, R. A. *J. Am. Chem. Soc.* **2011**, *133*, 2064-2067.

(168) Henke, S.; Schneemann, A.; Wütscher, A.; Fischer, R. A. *J. Am. Chem. Soc.* **2012**, *134*, 9464-9474.

(169) Alaerts, L.; Maes, M.; Giebeler, L.; Jacobs, P. A.; Martens, J. A.; Denayer, J. F. M.; Kirschhock, C. E. A.; De Vos, D. E. *J. Am. Chem. Soc.* **2008**, *130*, 14170-14178.

(170) Millange, F.; Guillou, N.; Walton, R. I.; Greneche, J.-M.; Margiolaki, I.; Ferey, G. *Chem. Commun.* **2008**, 4732-4734.

(171) Basu, S.; Cano-Odena, A.; Vankelecom, I. F. J. *Sep. Purif. Technol.* **2011**, *81*, 31-40.

(172) Rodenas, T.; van Dalen, M.; García-Pérez, E.; Serra-Crespo, P.; Zornoza, B.; Kapteijn, F.; Gascon, J. *Adv. Funct. Mater.* **2014**, *24*, 249-256.

(173) Bhattacharya, A.; Misra, B. N. *Prog. Polym. Sci.* **2004**, *29*, 767-814.

(174) Tien-Binh, N.; Vinh-Thang, H.; Chen, X. Y.; Rodrigue, D.; Kaliaguine, S. *J. Mater. Chem. A* **2015**, *3*, 15202-15213.

(175) Ahmadi Feijani, E.; Mahdavi, H.; Tavasoli, A. *Chem. Eng. Res. Des.* **2015**, *96*, 87-102.

(176) Ahmadi Feijani, E.; Tavasoli, A.; Mahdavi, H. *Ind. Eng. Chem. Res.* **2015**, *54*, 12124-12134.

(177) Cai, W.; Lee, T.; Lee, M.; Cho, W.; Han, D.-Y.; Choi, N.; Yip, A. C. K.; Choi, J. *J. Am. Chem. Soc.* **2014**, *136*, 7961-7971.

(178) Li, T.; Pan, Y.; Peinemann, K.-V.; Lai, Z. *J. Membr. Sci.* **2013**, *425–426*, 235-242.

(179) Rezakazemi, M.; Ebadi Amooghin, A.; Montazer-Rahmati, M. M.; Ismail, A. F.; Matsuura, T. *Prog. Polym. Sci.* **2014**, *39*, 817-861.

(180) Ding, Z.-D.; Chi, Z.; Gu, W.-X.; Gu, S.-M.; Liu, J.-H.; Wang, H.-J. *Carbohydr. Polym.* **2012**, *89*, 7-16.

(181) Santos, E.; Rodríguez-Fernández, E.; Casado-Coterillo, C.; Irabien, Á. *Int. J. Chem. React. Eng.* **2016**, *14*, 713-718.

(182) Casado-Coterillo, C.; Fernandez-Barquin, A.; Zornoza, B.; Téllez, C.; Coronas, J.; Irabien, A. *RSC Adv.* **2015**, *5*, 102350-102361.

(183) Zhou, F.; Koros, W. J. *Polymer* **2006**, *47*, 280-288.

(184) Bos, A.; Pünt, I. G. M.; Wessling, M.; Strathmann, H. *Sep. Purif. Technol.* **1998**, *14*, 27-39.

(185) Mahdi, E. M.; Tan, J.-C. *J. Membr. Sci.* **2016**, *498*, 276-290.

(186) Song, Q.; Nataraj, S. K.; Roussenova, M. V.; Tan, J. C.; Hughes, D. J.; Li, W.; Bourgoin, P.; Alam, M. A.; Cheetham, A. K.; Al-Muhtaseb, S. A.; Sivaniah, E. *Energy Environ. Sci.* **2012**, *5*, 8359-8369.

(187) Aroon, M. A.; Ismail, A. F.; Matsuura, T.; Montazer-Rahmati, M. M. *Sep. Purif. Technol.* **2010**, *75*, 229-242.

(188) Carne, A.; Carbonell, C.; Imaz, I.; Maspoch, D. *Chem. Soc. Rev.* **2011**, *40*, 291-305.

(189) Tanaka, D.; Henke, A.; Albrecht, K.; Moeller, M.; Nakagawa, K.; Kitagawa, S.; Groll, J. *Nat Chem* **2010**, *2*, 410-416.

(190) Tanaka, S.; Fujita, K.; Miyake, Y.; Miyamoto, M.; Hasegawa, Y.; Makino, T.; Van der Perre, S.; Cousin Saint Remi, J.; Van Assche, T.; Baron, G. V.; Denayer, J. F. M. *J. Phys. Chem. C* **2015**, *119*, 28430-28439.

(191) Yang, J.-M.; Liu, Q.; Sun, W.-Y. *J. Solid State Chem.* **2014**, *218*, 50-55.

(192) Stavitski, E.; Goesten, M.; Juan-Alcañiz, J.; Martinez-Joaristi, A.; Serra-Crespo, P.; Petukhov, A. V.; Gascon, J.; Kapteijn, F. *Angew. Chem., Int. Ed.* **2011**, *50*, 9624-9628.

(193) Taddei, M.; Dau, P. V.; Cohen, S. M.; Ranocchiari, M.; van Bokhoven, J. A.; Costantino, F.; Sabatini, S.; Vivani, R. *Dalton Trans.* **2015**, *44*, 14019-14026.

(194) Liu, B.; Zou, R.-Q.; Zhong, R.-Q.; Han, S.; Shioyama, H.; Yamada, T.; Maruta, G.; Takeda, S.; Xu, Q. *Microporous Mesoporous Mater.* **2008**, *111*, 470-477.

(195) Ziaee, A.; Chovan, D.; Lusi, M.; Perry, J. J.; Zaworotko, M. J.; Tofail, S. A. M. *Cryst. Growth Des.* **2016**, *16*, 3890-3897.

(196) Uemura, K.; Maeda, A.; Maji, T. K.; Kanoo, P.; Kita, H. *Eur. J. Inorg. Chem.* **2009**, *2009*, 2329-2337.

(197) Shekhah, O.; Belmabkhout, Y.; Chen, Z.; Guillerm, V.; Cairns, A.; Adil, K.; Eddaoudi, M. *Nat. Commun.* **2014**, *5*, 4228.

(198) Gong, H.; Nguyen, T. H.; Wang, R.; Bae, T.-H. *J. Membr. Sci.* **2015**, *495*, 169-175.

(199) Hu, Z.; Nalaparaju, A.; Peng, Y.; Jiang, J.; Zhao, D. *Inorg. Chem.* **2016**, *55*, 1134-1141.

(200) Hu, Z.; Kang, Z.; Qian, Y.; Peng, Y.; Wang, X.; Chi, C.; Zhao, D. *Ind. Eng. Chem. Res.* **2016**.

(201) Ricco, R.; Pfeiffer, C.; Sumida, K.; Sumby, C. J.; Falcaro, P.; Furukawa, S.; Champness, N. R.; Doonan, C. J. *CrystEngComm* **2016**, *18*, 6532-6542.

(202) Seoane, B.; Castellanos, S.; Dikhtiarenko, A.; Kapteijn, F.; Gascon, J. *Coord. Chem. Rev.* **2016**, *307, Part 2*, 147-187.

(203) Sabetghadam, A.; Seoane, B.; Keskin, D.; Duim, N.; Rodenas, T.; Shahid, S.; Sorribas, S.; Guillouzer, C. L.; Clet, G.; Téllez, C.; Daturi, M.; Coronas, J.; Kapteijn, F.; Gascon, J. *Adv. Funct. Mater.* **2016**, *26*, 3154-3163.

(204) Kang, Z.; Peng, Y.; Hu, Z.; Qian, Y.; Chi, C.; Yeo, L. Y.; Tee, L.; Zhao, D. *J. Mater. Chem. A* **2015**, *3*, 20801-20810.

(205) Rodenas, T.; Luz, I.; Prieto, G.; Seoane, B.; Miro, H.; Corma, A.; Kapteijn, F.; Llabrés i Xamena, F. X.; Gascon, J. *Nat. Mater.* **2015**, *14*, 48-55.

(206) Sanchez, C.; Julian, B.; Belleville, P.; Popall, M. *J. Mater. Chem.* **2005**, *15*, 3559-3592.

(207) Shahid, S.; Nijmeijer, K.; Nehache, S.; Vankelecom, I.; Deratani, A.; Quemener, D. *J. Membr. Sci.* **2015**, *492*, 21-31.

(208) Shahid, S.; Nijmeijer, K. *J. Membr. Sci.* **2014**, *470*, 166-177.

(209) Hwang, S.; Chi, W. S.; Lee, S. J.; Im, S. H.; Kim, J. H.; Kim, J. *J. Membr. Sci.* **2015**, *480*, 11-19.

(210) Sánchez-Laínez, J.; Zornoza, B.; Friebe, S.; Caro, J.; Cao, S.; Sabetghadam, A.; Seoane, B.; Gascon, J.; Kapteijn, F.; Le Guillouzer, C.; Clet, G.; Daturi, M.; Téllez, C.; Coronas, J. *J. Membr. Sci.* **2016**, *515*, 45-53.

(211) Brown, A. J.; Brunelli, N. A.; Eum, K.; Rashidi, F.; Johnson, J. R.; Koros, W. J.; Jones, C. W.; Nair, S. *Science* **2014**, *345*, 72-75.

(212) Biswal, B. P.; Bhaskar, A.; Banerjee, R.; Kharul, U. K. *Nanoscale* **2015**, *7*, 7291-7298.

(213) Cacho-Bailo, F.; Caro, G.; Etxeberria-Benavides, M.; Karvan, O.; Téllez, C.; Coronas, J. *Chem. Commun.* **2015**, *51*, 11283-11285.

(214) Cacho-Bailo, F.; Catalán-Aguirre, S.; Etxeberría-Benavides, M.; Karvan, O.; Sebastian, V.; Téllez, C.; Coronas, J. *J. Membr. Sci.* **2015**, *476*, 277-285.

(215) Cacho-Bailo, F.; Caro, G.; Etxeberria-Benavides, M.; Karvan, O.; Téllez, C.; Coronas, J. *RSC Adv.* **2016**, *6*, 5881-5889.

(216) Férey, G. *Eur. J. Inorg. Chem.* **2016**, *2016*, 4275-4277.

(217) Dechnik, J.; Nuhnen, A.; Janiak, C. *Cryst. Growth Des.* **2017**, in press, http://dx.doi.org/10.1021/acs.cgd.7b00202.

(218) Perea-Cachero, A.; Dechnik, J.; Lahoz, R.; Janiak, C.; Téllez, C.; Coronas, J. *CrystEngComm* **2017**, *19*, 1470-1478.

(219) Dechnik, J.; Mühlbach, F.; Dietrich, D.; Wehner, T.; Gutmann, M.; Lühmann, T.; Meinel, L.; Janiak, C.; Müller-Buschbaum, K. *Eur. J. Inorg. Chem.* **2016**, *27*, 4408-4415.

(220) *Solidworks*, Dassault Systèmes SolidWorks Corp.: 2017. http://www.solidworks.com

(221) Liu, C.; McCulloch, B.; Wilson, S. T.; Benin, A. I.; Schott, M. E. Metal organic framework—polymer mixed matrix membranes. US 7.637.983 B1, Dez 29, 2009.

(222) Schoenecker, P. M.; Carson, C. G.; Jasuja, H.; Flemming, C. J. J.; Walton, K. S. *Ind. Eng. Chem. Res.* **2012**, *51*, 6513-6519.

(223) Gaab, M.; Trukhan, N.; Maurer, S.; Gummaraju, R.; Müller, U. *Microporous Mesoporous Mater.* **2012**, *157*, 131-136.

(224) Rezk, A.; Al-Dadah, R.; Mahmoud, S.; Elsayed, A. *International Journal of Heat and Mass Transfer* **2012**, *55*, 7366-7374.

(225) Furukawa, H.; Gándara, F.; Zhang, Y.-B.; Jiang, J.; Queen, W. L.; Hudson, M. R.; Yaghi, O. M. *J. Am. Chem. Soc.* **2014**, *136*, 4369-4381.

(226) Biemmi, E.; Darga, A.; Stock, N.; Bein, T. *Microporous Mesoporous Mater.* **2008**, *114*, 380-386.

(227) Nijem, N.; Fürsich, K.; Kelly, S. T.; Swain, C.; Leone, S. R.; Gilles, M. K. *Cryst. Growth Des.* **2015**, *15*, 2948-2957.

8. Anhang

8.1 MOF-fillers, graphical representations and structure descriptions[iii]

8.1.1 HKUST-1

3D-$[Cu_3(btc)_2(H_2O)_3]$ (also called HKUST-1 or Cu-btc, btc = benzene-1,3,5-tricarboxylate) contains $\{Cu_2\}$ units coordinated by four carboxylate groups in the well-known paddle-wheel structure of copper acetate. $\{Cu_2(btc)_4\}$ building unit and views of the packing diagram with the cubic unit cell of 3D-$[Cu_3(btc)_2(H_2O)_3]\cdot\sim 10H_2O$ (HKUST-1, a = 26.34 Å) are shown to illustrate the zeolite analogy of this highly symmetric and porous framework. The 3D-coordination polymer $[Cu_3(btc)_2(H_2O)_3]$ crystallizes with formation of a highly porous cubic structure with a complicated 3D network of channels. Along the a-axis there are large square channels of 9x9 $Å^2$. The disordered water molecules in the pores are not shown, nor are the H atoms on the aqua ligands and on carbon in the packing diagrams. The different objects are not drawn to scale.[150]

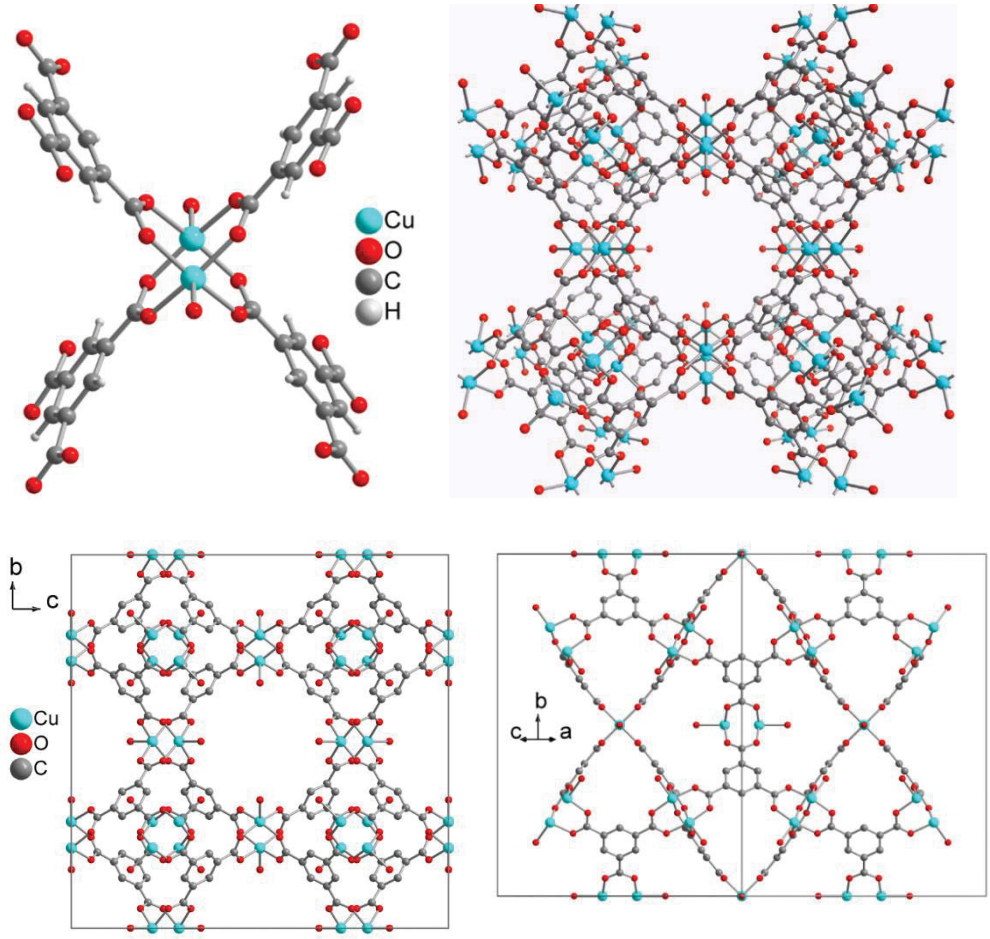

Figure 29 Structural depiction of HKUST-1

[iii] The following sections were published as electronic supporting information of the publication "Enhancing Mixed-Matrix Membrane Performance with Metal-Organic Framework Additives" *Cryst. Growth Des.*, **2017,** in press, 10.1021/acs.cgd.7b00595 from Ref.[1].

8.1.2 MOF-5

Section of the crystal packing diagram of MOF-5 (also named IRMOF-1). Six carboxylate groups span the six edges of the {Zn_4O} secondary building unit, a tetrahedron (depicted at left in polyhedral presentation) in an octahedral fashion to yield the three-dimensional primitive cubic pcu-a or cab, network shown here as ball-and-stick and as space-filling representation. The yellow sphere with a radius of 5 Å takes into account the van-der-Waals radii of the framework walls.[158]

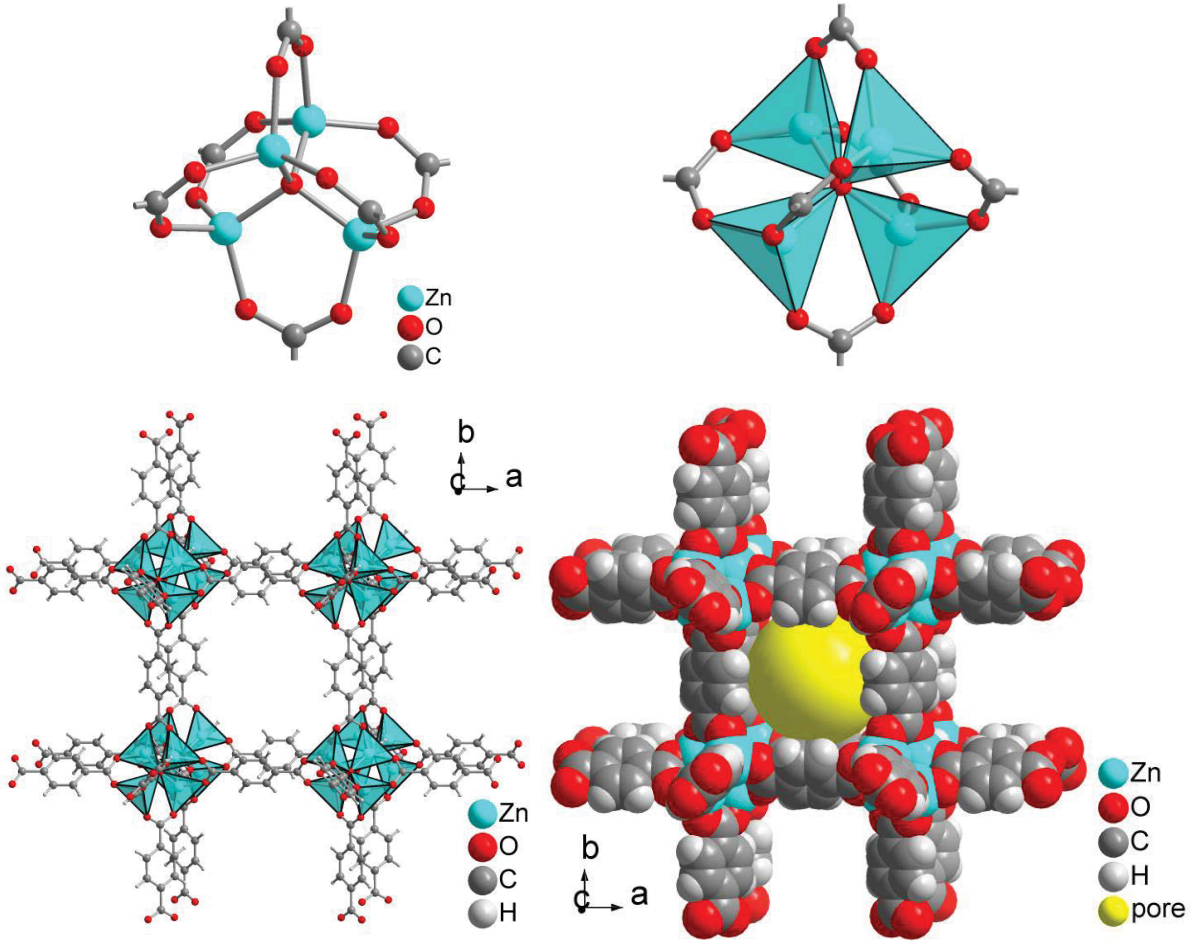

Figure 30 Structural depiction of MOF-5

8.1.3 MIL-53(M)

The important MIL-type structure [M(bdc)(μ-OH)], MIL-53(*M*) can contain *M* = Al(III)[169], Cr(III)[152] or Fe(III)[170] with benzene-1,4-dicarboxylate (bdc, terephthalate) as the linker. The framework of MIL-53 is a very flexible, 'breathing'-type network, that is, it can assume different shapes and porosities depending on the presence or absence of guest interactions.

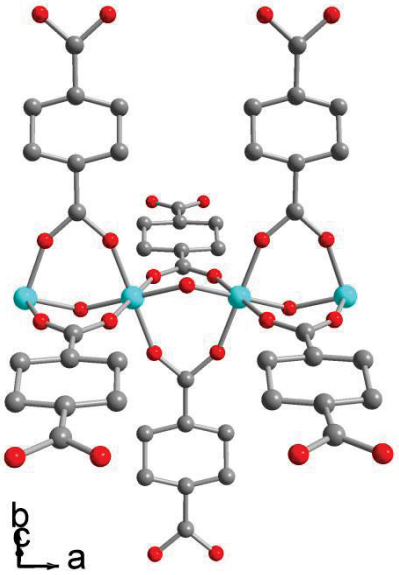

Figure 31 Section of the bdc- and OH^- bridged Al-strand of MIL-53

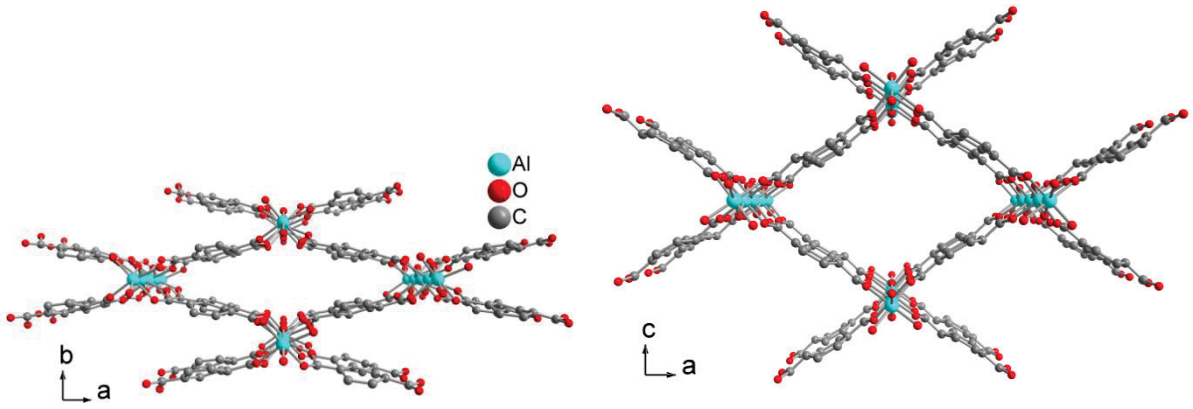

MIL-53*lt* MIL-53*as* = MIL-53*ht*

Figure 32 Section of the packing diagram of [Al(bdc)(μ-OH)], MIL-53(Al) with a flexible, 'breathing' network adapting to guest molecules. Each benzene-1,4-dicarboxylate ligand bridges between four Al atoms. The hydroxido-bridging occurs along the metal chains in the *b* direction. The channels can contain guest molecules in the *as*-synthesized high-temperature (*ht*) structure (MIL-53*as*) (right, guest molecules not shown) or be empty after a thermal guest removal in the identical activated high-temperature, large pore structure MIL-53*ht*. Cooling down to room temperature with adsorption of water from air then transforms the structure into the low-temperature, narrow pore form MIL-53*lt* (left).

8.1.4 MIL-101(*M*)

Compounds 3D-[$Cr_3(O)(bdc)_3(F,OH)(H_2O)_2$] · *n* H_2O or MIL-101(*M*) [94]

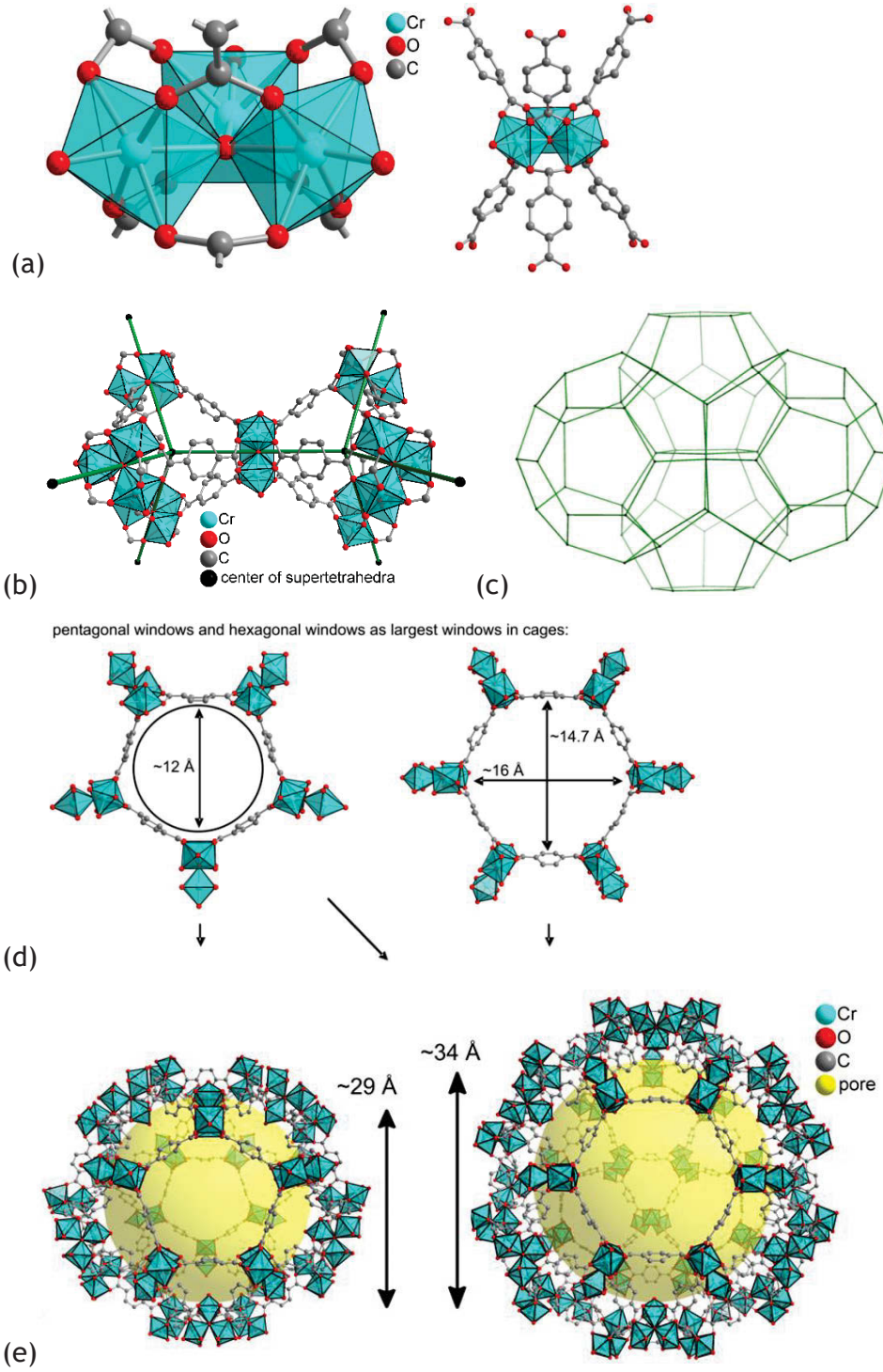

Figure 33 Building blocks for MIL-101(Cr). The benzene-1,4-dicarboxylate ligands bridge between trinuclear {Cr_3O} building units. (a) Trinuclear {$Cr_3(\mu_3\text{-}O)(bdc)_6(F,OH)(H_2O)_2$} building unit; (b) supertetrahedra; (c) mesoporous network of MTN zeolite topology; (d) the largest aperture windows of the mesoporous cages are pentagonal and hexagonal rings (windows); (e) small cage with pentagonal windows and large cage with pentagonal and hexagonal windows with pore diameters (yellow spheres). The yellow spheres in the mesoporous cages with diameter of 29 or 34 Å, respectively, take into account the van-der-Waals radii of the framework walls (water-guest molecules are not shown). Objects in (a) to (e) are not drawn to scale. Graphics have been created from the deposited cif-file for MIL-101Cr (CSD-Refcode OCUNAK).

8.1.5 MIL-125

For compound 3D-$[Ti_8O_8(OH)_4(bdc)_6]$ the SBU is an eight-membered ring of edge- and vertex-sharing TiO_6 octahedra, which is connected to 12 neighboring SBUs in a body-centered cubic (bcc) packing arrangement.[104]

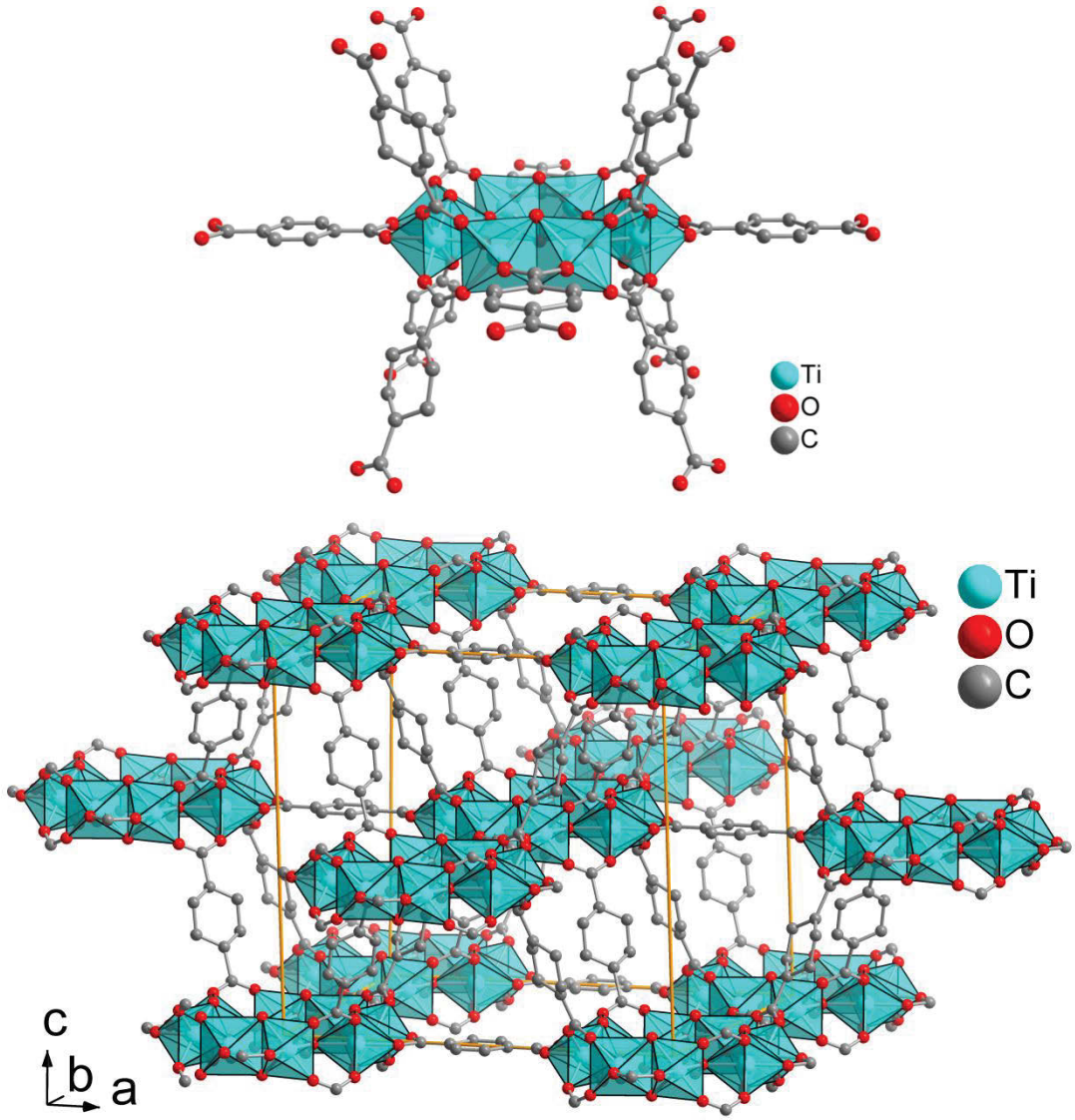

Figure 34 Structural depiction of MIL-125

8.1.6 CAU-1

3D-$[Al_4(OH)_2(OCH_3)_4(H_2N\text{-}bdc)_3]\cdot nH_2O$ - synthesized from 2-amino-terephthalic acid ($bdcH_2\text{-}NH_2$) and $AlCl_3$ in methanol - stable up to 580 K and built from $\{Al_8(OH)_4(OCH_3)_8\}^{12+}$ units.[141]

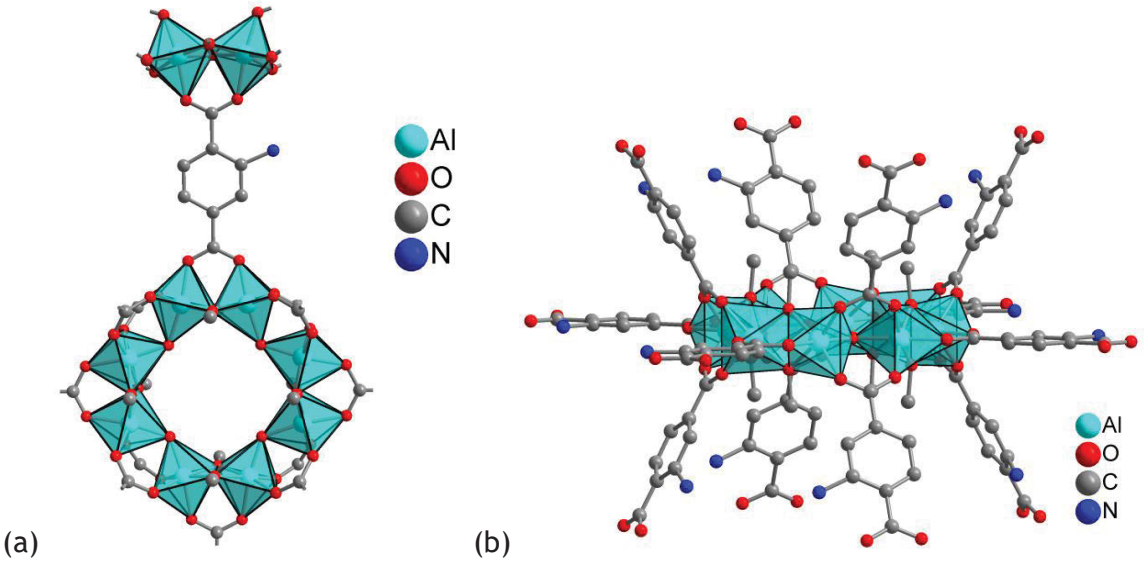

Figure 35 $\{Al_8(OH)_4(OCH_3)_8\}^{12+}$ building unit in polyhedral presentation in (a) top view showing only one of the 12 bdc-NH_2 connections and (b) side view with all 12 connecting bdc-NH_2 linkers to adjacent units. The NH_2-groups on the aromatic terephthalate ring are disordered.

Each Al_8-SBU is surrounded and interconnected by 12 amino-terephthalate anions to enclose tetrahedrally- and octahedrally-shaped voids with inner diameters of 0.5 and 1.0 nm, respectively.

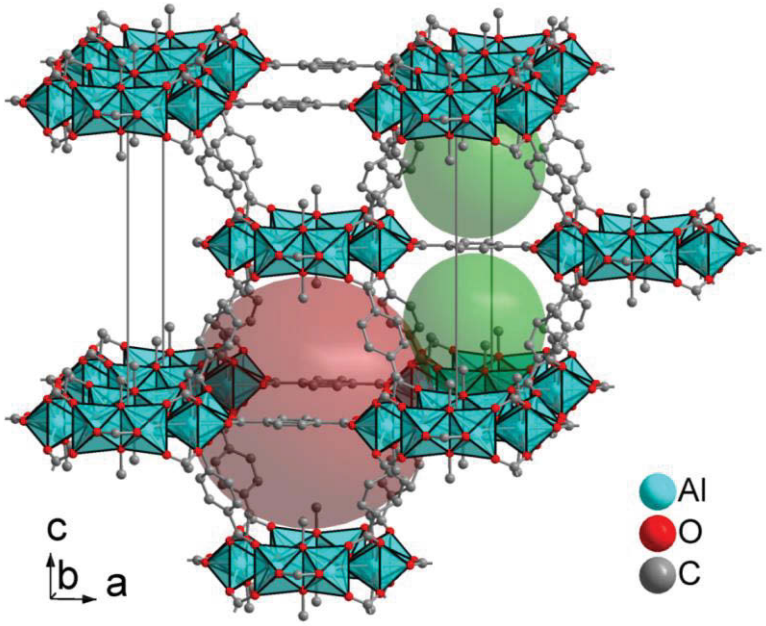

Figure 36 Packing diagram of 3D-$[Al_4(OH)_2(OCH_3)_4(bdc\text{-}NH_2)_3]\cdot xH_2O$ (CAU-1) with the two main types of octahedral (red) and tetrahedral (green) voids. Crystal water molecules in the voids are not shown. The body-centered cubic (bcc) packing arrangement corresponds to MIL-125 (see above).

8.1.7 UiO-66

In 3D-[$Zr_6O_4(OH)_4(bdc)_6$] the inner $Zr_6O_4(OH)_4$ core has the triangular faces of the Zr_6-octahedron alternatively capped by *μ_3-O* and *μ_3-OH groups*. The weakly bound μ_3-OH groups in this SBU can be reversibly dehydrated. The Zr-MOF structures can extended from phenyl over biphenyl to terphenyl with increasing length of the linkers forming 3D-[$Zr_6O_4(OH)_4(O_2C$-aryl-$CO_2)_6$] or UiO-66 to UiO-68 (scale chemistry = isoreticular chemistry). [128,131]

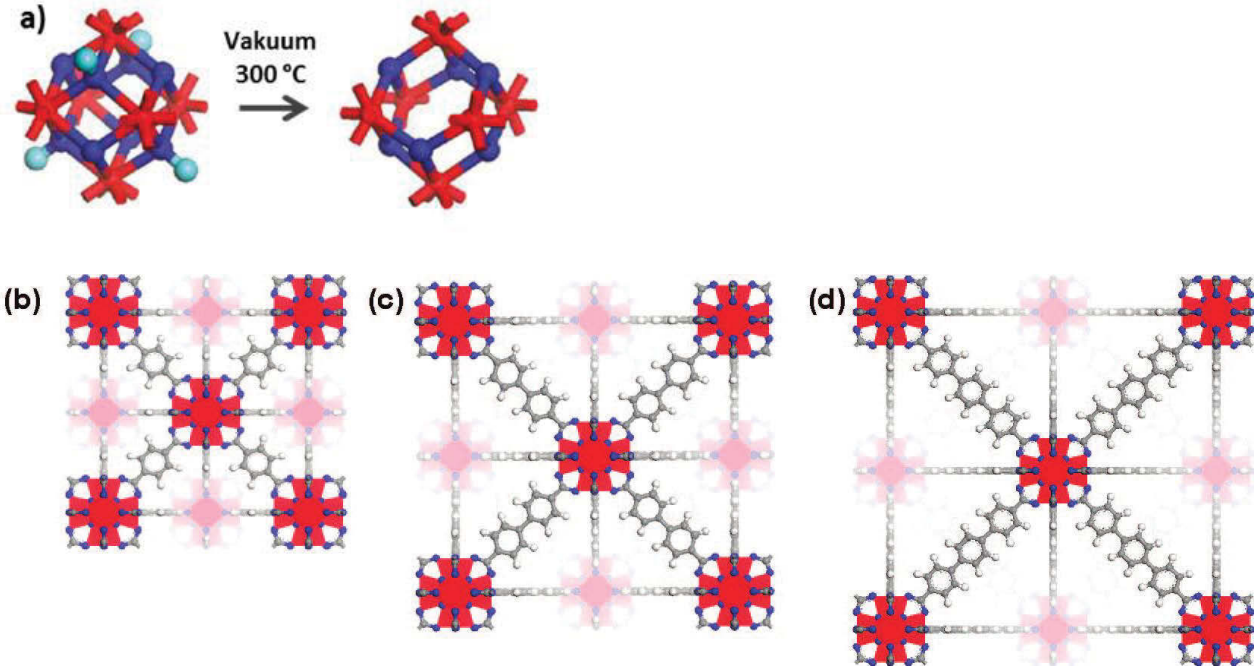

Figure 37 (a) dehydration of μ_3-OH groups in the SBU of [$Zr_6O_4(OH)_4(bdc)_6$], (b) Zr-MOF with 1,4-benzene-dicarboxylate (bdc) as linker, UiO-66, (c) Zr-MOF with 4,4'-biphenyl-dicarboxylate (bpdc) as linker, UiO-67, (d) Zr-MOF with terphenyl dicarboxylate (tpdc) as linker, UiO-68.

The {$Zr_6O_4(OH)_4$}- or {$Zr_6O_4(OH)_4(-CO_2)_{12}$}-SBU is 12 coordinated, the highest coordination reported for a MOF. 12-coordination is also the coordination of metal atoms in closed packed metal structures. The Zr-MOF structures formed with linear ligands are therefore expanded versions of the cubic close packed (CCP) structure (= fcc).

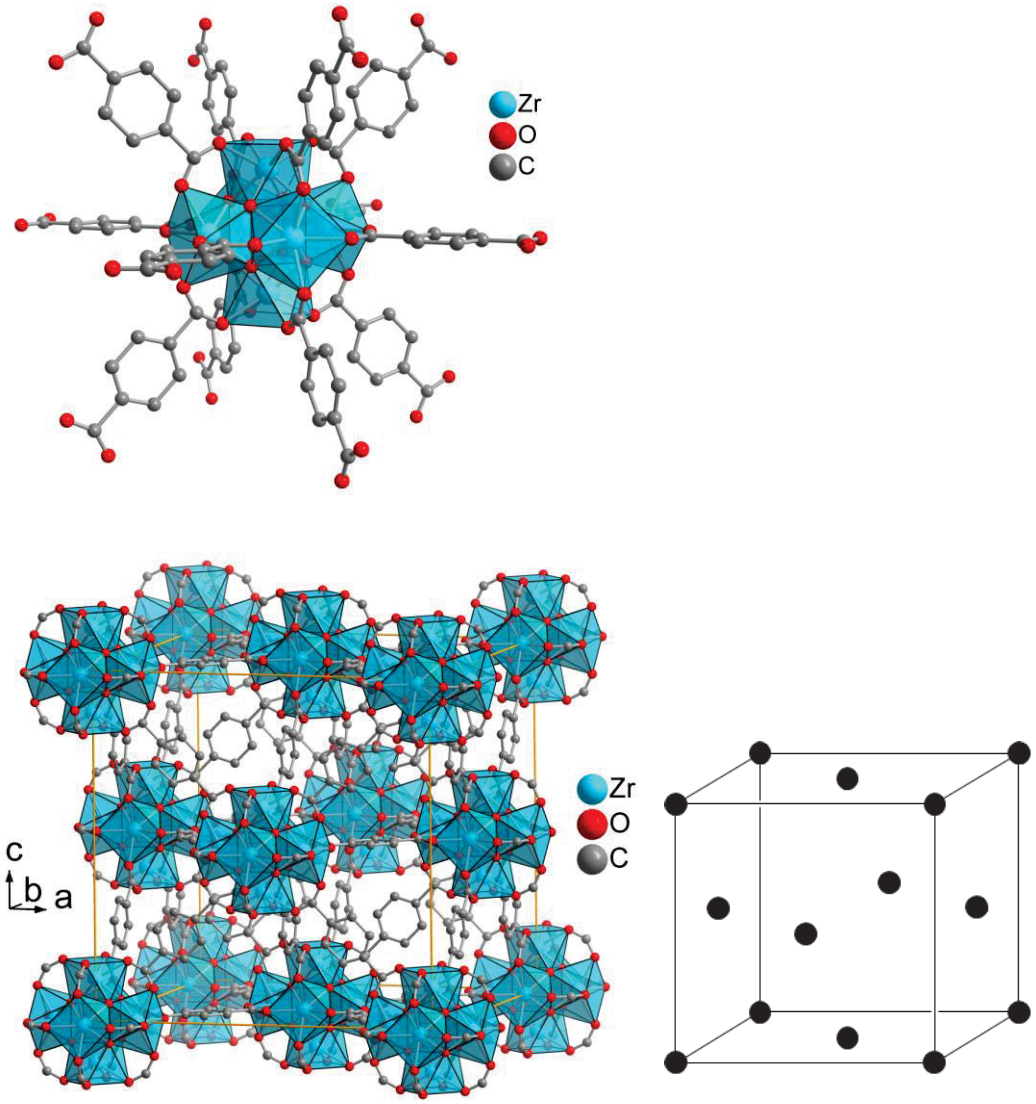

Figure 38. The SBU of UIO-66 is an octahedral cluster of six edge-sharing ZrO_8 square-antiprism, which is connected to 12 neighboring SBUs in a face-centered cubic (fcc) packing arrangement.

8.1.8 ZIFs

Zeolitic imidazolate frameworks or ZIFs are constructed from the bridging action of the anionic imidazolate ligand (or its derivatives) between zinc atoms. The imidazolate function in ZIFs do not tend to form metal clusters, which could serve as secondary building blocks (SBUs). ZIFs are porous but with less open pores than other MOFs due to smaller pore aperture windows. Access in ZIFs is limited to smaller molecules.

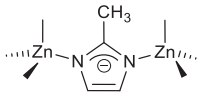

Figure 39 Bridging imidazolate ligand (or its derivatives) between zinc atoms in the Network of ZIF-8.

8.1.8.1 ZIF-8

3D-[Zn-$(mim)_2$]: The ZIF-8, [Zn(2-methylimidazolate)$_2$] pore aperture has a diameter of 3.4 Å allowing it to readily absorb small molecules such as H_2 and CO_2. Topologically ZIF-8 and ZIF-90 form sodalite frameworks. ZIF-8 is one of the most hydrolytically stable MOFs. [134-135]

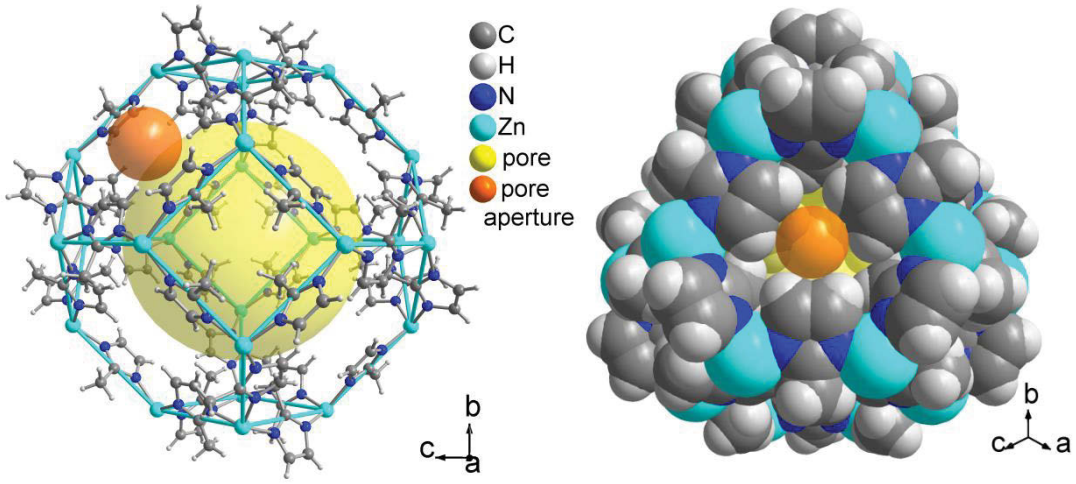

Figure 40 Section of the crystal packing diagram of ZIF-8. 2-Methylimidazolate ligands bridge between single zinc atoms and span the edges of a sodalite cage which is depicted by the blue topological lines connecting the Zn atoms. The yellow sphere with a diameter of 12 Å highlights the inner pore of the sodalite cage, the orange sphere with a diameter of 3.4 Å the pore aperture window of the six-membered rings. Both spheres take into account the van-der-Waals radii of the framework atoms.

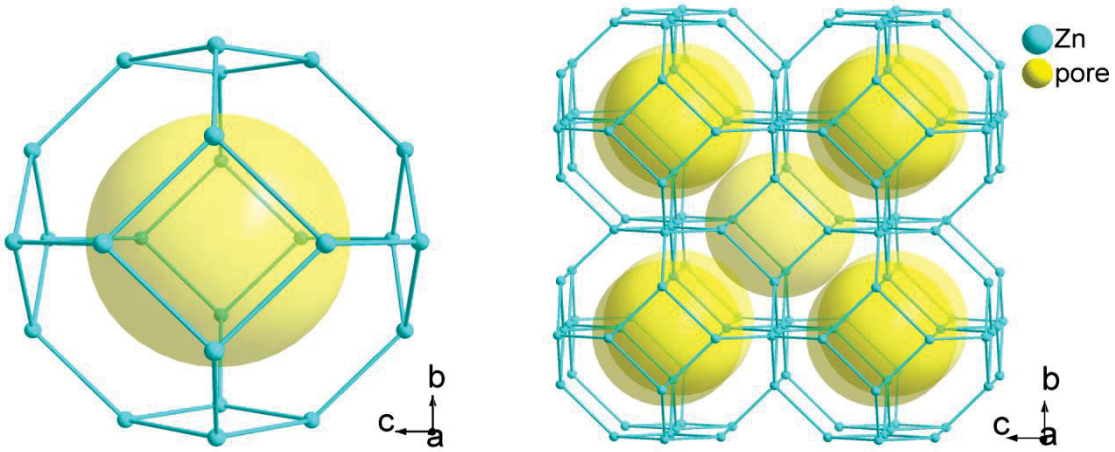

Figure 41 One and nine sodalite cages - depicted by the blue topological lines connecting the Zn atoms.

A charge density distribution study suggests exceptional electrostatic flexibility of the ZIF-8 framework, where small conformational changes lead to a significantly different electrostatic potential (EP) distribution, a feature which could be important for the function and dynamics of the ZIF-8 framework.[138]

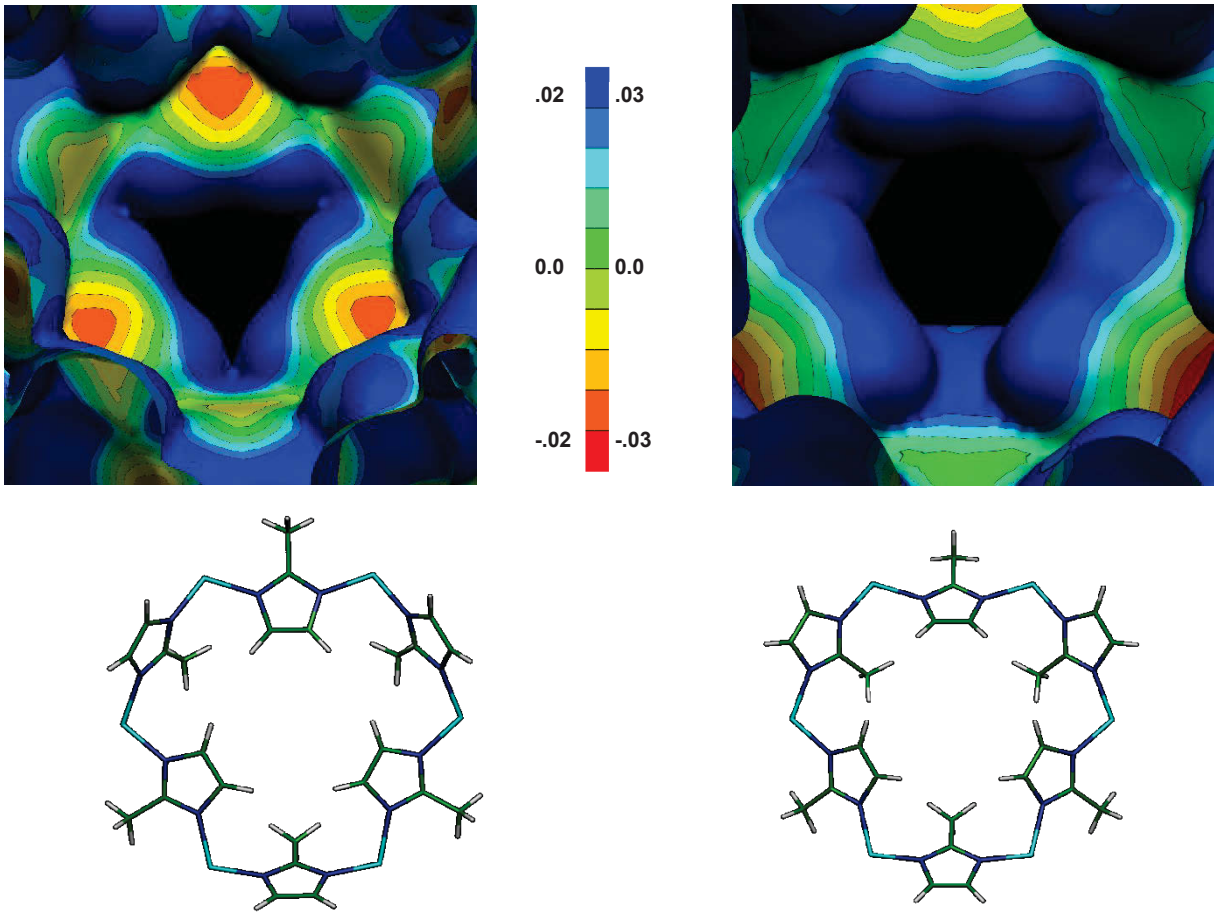

Figure 42 3D representation of the electrostatic potential on the molecular surface surrounding the two sides of the six-membered ring apertures (cf. orange sphere in above structure) in two configuration models:[138]

8.1.8.2 ZIF-7

The sodalite framework of ZIF-8 (see above) is changed to the zeolite-A (LTA) topology when replacing the imidazolate ligand by benzimidazolate to yield [Zn(benzimidazolate)$_2$], ZIF-7. Section of the crystal packing diagram of ZIF-7. Benzimidazolate ligands bridge between single zinc atoms and span the edges of a distorted cuboctahedral ▫-cage in the zeolite-A network, which is depicted by blue topological lines connecting the Zn atoms.[177]

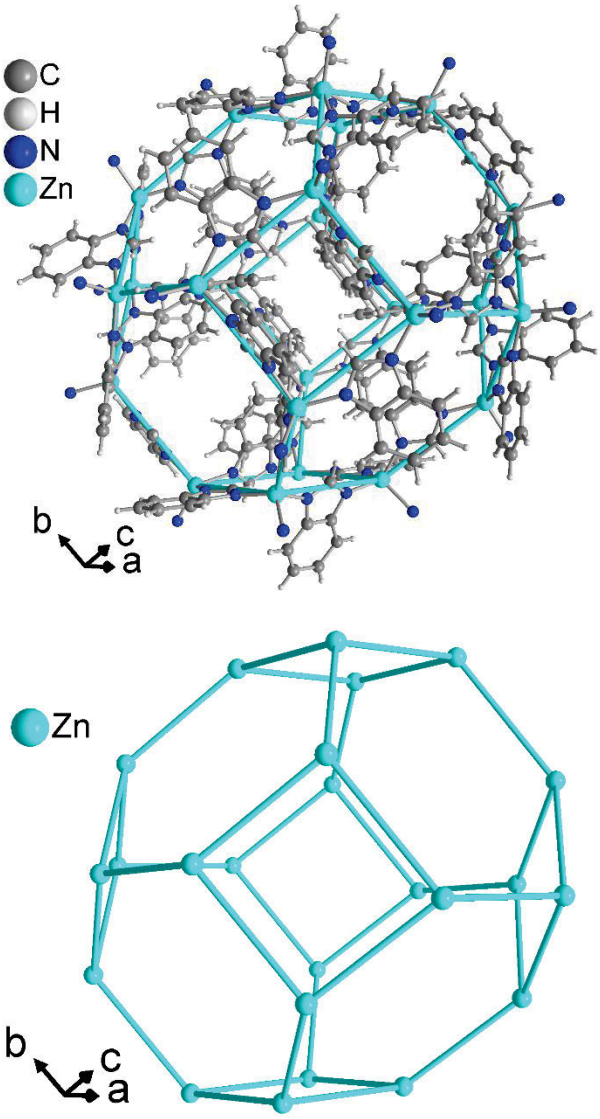

Figure 43 Structural depiction of ZIF-7

8.1.9 3D-[Zn(pyrazine)$_2$(SiF$_6$)], SiFSIX-3-Zn

The zinc(II) centre is octahedrally coordinated by four nitrogen atoms of four pyrazine ligands in an equatorial plane and by two axial hexafluoridosilicate, SiF_6^{2-} ions. In the equatorial plane, the pyrazine ligands bridge the zinc ions to produce 2D-{Zn(pyrazine)$_2$} grids with the closest Zn–Zn distance of 7.1 Å. In addition, the SiF_6^{2-} groups bridge zinc ions to 1D-{Zn(SiF$_6$)} chains with a Zn–Zn distance of 7.6 Å. Together the 2D-grids and 1D-chains yield an open three-dimensional framework. The neutral 3D-framework of [Zn(pyrazine)$_2$(SiF$_6$)] has open channels only along the *c* axis. The channels along *c* have a squared cross section of 4.5 x 4.5 Å^2 and are surrounded by pyrazine planes. Along *a* and *b* the space-filling view shows much smaller open channels, which could however open up (and subsequently close along *c*) upon rotation of the pyrazine rings.[195-196]

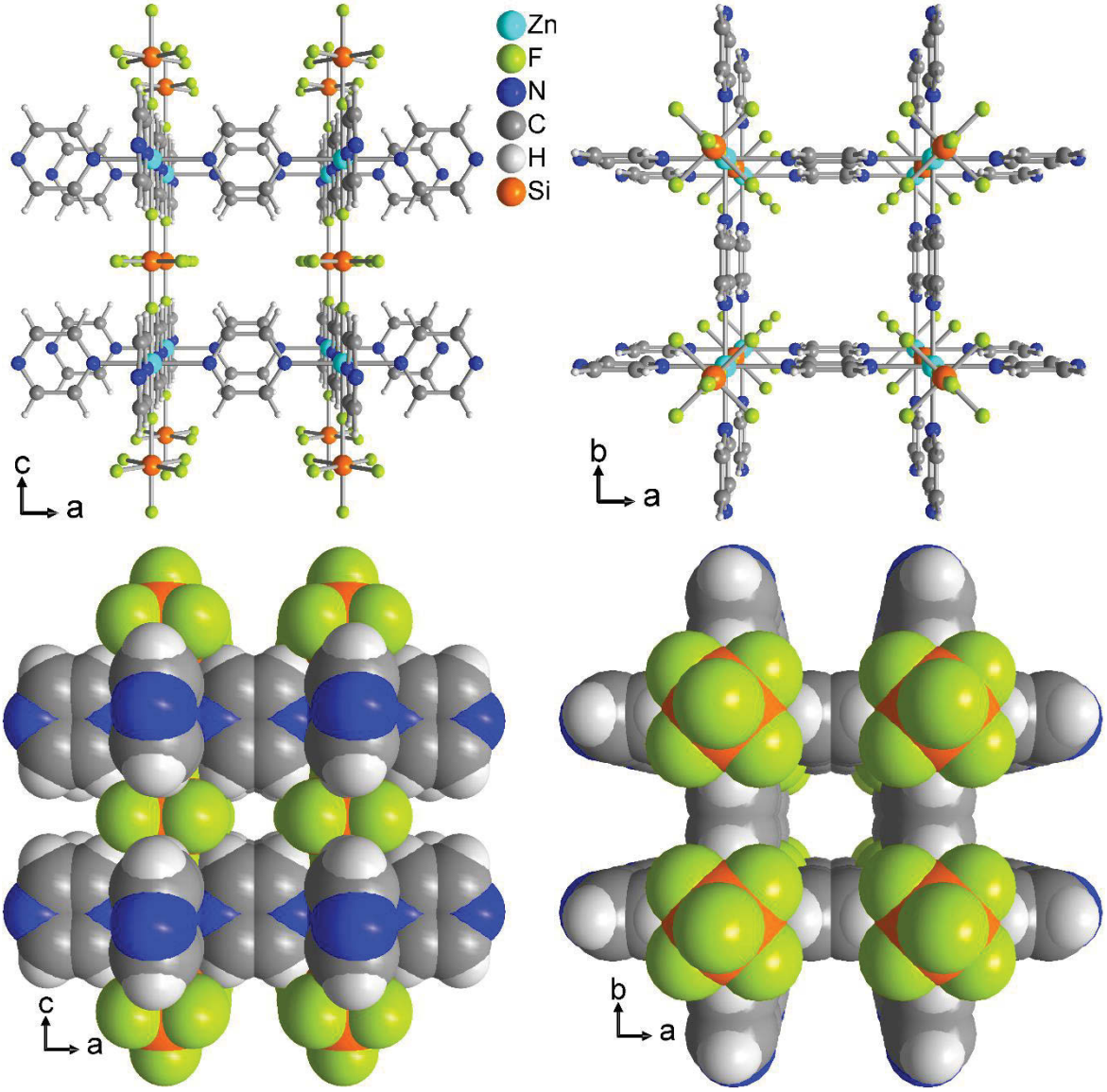

Figure 44 Structural depiction of [Zn(pyrazine)$_2$(SiF$_6$)]

Eidesstattliche Erklärung

Die hier vorliegende Dissertation habe ich selbstständig und ohne unerlaubte Hilfsmittel angefertigt. Die Dissertation wurde in der vorgelegten oder in ähnlicher Form noch bei keiner anderen Institution eingereicht. Ich habe bisher keine erfolglosen Promotionsversuche unternommen.

Janina Dechnik

Düsseldorf, den ___.___._____ _____

(Unterschrift)